Herstellung und Analyse von biopolymerbasierten Fasermaterialien

DISSERTATION

zur Erlangung des akademischen Grades eines
Doktors der Naturwissenschaften (Dr. rer. nat.)
in der Bayreuther Graduiertenschule für Mathematik und Naturwissenschaften
(BayNAT)
der Universität Bayreuth

vorgelegt von

Christian Haynl

aus *Erlangen*

Bayreuth, 2020

Die vorliegende Arbeit wurde in der Zeit von September 2013 bis März 2019 in Bayreuth am Lehrstuhl Biomaterialien, Fakultät für Ingenieurwissenschaften, unter Betreuung von Herrn Professor Dr. Thomas Scheibel angefertigt.

Vollständiger Abdruck der von der Bayreuther Graduiertenschule für Mathematik und Naturwissenschaften (BayNAT) der Universität Bayreuth genehmigten Dissertation zur Erlangung des akademischen Grades eines Doktors der Naturwissenschaften (Dr. rer. nat.).

Dissertation eingereicht am:	21.04.2020
Zulassung durch das Leitungsgremium:	30.04.2020
Wissenschaftliches Kolloquium:	19.10.2020

Amtierender Direktor: Prof. Dr. Markus Lippitz

Prüfungsausschuss:

Prof. Dr. Thomas Scheibel	(Gutachter)
Prof. Dr. Hans-Werner Schmidt	(Gutachter)
Prof. Dr. Birte Höcker	(Vorsitz)
Prof. Dr. Stefan Schuster	

ZUSAMMENFASSUNG

Im Laufe der Evolution hat die Natur Materialien mit bemerkenswerten Eigenschaften hervorgebracht, welche heutzutage vom Menschen entweder direkt verarbeitet werden oder als Vorbild für das Design synthetischer Materialien dienen. Hierbei sind besonders Kollagenfasern und Spinnenseide in den Fokus der Wissenschaft und Industrie gerückt. Kollagen bildet den Hauptbestandteil der extrazellulären Matrix in Wirbeltieren und ist aufgrund seiner biologischen Funktionalität für den Einsatz in der Biomedizin prädestiniert. Spinnenseide glänzt durch eine außergewöhnlich hohe mechanische Stabilität und ermöglicht die Absorption von Energie wie keine andere von der Natur oder von Menschenhand geschaffene Faser.

Gegenstand des ersten Teils der Arbeit bestand vorwiegend darin, zwei mikrofluidische Faserspinn-Verfahren zur Herstellung von Fasermaterialien mit verbesserten oder neuartigen Eigenschaften zu generieren.
In beiden mikrofluidischen Faserspinn-Verfahren wurde die Bildung von Fasern mittels hydrodynamischer Fokussierung eines zentralen (Bio)-Polymerlösungsflusses durch zwei dazu rechtwinklig-zuströmende Mantelflüsse eingeleitet.
Im ersten mikrofluidischen Faserspinn-Verfahren wurde zur Evaluierung der Prozessparameter ein kontinuierlicher Fluss einer Modell-Polymerlösung durch zwei Luftströme fokussiert (Flüssig-in-Gas Flussfokussierung). In Analogie zum Lösungsblasspinnen (engl. *Solution blow spinning*) wurde hierbei die Modell-Polymerlösung als Flüssigkeitsstrahl aus einer Düse ausgestoßen, woraufhin die Verdampfung des Lösungsmittels einsetzte und isotrope Vliesstoffe oder Vliesstoffgarne erzeugt werden konnten. Zukünftig kann dieses Verfahren interessant sein, da hiermit im Gegenteil z.B. zum Elektrospinn-Verfahren auf ein elektrostatisches Feld verzichtet wird, wodurch das Risiko der Denaturierung empfindlicher (Bio)-Polymere (z.B. Kollagen) oder anderer sensitiver Verbindungen reduziert wird und sich darüber hinaus auch neue Anwendungsmöglichkeiten ergeben (z.B. *in situ* Beschichtung von lebendem Gewebe).
Das zweite mikrofluidische Faserspinn-Verfahren behandelte die Herstellung von Kollagenendlosfasern, da bisherige Nassspinn-Verfahren Kollagenfasern mit nur mäßigen mechanischen Stabilitäten erzielten und die Herstellung mit dem Einsatz organischer Lösungsmittel, potenziell zellschädigender Vernetzungsreagenzien oder dem Risiko der Kollagendenaturierung einherging. In dem mikrofluidischen Faserspinn-Verfahren wurde ein zentraler Fluss einer sauer-eingestellten Kollagenlösung mit zwei neutralen, Polyethylenglykol-haltigen Pufferflüssen hydrodynamisch fokussiert (Flüssig-in-Flüssig Flussfokussierung). Die

Interaktion der Lösungen induzierte die Bildung von Kollagenfibrillen, welche wiederum durch die hydrodynamische Fokussierung zu makroskopischen Fasern verdichtet und assembliert wurden. Der Durchmesser der dadurch generierten Fasern war durch die Flussraten der Kollagen- und Pufferlösungen, als auch durch die Faserabnahmegeschwindigkeit einstellbar. Mit finalen Durchmessern zwischen 3 und 6 µm erwiesen sich diese Fasern als signifikant dünner und mechanisch signifikant stabiler verglichen mit Kollagenfasern aus bisherigen Nassspinn-Verfahren.
Um die Kollagenfasern auf ihre Eignung für die Biomedizin, speziell als Orientierungsstruktur für die periphere Nervenreparatur zu testen, wurden neuronale Zellen auf den Kollagenfasern kultiviert und differenziert. Die Zellen adhärierten auf den Kollagenfasern, zeigten elektrophysiologische Aktivität und ihre Neurite richteten sich effektiv entlang der Faserlängsachsen aus. Auch konnten die Kollagenfasern als Füllmaterial exemplarisch in Nervenleitröhren aus rekombinanter Spinnenseide eingesetzt werden. Alternativ zu vorgefertigten Nervenleitröhren aus rekombinanter Spinnenseide konnte mit selbst-rollenden Filmen zudem der simultane Einschluss von Füllmaterial und neuronalen Zellen praktikabler und schonender gestaltet werden.

Im zweiten Teil dieser Arbeit wurde im Rahmen eines mehrmonatigen Aufenthalts an der University of Melbourne die bisher materialanalytisch-undokumentierte Spinnenseide der australischen Krabbenspinne *Saccodomus formivorus* untersucht. Im Gegensatz zu Radnetzen und anderen Spinnenseidennetztypen besitzen die körbchenartigen Netze von *S. formivorus* eine grundsätzlich andere Gestalt und deuten bereits durch ihre Haptik auf eine außergewöhnliche Formstabilität hin. Die Körbchennetze wurden grundlegend licht- und rasterelektronenmikroskopisch untersucht. Dabei wurde festgestellt, dass die Seidenstränge des Netzes aus einem Verbund aus Mikrofasern und Submikrofasern bestehen. Mittels Synchrotron-Infrarotmikrospektroskopie wurde in beiden Fasertypen im Verbund ein unterschiedlicher Gehalt an C-O-C und C-OH-Gruppen ermittelt. Weiterhin zeigte sich, dass diese Verbundfasern signifikant geringere Werte für die Zugfestigkeit und das E-Modul im Vergleich zur *Major Ampullate* und *Minor Ampullate* Seide von Radnetzspinnen annahmen und keine Ähnlichkeit zum elastischen Materialverhalten der *Flagelliform* Seide besaßen. Jedoch waren die absoluten lateralen Widerstandskräfte der Verbundfasern gegenüber der *Major Ampullate* Seide der Modelradnetzspinne *Nephila edulis* deutlich erhöht. Aufgrund der strukturellen Ähnlichkeit beider Fasertypen mit den Fasern des Eierkokons anderer Spinnenarten wird angenommen, dass das Beutefangnetz von *S. formivorus* eine Erweiterung des ursprünglichen Eierkokons ist.

Zusammenfassend wurde mit dieser Arbeit einerseits eine neue Technologie geschaffen, um Vliesstoffe und -garne flexibel und ohne Einsatz eines elektrischen Feldes herzustellen. Darüber hinaus wurde die Herstellung von Kollagenendlosfasern mit verbesserten Eigenschaften im Vergleich zu früheren Pendants ermöglicht, welche zudem Anwendungspotenzial in der peripheren Nervenreparatur zeigten.

Die Erkenntnisse über die Spinnenseide von *S. formivorus* liefern hingegen wertvolle Einsichten in die Evolution des Spinnenseidennetzbaus und inspirieren die Entwicklung von neuen Fasermaterialien mit formstabilen Eigenschaften.

SUMMARY

Throughout the course of evolution, nature has generated remarkable materials. These materials can be used for various applications by processing them directly or using them as a blueprint for synthetic materials. Herein, collagen fibers and spider silk receive much attention in science and industry. Collagen forms the major component of the extracellular matrix in vertebrates and is well-suited for applications in biomedicine due to its biological functionality. Spider silk impresses due to its extraordinary high mechanical stability, thus enabling absorption of energy no other natural or synthetic fiber can compete with.

Part one of this dissertation dealt mainly with two microfluidic fiber spinning processes, which were used in order to produce fiber materials with improved or novel properties. In both microfluidic fiber spinning processes, the formation of fibers was induced using a core flow of a (bio)-polymer solution, which was hydrodynamically-focused by two perpendicularly-oriented sheat flows.

The first microfluidic fiber spinning process used a continuous flow of a model polymer solution in order to evaluate the process parameters. The model polymer solution was focused by two air flows (liquid-in-gas flow focusing). In accordance with solution blow spinning, the model polymer solution was jetted through a nozzle out of the device, followed by solvent evaporation and formation of isotropic nonwovens and nonwoven yarns. This process is of interest, as in contrast to, e.g. electro spinning, no electrostatic field is required, thereby the extend of denaturation of sensitive (bio)-polymers (e.g. collagen) or other sensitive compounds is reduced. Moreover, with using this process, other applications, such as *in situ* coating of living tissue, can be enabled.

The second microfluidic fiber spinning process concerned the fabrication of endless collagen fibers, since previous wet spinning devices yielded collagen fibers with only moderate mechanical stabilities. Furthermore, the previous wet-spun collagen fibers were associated with the use of organic solvents, putative cell toxic cross-linking agents and the chance of collagen denaturation. The microfluidic fiber spinning process based on a core flow comprising an acidic collagen solution, which was hydrodynamically-focused by two flows comprising neutral buffer solutions with polyethylene glycol (liquid-in-liquid flow focusing). The interaction of those solutions induced the formation of collagen fibrils. The latter ones were compressed and assembled using the hydrodynamic focusing, finally yielding macroscopic fibers. The diameter of those fibers depended on the collagen and buffer flow rates, as well as on the fiber collection velocity. The final fiber diameters laid in the range of 3 to 6 µm, thus those fiber diameters

were significantly lower compared to the values of collagen fibers originating from wet spinning devices. Furthermore, the collagen fibers produced using the microfluidic device exhibited a significantly higher mechanical stability.
In order to test the collagen fibers for peripheral nerve repair, neuronal cells were cultivated and differentiated thereon. The cells adhered on the collagen fibers, showed electrophysiological activity and their neurites were elongated along the fiber axes. The collagen fibers were further used as a filler for tubular nerve guidance conduits made of recombinant spider silk. As an alternative to prefabricated conduits, self-rolling films could be used to gently achieve the simultaneous incorporation of filler material and neuronal cells.

The second part of this work was carried out within a several months research stay at the University of Melbourne and focused on the, so far, structurally-undocumented silk of the Australian crab spider *Saccodomus formivorus*. In contrast to orb webs and other spider silk webs, those of *S. formivorus* are basket-like and indicate an extraordinary dimensional stability. The basket webs were examined using light- and scanning electron microscopy, revealing that the silk threads comprise a composite structure made of micro- and submicron fibers. Using synchrotron infrared microspectroscopy, both fiber types in the composite thread showed a distinct content of C-O-C and C-OH groups. Furthermore, the composite threads exhibited a significantly lower tensile strength and Young's modulus than *Major Ampullate* and *Minor Ampullate* silk of orb weavers, and the composite threads did not possess similarity to the elastic *Flagelliform* silk. However, the lateral resilience of the composite threads was significantly increased compared to *Major Ampullate* silk of the model orb weaver *Nephila edulis*. Due to the structural similarity of both fiber types with those of egg cases of other spider species, it is supposed that the basket web is an extension of a former egg case.

In conclusion, these dissertation studies yielded a novel technology to flexibly produce nonwovens and nonwoven yarns without the need of an electrostatic field. Furthermore, the fabrication of endless collagen fibers exhibiting improved properties compared to previous collagen fibers was enabled and those fibers showed suitability in peripheral nerve repair. The findings on the spider silk of *S. formivorus* yield valuable insights into the evolution of web building and inspire the development of novel fiber materials with high dimensional stability.

1. EINLEITUNG

1.1 Biopolymere

Die Natur hat unterschiedlichste Materialien mit erstaunlichen Eigenschaften hervorgebracht. Ein prominentes Beispiel ist zweifelsohne die besondere Beschaffenheit eines Lotusblattes, welche stets eine saubere Oberfläche sicherstellt.[1] Ebenso spannend sind biopolymerbasierte Fasern, die speziell an die Umwelt angepasste Materialeigenschaften aufweisen. Biopolymere sind einerseits definiert als biologisch-abbaubare Polymere, welche von lebenden Organismen produziert werden. Prominente Vertreter sind daher Proteine und Polypeptide, Polysaccharide und Polynukleotide (DNA, RNA), aber auch beispielsweise Polyhydroxyalkanoate oder Lignin.[2-4] Andererseits werden zu den Biopolymeren auch Polymere gerechnet, dessen Ausgangssubstanzen biogenen Ursprungs sind, aber durch chemische Modifikation für die Polymerisation zugänglich gemacht wurden (z.B. Polylactide) oder eine überdurchschnittlich gute Bioabbaubarkeit und/oder Bioverträglichkeit besitzen (z.B. Polycaprolacton).[5, 6]

Chitin ist nach Zellulose das zweithäufigste Polysaccharid in der Natur und ist in Exoskeletten von Krebstieren, Insekten und in einigen Pilzen präsent. Im Hinblick auf Materialanwendungen spielt vor allem das gut lösliche Chitosan eine große Rolle, welches durch Deacetylierungsreaktion aus dem schlecht löslichen Chitin hervorgeht und als Copolymer aus den Monomeren N-Acetyl-D-glucosamin and D-Glucosamin vorliegt.[7] Ein weiteres in der Natur sehr häufig anzutreffendes Polysaccharid wird von Braunalgen und Bakterien der Gattung *Pseudomonas* und *Azotobacter* produziert und als Alginat bezeichnet. Dieses liegt ebenfalls als Copolymer vor und ist aus β-D-Mannuronat- und L-Guluronat-Einheiten aufgebaut. Alginat besitzt in Organismen strukturgebende oder schützende Funktion und dient zur Ausbildung von Biofilmen.[8] Nukleinsäuren sind Biopolymere bestehend aus Nukleotid-Bausteinen. Letztere werden jeweils aus einer Pentose, einem Phosphatrest und einer (Nukleo)-Base gebildet. In der doppelsträngigen Desoxyribonukleinsäure (DNA) liegen die vier Basen Adenin, Guanin, Cytosin und Thymin vor, wohingegen die meist einzelsträngig-vorliegende Ribonukleinsäure (RNA) anstelle von Thymin die Base Uracil trägt. Generell dient DNA in Organismen der dauerhaften Speicherung genetischer Information, während RNA vorwiegend an der Informationsübertragung beteiligt ist.[9]

1.1.1 Proteine

Proteine basieren auf Aminosäuren, welche durch Peptidbindungen miteinander konjugiert vorliegen und langkettige Moleküle bilden. In der Natur existieren mehr als 20 proteinogene Aminosäuren, welche sich voneinander in jeweils einer Seitengruppe unterscheiden. In Abhängigkeit der jeweiligen Aminosäuresequenz ergeben sich für das Protein spezifische physikalisch-chemische Eigenschaften, welche durch Glykosilierungs und/oder Glykierungsreaktionen noch weiter modifiziert werden können.[10, 11] Proteine übernehmen ein mannigfaltiges Spektrum an Aufgaben und sind unter anderem in der Signalübertragung, Immunabwehr oder am zellulären Transport beteiligt,[12-14] wodurch diese damit wesentlich an der Regulation von biologischen Prozessen und der Funktionalität von Geweben und Organen mitwirken.

1.1.1.1 Proteinfasern

Proteine sind neben den bereits genannten Aufgaben vor allem auch an der Strukturgebung in Lebewesen beteiligt. Die involvierten Strukturproteine können in intra- und extrakorporalen Materialien fungieren. Dazu assemblieren Strukturproteine gewöhnlich zu Proteinfibrillen, welche sich wiederum zu makroskopischen Proteinfasern arrangieren können. Die Assemblierungsreaktionen sind sehr komplex und unter anderem von den molekularen Interaktionen der Proteine untereinander und von den Umgebungsbedingungen, d.h. von pH-Wert, Ionenstärke, Enzymen, Temperatur und Scherkräften abhängig.[15, 16] Zu prominenten Vertretern, die an der Ausbildung intrakorporaler Proteinfasern beteiligt sind, zählt beispielsweise das extrazelluläre Kollagen und Elastin sowie das intrazelluläre Aktin.[17, 18] Im Gegensatz dazu nutzen unter anderem Spinnen, Seidenspinner und Florfliegen extrakorporale Seidenproteinfasern zum Bau von Netzen, Eierkokons und -stielen.[19-21] Aber auch Haare von Säugetieren, welche vorwiegend aus dem Protein Keratin bestehen, sowie die Muschelbyssusfäden einiger Muschelarten zählen zu den extrakorporalen Proteinfasern.[22, 23] Die mechanischen Eigenschaften der Proteinfasern haben sich im Laufe der Evolution an ihre jeweilige Funktion angepasst und gehen aus dem Zusammenspiel der intrinsischen Proteineigenschaften, involvierten Matrixproteinen und weiteren Biomolekülen hervor.[24-28] Einige dieser Proteinfasern, wie vor allem Spinnenseide, zeichnen sich durch vergleichsweise hohe Elastizitäten oder Zugfestigkeiten aus (Tabelle 1), wohingegen die Besonderheit der Eierstiele aus Florfliegenseide in der Widerstandskraft gegenüber lateraler Belastung liegt.[29] Muschelbyssusfäden, als Verbindungskomponente zwischen harten Substraten und dem weichen Muskel, wiederum offenbaren eine Gradientenstruktur, wodurch auftretende

Radialspannungen minimiert werden und dadurch einem frühen Materialversagen entgegengewirkt wird.[30]

Tabelle 1. Mechanische Eigenschaften von intra- und extrakorporalen Proteinfasern.

Fasertyp	Hauptfunktion		Bruchdehnung [%]	Zugfestigkeit [MPa]	E-Modul [GPa]
Kollagenfaser[31, 32]	Extrazelluläre Matrix		13 - 26	120 - 180	1,2 - 2,4
Elastinfaser[33]			100 - 200	≈ 1	0,001
Spinnenseide[34]	Netzbau	Abseilfaden	21	1495	8,0
		Fangspirale	172	534	0,001
Seidenspinnerseide[35]	Kokon		20	570	14,0
Florfliegenseide[29]	Eiablagerung		3	68	5,8
Muschelbyssusfaden[36]	Verankerung	distal	50	200	1,8
		proximal	55	70	0,5
Keratinfaser[37]	Schutz		28 - 48	250 - 350	4,0 - 5,0

[31, 32, 33, 37]Säugetier; [34]*Argiope argentata*; [35]*Bombyx mori*; [29]*Chrysopa carnea*; [36]*Mytilus galloprovincialis*

Neben den interessanten mechanischen Eigenschaften ist vor allem auch die hervorragende Einsetzbarkeit von natürlichen, rekonstituierten oder bioinspirierten Proteinfasern als Biomaterial ein zentrales Argument für deren Erforschung. Generell handelt es sich bei Biomaterialien um Materialien, welche zu therapeutischen Zwecken mit dem menschlichen Körper in Kontakt stehen,[38] wie zum Beispiel Gerüstmaterialien für die Gewebezüchtung (engl. *Tissue engineering*), Implantate, Nahtmaterial oder Wundauflagen. Die biokompatiblen Eigenschaften von Proteinfasern sind einerseits auf ihre Bioabbaubarkeit zurückzuführen, da diese durch den Organismus mittels proteolytisch-aktiver Enzyme zu nicht-toxischen Aminosäuren abgebaut werden.[39] Andererseits enthalten einige Proteine, wie beispielsweise Kollagen oder Elastin, spezielle Sequenzmotive, welche förderliche Wechselwirkungen mit körpereigenen Zellen induzieren.[40, 41]

Darüber hinaus ist die Verwendung von Proteinfasen speziell für den Einsatz als Gerüstmaterial für die Züchtung von tierischem Gewebe prädestiniert, da der extrazellulären Matrix ebenfalls ein Fasernetzwerk mit komplexen Mikrostrukturen zu Grunde liegt.[42] Insbesondere weisen faserige Gerüststrukturen eine große Oberfläche für die Zelladhäsion auf und ermöglichen eine gute Zellinfiltration, wodurch auch der Nährstoff- und Gasaustausch begünstigt wird.[43] Des

Weiteren ermöglicht die faserige Beschaffenheit die Richtungskontrolle von Zellwachstum und die Ausbildung gerichteter Zellstrukturen.[44, 45]

In den nächsten Abschnitten werden Kollagenfasern und Spinnenseide hinsichtlich ihrer strukturellen Eigenschaften, ihrer Assemblierung und ihrem Einsatz in der Biomedizin eingehend beschrieben.

1.2 Struktur, Assemblierung und Herstellung von Kollagen

1.2.1 Kollagentypen

Der Begriff Kollagen stammt aus dem Griechischen und setzt sich aus *kolla* für „Leim“ und *gennan* für „erzeugen“ zusammen und geht auf die Beobachtung zurück, dass Kollagen nach Kochen in klebrige Gelatine überführt werden kann.[46]

Aus heutiger Sicht stellt Kollagen eine heterogene Proteinfamilie aus aktuell 29 bekannten Kollagentypen dar, welche den Hauptbestandteil der extrazellulären Matrix in Wirbeltieren bilden.[47] Die extrazelluläre Matrix fungiert innerhalb aller Gewebe und Organe als Gerüststruktur für Zellen und vermittelt durch ihre biochemischen und mechanischen Eigenschaften die Zelladhäsion, -migration und -differenzierung, unterstützt die Gewebebildung und -reparatur sowie die Angiogenese.[48, 49] Weiterhin spielen Kollagene eine Rolle bei molekularen Filtrationsprozessen in der Basalmembran oder übernehmen Funktionen als Transmembranproteine.[49] Anhand der spezifischen Funktionen und Proteindomänen-Homologien können die 29 Kollagentypen in die Fibrillen-bildenden, Netzwerk-bildenden und perlenkettig-filamentösen Kollagene, in Verankerungskollagenfibrillen, Fibrillen-assoziierte Kollagene mit unterbrochenen Tripelhelizes (FACIT, engl. *fibril-associated collagens with interrupted triple-helices*), Transmembrankollagene und in Endostatin-assoziierte Kollagene eingeteilt werden.[50]

Tabelle 2. Struktureller Charakter unterschiedlicher Kollagentypen.
Angaben entnommen aus Lin *et al*., 2019[50].

Struktureller Charakter	Kollagentyp
Fibrillen-bildende Kollagene	I, II, III, V, XI, XXIV, XXVII
Netzwerk-bildende Kollagene	IV, VIII, X
Perlenkettig-filamentöse Kollagene	VI, XXVI, XXVIII, XXIX
Verankerungskollagenfibrillen	VII
Fibrillen-assoziierte Kollagene mit unterbrochenen Tripelhelizes (FACIT)	IX, XII, XIV, XVI, XIX, XX, XXI, XXII
Transmembrankollagene	XIII, XVII, XXIII, XXV,
Endostatin-assoziierte Kollagene	XV, XVIII

Kollagen Typ I wird der Gruppe der Fibrillen-bildenden Kollagene zugeordnet, welches mit rund 90 % des Gesamtkollagengehalts in Organismen den dominierenden Typ darstellen.[51, 52] Kollagen I ist der organische Hauptbestandteil in Knochen und unter anderem maßgeblich in Sehnen, Bändern, Haut, Hornhaut und interstitiellem Bindegewebe vertreten.[53-58]

1.2.2 Molekulare Struktur von Kollagen Typ I

Alle Kollagene weisen eine rechtsgängige Tripelhelix-Struktur auf, welche sich aus jeweils drei linksgängigen, helikalen α-Polypeptidketten mit einer Polyprolin-Typ-II-Konformation zusammensetzt und durch Wasserstoffbrückenbindungen stabilisiert wird.[59, 60] Je nach Kollagentyp liegen die α-Polypeptidketten in der Tripelhelix als Homo- oder Heterotrimer vor und sind dabei immer für den jeweiligen Typ spezifisch. Kollagen Typ I besteht vorrangig aus zwei α1(I)-Ketten sowie einer α2(I)-Kette, existiert jedoch auch als Homotrimer aus drei α1(I)-Ketten.[61]

Die Tripelhelix basiert auf der für alle Kollagentypen einheitlichen Primärstruktur mit der repetitiven Aminosäuresequenz $(Gly\text{-}X\text{-}Y)_n$, wobei die Positionen X und Y grundsätzlich von jeder Aminosäure eingenommen werden können, aber meistens durch Prolin und Hydroxyprolin besetzt sind.[60] Glycin befindet sich jeweils im Kern der Tripelhelix und ist unzugänglich für Lösungsmittel. Hingegen ist die Aminosäure in der X-Position und in geringerem Ausmaß auch die Aminosäure in Y-Position dem umgebenden Lösungsmittel exponiert.[62] Die Besetzung von Position X und Y mit den alizyklischen Aminosäuren Prolin und Hydroxyprolin resultiert in einer Stabilisierung der Tripelhelix und führt zudem aufgrund der eingeschränkten Rotation der C-N-Bindung zu einer erhöhten Molekülsteifigkeit.[46] Mit

einer Gesamtlänge von ca. 300 nm und einem Durchmesser von ungefähr 1,5 nm stellt die Tripelhelix den Kernbereich des Kollagenmoleküls dar, welcher im final-prozessierten Zustand durch die nicht-repetitiven N- und C-terminalen Telopeptid-Domänen flankiert wird.[63, 64]

1.2.3 *In vivo* Assemblierung von Kollagen Typ I

Abbildung 1 veranschaulicht schematisch die *in vivo* Assemblierung von Kollagen Typ I. Nach Transkription und Translation der für die α-Ketten kodierenden mRNA in die entsprechenden Aminosäuresequenzen erfolgt eine Reihe posttranslationaler Modifikationen im Lumen des rauen endoplasmatischen Retikulums. Dies umfasst enzymatisch-katalysierte Hydroxylierungsreaktionen, welche die Funktionalisierung von Prolin- und Lysinresten zu Hydroxyprolin und -lysin zur Folge haben. Hydroxylysine werden häufig durch weitere Enzymkatalyse N- und O-glykosyliert. Es folgt die Trimerisierung der drei α-Ketten.[46, 51, 65, 66] Von besonderer Bedeutung ist hierbei das C-terminal-liegende C-Propeptid, welches durch Disulfid-Bindungen stabilisiert wird und eine geordnete Trimerisierung ermöglicht.[67] Die Faltung der Trimere in die Kollagen-Tripelhelix verläuft ausgehend vom C- zum N-Terminus und resultiert in Prokollagen.[46] Das Prokollagen wird über das Golgi-System in den extrazellulären Raum sekretiert, wobei in diesem Prozessabschnitt die flankierenden Propeptide durch Prokollagen-Proteinasen enzymatisch abgespalten werden, so dass die Tripelhelix nur noch von den nicht-helikalen Telopeptiden flankiert wird (Tropokollagen). Dadurch wird die Assemblierung der Tropokollagene zu supramolekularen Strukturen, den Kollagenfibrillen, induziert.[46, 51, 65-67]

Initial werden die Kollagenfibrillen nur durch polare, hydrophobe und andere nicht-kovalente Wechselwirkungen stabilisiert, weswegen die Fibrillenbildung stark abhängig von der Temperatur, Ionenstärke und noch von etwa 50 weiteren (bisher bekannten) Molekülen ist.[68, 69] Die Tropokollagene lagern sich während der Fibrillenbildung um jeweils ca. eine Viertel Moleküllänge versetzt zueinander an und bilden eine Mikrofibrille. Dadurch entstehen Überlappungs- und Lückenbereiche in der Kollagenfibrille, wodurch die Assemblate ein typisches Bandenmuster mit einer Periodizität von 67 nm aufweisen.[70, 71]

Die Telopeptide sind maßgeblich an der Assemblierung der Tropokollagene zu Fibrillen beteiligt und weisen Lysin- und Hydroxylysinreste auf, die in einer durch Lysyl-Oxidase-katalysierten Reaktion zu reaktiven Aldehydgruppen umgesetzt werden und Quervernetzungen ausbilden können.[72, 73] Zusätzliche Quervernetzungen werden durch Transglutaminase und durch nicht-enzymatische Glykierung eingeführt.[74, 75]

Nach vorangeschrittener Assemblierung liegen die Kollagenfibrillen final in Faserstrukturen

vor, welche die Anforderungen der jeweiligen Gewebe erfüllen. Beispielsweise nehmen die Kollagenfibrillen in der Hornhaut eine orthogonale, in der Haut eine eher geflochtene Struktur ein, wohingegen die Fibrillen in Sehnen und Bändern als parallel-strukturierte Bündel vorliegen.[76]

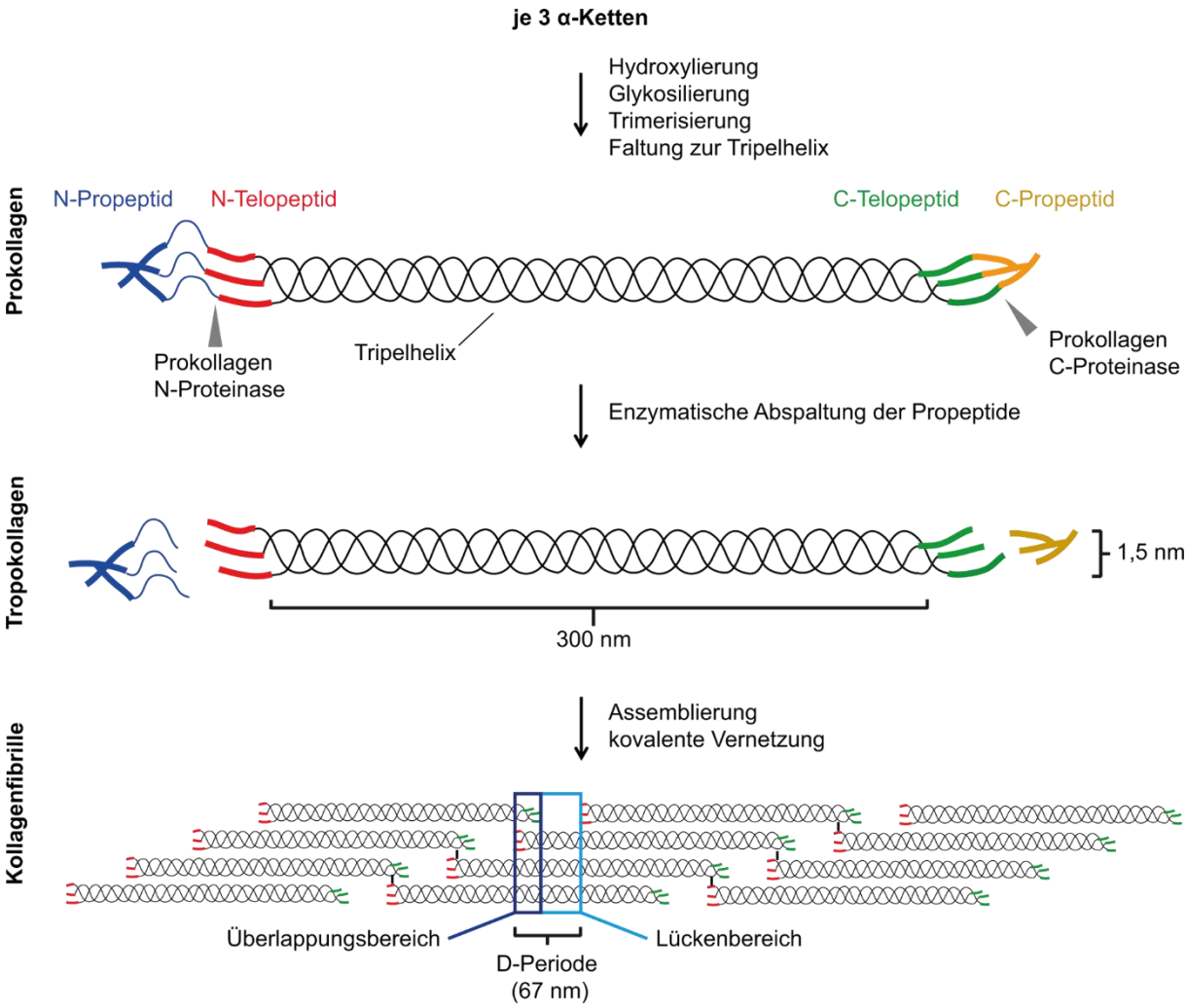

Abbildung 1. Schematischer Überblick über die *in vivo* Assemblierung von Kollagen Typ I.

1.2.4 *In vitro* Assemblierung von Kollagen Typ I

Die *in vitro* Assemblierung von Kollagen Typ I zu Fibrillen bzw. makroskopischen Fasern ist ein entropisch-gesteuerter Prozess, welcher auf dem Verlust von Lösungsmittelmolekülen von der Kollagenmolekülоberfläche durch fortschreitende Assemblierung basiert und eine Verringerung des Oberfläche/Volumen-Verhältnisses zur Folge hat.[69, 77]

Die Fibrillenbildung von Kollagen kann mittels Trübungsmessung näherungsweise zeitlich verfolgt werden und ist durch eine anfängliche Verzögerungsphase (engl. *lag phase*) und eine Wachstumsphase (engl. *log phase*) mit einem sigmoidalen Kurvenverlauf gekennzeichnet,[78-80] was auf eine Nukleations-Wachstums-Reaktion hindeutet.[81] Ausgehend von einer Kollagenlösung ist die Morphologie der entstehenden Fibrillen (Dimension und D-Periodizität) stark von pH-Wert und Elektrolytzusammensetzung (Abbildung 2), Temperatur, Kollagenkonzentration sowie ursprünglichem Kollagen-Vernetzungsgrad abhängig.[79, 82, 83] Die Fibrillenbildungsrate weist dabei eine indirekte Proportionalität zur Oberflächennettoladung auf. Die Oberflächennettoladung nimmt am isoelektrischen Punkt von Kollagen ein Minimum ein.[84]

In Jiang *et al*., 2004 wurde gezeigt, dass die Bildung von Kollagenfibrillen mit der charakteristischen D-Periodizität die Anwesenheit von Kaliumionen erfordert.[82] Im Widerspruch dazu wurde in Williams *et al*., 1978 eine starke Abhängigkeit der D-Periodizität von Phosphationen gefunden,[79] wohingegen in Harris *et al*., 2013 den Chloridionen eine tragende Rolle zugeschrieben wurde,[83] wodurch ersichtlich ist, dass die Assemblierung von Kollagen Typ I nach wie vor noch nicht vollends verstanden ist.

Neben Einstellung der intrinsischen Fibrillenstruktur konnte überdies in diskontinuierlichen Ansätzen, d.h. entweder durch Inkubation der Kollagenlösung in unterschiedlich-dimensionierten Mikrokanälen oder aber durch Aufbringen einer Kollagenlösung auf eine Oberfläche mittels eines initialen hydrodynamischen Flusses, die Orientierung der Kollagenfibrillen kontrolliert werden (Abbildung 2).[80, 82]

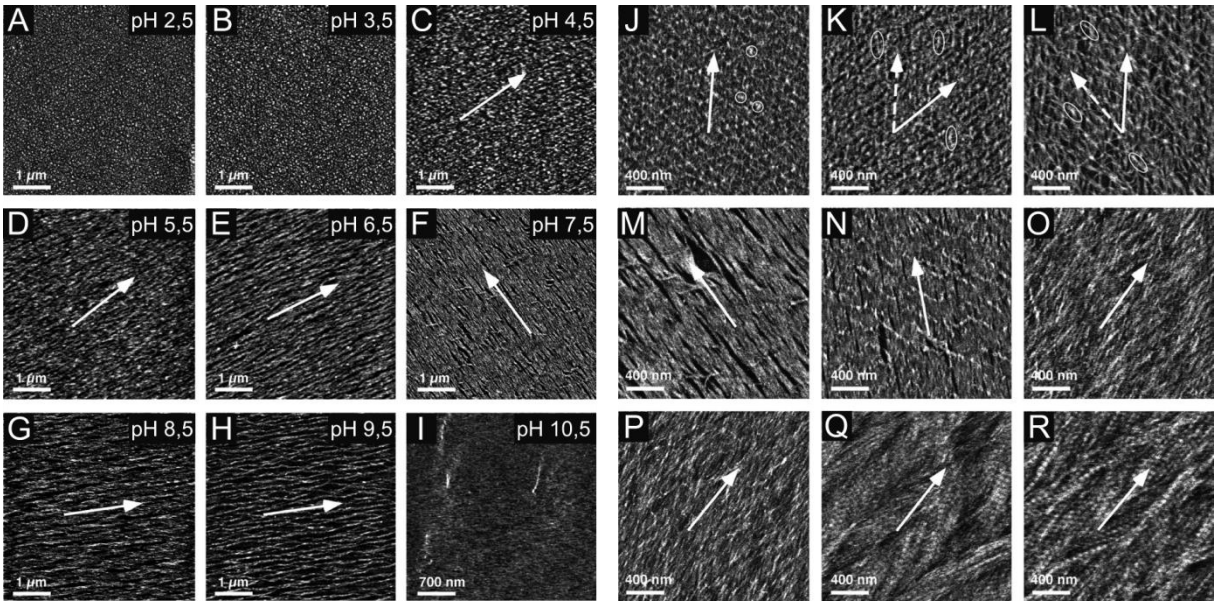

Abbildung 2. *In vitro* Assemblierung von Kollagen Typ I zu Kollagenfibrillen auf Mica-Plättchen. (A-I) pH-Abhängigkeit der Kollagenfibrillenmorphologie. Morphologie der Fibrillen bei pH = 7,5 in Anwesenheit von (J) 10 mM $MgCl_2$, (K) 50 mM NaCl, (L) 100 mM NaCl, (M) 200 mM NaCl, (N) 200 mM NaCl, 5 mM $MgCl_2$; (O) 50 mM KCl, (P) 100 mM KCl, (Q) 200 mM KCl und (R) 200 mM KCl, 5 mM $MgCl_2$. Die Pfeile verdeutlichen die Orientierung der Längsachse der gebildeten Kollagenfibrillen. Adapted from Jiang *et al.*[82] (DOI: 10.1016/j.jsb.2004.07.001), Copyright (2004), with permission from Elsevier.

1.2.5 Kollagenquellen

Kollagen für die *in vitro* Assemblierung kann durch Extraktion kollagenreicher Gewebe mit verdünnten Säurelösungen gewonnen werden. Stark kovalent-vernetztes, schwerlösliches Kollagen wird durch Zugabe proteolytisch-aktiver Enzyme (z.B. Pepsin) zugänglich.[46] Aktueller Gegenstand der Forschung liegt auch auf der Herstellung rekombinanter Kollagene, welche keine Infektionsrisiken (z.B. die bovine spongiforme Enzephalopathie, BSE) aufweisen,[85] und eine gleichbleibende Materialqualität gewährleisten. In bisherigen Studien konnten dazu Erfolge durch den Einsatz biotechnologischer Strategien mithilfe von Bakterien[86, 87], Hefepilzen,[88] menschlichen Zellen[89] oder Tabakpflanzen[90] erzielt werden.

1.3 Struktur, Assemblierung und Herstellung von Spinnenseide

Spinnenseide fasziniert die Menschheit seit Jahrtausenden. Bereits die alten Griechen nutzten Spinnenseide zur blutstillenden Wundabdeckung. Hingegen verwendeten die Ureinwohner des australischen Kontinents und von Neu Guinea Spinnenseide zum Fischen, als Kopfbedeckung oder als Taschen.[91]

Natürliche Spinnenseidenfasern bestehen hauptsächlich aus Proteinen, den sogenannten Spidroinen. Diese bestehen aus einem repetitiven Kern mit bis zu 100 Sequenzwiederholungen von jeweils 40-200 Aminosäuren und werden von einer nicht-repetitiven N-terminalen Domäne und einer nicht-repetitiven C-terminalen Domäne flankiert.[92]

1.3.1 *In vivo* Assemblierung von Spinnenseide

Die natürliche Assemblierung von Spinnenseide beginnt in den Drüsen des Abdomens der Spinne. Die zugrundeliegenden Proteine (Spidroine) werden dazu von Epithelzellen in den Drüsenfortsatz sekretiert, woraufhin die Speicherung einer hochkonzentrierten Spidroinlösung (bis zu 50 % w/v) im Drüsenreservoir bei neutralem pH und der Präsenz chaotroper Natrium- und Chloridionen folgt.[93, 94] Eine Stabilisierung der amphiphilen Spidroine gegen vorzeitige Aggregation durch Ausbildung einer mizellenartigen Quartärstruktur gilt als wahrscheinlich.[95] Ausgehend vom Drüsenreservoir passiert die Spidroin-Lösung einen S-förmigen Spinnkanal. In diesem Kanal wird der pH-Wert kontinuierlich abgesenkt (in *Nephila clavipes* von 7,2 auf 5,7).[96] Dadurch ergeben sich strukturelle Veränderungen in den terminalen Domänen.[97-99] Parallel dazu findet ein Austausch der chaotropen Natrium- und Chloridionen aus der Spidroin-Lösung mit den kosmotroperen Kalium- und Phosphationen aus dem umgebenden Gewebe statt, welches in Kombination mit Wasserentzug ein Aussalzen der Spidroine veranlasst.[100, 101] Die dabei entstehenden Spidroin-Assemblate unterliegen aufgrund des konisch-zulaufenden Spinnkanals hohen Scherkräften, wodurch ihre Längsausrichtung begünstigt wird.[102] Der daran anschließende mechanische Abzug der Spidroine aus der Spinnwarze unterstützt weiterhin deren Ausrichtung und führt letztendlich zur ausgehärteten Spinnenseidenfaser.[103]

1.3.2 Spinnenseidennetze

Heutzutage sind mehr als 48.000 verschiedene Spinnenarten (Araneae) bekannt,[104] welche in mehr als 380 Millionen Jahren Evolution eine Vielzahl an unterschiedlichen Seiden hervorgebracht haben.[105] Auch zeigt sich eine äußerst große morphologisch-funktionelle Varianz im Netzbau. Beispielsweise bauen Spinnen der Familie Agelenidae Trichternetze (Abbildung 3A). Die Netze der Linyphiidae sind horizontal angelegt und besitzen eine baldachinartige Struktur (Abbildung 3B). Dictynidae bilden unregelmäßige Netze, welche direkt in Pflanzenstrukturen integriert werden (Abbildung 3C). Uloboridae bauen unvollständige Radnetze (Abbildung 3D). Dahingegen bauen Aranaeidae komplette, vertikale Radnetze (Abbildung 3E), während Tetragnathidae komplette, horizontale Radnetze spinnen (Abbildung 3F). Vertreter der Theridiidae bauen Haubennetze (Abbildung 3G).[105-109]

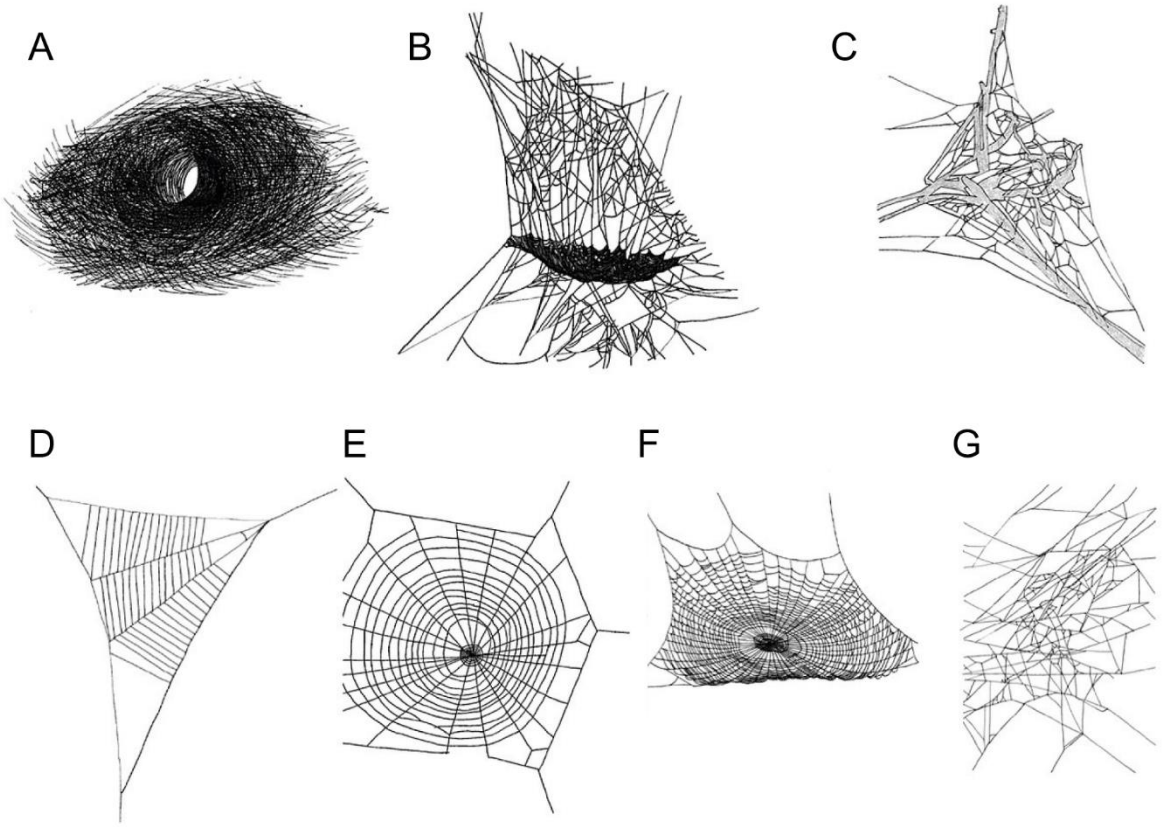

Abbildung 3. Schematische Darstellung einiger Beispiele für Spinnenseidennetze. (A) Trichternetz der Agelenidae, (B) Baldachinnetz der Linyphiidae, (C) Unregelmäßiges Netz der Dictynidae, (D) reduziertes Radnetz der Uloboridae, (E) vertikales Radnetz der Aranaeidae, (F) horizontales Radnetz der Tetragnathidae und (G) Haubennetz der Theridiidae. Adapted from Roberson *et al.*[106] (DOI: 10.7717/peerj.2538) with permission of PeerJ.

Krabbenspinnen (Thomisidae) bauen in der Regel keine Netze für den Beutefang,[110] jedoch nutzen diese dennoch Seide zur Fertigung von Eierkokons und zum Bau von Blattnestern.[111, 112] Bei Krabbenspinnen handelt es sich daher um aktive Jäger, welche ihre Beute aus dem Hinterhalt ergreifen[110, 113] und dazu auch umfangreiche Tarnungen und Täuschungsstrategien entwickelt haben.[114, 115] Eine Ausnahme ist die australische Krabbenspinne *Saccodomus formivorus*,[116] die ein körbchenförmiges Netz baut, um damit den Beutefang von Ameisen zu erleichtern.[116-120]

1.3.3 Spinnenseidentypen in Radnetzen

Von allen unterschiedlichen Spinnenseidennetztypen sind die Radnetze im Hinblick auf die Struktur-Funktionsbeziehungen der verarbeiteten Materialien am besten dokumentiert. Diese bestehen aus fünf verschiedenen Seidentypen.[121] Zudem bilden weibliche Radnetzspinnen zwei weitere Seiden, welche zum Bau von Kokons eingesetzt werden und damit dem Schutz der

Spinneneier gegenüber Jägern, Parasiten oder schädlichen Temperaturschwankungen dienen.[122, 123]

Alle sieben Seiden werden in jeweils unterschiedlichen Drüsen assembliert. Die Seide, welche den Rahmen und die Speichen der Radnetze bildet, wird in der *Major Ampullate* (*MA*) Drüse gebildet, weswegen diese auch als *MA* Seide bezeichnet wird. Da diese Seide auch als Abseilfaden fungiert und folglich hinterhergezogen wird, hat sich auch die Bezeichnung *Dragline* Seide etabliert. Eine Hilfsspirale bestehend aus der *Minor Ampullate* Seide gibt dem Radnetz zusätzliche Stabilität, wohingegen die *Pyriform* Seide eine Verankerung des Netzes an umgebenden Substraten ermöglicht. Des Weiteren weist das Radnetz die *Flagelliform* Seide auf, welche im Beutefang als Fangspirale Verwendung findet. Die *Flagelliform* Seide ist mit der adhäsiven *Aggregate* Seide modifiziert, welche die Anhaftung ins Netz geratener Beute vermittelt. Die *Tubuliform* und *Aciniform* Seiden werden jeweils als äußerer und innerer Bestandteil des Kokons verwendet. Letztere dient zudem auch zum Einwickeln der Beute (Abbildung 4).[28, 103, 124, 125]

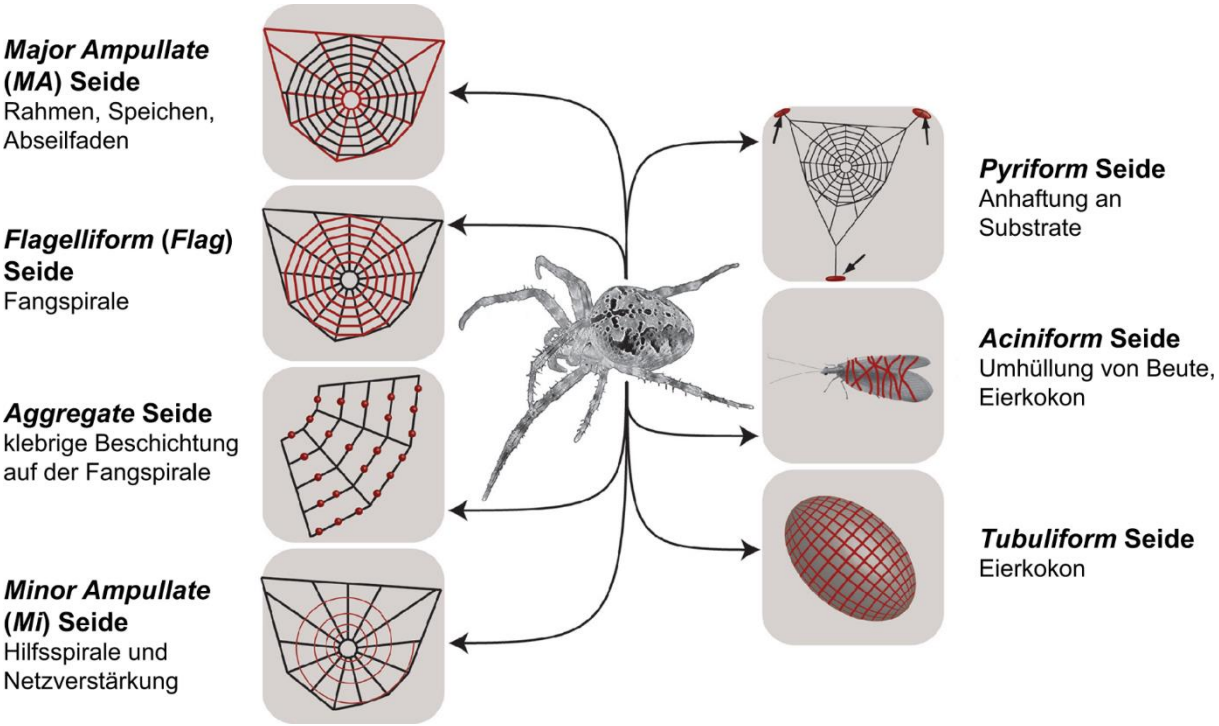

Abbildung 4. Schematische Darstellung der Seidentypen der weiblichen Modell-Radnetzspinne *Araneus diadematus*. Adapted from Eisoldt *et al.*, 2011[125] (DOI: 10.1016/S1369-7021(11)70057-8), Copyright (2011), with permission from Elsevier.

Die mechanischen Eigenschaften der Spinnenseide sind unter anderem abhängig von der Verstreckung der Faser während des Spinnvorgangs, der umgebenden Luftfeuchte, als auch vom Alter der Spinne und dem ihr zur Verfügung stehenden Nährstoffangebot.[126-128] Dennoch sind die Materialkennwerte (Tabelle 3) und die Verläufe der Spannungs-Dehnungs-Kurven der einzelnen Seidentypen klar voneinander unterscheidbar.[34, 124] *Major* und *Minor Ampullate* Seide sowie *Aciniform* Seide ist jeweils durch eine hohe Materialzähigkeit gekennzeichnet, welche aus einer guten Zugfestigkeit und einer moderaten Bruchdehnung resultiert und alle anderen natürlichen und synthetischen Fasern in den Schatten stellt.[34, 129, 130] Hingegen weist die *Flagelliform* Seide eine hohe Bruchdehnung auf, welche dadurch die kinetische Energie ins Netz fliegender Insekten absorbieren kann.[28] Ebenso auffällig gestalten sich die Unterschiede im Anstieg der Kurve bei Dehnungswerten oberhalb der Streckgrenze. Diesbezüglich weisen die *Major Ampullate* und *Minor Ampullate* Seiden stärkere Zunahmen der Spannung auf, als dies für *Tubuliform* und *Aciniform* Seiden beobachtet wurde.[34, 124]

Tabelle 3. Mechanische Eigenschaften der unterschiedlichen Seiden der Modell-Radnetzspinne *Argiope argentata* (± Standardfehler). Angaben entnommen aus Blackledge *et al*., 2006[34]. Alle Werte dieser Tabelle entstammen wahren Spannungs-Dehnungs-Kurven.

Spinnenart	Seidentyp	Bruchdehnung [%]	Zugfestigkeit [MPa]	E-Modul [GPa]	Zähigkeit [MJ m^{-3}]
Argiope argentata[34]	*Major Ampullate*	20,5 ± 0,5	1495 ± 65	8,0 ± 0,8	136 ± 7
	Minor Ampullate	33,0 ± 3,3	923 ± 154	10,6 ± 1,2	137 ± 22
	Flagelliform	172,0 ± 5,0	534 ± 40	0,001 ± 0,0001	75 ± 6
	Aciniform	40,4 ± 2,4	1052 ± 120	10,4 ± 1,4	230 ± 31
	Tubuliform	28,6 ± 1,5	476 ± 90	11,6 ± 2,1	95 ± 17

In Untersuchungen des Querschnitts der *Major Ampullate* Seide von *Nephila clavipes* zeigte sich, dass diese einen hierarchischen Aufbau besitzt (Abbildung 5). Diese Seide weist verschiedene äußere Schichten auf, welche aus Lipiden, Glykoproteinen und vermutlich *Minor Ampullate*-ähnlichen Spidroinen bestehen und höchstwahrscheinlich Schutz- und Sozialfunktionen übernehmen, an der Flexibilität der Faser mitwirken und den Wasserhaushalt regeln. Der Faserkern wiederum wird aus dem Prolin-freien *Major Ampullate Spidroin 1* (MaSp1) und dem Prolin-haltigen *Major Ampullate Spidroin 2* (MaSp2) gebildet, wobei in der äußeren Kernschicht nur MaSp1 vertreten ist. Beide Spidroine im Kern sind im Vergleich zu den äußeren Schichten deutlich stärker an der Ausprägung der mechanischen Eigenschaften der Spinnenseide involviert.[27] In *Araneus diadematus* wurden bisher zwei strukturgebende

Spidroine identifiziert, welche der Aminosäuresequenz des Prolin-haltigen MaSp2 ähneln und als *Araneus diadematus Fibroin 3* und *Araneus diadematus Fibroin 4* (ADF3 und ADF4) bezeichnet werden.[131, 132]

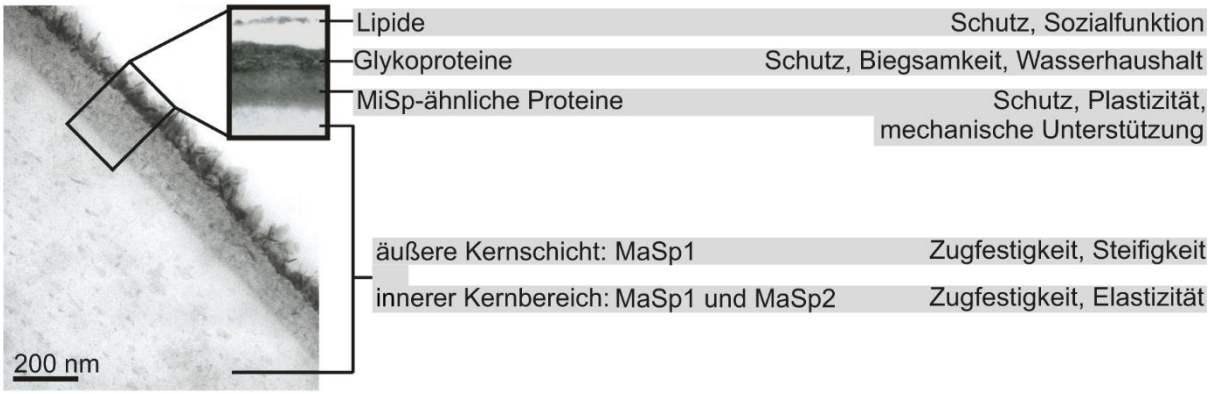

Abbildung 5. Querschnitt der *Major Ampullate* Seide der Modell-Radnetzspinne *Nephila clavipes*. MiSp: *Minor Ampullate Spidroin*, MaSp: *Major Ampullate Spidroin*. Adapted from Sponner *et al.*[27] (DOI: 10.1371/journal.pone.0000998) with permission from *PLoS*.

1.3.4 Molekulare Struktur von Radnetz-Spinnenseide

Wie bereits in Abbildung 5 anhand MaSp1 und MaSp2 angedeutet, vermitteln unterschiedliche Spidroine ein voneinander verschiedenes Materialverhalten, welches unter anderem anhand ihrer jeweiligen Aminosäuresequenzen und den damit verbundenen Sekundärstrukturen zu erklären ist (Abbildung 6).

Major Ampullate Seide besitzt Alanin-reiche Sequenzen, welche für die Ausbildung kristalliner *ß*-Faltblätter verantwortlich sind und die bemerkenswerten Materialfestigkeiten veranlassen.[133] Die *ß*-Faltblätter in der *Major Ampullate* Seide sind in eine Glycin-reiche, amorphe Phase eingebettet.[134] Diese geht aus den repetitiv-angelegten Aminosäuresequenzen GGX (X: Tyrosin, Leucin, Glutamin) und GPGXX hervor, welche jeweils Helizes und Spiralen aus *ß*-Schleifen einnehmen können und der *Major Ampullate* Seide Flexibilität und Elastizität verleihen. Konsequenterweise ist die außergewöhnlich-hohe Bruchdehnung (und moderate Zugfestigkeit) der *Flagelliform* Seide vorwiegend durch die Ausbildung von Spiralen aus *ß*-Schleifen, Helizes, unstrukturierten Bereichen und der Abwesenheit von *ß*-Faltblättern begründet.[28, 135, 136]

Spinnenart	Spidroin	ß-Schleifen-Spirale GPGXX Elastizität	kristallines ß-Faltblatt A-reich Zugfestigkeit	3_1-Helix GGX	Spacer
Nephila clavipes	MaSp1		✓	✓	
	MaSp2	✓	✓		
	Flag	✓		✓	✓
Araneus diadematus	ADF3	✓	✓	✓	
	ADF4	✓	✓		

Abbildung 6. Protein-Sekundärstrukturen in den Spidroinen der Modell-Radnetzspinnen *Nephila clavipes* und *Araneus diadematus*. MaSp: *Major Ampullate Spidroin*, Flag: *Flagelliform Spidroin*, ADF*: Araneus diadematus Fibroin*. G: Glycin, P: Prolin, A: Alanin, X: verschiedenartig. Abbildung angelehnt an Scheibel *et al.*[135] (DOI: 10.1186/1475-2859-3-14).

1.3.5 Rekombinante Spinnenseide

Aufgrund der guten Körperverträglichkeit und der außergewöhnlich hohen mechanischen Stabilität natürlicher Spinnenseide ist diese Materialklasse für verschiedenste biomedizinische und technische Anwendungen prädestiniert. Allerdings offenbart sich, dass die kommerzielle Gewinnung natürlicher Spinnenseide aufgrund des kannibalistischen Verhaltens der Spinnen ungeeignet ist.[137, 138]

Um dennoch Spinnenseiden-inspirierte Materialien zu entwickeln wurden biotechnologische Prozessstrategien etabliert, welche die Produktion größerer Mengen an Spidroinen mit gleichbleibender Qualität erlauben.[131, 139-141] Prinzipiell wird dabei die genetische Information, welche die Spidroine codiert, in Bakterien, Hefen, Säugetier- und Insektenzellen oder in transgene Tiere eingebracht und rekombinant exprimiert.[142]

Beispielsweise wurde aus dem repetitiven Aufbau des ADF4-Spidroins aus *Araneus diadematus* eine Konsensussequenz abgeleitet und davon ausgehend ein C-Modul generiert, welches durch 16-fache Aneinanderreihung in eine C16-Variante überführt wurde,[139] und als *engineered* ADF4(C16) [eADF4(C16)] bezeichnet wird. eADF4(C16) und weitere rekombinante Spidroine konnten anschließend beispielsweiße zur Herstellung von

Endlosfasern,[143] für Beschichtungen von Textilgeweben,[144] oder für die Modifikation von Filtermaterialien herangezogen werden.[145, 146] Die Modifikation von eADF4(C16) mit der Integrinrezeptor-bindenden RGD-Sequenz [eADF4(C16)RGD] resultierte überdies in einer rekombinanten Proteinvariante, welche eine erhöhte Zellproliferation und -adhäsion im Gegensatz zum unmodifizierten eADF4(C16) zeigte.[147]

1.4 Biomedizinische Anwendung von Kollagen und Spinnenseide

Natürliche und rekombinante Kollagen- und Spinnenseidenmaterialien werden generell als hochgradig biokompatibel, nicht toxisch und bioabbaubar angesehen.[148-151]

Kollagen zeigt nur eine geringe antigene Wirkung und diese kann mittels Umsetzung des Tropokollagens zu Atelokollagen durch enzymatische Abspaltung der Telopeptide noch erheblich niedriger ausfallen.[152-154] Die tripelhelikale Domäne ist resistent gegen die meisten Proteasen,[155] wodurch Kollagen im Körper eine längere Einsetzbarkeit aufweist. Die Bindung von Zellen an die extrazelluläre Matrix wird durch Interaktion der Integrin-Oberflächenrezeptoren mit Kollagen vermittelt, wodurch effektiv die Zellproliferation und -differenzierung unterstützt wird.[40, 156] Diese Eigenschaften und die relativ gute Verfügbarkeit haben dazu geführt, dass Kollagenmaterialien in den letzten Jahrzehnten einen festen Platz in der Wundheilung, der gezielten Wirkstofffreisetzung, der Gewebeneuzüchtung und der regenerativen Medizin als Transplantate, Fasern, Vliesstoffe, Filme, Schwämme und Hydrogele eingenommen haben.[46, 150, 151, 157, 158]

Spinnenseidenmaterialien haben sich ebenso als zukunftsweisend für den Einsatz in der Biomedizin erwiesen. Bestimmte, unmodifizierte Spinnenseidenmaterialien werden vom menschlichen Immunsystem kaum erkannt, weshalb sich diese besonders gut zur Maskierung von anderen Biomaterialien eignen.[159] Zudem unterstützt Spinnenseide die Wundheilung und initiiert die Blutgerinnung,[149] und kann als Nahtmaterial eingesetzt werden.[160, 161] Auch konnte für rekombinante Spinnenseide ein bakteriostatischer Effekt nachgewiesen werden.[162] Ebenso wie Kollagen kann rekombinante Spinnenseide in viele Materialmorphologien prozessiert werden,[148, 149] und zeigt besonders im Bereich als Biotinte für den 3D-Druck von zellbeladenen Hydrogelen,[163, 164] als Basismaterial für die Herzmuskel- oder Bindegewebszüchtung,[165, 166] oder als Implantatbeschichtung[159, 167] hohes Anwendungspotenzial.

Beide Proteinklassen sind insbesondere für die Entwicklung von Materialien für die periphere

Nervenreparatur prädestiniert und werden daher im folgenden Kapitel speziell für diese Anwendung beleuchtet.

1.4.1 Periphere Nervenreparatur

Von allen Geweben wird das Nervensystem als das komplexeste Gewebe angesehen - die Anzahl an Nervenzellen (Neurone) liegt bei Säugetieren bei etwa 10^{12} Zellen.[168] Die Gesamtheit des Nervengewebes wird in ein zentrales Nervensystem (ZNS), bestehend aus Gehirn und Rückenmark und in ein peripheres Nervensystem (PNS) eingeteilt, welches das ZNS mit dem Rest des Körpers verbindet. Die afferenten Neurone leiten dabei sensorische Informationen von den Körpereinheiten zum ZNS, während efferente Neurone Signale vom ZNS zu den entsprechenden Körperbereichen übermitteln.[169]

Nervenzellen bestehen grundsätzlich aus dem Zellkörper (Soma); Neuriten, welche in kurze (Dendrit) und lange Fortsätze (Axon) untergliedert sind; und den Endknöpfchen, mit denen der Kontakt zu anderen Zellen (Synapse) hergestellt und die Erregungsweiterleitung vollzogen wird. Eine humane, periphere Nervenfaser zeigt einen hierarchischen Aufbau, bei dem Schwann-Zellen die Axone mit einer Myelinscheide isolieren, welche wiederum in das Endoneurium, Perineurium und Epineurium eingebettet ist (Abbildung 7).[170] Die Erregungsweiterleitung wird im Nervensystem mithilfe eines Aktionspotenzials ermöglicht, welches als Änderung des anliegenden Membranpotentials (Ruhepotenzials) zu verstehen ist.[171]

Weltweit wird die jährliche Zahl an neu-eingetretenen Unfällen mit Schädigung des peripheren Nervengewebes auf mehr als eine Million geschätzt, wobei davon etwa 40 % allein auf Europa fallen.[172] Im Gegensatz zu geschädigten Axonen des zentralen Nervensystems besitzen die Axone des peripheren oder embryonalen Nervensystems ein gewisses Regenerationspotential.[173] Im Vergleich zu anderen Geweben ist die natürliche Regeneration peripherer Nerven jedoch relativ langsam und meistens nicht vollständig. Die Patienten leiden gewöhnlich unter sensorischen und motorischen Störungen bis hin zu Lähmungserscheinungen des geschädigten Bereichs und intensiven, neuropathischen Schmerzen.[174, 175]

Nach wie vor gilt hierbei der Einsatz körpereigenem Gewebes (engl. *Autograft*) für die Reparatur größerer Schäden als Stand der Technik, jedoch aufgrund von Funktionsverlusten an der körpereigenen Entnahmestelle, limitierter Verfügbarkeit und erhöhtem Infektions- oder Neurombildungsrisiko als nicht ideal.[176, 177] Im Zuges dessen ist die Entwicklung von künstlichen Nervenleitschienen seit längerem Gegenstand der Forschung.

Prinzipiell wird hierbei jeweils das proximale und distale Ende des geschädigten Nervs in eine

Nervenleitschiene, meist ein röhrenförmiges Konstrukt, eingefügt, so dass Axone ausgehend vom proximalen Ende durch die Schiene hindurchwachsen können.[178] Der natürliche Regenerationsprozess der geschädigten Nervenfaser verläuft in einer hohlen Nervenleitschiene sequentiell ab. Unmittelbar nach Schädigung tritt aus den proximalen und distalen Nervenenden Gewebswasser mit angereicherten neurotrophen Faktoren und extrazellulären Matrix-Vorläufermolekülen in die defekte Stelle, woraufhin sich aus den Vorläufermolekülen einzelne Fibrinfäden zwischen beiden Nervenfaserenden bilden. Entlang dieser migrieren Schwann-Zellen, Endothelzellen und Fibroblasten und bilden longitudinal-ausgerichtete Gewebebänder (Büngner-Bänder), welche schließlich als Orientierungsstruktur für proximal auswachsende Axone Anwendung finden. Final bilden Schwann-Zellen eine Myelinscheide um die neugebildeten Axone.[179]

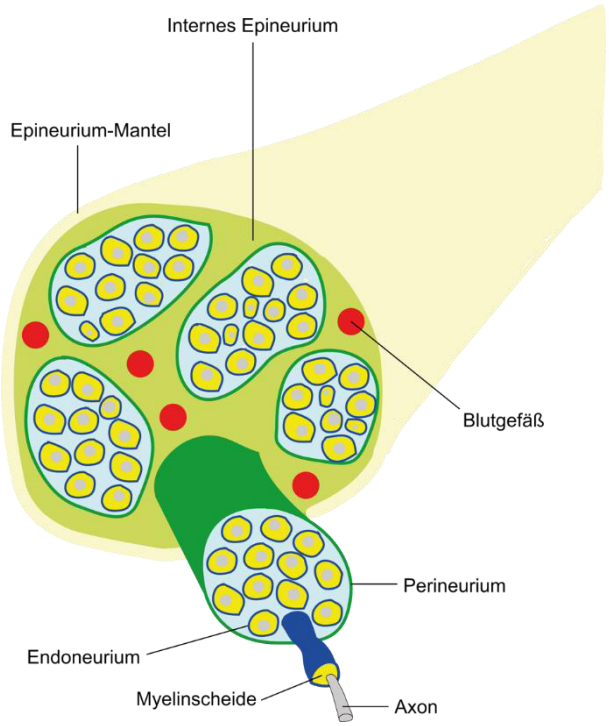

Abbildung 7. Aufbau einer peripheren Nervenfaser. Schematische Darstellung des Querschnitts einer peripheren Nervenfaser. Abbildung angelehnt an Grinsell *et al.*[174] (DOI: 10.1155/2014/698256).

Der klinische Erfolg größerer Nervendefekte (> 10 mm) ist jedoch mit hohlen, synthetischen Konstrukten gering, kann allerdings durch Anwesenheit biologisch aktiver Komponenten, wie Bestandteile der extrazellulären Matrix oder neurotropher Faktoren, optimiert werden.[180] Mögliche Modifizierungen der hohlen Konstrukte umfassen unter anderem die Einführung von Hydrogelen,[181, 182] Mikro- oder Nanofasern,[183-185] porösen Schwämmen,[186, 187]

Mehrfachlumen[188-190] oder Strukturierungen der Oberfläche auf der Röhreninnenseite,[191-193] und verfolgen stets das Ziel, eine geeignete Umgebung für die Zellproliferation und -differenzierung zu gewährleisten. Überdies soll mit Orientierungsstrukturen ein gerichtetes Wachstum der Zellen und eine Ausrichtung der Neurite erreicht werden.[44, 183, 194] Es wurde beobachtet, dass eine verbesserte Vaskularisierung und eine gewisse Permeabilität der Konstrukte zu einer effektiveren Diffusion von Nährstoffen und metabolischen Produkten führt und den klinischen Erfolg steigern kann.[195, 196]

1.4.1.1 Kollagen und Spinnenseide für die periphere Nervenreparatur

Seit längerer Zeit steht der Einsatz kollagenbasierter Nervenleitschienen im Fokus der Forschung.[197-202] Das ist generell auf die hervorragenden biomedizinischen Eigenschaften von Kollagen zurückzuführen. Insbesondere liegt Kollagen aber auch im Epineurium, Perineurium und Endoneurium in Form von einzelnen Fibrillen, Fibrillenbündel oder als ungeordnetes Fibrillennetzwerk vor.[203, 204] Zwischen dem Endoneurium und dem myelinisierten Axon liegt zudem eine kollagenreiche Basalmembran vor, welche von Schwann-Zellen hergestellt und reguliert wird. Als Binde- und Strukturgewebe fördert die Basalmembran die Funktion der Schwann-Zellen und neuronaler Axone.[205, 206]

Spinnenseide wurde ebenfalls für die Anwendung in der peripheren Nervenreparatur getestet. In einer Studie wurde diesbezüglich beobachtet, dass humane (NT2) Nervenzellen auf Spinnenseide adhärierten und ein Neuriten-Netzwerk zwischen und entlang einzelner Fasern ausbildeten.[207] Überdies zeigten weitere Studien, dass Spinnenseide in dezellularisierten Venen als Leitstruktur für die Schwann-Zellen-Migration und -proliferation einsetzbar war und in Tiermodellen den axonalen Neubewuchs über größere periphere Nervendefekte förderte.[208, 209] Auch auf einer Matrix bestehend aus rekombinanter Spinnenseide differenzierten neuronale Stammzellen effizient in Nervenzellen, Astrozyten und etwas weniger effektiv in Oligodendrozyten.[210] Eine weitere Studie untersuchte die Interaktion von Nervenzellen auf Filmen aus dem rekombinanten Spidroin MaSp1, wobei hier ebenfalls eine Förderung des neuronalen Wachstums beobachtet wurde, welche der Steifigkeit, der Oberflächenladung und einer zusätzlich eingeführten Neuronen-spezifischen Oberflächenbindesequenz zugeschrieben wurde.[211]

1.5 Technische Faserherstellung

1.5.1 Grundlegende Faserspinn-Verfahren im Überblick

Grundsätzlich kann die Herstellung von Fasern ausgehend von Polymerschmelzen oder Polymerlösungen erfolgen. Für das Verspinnen von Polymerschmelzen werden gewöhnlich thermoplastische Kunststoffe verwendet, welche durch eine entsprechende thermische Stabilität gekennzeichnet sind. Die Produktion der Fasern erfolgt hierbei durch Extrusion und rasches Abkühlen der Polymerschmelze.[212]

Im Gegensatz dazu basiert das Faserspinnen aus einer Polymerlösung entweder auf Fällung der in der Lösung enthaltenen Polymere oder durch Entfernen des Lösungsmittels. Die Faserbildung durch Fällung - das Nassspinnen - wird durch kontinuierliche Extrusion einer Polymerlösung $\dot{V}_P$ in ein entsprechendes Fällbad ermöglicht, in welchem das Polymer eine niedrigere Löslichkeit aufweist (Abbildung 8A). Hingegen wird die Faserbildung durch Entfernen des Lösungsmittels, dem sogenannten Trockenspinnen, durch Extrusion der Polymerlösung $\dot{V}_P$ in eine lösungsmittelfreie Umgebung mit meist sofortiger Wärmebestrahlung $\dot{Q}$ gewährleistet (Abbildung 8B). Die im Nass- und Trockenspinnprozess erzeugten Fasern weißen gewöhnlich Durchmesser im zweistelligen Mikrometerbereich auf.[25, 213-227]

Einen Sonderfall des Trockenspinnens stellt das Lösungsblasspinnen (engl. *Solution blow spinning*) dar, bei dem der Polymerlösungsfluss $\dot{V}_P$ durch einen Mantelfluss $\dot{V}_M$ aus Gas von der Extrusionsdüse wegbefördert wird (Abbildung 8C). Im weiteren Sinne, basiert auch das Elektrospinnen auf der Verdampfung des Lösungsmittels, jedoch wird der hierbei vorliegende Prozess durch Anlegen eines elektrischen Feldes initiiert (Abbildung 8D). Prinzipiell resultiert sowohl das Lösungsblasspinnen als auch das Elektrospinnen in Fasern mit Durchmessern vom Nanometer- bis in den einstelligen Mikrometermaßstab.[145, 228-234] Beide Prozesse basieren auf der Verwendung leichtflüchtiger Lösungsmittel, wie z.B. Fluoralkohole. Diese Lösungsmittel zeigen allerdings häufig ein erhöhtes Denaturierungspotential für Proteine, welches beim Elektrospinnen durch das angelegte elektrische Feld noch zusätzlich erhöht wird.[235] Beispielsweise wurde beim Elektrospinnen eine Denaturierung der tripelhelikalen Domänen im Kollagenmolekül beobachtet.[236] Im Gegensatz zum Elektrospinnen ermöglicht das Lösungsblasspinnen auch die *in situ* Beschichtung von lebendem Gewebe mit einer Vliesstoffschicht, die beispielsweise als Wundverschluss fungieren kann.[237]

Die Mikrofluidik als Faserspinn-Verfahren ist eine noch relativ junge Disziplin und basiert, je nach Auslegung, auf den Prinzipien der hier erwähnten Faserspinn-Verfahren. Die Grundlagen

und die Anwendungsmöglichkeiten dieser Technologie werden eingehend im folgenden Kapitel erläutert.

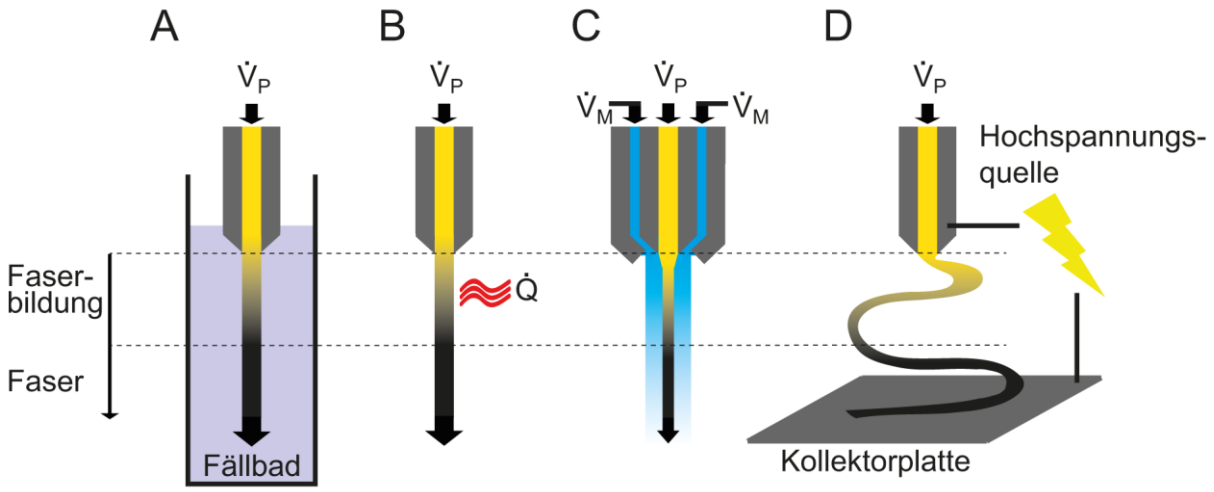

Abbildung 8. Schematische Übersicht lösungsmittelbasierter Faserspinn-Verfahren. (A) Nassspinnen: Die Faserbildung erfolgt durch kontinuierliche Extrusion einer Polymerlösung in ein Fällbad. (B) Trockenspinnen: Nach Extrusion der Polymerlösung in eine lösungsmittelfreie Umgebung erfolgt die Faserbildung durch instantanes Entfernen des Lösungsmittels, meist unter Anwendung eines Wärmeflusses. (C) Lösungsblasspinnen: Ein Polymerlösungsfluss wird in einen Mantelfluss aus Gas geleitet durch den die entstehende Faser von der Extrusionsdüse wegbefördert wird. (D) Elektrospinnen: Die Faserherstellung erfolgt durch Einsatz eines elektrischen Feldes und Verdampfung des Lösungsmittels. Abkürzungen: $\dot{V}_P$ = Polymerlösungsfluss, $\dot{V}_M$ = Mantelfluss, $\dot{Q}$ = Wärmefluss.

1.5.2 Mikrofluidik

Die Mikrofluidik gilt generell als die Technologie, welche sich mit der Verarbeitung geringer Fluidvolumina in Mikrostrukturen mit Dimensionen von 1 bis 500 µm befasst.[238] Dadurch ergibt sich eine Vielzahl an Vorzügen gegenüber makroskopischen Verfahren. Die Vorteile umfassen einen geringeren Verbrauch an Reagenzien oder Probenmaterial und weniger zeitintensive Arbeitsprozesse, wodurch sinkende Kosten ermöglicht werden. Aber auch aus Sicht der Fluiddynamik gilt die Mikrofluidik als äußerst interessant, da diese Systeme aufgrund der geringen charakteristischen Länge L äußerst niedrige Werte für die dimensionslose Reynolds-Zahl Re (Gleichung 1) annehmen ($Re << 2000$).[239]

$$Re = \frac{\rho v L}{\eta} = \frac{v L}{\nu} \qquad \text{(Gleichung 1)}$$

Hierbei entspricht ρ der Dichte des Fluids, v der Strömungsgeschwindigkeit des Fluids, L der charakteristischen Länge (hier dem Innendurchmesser des Mikrokanals), η der dynamischen Viskosität und ν der kinematischen Viskosität.

Systeme, die mit Reynolds-Zahlen von $Re < 2000$ beschrieben werden können sind durch

laminare Strömungsprofile gekennzeichnet.[240] Im Gegensatz zu den normalerweise turbulenten Strömungen in makroskopischen Systemen (Re > 2000)[240] erfolgt eine Vermischung zweier parallel zueinander fließender Fluide bei laminarem Fluss nur durch Diffusion entlang deren Grenzfläche.[241] Des Weiteren ist der Effekt der Gravitationskraft auf Fluide in Mikrokanälen weniger stark ausgeprägt als in makroskopischen Systemen, wohingegen Oberflächenspannungs- und Kapillareffekte wiederum in den Mikrokanälen deutlich dominanter sind.[242]

Aufgrund dieser Eigenschaften hat die Mikrofluidik in einer Vielzahl unterschiedlicher Forschungsbereiche Einzug gehalten. Die Anwendungen umfassen beispielsweise analytische Systeme für die Genomik und Proteomik, Nachweistests für die Diagnostik und Rückstandsanalyse, Hochdurchsatz-Screenings, implantierbare Einheiten für die Wirkstofffreisetzung sowie Systeme für die organische Synthese und die Grundlagenforschung an Fluiden oder chemischen Reaktionen.[243]

1.5.2.1 Mikrofluidisches Faserspinnen

Die Mikrofluidik als Faserspinn-Verfahren erweist sich als besonders vielseitig, da mithilfe des *Rapid Prototypings* individualisierte Mikrokanalstrukturen erzeugt werden können, welche in Kombination mit dem laminaren Strömungsprofil in der Herstellung von Fasern mit maßgeschneiderten Eigenschaften resultieren können.

Das mikrofluidische Faserspinnen durch Fällungsreaktion - die mikrofluidische Flüssig-in-Flüssig Flussfokussierung - erfolgt grundsätzlich in Mikrokanälen, in denen ein zentraler Polymerlösungsfluss $\dot{V}_P$ durch zwei seitlich dazu ausgerichtete Mantelflüsse $\dot{V}_M$ hydrodynamisch fokussiert wird. Hierbei bewirkt $\dot{V}_M$ eine Veränderung des chemischen Milieus in $\dot{V}_P$ und eine Verdichtung der in $\dot{V}_P$ gelösten Polymere (oder auch suspendierten Nanofibrillen), wodurch diese in eine feste Phase übergehen (Abbildung 9A).[244-267] Abbildung 9B zeigt die Umsetzung des Schemas aus 9A zum einsatzfähigen Mikrofluidik-Chip.

Für Dispersionen aus Zellulose- und Proteinnanofibrillen konnte außerdem durch polarisationsmikroskopische Untersuchungen und *in situ* Kleinwinkelstreuungs-Experimente (SAXS) gezeigt werden, dass die hydrodynamische Fokussierung zu einer Ausrichtung nanofibrillärer Strukturen in Flussrichtung führt.[262, 263, 268] Die resultierenden Zellulosefasern aus diesen Mikrofluidik-Setups wiesen beträchtlich höhere mechanische Eigenschaften auf als Zellulosefasern aus früheren Studien, in welchen die Faserherstellung ohne die Verwendung einer mikrofluidischen Flüssig-in-Flüssig Flussfokussierung durchgeführt wurde.[262, 263]

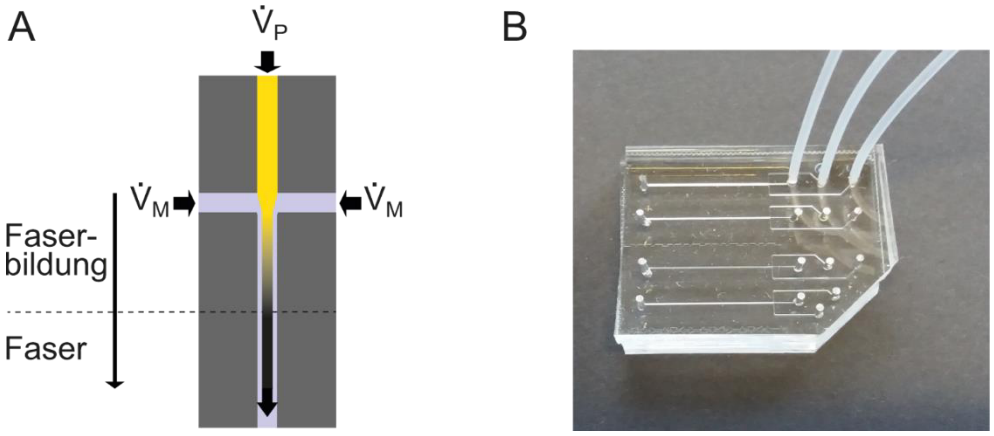

Abbildung 9. Schematische Darstellung des mikrofluidischen Faserspinnens basierend auf der Flüssig-in-Flüssig Flussfokussierung. (A) Die hydrodynamische Fokussierung eines Polymerlösungsflusses durch zwei seitlich dazu ausgerichtete Mantelflüsse bewirkt eine Änderung des chemischen Milieus und eine Verdichtung der im Polymerlösungsfluss befindlichen Polymere, wodurch die Faserbildung induziert wird. Abkürzungen: $\dot{V}_P$ = Polymerlösungsfluss, $\dot{V}_M$ = Mantelfluss. (B) Beispiel eines Mikrofluidik-Chips aus Polydimethylsiloxan (PDMS) inklusive angeschlossener Schläuche zur Lösungsinjizierung. Aus praktischen Gründen befinden sich auf dem Chip vier voneinander unabhängige Mikrokanalstruktureinheiten.

Der Großteil der publizierten mikrofluidischen Flüssig-in-Flüssig Flussfokussierungen, behandelt die Herstellung von Alginatfasern und Mischfasern aus Alginat und additiv-fungierenden Biopolymeren. Die Alginatfasern wurden durch hydrodynamische Fokussierung eines Alginatlösungsflusses $\dot{V}_P$ durch zwei Mantelflüsse $\dot{V}_M$ aus jeweils einer $CaCl_2$-Lösung zum Gelieren gebracht.[244-258] Neben Alginat wurden als weitere Polysaccharide auch Chitosan-,[259-261] und Zellulosefasern[262, 263] hergestellt. Auch im Bereich synthetischer Polymere konnten durch die mikrofluidische Flüssig-in-Flüssig Flussfokussierung Fasern aus Polycaprolacton (PCL),[264] Polylactid-co-Glycolid (PLGA)[265, 266] und Polyvinylacetat (PVA)[267] gesponnen werden.

Neben den Polysacchariden und synthetischen Polymeren stehen aktuell vor allem Proteinfasern im Fokus der mikrofluidischen Flüssig-in-Flüssig Flussfokussierung. Diesbezüglich konnte Molkeprotein[268] und rekonstituierte Seide des Seidenspinners *Bombyx mori*[269] zu Fasern verarbeitet werden. Kollagen und rekombinante Spinnenseide sind zwar bisher in einigen wenigen Studien auch mit der Mikrofluidik assoziiert, allerdings widmeten sich die Untersuchungen ausschließlich der Analyse der Assemblierungsmechanismen in Mikrokanälen. Ein kontinuierliches Faserspinn-Verfahren wurde mit diesen Studien nicht geschaffen.[80, 270-272]

Neben der Flüssig-in-Flüssig Flussfokussierung wurde die Mikrofluidik bisher auch in geringerem Umfang für Trocken- und Elektrospinn-basierte Verfahren eingesetzt. Beispielsweise wurde eine hochkonzentrierte Lösung aus *Bombyx mori* Fibroin ohne

Flussfokussierung mittels eines bioinspirierten Mikrokanals trocken versponnen.[273, 274] Im Fall des Elektrospinnens wurde die Mikrofluidik herangezogen, um Mehrfachdüsen für den Prozess-*Scale-Up* zu generieren,[275] hohle oder Kern-Schale-Fasern,[276] Janusfasern[277] oder Gradientenvliesstoffe[278] zu erzeugen.

1.5.2.2 Einsatz des mikrofluidischen Faserspinnens in der Biomedizin

Das mikrofluidische Faserspinnen nimmt einen hohen Stellenwert in der Gewebeneuzüchtung ein.[279] Mittels der Mikrofluidik wird die Verkapselung von Zellen und Wirkstoffen in Fasern sowie die Herstellung unterschiedlicher Fasermorphologien für spezialisierte Anwendungen ermöglicht. Beispielsweise wurden Alginat-Seidenfibroin-, Alginat-Chitosan- und Alginat-Kollagen/Fibrinogen-Fasern mit verkapselten Bindegewebs-, Karzinom-, Pankreas-Insel-, Endothel-, Nerven- und Muskelzellen beschrieben.[244, 253, 257, 258] In allen hier erwähnten Fällen basierte der Faserbildungsprozess auf der ionischen Vernetzung des Alginats, wohingegen Seidenfibroin, Chitosan, Kollagen oder Fibrinogen zur Erhöhung der Biokompatibilität und/oder Stabilität beigemischt wurde.[244, 253, 257, 258]

Überdies konnte gezeigt werden, dass sich Fasern aus mikrofluidischen Faserspinn-Verfahren auch zur Wirkstoffverkapselung eignen. In Kang *et al.*, 2011 wurde demonstriert wie durch die Abgabe des chemischen Lockstoffes Formyl-Met-Leu-Phe (fMLP) aus Alginatfasern die Migration von Neutrophilzellen vermittelt wurde.[252] In Ahn *et al.*, 2015 wurde die erfolgreiche Freisetzung des Antibiotikawirkstoffes Ampicillin aus Alginatfasern dargelegt.[247]

Neben dem Einschluss funktionaler Zellen oder Wirkstoffe ermöglicht die Mikrofluidik auch die kontinuierliche Herstellung hochkomplexer Fasern bestehend aus mehreren Komponenten, welche entsprechend dem angelegten Flussprofil in der Faser vorliegen. Daraus kann die Wirkstofffreisetzung kontrollierbarer gestaltet werden und das hergestellte Fasermaterial der differenzierten, natürlichen Gewebsstruktur näherkommen. In einer Studie stellten dazu Kang *et al.*, 2011 ein mikrofluidisches Faserspinn-Verfahren vor, welches die Herstellung einer seriellen oder parallelen Verteilung von Wirkstoffen oder Zellen in der resultierenden Alginatfaser ermöglichte.[252]

Die Neuzüchtung anisotroper Gewebe erfordert oftmals eine faserige Gerüststruktur, welche ein kontrolliertes Zellwachstum und die Ausrichtung zellulärer Strukturen ermöglicht.[44, 183, 194, 280] Mithilfe des mikrofluidischen Faserspinnens können Endlosfasern mit Durchmessern bis in den einstelligen Mikrometer-Bereich hergestellt werden,[264-267] wodurch eine effizientere Ausrichtung der Zellkörper- und fortsätze erreicht wird, als dies mit dickeren Fasern möglich ist.[225, 265, 266]

Speziell auf Kollagen bezogen, bietet das mikrofluidische Faserspinnen im Vergleich zu bisherigen Nassspinn-Verfahren aufgrund der andersartigen fluiddynamischen Grundlagen einen interessanten Ansatzpunkt, um Kollagenfasern mit besseren mechanischen Stabilitäten und geringeren Faserdurchmessern herzustellen. Bislang sind die aktuellen Kollagenfaserspinn-Verfahren durch die relativ niedrige Assemblierungssrate von Kollagen zu Fibrillen und Fasern limitiert,[253] und erfordern dadurch geringe Extrusionsgeschwindigkeiten, organische Lösungsmittel als Fällungs-, Dehydratisierungs-, oder Waschreagenz[214-220, 222, 223, 225] und zusätzliche Verweilzeiten der extrudierten Faser im Fäll- bzw. Nachbehandlungsbad.[25, 215, 216, 218-221, 223, 225, 226] Oftmals werden die resultierenden Kollagenfasern zudem nachträglich mit Glutaraldehyd,[215, 216, 219, 220, 222, 225] EDC ± NHS (1-Ethyl-3-(3-dimethyl-aminopropyl)-carbodiimid ± N-Hydroxysuccinimid),[214, 215, 218, 225] Genipin[222] oder durch die dehydrothermale Behandlung ± Cyanamid[25, 217, 219-221, 223] vernetzt, um die mechanische Stabilität zu erhöhen. Diese diskontinuierliche Prozessführung wirkt sich in einer geringen Produktivität aus. Auch birgt der Einsatz toxischer Vernetzungsreagenzien, wie Glutaraldehyd, das Risiko während der Anwendung der Kollagenfasern am Menschen Zellschäden zu verursachen,[281] wohingegen die dehydrothermale Behandlung zur Denaturierung der tripelhelikalen Domänen in Kollagen führen kann.[282] Des Weiteren besitzen rekonstituierte Kollagenfasern aus bisherigen Nassspinn-Verfahren Durchmesser mit Werten größer 20 µm,[214, 215, 217, 222, 226, 283] wodurch mit diesen Fasern in der Gewebeneuzüchtung nur eine maximal mäßige Ausrichtung von Zellen und ihren Fortsätzen erwartet wird.[265, 266]

2 ZIELSETZUNG

Aktueller Gegenstand der Forschung sind Fasermaterialien für die Anwendung in der Biomedizin. Diese Arbeit sollte daher einerseits neue Faserspinn-Verfahren etablieren, welche zur Herstellung von Fasermaterialien mit verbesserten oder neuartigen Eigenschaften herangezogen werden können. Andererseits sollte die bisher undokumentierte, aber aufgrund ihrer mechanischen Eigenschaften äußerst interessante Spinnenseide der australischen Krabbenspinne *S. formivorus* analysiert werden, um bioinspiriert eine Grundlage für die Herstellung belastbarer, neuer Fasermaterialien zu generieren.

Daher sollte zunächst die Idee verfolgt werden ein mikrofluidisches Faserspinn-Verfahren zur Herstellung von Vliesstoffgarnen und isotropen Vliesstoffen einzuführen, welches zukünftig speziell auch auf Kollagen angewendet werden könnte und im Gegensatz zum Elektrospinnen kein elektrisches Feld erfordert. Durch Einführung dieses neuen Verfahrens könnte das mit dem Elektrospinnen-assoziierte Denaturierungsrisiko von Kollagen gemindert werden, wodurch die bemerkenswerten Eigenschaften dieses Biopolymers besser zur Geltung kommen würden.[235, 236]

Schwerpunkt sollte allerdings auf der Entwicklung eines mikrofluidischen Faserspinn-Verfahrens zur Herstellung von Kollagenendlosfasern mit verbesserten Eigenschaften, d.h. höheren mechanischen Stabilitäten und niedrigeren Faserdurchmessern im Vergleich zu bisherigen Kollagenfasern aus Nassspinn-Verfahren liegen. Dazu sollte ein innovativer Mikrofluidik-Chip hergestellt und die *in vitro* Kollagenfibrillenbildung in diesem getestet, optimiert sowie in eine kontinuierliche Prozessführung übertragen werden. Wesentlicher Bestandteil sollte zudem sein, die resultierenden Kollagenfasern morphologisch, mechanisch, strukturell und bezüglich ihrer thermischen Eigenschaften zu untersuchen.
Um die Biokompatibilität und die biologische Funktionalität der Kollagenfasern zu bewerten, sollten diese anschließend als Orientierungsstruktur für die periphere Nervenreparatur getestet werden. Dazu sollte eine neuronale Zelllinie in Zellkulturversuchen auf den Kollagenfasern differenziert werden und die resultierende Zelladhäsion, Neuriten- und Synapsenbildung sowie die elektrophysiologische Aktivität untersucht werden. Darüber hinaus sollten die Kollagenfasern auch als Füllmaterial in Nervenleitschienen aus rekombinanter Spinnenseide eingesetzt werden, um die Funktionalität dieser auch unter Bedingungen zu testen, die dem späteren Einsatz näherkommen. Ergänzend zu diesen Untersuchungen sollten auch alternative Nervenleitschienen, basierend auf selbstrollenden Filmen, generiert werden, welche eine

Gewebeneuzüchtung in diesen durch einen schonenderen Einschluss von Nervenzellen und empfindlichen Materialien im Vergleich zu bereits vorgefertigten Röhren ermöglichen könnten.

Neben der Generierung innovativer Faserherstellungs-Verfahren und Materialien sollte die biegesteife Spinnenseide der australischen Krabbenspinne *S. formivorus* untersucht werden. Dazu sollten vorab die Spinnenseidennetze von *S. formivorus* grundlegend dokumentiert werden. Anschließend sollten die darin identifizierten Fasern auf makroskopischer, mikroskopischer und molekularer Ebene analysiert werden. Die Analyse auf molekularer Ebene sollte auch Messungen mittels synchrotroner Infrarotmikrospektroskopie einschließen, um hochaufgelöste Informationen über die chemische Faserzusammensetzung zu erhalten. Einen wesentlichen Bestandteil sollte daneben die Analyse der mechanischen Eigenschaften der Fasern unter Zug- und lateraler Belastung darstellen.

3 SYNOPSIS

Diese Dissertation umfasst fünf Teilarbeiten, welche sich mit der Herstellung, Charakterisierung und Anwendung von biopolymerbasierten Fasermaterialien befassen. Die Teilarbeiten sind in Kapitel 7 dieser Arbeit detailliert beschrieben.

Teilarbeit 1 und 2 beschäftigte sich mit der Entwicklung zweier unterschiedlicher mikrofluidischer Verfahren zur kontinuierlichen Faserherstellung. Die erzielten Fasern aus Teilarbeit 2 wurden anschließend ausführlicher in Teilarbeit 3 hinsichtlich deren Funktionalität für die Anwendung in der peripheren Nervenreparatur getestet und als Füllmaterial in Nervenleitschienen aus rekombinanter Spinnenseide eingesetzt. Teilarbeit 4 befasste sich mit dem Design alternativer Nervenleitschienen. In Teilarbeit 5 wurde die einzigartige Seide der australischen Krabbenspinne *S. formivorus* untersucht. Eine Übersicht der jeweiligen Teilarbeiten und deren Bezug zueinander ist in Abbildung 10 dargestellt.

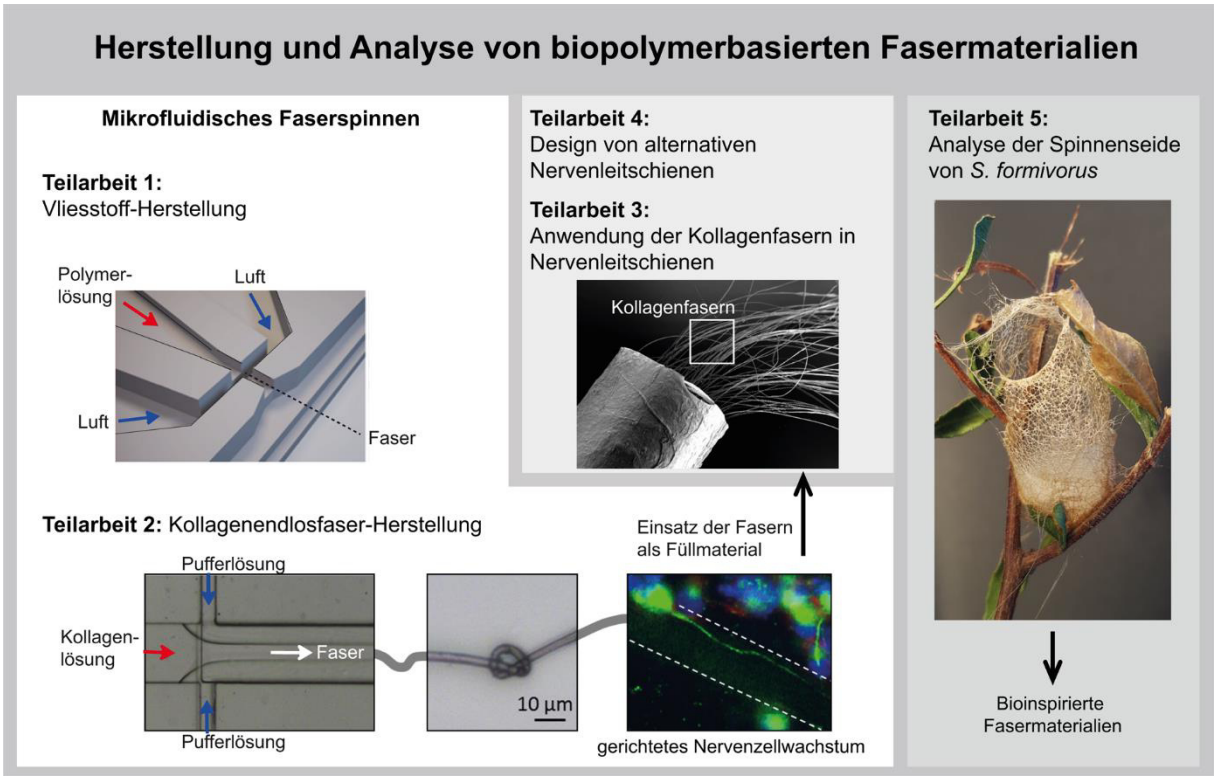

Abbildung 10. Übersicht der Teilarbeiten, welche aus dieser Dissertation hervorgehen. Adapted from Hofmann *et al.*[284] (DOI: 10.1039/C8LC00304A) with permission from The Royal Society of Chemistry. Adapted with permission from Haynl *et al.*[285] (DOI: 10.1021/acs.nanolett.6b02828). Copyright (2016) American Chemical Society. Adapted from Pawar *et al.*[286] (DOI: 10.1021/acsabm.9b00628). Copyright (2019) American Chemical Society.

Neben diesen fünf Teilarbeiten wurde zudem an der Entstehung von Teilarbeit 6 mitgewirkt, welche sich mit der Entwicklung eines automatisierten, biomechatronischen Systems befasste. Jedoch ist diese Arbeit aufgrund des abweichenden fachlichen Bezugs im Vergleich zur gegenwärtigen Ausrichtung dieser Dissertation in der Publikationsliste lediglich aus Gründen der Vollständigkeit erfasst.

3.1 Mikrofluidisches Faserspinnen

3.1.1 Herstellung von Mikrofluidik-Chips

Das mikrofluidische Faserspinnen basierte auf dem Einsatz von Mikrofluidik-Chips, welche aus dem elastomeren Kunststoff Polydimethylsiloxan (PDMS) bestanden. Die Herstellung dieser gliederte sich in drei Teilschritte, welche in Abbildung 11 (Figure 1 in Teilarbeit 1) exemplarisch für einen Chip gezeigt sind, wie er zum mikrofluidischen Faserspinnen basierend auf der Flüssig-in-Gas Flussfokussierung eingesetzt wurde (siehe 3.1.2).
Im ersten Prozessabschnitt wurden dazu Mikrostrukturen bestehend aus dem Fotolack SU-8 mit Hilfe der Fotolithographie auf einem Siliziumwafer erzeugt, welche in einem späteren Prozess-Abschnitt als Abdruckform für die Mikrokanäle Verwendung fanden. Die Aushärtung der Mikrostrukturen erfolgte hierbei durch selektive Belichtung des SU-8 Lackes mittels einer Fotomaske und UV-Licht der Wellenlänge 365 nm, wohingegen nicht-belichteter Fotolack stets entfernt wurde (Abbildung 11A). Die Mikrostrukturen des Siliziumwafers wurden anschließend mittels Softlithographie in einen PDMS-Abguss überführt und letzterer durch Temperaturerhöhung ausgehärtet, entformt und zurechtgeschnitten (Abbildung 11B). Die komplexe innere Geometrie der in dieser Arbeit eingesetzten Mikrofluidik-Chips erforderte einen Aufbau aus zwei zueinander komplementären Chiphälften, welche durch Oberflächenaktivierung mit Luftplasma irreversibel miteinander verbunden wurden (Abbildung 11C).

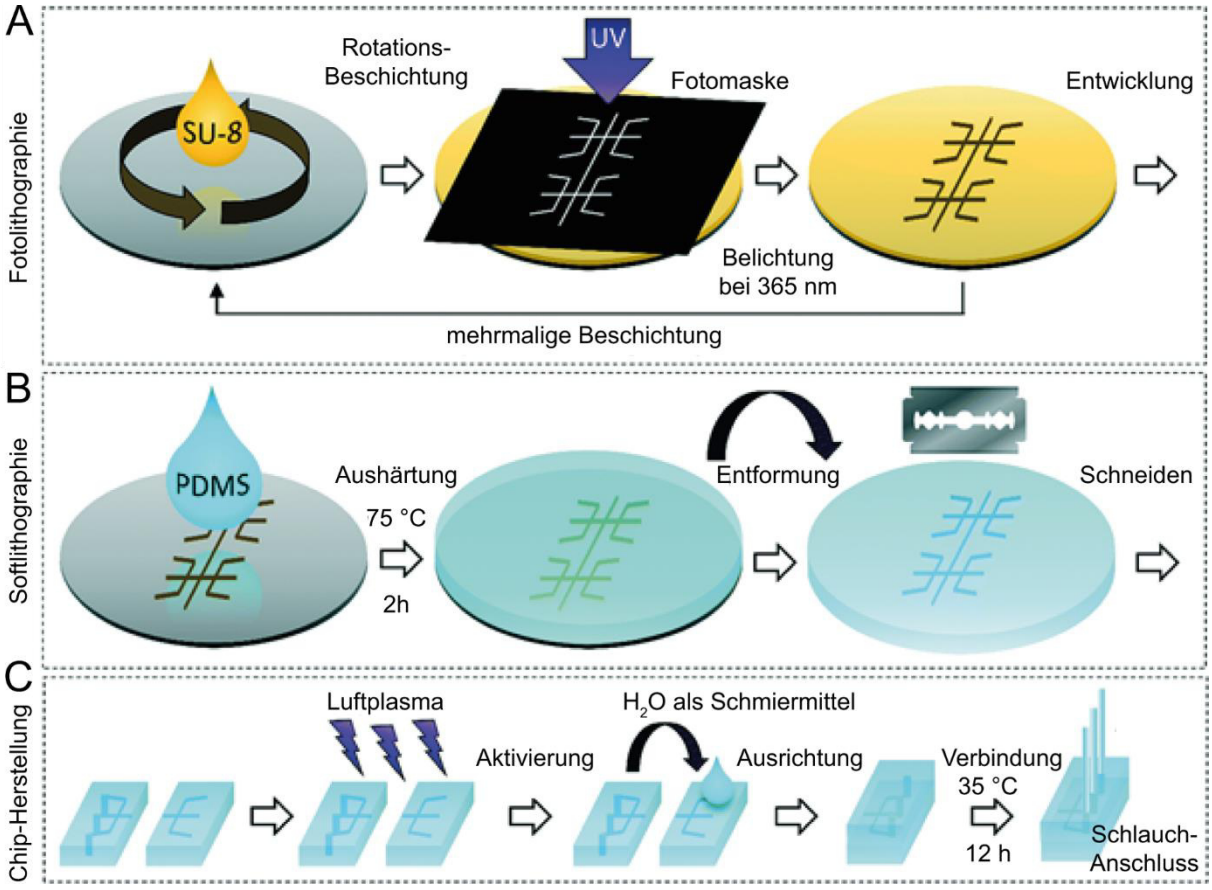

Abbildung 11. Dreistufige Mikrofluidik-Chip-Herstellung. (A) Fotolithographische Generierung einer mikrostrukturierten Siliziumwafer-Oberfläche durch selektive Belichtung eines SU-8 Fotolackes mittels einer Fotomaske und Licht einer Wellenlänge von 365 nm. (B) Softlithographische Überführung der Mikrostruktur in einen PDMS-Abguss. Letzterer wird bei einer Temperatur von 75 °C für 2 h vollständig ausgehärtet und lässt sich anschließend entformen und zurechtschneiden. (C) Die Oberflächen zueinander komplementärer Chiphälften werden durch Luftplasma aktiviert und mithilfe eines Wasserfilms aufeinander ausgerichtet. Nach 12 h Inkubation bei 35 °C sind die Chiphälften irreversibel miteinander verbunden. Adapted from Hofmann *et al.*[284] (DOI: 10.1039/C8LC00304A) with permission from The Royal Society of Chemistry.

3.1.2 Faserspinnen durch mikrofluidische Flüssig-in-Gas Flussfokussierung

Das mikrofluidische Faserspinn-Verfahren aus Teilarbeit 1 beruhte auf der hydrodynamischen Fokussierung eines (Bio)-Polymerlösungsflusses $\dot{V}_P$ mittels zweier rechtwinklig dazu ausgerichteter Mantelflüsse $\dot{V}_M$ aus Luft (Abbildung 12A) und konnte mit dem Prinzip der gasdynamischen virtuellen Düse (GDVN, engl. *gas dynamic virtual nozzle*) beschrieben werden. Generell bezeichnet dieses Prinzip ein System in dem der Fluss und die Form eines Fluids mittels eines Gasstroms kontrolliert werden können und die Ausbildung eines freistehenden Fluidstrahls (engl. *Liquid Jet*) ermöglicht wird. Der freistehende Fluidstrahl weist hierbei geringere Dimensionen als der ursprüngliche Flüssigkeitskanal auf, wodurch der Fluidstrahl theoretisch nicht in Kontakt mit der Kanalinnenwand gerät.[287-289]

Für die Umsetzung dieses Prinzips in ein Faserspinn-Verfahren wurde in dieser Arbeit ein

Mikrofluidik-Chip entwickelt (Abbildung 12B, Figure 2 in Teilarbeit 1), dessen wesentliches Design auf der Mikrokanalgeometrie von Trebbin *et al.*, 2014 zur Generierung eines freistehenden Wasserstrahls basierte.[287] Zur experimentellen Beschreibung des mikrofluidischen Faserspinn-Verfahrens wurde eine Lösung aus dem Fluorocopolymer THV 221 (Tetrafluoroethylen, Hexafluoropropylen und Vinylidenfluorid) in Aceton als Modell-Polymerlösung gewählt. Das lag darin begründet, dass THV 221 als fluoriertes Polymer bei einem möglichen Kontakt mit der Kanalinnenwand nur minimale Wechselwirkungen einging und dadurch besonders gut für störungsfreie Systemparameter-Untersuchungen geeignet war. Darüber hinaus wurde eine Lösung aus Polycaprolacton (PCL) in Hexafluoroisopropanol (HFIP) getestet, um die Anwendbarkeit dieser Methode um ein für die Biomaterialwissenschaften bedeutsames Biopolymer zu erweitern.

Ohne weitere Modifikationen des experimentellen Aufbaus konnten hiermit isotrope Vliesstoffe erzeugt werden. Mit Einführung einer nachgeschalteten, rotierenden Spule als Faseraufwickelvorrichtung wurde zudem auch die Bildung eines anisotropen Vliesstoffgarns ermöglicht (Abbildung 12C, Figure 3 und 4 in Teilarbeit 1). Für das Modell-Polymer THV 221 konnte gezeigt werden, dass der finale Faserdurchmesser von der Flussrate, der angelegten Luftdruckdifferenz sowie der eingestellten Faseraufwickelgeschwindigkeit abhängig und zwischen 1,6 und 4,2 µm einstellbar war (Figure 6 in Teilarbeit 1).

Zukünftig könnte dieser hier etablierte Mikrofluidik-Chip herangezogen werden, um auch Kollagenlösungen zu verspinnen. Vor allem könnten die aus der Kollagenlösung resultierenden Fasern aufgrund der Abwesenheit eines elektrischen Feldes (im Gegensatz zum Elektrospinnen) nativere Eigenschaften, d.h. einen höheren Anteil an intakten tripelhelikalen Domänen aufweisen.

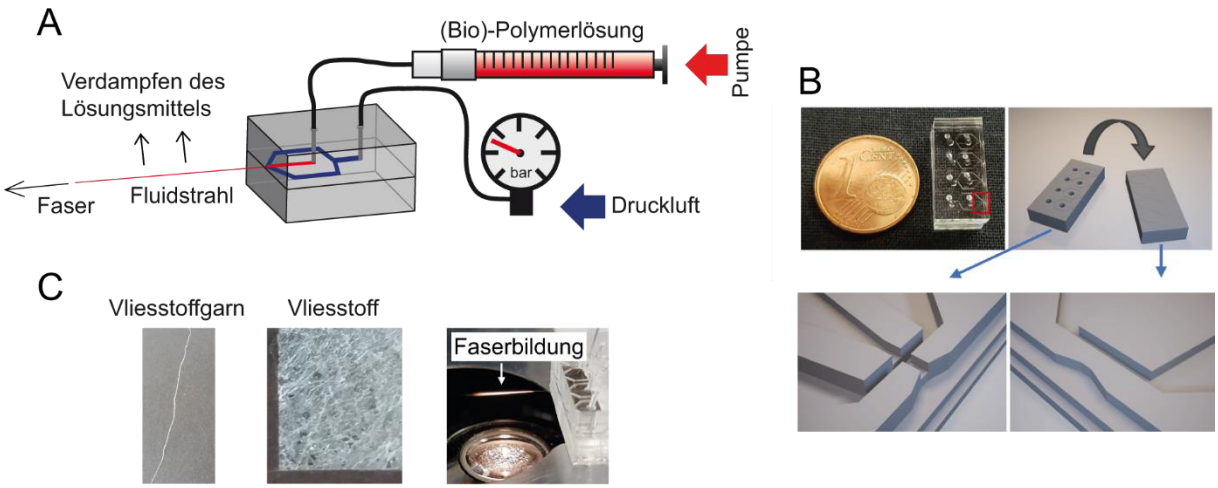

Abbildung 12. Mikrofluidisches Faserspinnen mittels der Flüssig-in-Gas Flussfokussierung. (A) Schematische Darstellung des Mikrofluidik-Chips. Ein (Bio)-Polymerlösungsfluss verlässt mithilfe eines Mantelflusses aus Luft den Mikrofluidik-Chip als Fluidstrahl, wodurch in Kombination mit dem Verdampfen des Lösungsmittels die Faserbildung einsetzt. (B) Fotographische Darstellung und schematische Abbildung des eingesetzten Mikrofluidik-Chips, welcher durch Verbindung zweier zueinander komplementärer Hälften hervorgeht. (C) Fotographische Abbildung des eingesetzten Mikrofluidik-Chips während des Spinnprozesses und die damit erzielbaren Morphologien Vliesstoffgarn und isotroper Vliesstoff. Figure 12B and parts of 12C are adapted from Hofmann *et al.*[284] (DOI: 10.1039/C8LC00304A) with permission from The Royal Society of Chemistry.

3.1.3 Faserspinnen durch mikrofluidische Flüssig-in-Flüssig Flussfokussierung

Die Herstellung einer Kollagenendlosfaser beruhte auf der mikrofluidischen Flüssig-in-Flüssig Flussfokussierung (Teilarbeit 2). Das grundlegende Design des eingesetzten Mikrofluidik-Chips basierte auf Vorarbeiten, in denen das Verspinnen einer Lösung aus Seidenfibroin des Seidenspinners *Bombyx mori* demonstriert wurde.[269]

Der Chip wies eine dreidimensionale Struktur auf, in welcher ein Kollagenlösungsfluss im zentralen Kanal durch zwei rechtwinklig dazu ausgerichtete und zueinander höhenversetzt-zuströmende Mantelflüsse hydrodynamisch fokussiert wurde. Diese spezielle Geometrie reduzierte die Wechselwirkung der entstehenden Kollagenassemblate mit den Kanalwänden, wodurch das Ausmaß an Kanalverstopfungen gesenkt werden konnte.

Zur Kollagenfaser-Herstellung wurde in den Kernkanal eine Lösung aus Kollagen Typ I in Essigsäure bei pH 3 mit einer definierten Flussrate injiziert ($\dot{V}_P$), wohingegen die beiden Mantelflüsse $\dot{V}_M$ jeweils aus neutralen Pufferlösungen, pH 8 mit 10 % (w/v) Polyethylenglykol (PEG) bestanden. Die Interaktion des sauren Kollagenflusses mit den beiden neutralen Pufferflüssen am Kanalkreuz führte zu einer Neutralisierung des Kollagenflusses, wodurch die Bildung von Kollagenfibrillen induziert wurde. Durch die hydrodynamische Fokussierung wurden die Fibrillen verdichtet und dadurch die intermolekularen Wechselwirkungen erhöht.

Mutmaßlich fand durch die auftretenden Scherkräfte während der Fokussierung auch eine longitudinale Ausrichtung der Fibrillen statt. Die dabei hervorgehende Faser wurde kontinuierlich in ein Wasserbad zur Entfernung der Pufferbestandteile extrudiert, bevor sie mittels einer rotierenden Spule aufgewickelt wurde (Abbildung 13A und B, Figure 1A und B in Teilarbeit 2).

Interessanterweise war die Herstellung mechanisch stabiler, und damit aufwickelbarer, Kollagenfasern nur durch die Beimischung von PEG zu den Pufferlösungen möglich. Dieser Effekt konnte darauf zurückgeführt werden, dass das hygroskopisch-wirkende PEG die Wassermoleküle zwischen den Kollagenmolekülen entzog und dadurch die intermolekularen Wechselwirkungen zwischen diesen erhöht wurden.[290, 291]

Der Durchmesser der ins Wasserbad extrudierten, noch gelartigen Fasern konnte über die angelegten Kollagen- und Pufferflussraten kontrolliert werden (Abbildung 13B und C, Figure 1B und C in Teilarbeit 2). Dabei war die Entnahme von mechanisch-stabilen Kollagenfasern nur unter definierten Flussraten gewährleistet (siehe gestrichelter Kasten in Abbildung 13C bzw. in Figure 1C in Teilarbeit 2). Einerseits führte ein im Verhältnis zum Kollagenfluss zu geringer Pufferfluss zu einer reduzierten hydrodynamischen Fokussierung, welche vermutlich in einer geringeren Verdichtung und einer schlechteren longitudinalen Ausrichtung der Kollagenfibrillen resultierte. Sehr wahrscheinlich war auch die Diffusion der neutralen Pufferlösung in vergleichsweise hohe Kollagenflüsse, welche ohnehin bei laminaren Strömungsprofilen nur über die Grenzfläche zweier Medien stattfindet,[241] unzureichend. Hingegen verhinderte ein zu hohes Verhältnis an Puffer- zu Kollagenfluss grundsätzlich die Bildung von Fasern, da der Pufferfluss zu einer Zurückdrängung des Kollagenflusses in dessen ursprünglichen Kanal führte.

Der Faserdurchmesser war zusätzlich von der Aufwickelgeschwindigkeit der rotierenden Spule abhängig (Abbildung 13D, Figure 1D in Teilarbeit 2). Es wurde beobachtet, dass die Fasern nach Verlassen des Wasserbads eine signifikante Reduzierung ihrer Durchmesser erfuhren, wodurch eine zusätzliche Ausrichtung der Kollagenmoleküle bzw. -fibrillen in Faserrichtung vermutet wurde. Die finalen Faserdurchmesser bewegten sich in einem Bereich von 3 bis 6 µm und wiesen dadurch signifikant geringere Durchmesser auf, als dies für Kollagen Typ I Fasern in Nassspinn-Prozessen beobachtet wurde (Tabelle 4).

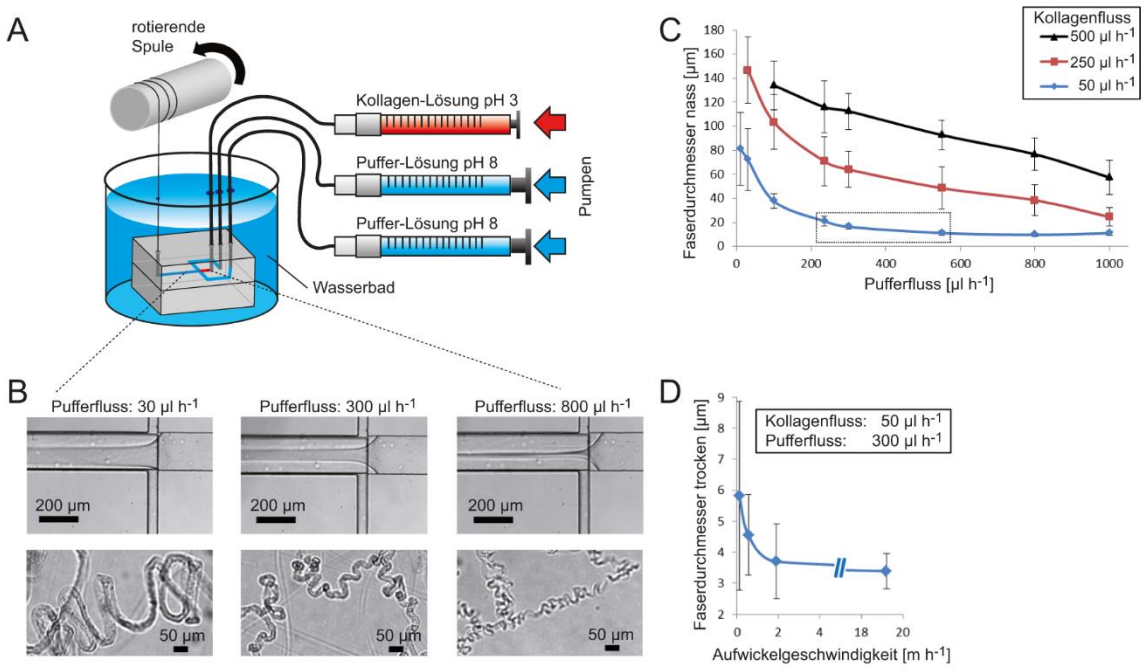

Abbildung 13. Mikrofluidisches Kollagenfaserspinnen mittels Flüssig-in-Flüssig Flussfokussierung. (A) Schematische Darstellung des mikrofluidischen Kollagenfaserspinnens. Der Mikrofluidik-Chip ist über Schläuche mit drei unabhängig voneinander ansteuerbaren Spritzenpumpen verbunden, welche eine simultane Dosierung einer Kollagenlösung mit pH 3 (rot) und zweier identischer Polyethylenglykol-haltiger Pufferlösungen mit pH 8 (blau) ermöglichen. Die Faserbildung wird am Flusskreuz durch die Erhöhung des pH-Wertes und in Anwesenheit von Polyethylenglykol induziert. Die dabei entstehenden Fasern werden ins Wasserbad extrudiert und mit Hilfe einer rotierenden Spule abgezogen. (B) Eine konstante Kollagenflussrate (hier: 50 µl h^{-1}) und variierende Pufferflussraten ermöglichen die Einstellung der Durchmesser der ins Wasserbad extrudierten Fasern. (C) Die Durchmesser der ins Wasserbad extrudierten Fasern korrelieren mit den Kollagen- und Pufferflussraten. Die Herstellung mechanisch-stabiler (d.h. abziehbarer) Fasern ist mit einem Kollagenfluss von 50 µl h^{-1} in Kombination mit Pufferflussraten zwischen 235 und 550 µl h^{-1} möglich (hier durch einen Rahmen verdeutlicht). (D) Der Durchmesser der trockenen Fasern ist durch die Aufwickelgeschwindigkeit der rotierenden Spule bei konstantem Kollagen- und Pufferfluss einstellbar. Adapted with permission from Haynl *et al.*[285] (DOI: 10.1021/acs.nanolett.6b02828). Copyright (2016) American Chemical Society.

Die aus dieser Teilarbeit hervorgehenden Kollagenfasern zeichnen sich durch einen homogenen Faserdurchmesser (Abbildung 14A, Figure 2A und B in Teilarbeit 2) und schwach-ausgeprägte, longitudinal-verlaufende Rillen aus (Abbildung 14A bzw. Figure 2B in Teilarbeit 2), was eine Orientierung fibrillärer Strukturen vermuten lässt. Anhand der polarisiertern Fourier-Transform Infrarotspektroskopie (FTIR) konnte eine Orientierung der Kollagenmoleküle in Richtung der Faserlängsachse bestätigt werden. Dazu wurden die Kollagenfasern mit polarisiertem Infrarotlicht analysiert, welches entweder parallel oder im rechten Winkel zur Faserlängsachse eingestrahlt wurde. Hierbei wurden für diese beiden Einfallswinkel unterschiedliche Amid I /Amid II-Bandenflächen-Verhältnisse erhalten. Diese betrugen 2,7 für den rechtwinkligen und 1,1 für den parallelen Einfallswinkel im Vergleich zu 1,7 für nicht-polarisiertes Infrarotlicht (Abbildung 14B, Figure 3A in Teilarbeit 2). Die Unterschiede im Absorptionsverhalten gehen

darauf zurück, dass die Carbonyl-Gruppen in Kollagenmolekülen rechtwinklig zur Moleküllängsachse stehen, wodurch diese Eigenschaft gezielt als Indikator für die Kollagenmolekül- bzw. Kollagenfibrillenorientierung herangezogen werden kann.[292, 293] Daneben waren die Kollagenfasern erstaunlicherweise zugfest und elastisch genug, um händisch geknotet zu werden (Abbildung 14A, Figure 2A in Teilarbeit 2).

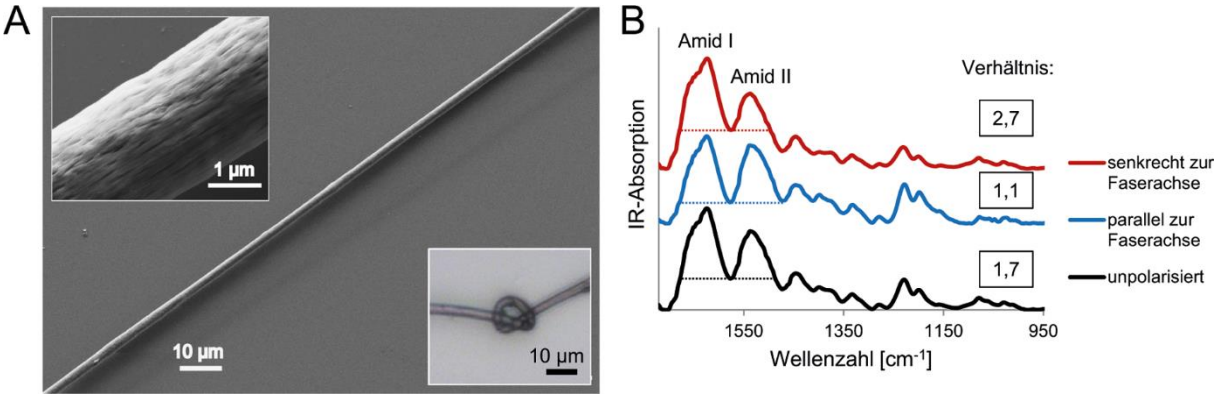

Abbildung 14. Morphologische und spektroskopische Charakterisierung der Kollagenfasern. (A) Rasterelektronenmikroskopische (REM) Aufnahme einer Kollagenfaser. Die Kollagenfaseroberfläche ist im kleinen Bild oben-links ersichtlich. Händisch-gefertigter Knoten in der Kollagenfaser (kleines Bild unten-rechts). (B) Fourier-Transform Infrarot (FTIR)-Spektren einer Kollagenfaser nach Analyse mit unpolarisiertem oder polarisiertem Licht. Polarisiertes Infrarotlicht wurde entweder im rechten Winkel oder parallel zur Faserlängsachse eingestrahlt. Adapted with permission from Haynl *et al.*[285] (DOI: 10.1021/acs.nanolett.6b02828). Copyright (2016) American Chemical Society.

Zur Analyse der mechanischen Eigenschaften wurden Zugprüfungen bei einer relativen Luftfeuchte von 30 % durchgeführt. Dabei wurde eine Zugfestigkeit von 383 ± 85 MPa, eine Bruchdehnung von 25,0 ± 3,7 % und ein E-Modul von 4138 ± 512 MPa ermittelt, wodurch eine Zähigkeit von 52,9 ± 14,7 MJ m^{-3} resultierte. Die Zugfestigkeit und das E-Modul waren damit signifikant höher im Vergleich zu den mechanischen Eigenschaften nassgesponnener Kollagenfasern aus vorherigen Studien (Tabelle 4).

Zum mikrofluidischen Kollagenfaserspinnen wurde eine Konzentration von 0,48 % (w/v) eingesetzt, welche im Vergleich zu den Konzentrationen in Nassspinnverfahren geringer war. Vergleichsweise niedrigere Kollagenkonzentrationen und damit niedrigere Viskositäten haben zur Konsequenz, dass die Entschlaufung einzelner Kollagenmoleküle effizienter erfolgt und eine dicht gepackte Anordnung ausgerichteter Kollagenmoleküle realisierbarer wird,[214, 222] wodurch die intermolekularen Wechselwirkungen zunehmen (und damit die mechanische Stabilität). Analog zu früheren Studien mit Zellulosenanofibrillen bewirkt vermutlich auch die hydrodynamische Fokussierung eine Zunahme der intermolekularen Wechselwirkungen durch

Verdichtung und Ausrichtung der Kollagenfibrillen.[262, 263] Die geringer eingesetzte Kollagenkonzentration in Kombination mit den geringen Dimensionen der Mikrofluidikkanäle führten schließlich auch zu Fasern mit einem signifikant geringeren Durchmesser im Vergleich zu nassgesponnenen Kollagenfasern. Durch die dabei kleinere Faserquerschnittsfläche wird die Wahrscheinlichkeit für Materialdefekte, wie beispielsweise Luft- oder Fremdpartikel-einschlüsse, Kettenverschlaufungen und -abbrüche minimiert, welches im Allgemeinen eine Erhöhung der Zugfestigkeit bewirkt.[217, 294]

Tabelle 4. Mechanische Daten von Kollagen Typ I-Fasern. Alle hier aufgelisteten Daten gehen aus technischen Spannungs-Dehnungs-Kurven von trockenen und nicht-nachbehandelten Kollagen Typ I-Fasern hervor (aus den Studien wurden die mechanischen Werte der Kollagenfasern mit der jeweils höchsten Zugfestigkeit zitiert). Tabelle basierend auf Haynl *et al*.[285].

Kollagenfaser	Bruchdehnung [%]	Zugfestigkeit [MPa]	E-Modul [MPa]	Durchmesser [µm]	Kollagen-konzentration [mg mL^{-1}]
Mikrofluidik:					
Haynl *et al.*, 2016[285]	**25,0 ± 3,7**	**383 ± 85**	**4138 ± 512**	**3,7 ± 1,2**	**4,8**
Nassspinnen:					
Dunn *et al.*, 1993[217]	-	≈ 160	-	≈ 20,0	10,0
Cavallaro *et al.*, 1994[215]	-	224 ± 19	-	≥ 25,0	5,0
Zeugolis *et al.*, 2008[226]	27,0 ± 5,0	208 ± 57	1580 ± 490	119,0 ± 15,0	6,0
Siriwardane *et al.*, 2014[222]	18,4 ± 4,9	262 ± 62	1265 ± 171	46,5 ± 10,9	7,5
Arafat *et al.*, 2015[214]	-	72	2200	≈ 80,0	12,0
Huang *et al.*, 2018[283]	≈ 17,5	313	5849	36,9 ± 4,5	10,0

Aufgrund der hervorragenden mechanischen Eigenschaften der Kollagenfasern aus dem mikrofluidischen Faserspinn-Verfahren waren keine nachfolgenden Vernetzungsreaktionen mit gegebenenfalls potenziell zelltoxischen Reagenzien (wie Glutaraldehyd[281]) oder der Gefahr der Denaturierung der tripelhelikalen Kollagendomänen (wie im Fall der Dehydrothermalen Behandlung[282]) erforderlich.

Die dynamische Differenzkalorimetrie (DSC) zeigte eine Denaturierung der tripelhelikalen Kollagendomänen in den Fasern bereits bei 59 °C (Figure 4B in Teilarbeit 2). Daher können diese Kollagenfasern für biomedizinische Anwendungen oder in der Gewebeneuzüchtung ohne Verlust der nativen Strukturen eingesetzt werden. Die Verarbeitung dieser Fasern zu Garnen oder zu höherstrukturierteren Geweben durch beispielsweise Weben, Stricken oder Sticken

sollte jedoch unterhalb von 59 °C durchgeführt werden, um die kollagentypischen Eigenschaften der Fasern in vollem Umfang zu gewährleisten.

3.1.4 Zellkulturversuche mit neuronalen Zellen

Die mittels Mikrofluidik hergestellten Kollagenfasern wurden in Zellkulturexperimenten mit der neuronalen Zelllinie NG108-15 getestet. Dazu wurden die Fasern mit den Zellen besiedelt und nach erfolgter Differenzierung untersucht (Teilarbeit 2 und 3).

Durch Anfärbung der Zellkerne mit dem Fluoreszenzfarbstoff 4′,6-Diamidin-2-phenylindol (DAPI) wurde eine gute Adhäsion der Zellen auf den freistehenden Fasern beobachtet (Abbildung 15A, Figure 5A und C in Teilarbeit 2). Anschließend wurde das Protein *ß*-Tubulin III mittels Antikörper-Färbung visualisiert, welches in neuronalen Zellstrukturen prominent vertreten ist.[295] Es zeigte sich dabei, dass die Zellen nicht nur adhärierten, sondern auch Neurite ausbildeten, welche entlang der Faserlängsachse orientiert vorlagen (Abbildung 15B, Figure 5 E in Teilarbeit 2, Figure 3 in Teilarbeit 3). Die gute Orientierung der Neurite war auf das geringe Verhältnis von Kollagenfaserdurchmesser zu Zellsomagröße zurückzuführen, da bereits in vorhergehenden Arbeiten in einem gewissen Bereich eine indirekte Proportionalität zwischen dem Faserdurchmesser und der longitudinalen Ausrichtung von Zellen und ihrer Fortsätze gezeigt wurde.[225, 265, 266]

Überdies konnte in differenzierten NG108-15 Zellen auf Kollagenfasern die Expression des SNAP-25 Proteins beobachtet werden (Figure 4F in Teilarbeit 3), welches entscheidend an der exozytotischen Freisetzung der Neurotransmitter in den synaptischen Spalt beteiligt,[296, 297] und als Indiz für das Vorhandensein funktioneller Synapsen aufzufassen ist.

Um die elektrophysiologische Funktionalität der NG108-15 Zellen auf den Kollagenfasern zu beurteilen und die neuronale Erregbarkeit sowie die Befähigung zur Ausbildung von Aktionspotenzialen zu untersuchen wurden *Patch Clamp*-Aufnahmen im Ganzzell-Modus (engl. *whole-cell patch clamp*) generiert (Figure 4G in Teilarbeit 3). Hier zeigte sich, dass die Zellen voll funktionstüchtig waren und Aktionspotenziale ausbildeten.

Aufgrund dieser Resultate sind die Kollagenfasern für den Einsatz als Orientierungsstruktur in Nervenleitschienen prädestiniert. Daher wurden die Kollagenfasern in eine ebenso biokompatible und differenzierungsfördernde Röhre aus einem Vliesstoff aus dem rekombinanten Spinnenseidenprotein eADF4(C16)RGD gefüllt (Abbildung 15C, Figure 5 in Teilarbeit 3). Die dadurch hervorgehende Nervenleitschiene wurde anschließend mit NG108-15 Zellen besiedelt.

Hierbei wurde festgestellt, dass die NG108-15 Zellen auf den Kollagenfasern auch im Inneren der Vliesstoffröhre Neurite ausbildeten (Figure 6 in Teilarbeit 3).

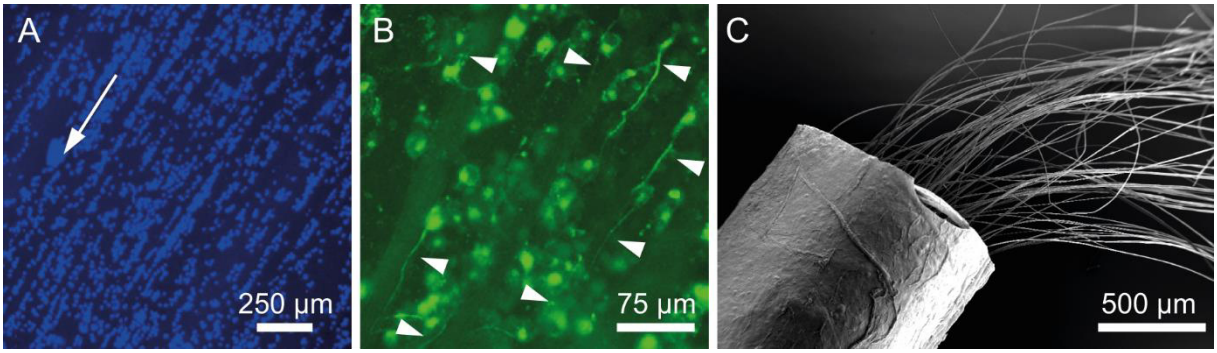

Abbildung 15. Kollagenfasern in neuronalen Zellkulturexperimenten. (A) 4′,6-Diamidin-2-phenylindol (DAPI)-gefärbte Zellkerne (blau) veranschaulichen die Adhäsion von NG108-15 Zellen auf Kollagenfasern. Der Pfeil verdeutlicht die Ausrichtung der Kollagenfasern. (B) Expression von *ß*-Tubulin III (grün) in NG108-15 Zellen auf Kollagenfasern. Die Pfeile markieren faserlängsachsig-orientierte Neurite. (C) Rasterelektronen-mikroskopische (REM) Aufnahme einer Nervenleitschiene bestehend aus einem zu einer Röhre gerollten Vliesstoff aus dem rekombinanten Spinnenseidenprotein eADF4(C16)RGD und Kollagenfasern als Füllmaterial. Adapted with permission from Haynl *et al.*[285] (DOI: 10.1021/acs.nanolett.6b02828). Copyright (2016) American Chemical Society. Adapted with permission from Pawar *et al.*[286] (DOI: 10.1021/acsabm.9b00628). Copyright (2019) American Chemical Society.

Die erzielten Ergebnisse lassen schlussfolgern, dass die hier hergestellten Kollagenfasern ein vielversprechendes Material für die periphere Nervenreparatur darstellen.

Als Alternative zu bereits vorgefertigten Vliesstoffröhren aus rekombinanter Spinnenseide wurden auch Röhren aus einem selbstrollenden Film in Teilarbeit 4 getestet. Die Fähigkeit von Chitosanfilmen zur Selbstrollung, welche durch Kontakt mit dem Zellmedium induziert wird, ermöglicht einen schonenden und homogen-verteilten Einschluss der sich ursprünglich im Zellmedium-befindlichen Nervenzellen (hier: PC-12 Zellen). Durch Modifikation der Röhreninnenwand mit a) einer Beschichtung aus dem bioaktiven eADF4(C16)RGD, b) mit einem anisotropen Vliesstoff aus eADF4(C16) sowie mit dem Einschluss c) eines anisotropen Kollagen-Kryogels als Füllmaterial (Figure 1 und 2 in Teilarbeit 4) konnten die Nervenzellen im Inneren der modifizierten Röhren differenzieren und die Strukturierung ermöglichte eine Ausrichtung der Neurite entlang der anisotropen Strukturen des Vliesstoffs bzw. des Kryogels (Figure 3 in Teilarbeit 4).

3.2 Analyse natürlicher Biopolymerfasern: Spinnenseide von *S. formivorus*

In Teilarbeit 5 wurde das morphologisch-einzigartige Spinnenseidennetz von *S. formivorus* untersucht. Dieses bestand aus einem Geflecht aus vernetzten Seidensträngen variablen Durchmessers (Abbildung 16A, Figure 1a in Teilarbeit 5). Bei genauerer Betrachtung mit dem Rasterelektronenmikroskop (REM) wurden im Netz zwei Fasertypen identifiziert, welche sich maßgeblich in ihren Durchmessern unterschieden und in Mikrofasern und Submikrofasern eingeteilt werden konnten (Figure 1d und f in Teilarbeit 5). Herausstehende Seidenstränge des Netzkörpers (Abbildung 16A Kästchen und 16B, Figure 1a und g in Teilarbeit 5) ermöglichen die Fixierung des Netzes mit den Umgebungsstrukturen und offenbaren, ebenso wie auch die Seidenstränge des Netzkörpers, eine zweiphasige Querschnittsstruktur (Abbildung 16C, Figure 1h in Teilarbeit 5). Diese besteht aus den longitudinal-ausgerichteten Mikrofasern, welche in einer Matrix aus den ebenfalls longitudinal-ausgerichteten Submikrofasern eingebettet sind (im Folgenden: Verbundfaser). Die Mikrofasern zeigten Durchmesser von 2-4 µm, wohingegen die Submikrofasern im Durchmesser ca. 400 nm betrugen.

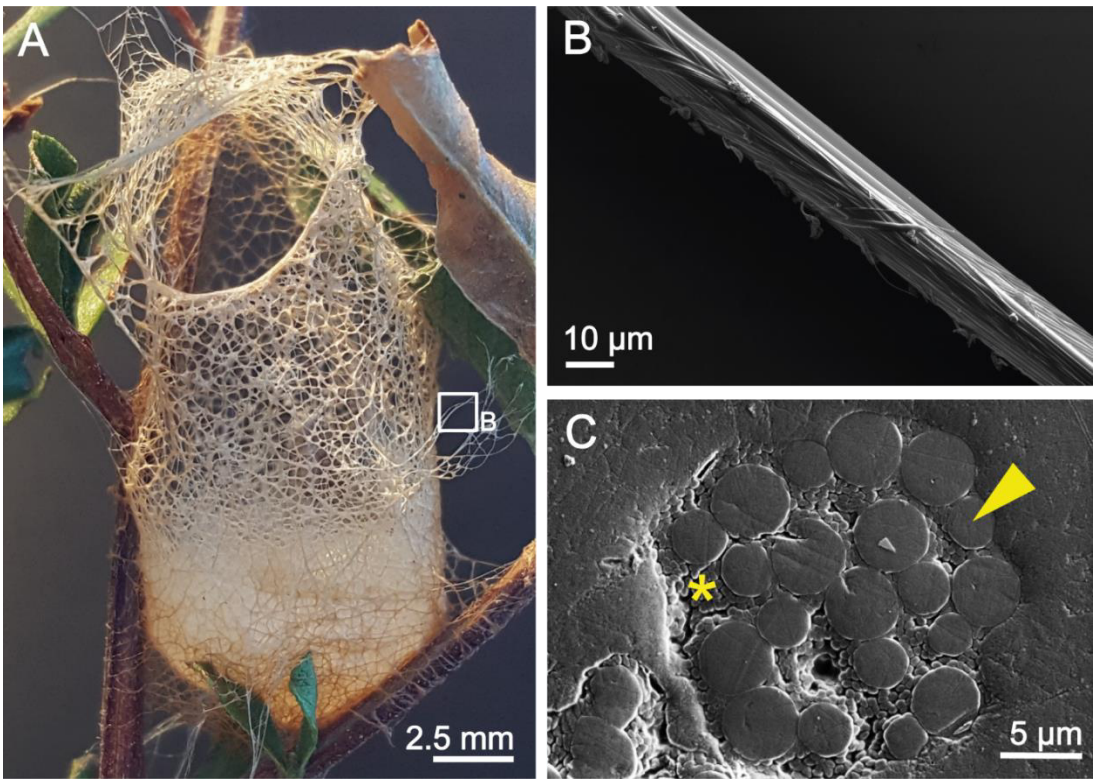

Abbildung 16. Morphologie eines Spinnenseidennetzes von *S. formivorus*. (A) Fotographische Darstellung eines Netzes von *S. formivorus*. (B) Rasterelektronenmikroskopische (REM)-Aufnahme eines herausstehenden Seidenstrangs basierend auf der Kennzeichnung in A. (C) Die REM-Aufnahme eines Seidenstrangquerschnitts zeigt einen zweiphasigen Aufbau aus einzelnen Mikrofasern, die in einer Matrix aus Submikrofasern eingebettet sind (Pfeil markiert eine Mikrofaser, Sternchen weist auf die Ansammlung von Submikrofasern hin). Adapted from Haynl *et al.*[307] (DOI: 10.1038/s41598-020-74469-z) with permission of Springer Nature.

Der Querschnitt der Verbundfaser (Abbildung 17A, Figure 2a in Teilarbeit 5) wurde mittels Infrarotmikrospektroskopie an der *IRM Beamline* des *Australian Synchrotron* untersucht. Vom Verbundfaserquerschnitt wurden positionsabhängig Spektren aufgenommen, die durch spezifische Bandenintegration und anschließende Abbildung der integrierten Flächen als Falschfarbendarstellung die ortsaufgelöste Verteilung chemischer Gruppen und deren Intensitäten wiedergab. Die Visualisierung der Fläche unterhalb der Amid I-Bande (1720-1590 cm^{-1}) (Abbildung 17B, Figure 2b in Teilarbeit 5), d.h. in Spinnenseide die Absorption der Proteine, vorrangig Spidroine, zeigte eine gute Übereinstimmung mit dem Verbundfaserquerschnitt, so dass einzelne Mikrofaserquerschnitte deutlich ersichtlich waren. Besonders auffällig war, dass in Bereichen mit hoher Submikrofaserdichte eine im Vergleich zu den Mikrofaserquerschnitten stärkere Absorption der C-OH und C-O-C Gruppen im Bereich 1200-990 cm^{-1} beobachtet wurde und eine erhöhte Konzentration an Saccharide[298-300] und/oder der Aminosäuren Serin, Tyrosin und/oder Threonin vermuten lässt (Abbildung 17C, Figure 2c in Teilarbeit 5).

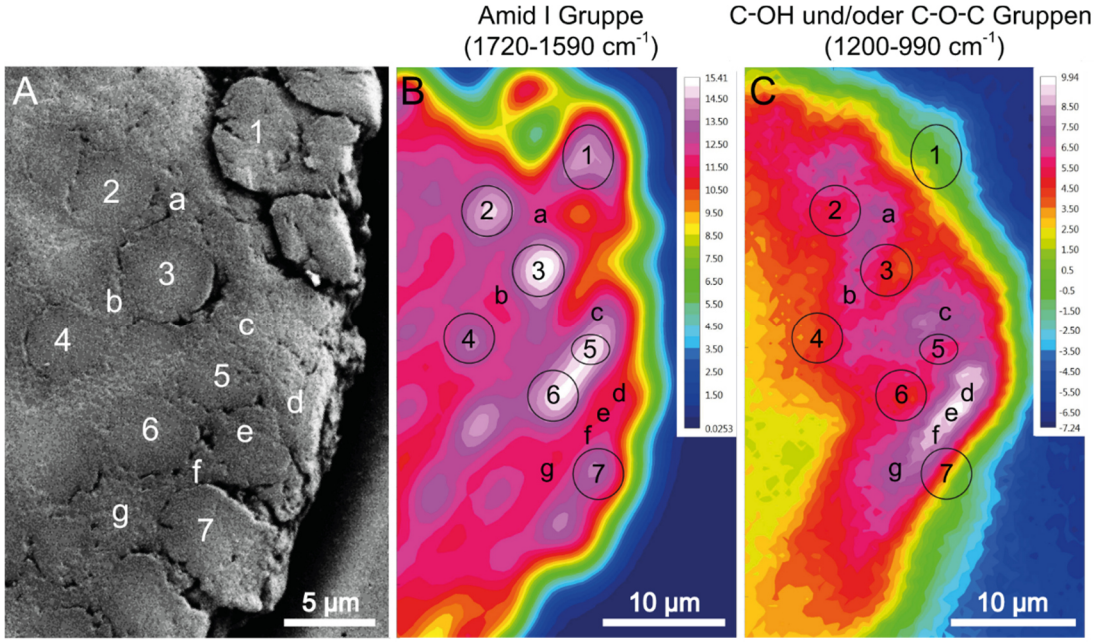

Abbildung 17. Analyse des Querschnitts der Spinnenseide von *S. formivorus* mittels synchrotroner Infrarotmikrospektroskopie. (A) Die rasterelektronenmikroskopische Aufnahme (REM) des Verbundfaserquerschnitts zeigt dessen Aufbau aus einzelnen Mikrofasern (1-7), die in einer Matrix aus Submikrofasern eingebettet sind (a-g). (B) Der 2D-Plot basierend auf den integrierten Flächen unter der Amid I-Bande (1720-1590 cm^{-1}) repräsentiert die Proteinverteilung in der Verbundfaser, wohingegen (C) die Darstellung der Flächen unter den Banden im Bereich 1200-990 cm^{-1} die Verteilung von C–OH und C–O–C Gruppen anzeigt. Die Absorptionsbereiche 1-7 stimmen mit der Anordnung der Mikrofasern in A überein. Die Absorptionsbereiche a-g in den 2D-Plots können der Submikrofasermatrix zugeordnet werden. Absorptionsintensitäten korrelieren mit den Farbskalen, wobei blau die geringste und weiß die stärkste Intensität anzeigt. Blaue Bereiche außerhalb der Verbundfaser repräsentieren das Einbettmedium. Adapted from Haynl *et al.*[307] (DOI: 10.1038/s41598-020-74469-z) with permission of Springer Nature.

Neben der morphologischen Einzigartigkeit weisen die Netze eine außergewöhnliche Formstabilität auf. In Zugprüfungen der herausstehenden Verbundfasern, entnommen aus zwei individuellen Netzen, wurden Werte für die Bruchdehnung, Zugfestigkeit, E-Modul und Zähigkeit entsprechend Tabelle 5 (Figure 3 und Tabelle 1 in Teilarbeit 5) ermittelt.

Tabelle 5. Mechanische Eigenschaften der herausstehenden Verbundfasern zweier individueller Netze (#1 und #2) von *S. formivorus* (± Standardabweichung). Die Werte dieser Tabelle entstammen wahren Spannungs-Dehnungs-Kurven.

Seidennetz	Bruchdehnung [%]	Zugfestigkeit [MPa]	E-Modul [GPa]	Zähigkeit [MJ m^{-3}]
#1	17 ± 4	314 ± 75	6,2 ± 1.2	38 ± 12
#2	15 ± 6	271 ± 95	4,3 ± 1.6	27 ± 15

Die Zugfestigkeit und das E-Modul der Seidenstränge waren signifikant geringer als bei *Major Ampullate*[34, 124, 126, 301] und *Minor Ampullate* Seide[34, 124, 302] von Radnetzspinnen. Auch zeigten die Verbundfasern nicht die stark-ausgeprägte Elastizität von *Flagelliform* Seide.[34, 124, 303] Allerdings ergab sich, dass die Verbundfasern in Abhängigkeit ihres Durchmessers laterale Belastungen gut aufnehmen konnten. Die maximalen Belastungskräfte lagen für repräsentative Verbundfasern eines Netzes zwischen 19 und 625 mN und übertrafen damit die Werte der *Major Ampullate* Seide der Modell-Radnetzspinne *Nephila edulis* (25 - 107 mN) (Figure 3 in Teilarbeit 5).

Die in dieser Studie identifizierten strukturellen, molekularen und mechanischen Eigenschaften der Seide von *S. formivorus* könnten eine Basis für zukünfige Entwicklungen auf dem Gebiet von Fasermaterialien darstellen, welche sich durch eine verbesserte Stabilität gegenüber lateraler Belastung auszeichnen sollen.
Auch aus biologischer Sicht ist das Netz von *S. formivorus* äußerst interessant, da es nicht nur zum Beutefang dient, sondern auch gleichzeitig als Eierkokon eingesetzt wird (Figure 1i in Teilarbeit 5). Die zwei identifizierten Spinnenseidentypen ähneln in ihren Faserdurchmessern tatsächlich der dickeren *Tubuliform* und dünneren *Aciniform* Seide der Eierkokons anderer Spinnenarten, wie z.B. von *Argiope bruennichi* (7-8 µm und 600 nm),[304] von *Latrodectus hesperus* (4-5 µm und 500 nm)[305] und von *Argiope aurantia* (5-10 µm und 100-200 nm).[306] Auch der Verlauf der Spannungs-Dehnungs-Kurven der *S. formivorus* Verbundfasern (Figure 3e in Teilarbeit 5) besitzt ähnliche Merkmale wie der von *Tubuliform* und *Aciniform* Seide von

Radnetzspinnen.[34, 124] Daher wird vermutet, dass die Körbchennetze aus *Tubuliform* und *Aciniform* Seide bestehen und ursprünglich als reine Eierkokons fungierten, welche im Lauf der Evolution zum Beutefang ausgebaut wurden.

4 LITERATURVERZEICHNIS

1. Neinhuis, C.; Barthlott, W., Characterization and distribution of water-repellent, self-cleaning plant surfaces. *Annals of Botany* **1997,** *79* (6), 667-677.
2. Ayyachamy, M.; Cliffe, F. E.; Coyne, J. M.; Collier, J.; Tuohy, M. G., Lignin: untapped biopolymers in biomass conversion technologies. *Biomass Conversion and Biorefinery* **2013,** *3* (3), 255-269.
3. Pattanashetti, N. A.; Heggannavar, G. B.; Kariduraganavar, M. Y., Smart biopolymers and their biomedical applications. *Procedia Manufacturing* **2017,** *12*, 263-279.
4. Steinbüchel, A., Perspectives for biotechnological production and utilization of biopolymers: metabolic engineering of polyhydroxyalkanoate biosynthesis pathways as a successful example. *Macromolecular Bioscience* **2001,** *1* (1), 1-24.
5. Cristescu, R.; Doraiswamy, A.; Socol, G.; Grigorescu, S.; Axente, E.; Mihaiescu, D.; Moldovan, A.; Narayan, R. J.; Stamatin, I.; Mihailescu, I. N.; Chisholm, B. J.; Chrisey, D. B., Polycaprolactone biopolymer thin films obtained by matrix assisted pulsed laser evaporation. *Applied Surface Science* **2007,** *253* (15), 6476-6479.
6. Ahmed, J.; Varshney, S. K., Polylactides - chemistry, properties and green packaging technology: a review. *International Journal of Food Properties* **2011,** *14* (1), 37-58.
7. Dash, M.; Chiellini, F.; Ottenbrite, R. M.; Chiellini, E., Chitosan - a versatile semi-synthetic polymer in biomedical applications. *Progress in Polymer Science* **2011,** *36* (8), 981-1014.
8. Hay, I. D.; Ur Rehman, Z.; Moradali, M. F.; Wang, Y.; Rehm, B. H., Microbial alginate production, modification and its applications. *Microbial Biotechnology* **2013,** *6* (6), 637-650.
9. Belmont, P.; Constant, J. F.; Demeunynck, M., Nucleic acid conformation diversity: from structure to function and regulation. *Chemical Society Reviews* **2001,** *30* (1), 70-81.
10. Lee, H. S.; Qi, Y.; Im, W., Effects of N-glycosylation on protein conformation and dynamics: protein data bank analysis and molecular dynamics simulation study. *Scientific Reports* **2015,** *5*, 8926-8926.
11. Fournet, M.; Bonté, F.; Desmoulière, A., Glycation damage: a possible hub for major pathophysiological disorders and aging. *Aging and Disease* **2018,** *9* (5), 880-900.
12. Lee, M. J.; Yaffe, M. B., Protein regulation in signal transduction. *Cold Spring Harbor Perspectives in Biology* **2016,** *8* (6), a005918.
13. Nicholson, L., The immune system. *Essays in Biochemistry* **2016,** *60* (3), 275-301.
14. Knutson, M. D., Iron transport proteins: gateways of cellular and systemic iron homeostasis. *Journal of Biological Chemistry* **2017,** *292* (31), 12735-12743.
15. Lammel, A.; Keerl, D.; Römer, L.; Scheibel, T., Proteins: polymers of natural origin. *In: Hu, J. (Ed.): Recent Advances in Biomaterials Research. - Trivandrum: Transworld Research Network* **2008**, 1.
16. Wang, L.; Gong, C.; Yuan, X.; Wei, G., Controlling the self-assembly of biomolecules into functional nanomaterials through internal interactions and external stimulations: a review. *Nanomaterials* **2019,** *9* (2), 285.
17. Dominguez, R.; Holmes, K. C., Actin structure and function. *Annual Review of Biophysics* **2011,** *40* (1), 169-186.
18. Daamen, W. F.; van Moerkerk, H. T. B.; Hafmans, T.; Buttafoco, L.; Poot, A. A.; Veerkamp, J. H.; van Kuppevelt, T. H., Preparation and evaluation of molecularly-defined collagen-elastin-glycosaminoglycan scaffolds for tissue engineering. *Biomaterials* **2003,** *24* (22), 4001-4009.

19. Vollrath, F.; Holtet, T.; Thogersen, H. C.; Frische, S., Structural organization of spider silk. *Proceedings of the Royal Society B-Biological Sciences* **1996,** *263* (1367), 147-151.
20. Rockwood, D. N.; Preda, R. C.; Yucel, T.; Wang, X. Q.; Lovett, M. L.; Kaplan, D. L., Materials fabrication from Bombyx mori silk fibroin. *Nature Protocols* **2011,** *6* (10), 1612-1631.
21. Ruzicka, Z., Protective role of the egg stalk in Chrysopidae (Neuroptera). *European Journal of Entomology* **1997,** *94* (1), 111-114.
22. Moll, R.; Divo, M.; Langbein, L., The human keratins: biology and pathology. *Histochemistry and Cell Biology* **2008,** *129* (6), 705-733.
23. Hagenau, A.; Papadopoulos, P.; Kremer, F.; Scheibel, T., Mussel collagen molecules with silk-like domains as load-bearing elements in distal byssal threads. *Journal of Structural Biology* **2011,** *175* (3), 339-347.
24. Robinson, K. A.; Sun, M.; Barnum, C. E.; Weiss, S. N.; Huegel, J.; Shetye, S. S.; Lin, L. D.; Saez, D.; Adams, S. M.; Iozzo, R. V.; Soslowsky, L. J.; Birk, D. E., Decorin and biglycan are necessary for maintaining collagen fibril structure, fiber realignment, and mechanical properties of mature tendons. *Matrix Biology* **2017,** *64*, 81-93.
25. Pins, G. D.; Christiansen, D. L.; Patel, R.; Silver, F. H., Self-assembly of collagen fibers. Influence of fibrillar alignment and decorin on mechanical properties. *Biophysical Journal* **1997,** *73* (4), 2164-2172.
26. Suhre, M. H.; Gertz, M.; Steegborn, C.; Scheibel, T., Structural and functional features of a collagen-binding matrix protein from the mussel byssus. *Nature Communications* **2014,** *5*, 3392.
27. Sponner, A.; Vater, W.; Monajembashi, S.; Unger, E.; Grosse, F.; Weisshart, K., Composition and hierarchical organisation of a spider silk. *Plos One* **2007,** *2* (10), e998.
28. Römer, L.; Scheibel, T., The elaborate structure of spider silk: structure and function of a natural high performance fiber. *Prion* **2008,** *2* (4), 154-161.
29. Bauer, F.; Bertinetti, L.; Masic, A.; Scheibel, T., Dependence of mechanical properties of lacewing egg stalks on relative humidity. *Biomacromolecules* **2012,** *13* (11), 3730-3735.
30. Waite, J. H.; Lichtenegger, H. C.; Stucky, G. D.; Hansma, P., Exploring molecular and mechanical gradients in structural bioscaffolds. *Biochemistry* **2004,** *43* (24), 7653-7662.
31. Gosline, J.; Lillie, M.; Carrington, E.; Guerette, P.; Ortlepp, C.; Savage, K., Elastic proteins: biological roles and mechanical properties. *Philosophical transactions of the Royal Society of London. Series B, Biological sciences* **2002,** *357* (1418), 121-132.
32. Hepworth, D. G.; Smith, J. P., The mechanical properties of composites manufactured from tendon fibres and pearl glue (animal glue). *Composites Part a-Applied Science and Manufacturing* **2002,** *33* (6), 797-803.
33. Aaron, B. B.; Gosline, J. M., Elastin as a random-network elastomer: a mechanical and optical analysis of single elastin fibers. *Biopolymers* **1981,** *20* (6), 1247-1260.
34. Blackledge, T. A.; Hayashi, C. Y., Silken toolkits: biomechanics of silk fibers spun by the orb web spider Argiope argentata (Fabricius 1775). *Journal of Experimental Biology* **2006,** *209* (13), 2452-2461.
35. Plaza, G. R.; Corsini, P.; Perez-Rigueiro, J.; Marsano, E.; Guinea, G. V.; Elices, M., Effect of water on Bombyx mori regenerated silk fibers and its application in modifying their mechanical properties. *Journal of Applied Polymer Science* **2008,** *109* (3), 1793-1801.
36. Hagenau, A.; Suhre, M. H.; Scheibel, T. R., Nature as a blueprint for polymer material concepts: protein fiber-reinforced composites as holdfasts of mussels. *Progress in Polymer Science* **2014,** *39* (8), 1564-1583.

37. Popescu, C.; Wortmann, F.-J., Wool – Structure, mechanical properties and technical products based on animal fibres. *In: Stevens, C. V.; Müssig, J.(Ed.): Industrial Applications of Natural Fibres - John Wiley & Sons Ltd.* **2010**.
38. Griffith, L. G., Polymeric biomaterials. *Acta Materialia* **2000,** *48* (1), 263-277.
39. Wang, H.-J.; Di, L.; Ren, Q.-S.; Wang, J.-Y., Applications and degradation of proteins used as tissue engineering materials *Materials* **2009,** *2* (2), 613-635.
40. Jokinen, J.; Dadu, E.; Nykvist, P.; Kapyla, J.; White, D. J.; Ivaska, J.; Vehvilainen, P.; Reunanen, H.; Larjava, H.; Hakkinen, L.; Heino, J., Integrin-mediated cell adhesion to type I collagen fibrils. *The Journal of Biological Chemistry* **2004,** *279* (30), 31956-31963.
41. Groult, V.; Hornebeck, W.; Ferrari, P.; Tixier, J. M.; Robert, L.; Jacob, M. P., Mechanisms of interaction between human skin fibroblasts and elastin: differences between elastin fibres and derived peptides. *Cell Biochemistry and Function* **1991,** *9* (3), 171-182.
42. Pei, B. Q.; Wang, W.; Fan, Y.; Wang, X. M.; Watari, F.; Li, X. M., Fiber-reinforced scaffolds in soft tissue engineering. *Regenerative Biomaterials* **2017,** *4* (4), 257-268.
43. Zhu, X.; Cui, W.; Li, X.; Jin, Y., Electrospun fibrous mats with high porosity as potential scaffolds for skin tissue engineering. *Biomacromolecules* **2008,** *9* (7), 1795-1801.
44. Chew, S. Y.; Mi, R.; Hoke, A.; Leong, K. W., The effect of the alignment of electrospun fibrous scaffolds on Schwann cell maturation. *Biomaterials* **2008,** *29* (6), 653-661.
45. Yin, Z.; Chen, X.; Chen, J. L.; Shen, W. L.; Hieu Nguyen, T. M.; Gao, L.; Ouyang, H. W., The regulation of tendon stem cell differentiation by the alignment of nanofibers. *Biomaterials* **2010,** *31* (8), 2163-2175.
46. Sorushanova, A.; Delgado, L. M.; Wu, Z. N.; Shologu, N.; Kshirsagar, A.; Raghunath, R.; Mullen, A. M.; Bayon, Y.; Pandit, A.; Raghunath, M.; Zeugolis, D. I., The collagen suprafamily: from biosynthesis to advanced biomaterial development. *Advanced Materials* **2019,** *31* (1), 1801651.
47. Silvipriya, K. S.; Krishna Kumar, K.; Dinesh Kumar, B.; John, A.; Lakshmanan, P., Fish processing waste: a promising source of type-I collagen. *Current Trends in Biotechnology and Pharmacy* **2016,** *10* (4), 374-383.
48. Frantz, C.; Stewart, K. M.; Weaver, V. M., The extracellular matrix at a glance. *Journal of Cell Science* **2010,** *123* (24), 4195-4200.
49. Kadler, K. E.; Baldock, C.; Bella, J.; Boot-Handford, R. P., Collagens at a glance. *Journal of Cell Science* **2007,** *120* (12), 1955-1958.
50. Lin, K. L.; Zhang, D. W.; Macedo, M. H.; Cui, W. G.; Sarmento, B.; Shen, G. F., Advanced collagen-based biomaterials for regenerative biomedicine. *Advanced Functional Materials* **2019,** *29* (3), 1804943.
51. Gelse, K.; Poschl, E.; Aigner, T., Collagens - structure, function, and biosynthesis. *Advanced Drug Delivery Reviews* **2003,** *55* (12), 1531-1546.
52. Liu, S. H.; Yang, R. S.; al-Shaikh, R.; Lane, J. M., Collagen in tendon, ligament, and bone healing. A current review. *Clinical Orthopaedics and Related Research* **1995,** (318), 265-278.
53. Williams, I. F.; Heaton, A.; McCullagh, K. G., Cell morphology and collagen types in equine tendon scar. *Research in Veterinary Science* **1980,** *28* (3), 302-310.
54. Silver, F. H.; Freeman, J. W.; DeVore, D., Viscoelastic properties of human skin and processed dermis. *Skin Research & Technology* **2001,** *7* (1), 18-23.
55. Provenzano, P. P.; Vanderby, R., Jr., Collagen fibril morphology and organization: implications for force transmission in ligament and tendon. *Matrix Biology* **2006,** *25* (2), 71-84.

56. Kern, P.; Menasche, M.; Robert, L., Relative rates of biosynthesis of collagen type I, type V and type VI in calf cornea. *The Biochemical journal* **1991,** *274 (Pt 2)*, 615-617.
57. Nerlich, A. G.; Boos, N.; Wiest, I.; Aebi, M., Immunolocalization of major interstitial collagen types in human lumbar intervertebral discs of various ages. *Virchows Archiv* **1998,** *432* (1), 67-76.
58. Niyibizi, C.; Eyre, D. R., Structural characteristics of cross-linking sites in type V collagen of bone. Chain specificities and heterotypic links to type I collagen. *European Journal of Biochemistry* **1994,** *224* (3), 943-950.
59. Shoulders, M. D.; Raines, R. T., Collagen structure and stability. *Annual Review of Biochemistry* **2009,** *78*, 929-958.
60. Brodsky, B.; Ramshaw, J. A., The collagen triple-helix structure. *Matrix Biology* **1997,** *15* (8-9), 545-554.
61. Fallas, J. A.; O'Leary, L. E.; Hartgerink, J. D., Synthetic collagen mimics: self-assembly of homotrimers, heterotrimers and higher order structures. *Chemical Society reviews* **2010,** *39* (9), 3510-3527.
62. Chan, V. C.; Ramshaw, J. A.; Kirkpatrick, A.; Beck, K.; Brodsky, B., Positional preferences of ionizable residues in Gly-X-Y triplets of the collagen triple-helix. *The Journal of Biological Chemistry* **1997,** *272* (50), 31441-31446.
63. Banos, C. C.; Thomas, A. H.; Kuo, C. K., Collagen fibrillogenesis in tendon development: current models and regulation of fibril assembly. *Birth defects research. Part C, Embryo Today: Reviews* **2008,** *84* (3), 228-244.
64. Freudenberg, U.; Behrens, S. H.; Welzel, P. B.; Muller, M.; Grimmer, M.; Salchert, K.; Taeger, T.; Schmidt, K.; Pompe, W.; Werner, C., Electrostatic interactions modulate the conformation of collagen I. *Biophysical Journal* **2007,** *92* (6), 2108-2119.
65. Hulmes, D. J. S., Vertebrate collagens - Structures, functions and biomedical applications. *In: Scheibel, T.: Fibrous Proteins.-Landes Bioscience: Austin, Tex.* **2008**, 12-29.
66. Patino, M. G.; Neiders, M. E.; Andreana, S.; Noble, B.; Cohen, R. E., Collagen: an overview. *Implant Dentistry* **2002,** *11* (3), 280-285.
67. Hulmes, D. J., Building collagen molecules, fibrils, and suprafibrillar structures. *Journal of Structural Biology* **2002,** *137* (1-2), 2-10.
68. Ottani, V.; Martini, D.; Franchi, M.; Ruggeri, A.; Raspanti, M., Hierarchical structures in fibrillar collagens. *Micron* **2002,** *33* (7-8), 587-596.
69. Ghazanfari, S.; Khademhosseini, A.; Smit, T. H., Mechanisms of lamellar collagen formation in connective tissues. *Biomaterials* **2016,** *97*, 74-84.
70. Orgel, J. P.; Miller, A.; Irving, T. C.; Fischetti, R. F.; Hammersley, A. P.; Wess, T. J., The in situ supermolecular structure of type I collagen. *Structure* **2001,** *9* (11), 1061-1069.
71. Paige, M. F.; Rainey, J. K.; Goh, M. C., A study of fibrous long spacing collagen ultrastructure and assembly by atomic force microscopy. *Micron* **2001,** *32* (3), 341-353.
72. Mäki, J. M., Lysyl oxidases in mammalian development and certain pathological conditions. *Histology and histopathology* **2009,** *24* (5), 651-660.
73. Ricard-Blum, S., The collagen family. *Cold Spring Harbor Perspectives in Biology* **2011,** *3* (1), a004978.
74. Orban, J. M.; Wilson, L. B.; Kofroth, J. A.; El-Kurdi, M. S.; Maul, T. M.; Vorp, D. A., Crosslinking of collagen gels by transglutaminase. *Journal of Biomedical Materials Research. Part A* **2004,** *68* (4), 756-762.
75. Paul, R. G.; Bailey, A. J., Glycation of collagen: the basis of its central role in the late complications of ageing and diabetes. *The International Journal of Biochemistry & Cell Biology* **1996,** *28* (12), 1297-1310.

76. Kadler, K. E., Fell Muir Lecture: collagen fibril formation in vitro and in vivo. *International Journal of Experimental Pathology* **2017,** *98* (1), 4-16.
77. Kadler, K. E.; Holmes, D. F.; Trotter, J. A.; Chapman, J. A., Collagen fibril formation. *The Biochemical Journal* **1996,** *316 (Pt 1)*, 1-11.
78. Na, G. C.; Butz, L. J.; Carroll, R. J., Mechanism of in vitro collagen fibril assembly. Kinetic and morphological studies. *The Journal of Biological Chemistry* **1986,** *261* (26), 12290-12299.
79. Williams, B. R.; Gelman, R. A.; Poppke, D. C.; Piez, K. A., Collagen fibril formation. Optimal in vitro conditions and preliminary kinetic results. *The Journal of Biological Chemistry* **1978,** *253* (18), 6578-6585.
80. Lee, P.; Lin, R.; Moon, J.; Lee, L. P., Microfluidic alignment of collagen fibers for in vitro cell culture. *Biomedical Microdevices* **2006,** *8* (1), 35-41.
81. Wallace, D. G.; Thompson, A., Description of collagen fibril formation by a theory of polymer crystallization. *Biopolymers* **1983,** *22* (7), 1793-1811.
82. Jiang, F.; Hörber, H.; Howard, J.; Müller, D. J., Assembly of collagen into microribbons: effects of pH and electrolytes. *Journal of Structural Biology* **2004,** *148* (3), 268–278.
83. Harris, J. R.; Soliakov, A.; Lewis, R. J., In vitro fibrillogenesis of collagen type I in varying ionic and pH conditions. *Micron* **2013,** *49*, 60-68.
84. Li, Y.; Asadi, A.; Monroe, M. R.; Douglas, E. P., pH effects on collagen fibrillogenesis in vitro: electrostatic interactions and phosphate binding. *Materials Science and Engineering: C* **2009,** *29* (5), 1643-1649.
85. Nemoto, T.; Horiuchi, M.; Ishiguro, N.; Shinagawa, M., Detection methods of possible prion contaminants in collagen and gelatin. *Archives of Virology* **1999,** *144* (1), 177-184.
86. Golser, A. V.; Röker, M.; Börner, H. G.; Scheibel, T., Engineered collagen: a redox switchable framework for tunable assembly and fabrication of biocompatible surfaces. *ACS Biomaterials Science & Engineering* **2018,** *4* (6), 2106-2114.
87. Peng, Y. Y.; Yoshizumi, A.; Danon, S. J.; Glattauer, V.; Prokopenko, O.; Mirochnitchenko, O.; Yu, Z.; Inouye, M.; Werkmeister, J. A.; Brodsky, B.; Ramshaw, J. A., A Streptococcus pyogenes derived collagen-like protein as a non-cytotoxic and non-immunogenic cross-linkable biomaterial. *Biomaterials* **2010,** *31* (10), 2755-2761.
88. Vaughan, P. R.; Galanis, M.; Richards, K. M.; Tebb, T. A.; Ramshaw, J. A. M.; Werkmeister, J. A., Production of recombinant hydroxylated human type III collagen fragment in Saccharomyces cerevisiae. *DNA and Cell Biology* **1998,** *17* (6), 511-518.
89. Fichard, A.; Tillet, E.; Delacoux, F.; Garrone, R.; Ruggiero, F., Human recombinant α1(V) collagen chain: homotrimeric assembly and subsequent processing. *Journal of Biological Chemistry* **1997,** *272* (48), 30083-30087.
90. Stein, H.; Wilensky, M.; Tsafrir, Y.; Rosenthal, M.; Amir, R.; Avraham, T.; Ofir, K.; Dgany, O.; Yayon, A.; Shoseyov, O., Production of bioactive, post-translationally modified, heterotrimeric, human recombinant type-I collagen in transgenic tobacco. *Biomacromolecules* **2009,** *10* (9), 2640-2645.
91. Lewis, R., Unraveling the Weave of Spider Silk. *BioScience* **1996,** *46* (9), 636-638.
92. Eisoldt, L.; Thamm, C.; Scheibel, T., Review the role of terminal domains during storage and assembly of spider silk proteins. *Biopolymers* **2012,** *97* (6), 355-361.
93. Hijirida, D. H.; Do, K. G.; Michal, C.; Wong, S.; Zax, D.; Jelinski, L. W., 13C NMR of Nephila clavipes major ampullate silk gland. *Biophysical Journal* **1996,** *71* (6), 3442-3447.

94. Gronau, G.; Qin, Z.; Buehler, M. J., Effect of sodium chloride on the structure and stability of spider silk's N-terminal protein domain. *Biomaterials Science* **2013,** *1* (3), 276-284.
95. Heim, M.; Keerl, D.; Scheibel, T., Spider silk: from soluble protein to extraordinary fiber. *Angewandte Chemie* **2009,** *48* (20), 3584-3596.
96. Andersson, M.; Chen, G.; Otikovs, M.; Landreh, M.; Nordling, K.; Kronqvist, N.; Westermark, P.; Jornvall, H.; Knight, S.; Ridderstrale, Y.; Holm, L.; Meng, Q.; Jaudzems, K.; Chesler, M.; Johansson, J.; Rising, A., Carbonic anhydrase generates CO2 and H+ that drive spider silk formation via opposite effects on the terminal domains. *PLOS Biology* **2014,** *12* (8), e1001921.
97. Bauer, J.; Schaal, D.; Eisoldt, L.; Schweimer, K.; Schwarzinger, S.; Scheibel, T., Acidic residues control the dimerization of the N-terminal domain of black widow spiders' major ampullate spidroin 1. *Scientific Reports* **2016,** *6*, 34442.
98. Bauer, J.; Scheibel, T., Dimerization of the conserved N-terminal domain of a spider silk protein controls the self-assembly of the repetitive core domain. *Biomacromolecules* **2017,** *18* (8), 2521-2528.
99. Bauer, J.; Scheibel, T., Conformational stability and interplay of helical N- and C-terminal domains with implications on major ampullate spidroin assembly. *Biomacromolecules* **2017,** *18* (3), 835-845.
100. Knight, D. P.; Vollrath, F., Changes in element composition along the spinning duct in a Nephila spider. *Naturwissenschaften* **2001,** *88* (4), 179-182.
101. Chen, X.; Knight, D. P.; Vollrath, F., Rheological characterization of Nephila spidroin solution. *Biomacromolecules* **2002,** *3* (4), 644-648.
102. Knight, D. P.; Vollrath, F., Liquid crystals and flow elongation in a spider's silk production line. *Proceedings of the Royal Society B: Biological Sciences* **1999,** *266*, 519-523.
103. Doblhofer, E.; Heidebrecht, A.; Scheibel, T., To spin or not to spin: spider silk fibers and more. *Applied Microbiology and Biotechnology* **2015,** *99* (22), 9361-9380.
104. World Spider Catalog (2018). World Spider Catalog. Version 19.5. Natural History Museum Bern, online at http://wsc.nmbe.ch, accessed on 09.25.2018 doi: 10.24436/2. **2018**.
105. Babb, P. L.; Lahens, N. F.; Correa-Garhwal, S. M.; Nicholson, D. N.; Kim, E. J.; Hogenesch, J. B.; Kuntner, M.; Higgins, L.; Hayashi, C. Y.; Agnarsson, I.; Voight, B. F., The Nephila clavipes genome highlights the diversity of spider silk genes and their complex expression. *Nature Genetics* **2017,** *49* (6), 895–903.
106. Roberson, E. J.; Chips, M. J.; Carson, W. P.; Rooney, T. P., Deer herbivory reduces web-building spider abundance by simplifying forest vegetation structure. *Peerj* **2016,** *4*, e2538.
107. Benjamin, S. P.; Zschokke, S., Webs of theridiid spiders: construction, structure and evolution. *Biological Journal of the Linnean Society* **2003,** *78* (3), 293-305.
108. Benjamin, S. P.; Zschokke, S., Homology, behaviour and spider webs: web construction behaviour of *Linyphia hortensis* and *L-triangularis* (Araneae : Linyphiidae) and its evolutionary significance. *Journal of Evolutionary Biology* **2004,** *17* (1), 120-130.
109. Gonzalez, M.; Costa, F. G.; Peretti, A. V., Funnel-web construction and estimated immune costs in Aglaoctenus lagotis (Araneae: Lycosidae). *Journal of Arachnology* **2015,** *43* (2), 158-167.
110. Benjamin, S. P.; Dimitrov, D.; Gillespie, R. G.; Hormiga, G., Family ties: molecular phylogeny of crab spiders (Araneae : Thomisidae). *Cladistics* **2008,** *24* (5), 708-722.
111. Evans, T. A.; Wallis, E. J.; Elgar, M. A., Making a meal of mother. *Nature* **1995,** *376* (6538), 299-299.

112. Dumke, M.; Herberstein, M. E.; Schneider, J. M., Advantages of social foraging in crab spiders: groups capture more and larger prey despite the absence of a web. *Ethology* **2018,** *124* (10), 695-705.
113. Gawryszewski, F. M.; Calero-Torralbo, M. A.; Gillespie, R. G.; Rodriguez-Girones, M. A.; Herberstein, M. E., Correlated evolution between coloration and ambush site in predators with visual prey lures. *Evolution* **2017,** *71* (8), 2010-2021.
114. Vieira, C.; Ramires, E. N.; Vasconcellos-Neto, J.; Poppi, R. J.; Romero, G. Q., Crab spider lures prey in flowerless neighborhoods. *Scientific Reports* **2017,** *7* (1), 9188.
115. Llandres, A. L.; Rodriguez-Girones, M. A., Spider movement, UV reflectance and size, but not spider crypsis, affect the response of honeybees to Australian crab spiders. *Plos One* **2011,** *6* (2), e17136.
116. Rainbow, W. J., Two new thomisids. *Records of the Australian Museum* **1900,** *3* (7), 169–175.
117. Rainbow, W. J., Descriptions of some new araneidae of New South Wales. *Proceedings of the Linnean Society of New South Wales* **1897,** *22*, 514–553.
118. McKeown, K. C., Australian spiders: their lives and habits. *Angus & Robertson, Sydney, Australia* **1952**.
119. Elgar, M. A., Inter-specific associations involving spiders: kleptoparasitism, mimicry and mutualism. *Memoirs of the Queensland Museum* **1993,** *33* (2), 411-430.
120. Cushing, P. E., Spider-ant associations: an updated review of myrmecomorphy, myrmecophily, and myrmecophagy in spiders. *Psyche* **2012,** *2012*, 151989.
121. Vollrath, F.; Selden, P., The role of behavior in the evolution of spiders, silks, and webs. *Annual Review of Ecology Evolution and Systematics* **2007,** *38*, 819-846.
122. Hieber, C. S., Spider cocoons and their suspension systems as barriers to generalist and specialist predators. *Oecologia* **1992,** *91* (4), 530-535.
123. Hieber, C. S., The “insulation” layer in the cocoons of Argiope aurantia (Araneae: Araneidae). *Journal of Thermal Biology* **1985,** *10* (3), 171-175.
124. Vollrath, F.; Porter, D., Spider silk as archetypal protein elastomer. *Soft Matter* **2006,** *2* (5), 377-385.
125. Eisoldt, L.; Smith, A.; Scheibel, T., Decoding the secrets of spider silk. *Materials Today* **2011,** *14* (3), 80-86.
126. Madsen, B.; Shao, Z. Z.; Vollrath, F., Variability in the mechanical properties of spider silks on three levels: interspecific, intraspecific and intraindividual. *International Journal of Biological Macromolecules* **1999,** *24* (2-3), 301-306.
127. Madurga, R.; Plaza, G. R.; Blackledge, T. A.; Guinea, G. V.; Elices, M.; Perez-Rigueiro, J., Material properties of evolutionary diverse spider silks described by variation in a single structural parameter. *Scientific Reports* **2016,** *6*, 18991.
128. Vehoff, T.; Glisovic, A.; Schollmeyer, H.; Zippelius, A.; Salditt, T., Mechanical properties of spider dragline silk: humidity, hysteresis, and relaxation. *Biophysical Journal* **2007,** *93* (12), 4425-4432.
129. Heidebrecht, A.; Eisoldt, L.; Diehl, J.; Schmidt, A.; Geffers, M.; Lang, G.; Scheibel, T., Biomimetic fibers made of recombinant spidroins with the same toughness as natural spider silk. *Advanced Materials* **2015,** *27* (13), 2189–2194.
130. Anton, A. M.; Heidebrecht, A.; Mahmood, N.; Beiner, M.; Scheibel, T.; Kremer, F., Foundation of the outstanding toughness in biomimetic and natural spider silk. *Biomacromolecules* **2017,** *18* (12), 3954-3962.
131. Huemmerich, D.; Scheibel, T.; Vollrath, F.; Cohen, S.; Gat, U.; Ittah, S., Novel assembly properties of recombinant spider dragline silk proteins. *Current Biology* **2004,** *14* (22), 2070-2074.

132. Guerette, P. A.; Ginzinger, D. G.; Weber, B. H. F.; Gosline, J. M., Silk properties determined by gland-specific expression of a spider fibroin gene family. *Science* **1996,** *272* (5258), 112-115.
133. Termonia, Y., Molecular modeling of spider silk elasticity. *Macromolecules* **1994,** *27* (25), 7378-7381.
134. Simmons, A. H.; Michal, C. A.; Jelinski, L. W., Molecular orientation and two-component nature of the crystalline fraction of spider dragline silk. *Science* **1996,** *271* (5245), 84-87.
135. Scheibel, T., Spider silks: recombinant synthesis, assembly, spinning, and engineering of synthetic proteins. *Microbial Cell Factories* **2004,** *3* (1), 14.
136. Hardy, J. G.; Römer, L. M.; Scheibel, T. R., Polymeric materials based on silk proteins. *Polymer* **2008,** *49* (20), 4309-4327.
137. Wise, D. H., Cannibalism, food limitation, intraspecific competition, and the regulation of spider populations. *Annual Review of Entomology* **2006,** *51*, 441-465.
138. Elgar, M. A.; Nash, D. R., Sexual cannibalism in the garden spider Araneus diadematus. *Animal Behaviour* **1988,** *36* (5), 1511-1517.
139. Huemmerich, D.; Helsen, C. W.; Quedzuweit, S.; Oschmann, J.; Rudolph, R.; Scheibel, T., Primary structure elements of spider dragline silks and their contribution to protein solubility. *Biochemistry* **2004,** *43* (42), 13604-13612.
140. Thamm, C.; Scheibel, T., Recombinant production, characterization, and fiber spinning of an engineered short major ampullate spidroin (MaSp1s). *Biomacromolecules* **2017,** *18* (4), 1365-1372.
141. Teule, F.; Cooper, A. R.; Furin, W. A.; Bittencourt, D.; Rech, E. L.; Brooks, A.; Lewis, R. V., A protocol for the production of recombinant spider silk-like proteins for artificial fiber spinning. *Nature Protocols* **2009,** *4* (3), 341-355.
142. Heidebrecht, A.; Scheibel, T., Recombinant production of spider silk proteins. *Advances in Applied Microbiology* **2013,** *82*, 115-153.
143. Salehi, S.; Scheibel, T., Biomimetic spider silk fibres: from vision to reality *The Biochemist* **2018,** *40* (1), 4-7.
144. Jokisch, S.; Scheibel, T., Spider silk foam coating of fabric. *Pure and Applied Chemistry* **2017,** *89* (12), 1769-1776.
145. Lang, G.; Jokisch, S.; Scheibel, T., Air filter devices including nonwoven meshes of electrospun recombinant spider silk proteins. *Journal of Visualized Experiments: JoVE* **2013,** (75), e50492.
146. Jokisch, S.; Neuenfeldt, M.; Scheibel, T., Silk-based fine dust filters for air filtration. *Advanced Sustainable Systems* **2017,** *1* (10), 1700079.
147. Wohlrab, S.; Müller, S.; Schmidt, A.; Neubauer, S.; Kessler, H.; Leal-Egana, A.; Scheibel, T., Cell adhesion and proliferation on RGD-modified recombinant spider silk proteins. *Biomaterials* **2012,** *33* (28), 6650-6659.
148. Aigner, T. B.; DeSimone, E.; Scheibel, T., Biomedical applications of recombinant silk-based materials. *Advanced Materials* **2018,** *30* (19), e1704636.
149. Schacht, K.; Scheibel, T., Processing of recombinant spider silk proteins into tailor-made materials for biomaterials applications. *Current Opinion in Biotechnology* **2014,** *29*, 62-69.
150. Chattopadhyay, S.; Raines, R. T., Review collagen-based biomaterials for wound healing. *Biopolymers* **2014,** *101* (8), 821-833.
151. Lee, C. H.; Singla, A.; Lee, Y., Biomedical applications of collagen. *International Journal of Pharmaceutics* **2001,** *221* (1-2), 1-22.
152. Rauterberg, J.; Timpl, R.; Furthmayr, H., Structural characterization of N-terminal antigenic determinants in calf and human collagen. *European Journal of Biochemistry* **1972,** *27* (2), 231-237.

153. Cooperman, L.; Michaeli, D., The immunogenicity of injectable collagen. I. A 1-year prospective study. *Journal of the American Academy of Dermatology* **1984,** *10* (4), 638-646.
154. Lynn, A. K.; Yannas, I. V.; Bonfield, W., Antigenicity and immunogenicity of collagen. *Journal of Biomedical Materials Research Part B Applied Biomaterials* **2004,** *71* (2), 343-354.
155. Perumal, S.; Antipova, O.; Orgel, J. P., Collagen fibril architecture, domain organization, and triple-helical conformation govern its proteolysis. *Proceedings of the National Academy of Sciences of the United States of America* **2008,** *105* (8), 2824-2829.
156. Xu, Y.; Gurusiddappa, S.; Rich, R. L.; Owens, R. T.; Keene, D. R.; Mayne, R.; Hook, A.; Hook, M., Multiple binding sites in collagen type I for the integrins alpha1beta1 and alpha2beta1. *Journal of Biological Chemistry* **2000,** *275* (50), 38981-38989.
157. Parenteau-Bareil, R.; Gauvin, R.; Berthod, F., Collagen-based biomaterials for tissue engineering applications. *Materials* **2010,** *3* (3), 1863-1887.
158. Maeda, M.; Tani, S.; Sano, A.; Fujioka, K., Microstructure and release characteristics of the minipellet, a collagen-based drug delivery system for controlled release of protein drugs. *Journal of Controlled Release* **1999,** *62* (3), 313-324.
159. Zeplin, P. H.; Berninger, A. K.; Maksimovikj, N. C.; van Gelder, P.; Scheibel, T.; Walles, H., Improving the biocompatibility of silicone implants using spider silk coatings: immunohistochemical analysis of capsule formation. *Handchirurgie · Mikrochirurgie · Plastische Chirurgie* **2014,** *46* (6), 336-341.
160. Hennecke, K.; Redeker, J.; Kuhbier, J. W.; Strauss, S.; Allmeling, C.; Kasper, C.; Reimers, K.; Vogt, P. M., Bundles of spider silk, braided into sutures, resist basic cyclic tests: potential use for flexor tendon repair. *Plos One* **2013,** *8* (4), e61100.
161. Kuhbier, J. W.; Reimers, K.; Kasper, C.; Allmeling, C.; Hillmer, A.; Menger, B.; Vogt, P. M.; Radtke, C., First investigation of spider silk as a braided microsurgical suture. *Journal of Biomedical Materials Research B: Applied Biomaterials* **2011,** *97* (2), 381-387.
162. Zha, R. H.; Delparastan, P.; Fink, T. D.; Bauer, J.; Scheibel, T.; Messersmith, P. B., Universal nanothin silk coatings via controlled spidroin self-assembly. *Biomaterials Science* **2019,** *7* (2), 683-695.
163. Schacht, K.; Jüngst, T.; Schweinlin, M.; Ewald, A.; Groll, J.; Scheibel, T., Biofabrication of cell-loaded 3D spider silk constructs. *Angewandte Chemie-International Edition* **2015,** *54* (9), 2816-2820.
164. DeSimone, E.; Schacht, K.; Pellert, A.; Scheibel, T., Recombinant spider silk-based bioinks. *Biofabrication* **2017,** *9* (4), 044104.
165. Petzold, J.; Aigner, T. B.; Touska, F.; Zimmermann, K.; Scheibel, T.; Engel, F. B., Surface features of recombinant spider silk protein eADF4(kappa 16)-made materials are well-Ssuited for cardiac tissue engineering. *Advanced Functional Materials* **2017,** *27* (36), 1701427.
166. Schacht, K.; Vogt, J.; Scheibel, T., Foams made of engineered recombinant spider silk proteins as 3D scaffolds for cell growth. *ACS Biomaterials Science & Engineering* **2016,** *2* (4), 517-525.
167. Borkner, C. B.; Wohlrab, S.; Moller, E.; Lang, G.; Scheibel, T., Surface modification of polymeric biomaterials using recombinant spider silk proteins. *ACS Biomaterials Science & Engineering* **2017,** *3* (5), 767-775.
168. McKay, R. D. G., The origins of cellular diversity in the mammalian central nervous system. *Cell* **1989,** *58* (5), 815-821.

169. Wieringa, P. A.; Goncalves de Pinho, A. R.; Micera, S.; van Wezel, R. J. A.; Moroni, L., Biomimetic architectures for peripheral nerve repair: a review of biofabrication strategies. *Advanced Healthcare Materials* **2018,** *7* (8), e1701164.
170. Scopel, J. F.; de Souza Queiroz, L.; O'Dowd, F. P.; Junior, M. C.; Nucci, A.; Honnicke, M. G., Are human peripheral nerves sensitive to X-ray imaging? *Plos One* **2015,** *10* (3), e0116831.
171. Barnett, M. W.; Larkman, P. M., The action potential. *Practical Neurology* **2007,** *7* (3), 192-197.
172. Magaz, A.; Faroni, A.; Gough, J. E.; Reid, A. J.; Li, X.; Blaker, J. J., Bioactive silk-based nerve guidance conduits for augmenting peripheral nerve repair. *Advanced Healthcare Materials* **2018,** *7* (23), 1800308.
173. Yiu, G.; He, Z. G., Glial inhibition of CNS axon regeneration. *Nature Reviews Neuroscience* **2006,** *7* (8), 617-627.
174. Grinsell, D.; Keating, C. P., Peripheral nerve reconstruction after injury: a review of clinical and experimental therapies. *BioMed Research International* **2014,** *2014*, 698256.
175. Stenberg, L.; Stößel, M.; Ronchi, G.; Geuna, S.; Yin, Y.; Mommert, S.; Mårtensson, L.; Metzen, J.; Grothe, C.; Dahlin, L. B.; Haastert-Talini, K., Regeneration of long-distance peripheral nerve defects after delayed reconstruction in healthy and diabetic rats is supported by immunomodulatory chitosan nerve guides. *Bmc Neuroscience* **2017,** *18* (1), 53.
176. Bozkurt, A.; Boecker, A.; Tank, J.; Altinova, H.; Deurnens, R.; Dabhi, C.; Tolba, R.; Weis, J.; Brook, G. A.; Pallua, N.; van Neerven, S. G. A., Efficient bridging of 20 mm rat sciatic nerve lesions with a longitudinally micro-structured collagen scaffold. *Biomaterials* **2016,** *75*, 112-122.
177. Patel, N. P.; Lyon, K. A.; Huang, J. H., An update-tissue engineered nerve grafts for the repair of peripheral nerve injuries. *Neural Regeneration Research* **2018,** *13* (5), 764-774.
178. Muheremu, A.; Ao, Q., Past, present, and future of nerve conduits in the treatment of peripheral nerve Injury. *BioMed Research International* **2015,** *2015*, 237507-237507.
179. Daly, W.; Yao, L.; Zeugolis, D.; Windebank, A.; Pandit, A., A biomaterials approach to peripheral nerve regeneration: bridging the peripheral nerve gap and enhancing functional recovery. *Journal of the Royal Society Interface* **2012,** *9* (67), 202-221.
180. Fine, E. G.; Decosterd, I.; Papaloizos, M.; Zurn, A. D.; Aebischer, P., GDNF and NGF released by synthetic guidance channels support sciatic nerve regeneration across a long gap. *European Journal of Neuroscience* **2002,** *15* (4), 589-601.
181. Lu, J. J.; Sun, X.; Yin, H. Y.; Shen, X. Z.; Yang, S. H.; Wang, Y.; Jiang, W. L.; Sun, Y.; Zhao, L. Y.; Sun, X. D.; Lu, S. B.; Mikos, A. G.; Peng, J.; Wang, X. M., A neurotrophic peptide-functionalized self-assembling peptide nanofiber hydrogel enhances rat sciatic nerve regeneration. *Nano Research* **2018,** *11* (9), 4599-4613.
182. Meyer, C.; Wrobel, S.; Raimondo, S.; Rochkind, S.; Heimann, C.; Shahar, A.; Ziv-Polat, O.; Geuna, S.; Grothe, C.; Haastert-Talini, K., Peripheral nerve regeneration through hydrogel-enriched chitosan conduits containing engineered Schwann cells for drug delivery. *Cell Transplantation* **2016,** *25* (1), 159-182.
183. Cai, J.; Peng, X. J.; Nelson, K. D.; Eberhart, R.; Smith, G. M., Permeable guidance channels containing microfilament scaffolds enhance axon growth and maturation. *Journal of Biomedical Materials Research Part A* **2005,** *75A* (2), 374-386.
184. Sun, B.; Zhou, Z.; Wu, T.; Chen, W.; Li, D.; Zheng, H.; El-Hamshary, H.; Al-Deyab, S. S.; Mo, X.; Yu, Y., Development of nanofiber sponges-containing nerve guidance conduit for peripheral nerve regeneration in vivo. *ACS Applied Materials & Interfaces* **2017,** *9* (32), 26684-26696.

185. Quigley, A. F.; Bulluss, K. J.; Kyratzis, I. L. B.; Gilmore, K.; Mysore, T.; Schirmer, K. S. U.; Kennedy, E. L.; O'Shea, M.; Truong, Y. B.; Edwards, S. L.; Peeters, G.; Herwig, P.; Razal, J. M.; Campbell, T. E.; Lowes, K. N.; Higgins, M. J.; Moulton, S. E.; Murphy, M. A.; Cook, M. J.; Clark, G. M.; Wallace, G. G.; Kapsa, R. M. I., Engineering a multimodal nerve conduit for repair of injured peripheral nerve. *Journal of Neural Engineering* **2013,** *10* (1), 016008.
186. Rao, F.; Yuan, Z. P.; Li, M.; Yu, F.; Fang, X. X.; Jiang, B. G.; Wen, Y. Q.; Zhang, P. X., Expanded 3D nanofibre sponge scaffolds by gas-foaming technique enhance peripheral nerve regeneration. *Artificial Cells Nanomedicine and Biotechnology* **2019,** *47* (1), 491-500.
187. Singh, A.; Asikainen, S.; Teotia, A. K.; Shiekh, P. A.; Huotilainen, E.; Qayoom, I.; Partanen, J.; Seppälä, J.; Kumar, A., Biomimetic photocurable three-dimensional printed nerve guidance channels with aligned cryomatrix lumen for peripheral nerve regeneration. *ACS Applied Materials & Interfaces* **2018,** *10* (50), 43327-43342.
188. Zhu, W.; Tringale, K. R.; Woller, S. A.; You, S. T.; Johnson, S.; Shen, H. X.; Schimelman, J.; Whitney, M.; Steinauer, J.; Xu, W. Z.; Yaksh, T. L.; Nguyen, Q. T.; Chen, S. C., Rapid continuous 3D printing of customizable peripheral nerve guidance conduits. *Materials Today* **2018,** *21* (9), 951-959.
189. Frost, H. K.; Andersson, T.; Johansson, S.; Englund-Johansson, U.; Ekström, P.; Dahlin, L. B.; Johansson, F., Electrospun nerve guide conduits have the potential to bridge peripheral nerve injuries in vivo. *Scientific Reports* **2018,** *8* (1), 16716.
190. Zhao, Y.; Zhang, Q.; Zhao, L.; Gan, L.; Yi, L.; Zhao, Y.; Xue, J.; Luo, L.; Du, Q.; Geng, R.; Sun, Z.; Benkirane-Jessel, N.; Chen, P.; Li, Y.; Chen, Y., Enhanced peripheral nerve regeneration by a high surface area to volume ratio of nerve conduits fabricated from hydroxyethyl cellulose/soy protein composite sponges. *ACS Omega* **2017,** *2* (11), 7471-7481.
191. Quan, Q.; Meng, H. Y.; Chang, B.; Liu, G. B.; Cheng, X. Q.; Tang, H.; Wang, Y.; Peng, J.; Zhao, Q.; Lu, S. B., Aligned fibers enhance nerve guide conduits when bridging peripheral nerve defects focused on early repair stage. *Neural Regeneration Research* **2019,** *14* (5), 903-912.
192. Jiang, X.; Mi, R. F.; Hoke, A.; Chew, S. Y., Nanofibrous nerve conduit-enhanced peripheral nerve regeneration. *Journal of Tissue Engineering and Regenerative Medicine* **2014,** *8* (5), 377-385.
193. Wang, Y.; Wang, W.; Wo, Y.; Gui, T.; Zhu, H.; Mo, X.; Chen, C.-C.; Li, Q.; Ding, W., Orientated guidance of peripheral nerve regeneration using conduits with a microtube array sheet (MTAS). *ACS Applied Materials & Interfaces* **2015,** *7* (16), 8437-8450.
194. Sarker, M.; Naghieh, S.; McInnes, A. D.; Schreyer, D. J.; Chen, X., Strategic design and fabrication of nerve guidance conduits for peripheral nerve regeneration. *Biotechnology Journal* **2018,** *13* (7), 1700635.
195. Chang, J.-Y.; Ho, T.-Y.; Lee, H.-C.; Lai, Y.-L.; Lu, M.-C.; Yao, C.-H.; Chen, Y.-S., Highly permeable genipin-cross-linked gelatin conduits enhance peripheral nerve regeneration. *Artificial Organs* **2009,** *33* (12), 1075-1085.
196. Iijima, Y.; Ajiki, T.; Murayama, A.; Takeshita, K., Effect of artificial nerve conduit vascularization on peripheral nerve in a necrotic bed. *PRS Global Open* **2016,** *4* (3), e665-e665.
197. Bozkurt, A.; Lassner, F.; O'Dey, D.; Deumens, R.; Bocker, A.; Schwendt, T.; Janzen, C.; Suschek, C. V.; Tolba, R.; Kobayashi, E.; Sellhaus, B.; Tholl, S.; Eummelen, L.; Schugner, F.; Damink, L. O.; Weis, J.; Brook, G. A.; Pallua, N., The role of microstructured and interconnected pore channels in a collagen-based nerve

guide on axonal regeneration in peripheral nerves. *Biomaterials* **2012,** *33* (5), 1363-1375.
198. Yoshii, S.; Oka, M., Peripheral nerve regeneration along collagen filaments. *Brain Research* **2001,** *888* (1), 158-162.
199. Lee, J. Y.; Giusti, G.; Friedrich, P. F.; Archibald, S. J.; Kemnitzer, J. E.; Patel, J.; Desai, N.; Bishop, A. T.; Shin, A. Y., The effect of collagen nerve conduits filled with collagen-glycosaminoglycan matrix on peripheral motor nerve regeneration in a rat model. *Journal of Bone and Joint Surgery* **2012,** *94A* (22), 2084-2091.
200. Jin, J.; Limburg, S.; Joshi, S. K.; Landman, R.; Park, M.; Zhang, Q.; Kim, H. T.; Kuo, A. C., Peripheral nerve repair in rats using composite hydrogel-filled aligned nanofiber conduits with incorporated nerve growth factor. *Tissue Engineering. Part A* **2013,** *19* (19-20), 2138-2146.
201. Ryan, A. J.; Lackington, W. A.; Hibbitts, A. J.; Matheson, A.; Alekseeva, T.; Stejskalova, A.; Roche, P.; O'Brien, F. J., A physicochemically optimized and neuroconductive biphasic nerve guidance conduit for peripheral nerve repair. *Advanced Healthcare Materials* **2017,** *6* (24), 1700954.
202. Xu, Y.; Zhang, Z.; Chen, X.; Li, R.; Li, D.; Feng, S., A silk fibroin/collagen nerve scaffold seeded with a co-culture of Schwann cells and adipose-derived stem cells for sciatic nerve regeneration. *Plos One* **2016,** *11* (1), e0147184-e0147184.
203. Kaemmer, D.; Bozkurt, A.; Otto, J.; Junge, K.; Klink, C.; Weis, J.; Sellhaus, B.; O'Dey, D. M.; Pallua, N.; Jansen, M.; Schumpelick, V.; Klinge, U., Evaluation of tissue components in the peripheral nervous system using Sirius red staining and immunohistochemistry: a comparative study (human, pig, rat). *Journal of Neuroscience Methods* **2010,** *190* (1), 112-116.
204. Ushiki, T.; Ide, C., Three-dimensional organization of the collagen fibrils in the rat sciatic nerve as revealed by transmission- and scanning electron microscopy. *Cell and Tissue Research* **1990,** *260* (1), 175-184.
205. Koopmans, G.; Hasse, B.; Sinis, N., The role of collagen in peripheral nerve repair. *Essays on Peripheral Nerve Repair and Regeneration* **2009,** *87*, 363-379.
206. Lackington, W. A.; Ryan, A. J.; O'Brien, F. J., Advances in nerve guidance conduit-based therapeutics for peripheral nerve repair. *ACS Biomaterials Science & Engineering* **2017,** *3* (7), 1221-1235.
207. Roloff, F.; Strauß, S.; Vogt, P. M.; Bicker, G.; Radtke, C., Spider silk as guiding biomaterial for human model neurons. *BioMed Research International* **2014,** *2014*, 906819-906819.
208. Allmeling, C.; Jokuszies, A.; Reimers, K.; Kall, S.; Choi, C. Y.; Brandes, G.; Kasper, C.; Scheper, T.; Guggenheim, M.; Vogt, P. M., Spider silk fibres in artificial nerve constructs promote peripheral nerve regeneration. *Cell Proliferation* **2008,** *41* (3), 408-420.
209. Radtke, C.; Allmeling, C.; Waldmann, K. H.; Reimers, K.; Thies, K.; Schenk, H. C.; Hillmer, A.; Guggenheim, M.; Brandes, G.; Vogt, P. M., Spider silk constructs enhance axonal regeneration and remyelination in long nerve defects in sheep. *Plos One* **2011,** *6* (2), e16990.
210. Lewicka, M.; Hermanson, O.; Rising, A. U., Recombinant spider silk matrices for neural stem cell cultures. *Biomaterials* **2012,** *33* (31), 7712-7717.
211. An, B.; Tang-Schomer, M. D.; Huang, W. W.; He, J. Y.; Jones, J. A.; Lewis, R. V.; Kaplan, D. L., Physical and biological regulation of neuron regenerative growth and network formation on recombinant dragline silks. *Biomaterials* **2015,** *48*, 137-146.
212. Katayama, K.; Amano, T.; Nakamura, K., Structural formation during melt spinning process *Colloid and Polymer Science* **1968,** *226* (2), 125–134.

213. Szosland, L.; East, G. C., The dry spinning of dibutyrylchitin fibers. *Journal of Applied Polymer Science* **1995,** *58* (13), 2459-2466.
214. Arafat, M. T.; Tronci, G.; Yin, J.; Wood, D. J.; Russell, S. J., Biomimetic wet-stable fibres via wet spinning and diacid-based crosslinking of collagen triple helices. *Polymer* **2015,** *77*, 102-112.
215. Cavallaro, J. F.; Kemp, P. D.; Kraus, K. H., Collagen fabrics as biomaterials. *Biotechnology and Bioengineering* **1994,** *43* (8), 781-791.
216. Caves, J. M.; Kumar, V. A.; Wen, J.; Cui, W.; Martinez, A.; Apkarian, R.; Coats, J. E.; Berland, K.; Chaikof, E. L., Fibrillogenesis in continuously spun synthetic collagen fiber. *Journal of biomedical materials research. Part B, Applied biomaterials* **2010,** *93* (1), 24-38.
217. Dunn, M. G.; Avasarala, P. N.; Zawadsky, J. P., Optimization of extruded collagen-fibers for ACL reconstruction. *Journal of Biomedical Materials Research* **1993,** *27* (12), 1545-1552.
218. Gentleman, E.; Lay, A. N.; Dickerson, D. A.; Nauman, E. A.; Livesay, G. A.; Dee, K. C., Mechanical characterization of collagen fibers and scaffolds for tissue engineering. *Biomaterials* **2003,** *24* (21), 3805-3813.
219. Kato, Y. P.; Christiansen, D. L.; Hahn, R. A.; Shieh, S. J.; Goldstein, J. D.; Silver, F. H., Mechanical-properties of collagen-fibers - a comparison of reconstituted and rat tail tendon fibers. *Biomaterials* **1989,** *10* (1), 38-41.
220. Kato, Y. P.; Silver, F. H., Formation of continuous collagen fibres: evaluation of biocompatibility and mechanical properties. *Biomaterials* **1990,** *11* (3), 169-175.
221. Pins, G. D.; Huang, E. K.; Christiansen, D. L.; Silver, F. H., Effects of static axial strain on the tensile properties and failure mechanisms of self-assembled collagen fibers. *Journal of Applied Polymer Science* **1997,** *63* (11), 1429-1440.
222. Siriwardane, M. L.; DeRosa, K.; Collins, G.; Pfister, B. J., Controlled formation of cross-linked collagen fibers for neural tissue engineering applications. *Biofabrication* **2014,** *6* (1), 015012.
223. Wang, M. C.; Pins, G. D.; Silver, F. H., Collagen-fibers with improved strength for the repair of soft-tissue injuries. *Biomaterials* **1994,** *15* (7), 507-512.
224. Wang, X.; Wu, T.; Wang, W.; Huang, C.; Jin, X. Y., Regenerated collagen fibers with grooved surface texture: physicochemical characterization and cytocompatibility. *Materials Science & Engineering C-Materials for Biological Applications* **2016,** *58*, 750-756.
225. Yaari, A.; Schilt, Y.; Tamburu, C.; Raviv, U.; Shoseyov, O., Wet spinning and drawing of human recombinant collagen. *ACS Biomaterials-Science & Engineering* **2016,** *2* (3), 349-360.
226. Zeugolis, D. I.; Paul, R. G.; Attenburrow, G., Engineering extruded collagen fibers for biomedical applications. *Journal of Applied Polymer Science* **2008,** *108* (5), 2886-2894.
227. Cong, H. P.; Ren, X. C.; Wang, P.; Yu, S. H., Wet-spinning assembly of continuous, neat, and macroscopic graphene fibers. *Scientific reports* **2012,** *2*, 613.
228. Leal-Egana, A.; Lang, G.; Mauerer, C.; Wickinghoff, J.; Weber, M.; Geimer, S.; Scheibel, T., Interactions of fibroblasts with different morphologies made of an engineered spider silk protein. *Advanced Engineering Materials* **2012,** *14* (3), B67-B75.
229. Jun, I.; Han, H. S.; Edwards, J. R.; Jeon, H., Electrospun fbrous scaffolds for tissue engineering: viewpoints on architecture and fabrication. *International Journal of Molecular Sciences* **2018,** *19* (3), 745.
230. Magaz, A.; Roberts, A. D.; Faraji, S.; Nascimento, T. R. L.; Medeiros, E. S.; Zhang, W.; Greenhalgh, R. D.; Mautner, A.; Li, X.; Blaker, J. J., Porous, aligned, and biomimetic fibers of regenerated silk fibroin produced by solution blow spinning. *Biomacromolecules* **2018,** *19* (12), 4542-4553.

231. Chen, C. P.; Townsend, A. D.; Sell, S. A.; Martin, R. S., Microchip-based 3D-cell culture using polymer nanofibers generated by solution blow spinning. *Analytical Methods* **2017,** *9* (22), 3274-3283.
232. Daristotle, J. L.; Behrens, A. M.; Sandler, A. D.; Kofinas, P., A review of the fundamental principles and applications of solution blow spinning. *ACS Applied Materials & Interfaces* **2016,** *8* (51), 34951-34963.
233. Medeiros, E. S.; Glenn, G. M.; Klamczynski, A. P.; Orts, W. J.; Mattoso, L. H. C., Solution blow spinning: a new method to produce micro- and nanofibers from polymer solutions. *Journal of Applied Polymer Science* **2009,** *113* (4), 2322-2330.
234. Smit, E.; Bűttner, U.; Sanderson, R. D., Continuous yarns from electrospun fibers. *Polymer* **2005,** *46* (8), 2419-2423.
235. Cheng, J.; Jun, Y.; Qin, J. H.; Lee, S. H., Electrospinning versus microfluidic spinning of functional fibers for biomedical applications. *Biomaterials* **2017,** *114*, 121-143.
236. Zeugolis, D. I.; Khew, S. T.; Yew, E. S. Y.; Ekaputra, A. K.; Tong, Y. W.; Yung, L. Y. L.; Hutmacher, D. W.; Sheppard, C.; Raghunath, M., Electro-spinning of pure collagen nano-fibres - Just an expensive way to make gelatin? *Biomaterials* **2008,** *29* (15), 2293-2305.
237. Behrens, A. M.; Lee, N. G.; Casey, B. J.; Srinivasan, P.; Sikorski, M. J.; Daristotle, J. L.; Sandler, A. D.; Kofinas, P., Biodegradable-polymer-blend-based surgical sealant with body-temperature-mediated adhesion. *Advanced Materials* **2015,** *27* (48), 8056-8061.
238. Nge, P. N.; Rogers, C. I.; Woolley, A. T., Advances in microfluidic materials, functions, integration, and applications. *Chemical Reviews* **2013,** *113* (4), 2550-2583.
239. Squires, T. M.; Quake, S. R., Microfluidics: fluid physics at the nanoliter scale. *Reviews of Modern Physics* **2005,** *77* (3), 977-1026.
240. Kenis, P. J. A.; Ismagilov, R. F.; Whitesides, G. M., Microfabrication inside capillaries using multiphase laminar flow patterning. *Science* **1999,** *285* (5424), 83-85.
241. Whitesides, G. M., The origins and the future of microfluidics. *Nature* **2006,** *442* (7101), 368-373.
242. Sackmann, E. K.; Fulton, A. L.; Beebe, D. J., The present and future role of microfluidics in biomedical research. *Nature* **2014,** *507* (7491), 181-189.
243. McDonald, J. C.; Duffy, D. C.; Anderson, J. R.; Chiu, D. T.; Wu, H.; Schueller, O. J.; Whitesides, G. M., Fabrication of microfluidic systems in poly(dimethylsiloxane). *Electrophoresis* **2000,** *21* (1), 27-40.
244. Jun, Y.; Kim, M. J.; Hwang, Y. H.; Jeon, E. A.; Kang, A. R.; Lee, S. H.; Lee, D. Y., Microfluidics-generated pancreatic islet microfibers for enhanced immunoprotection. *Biomaterials* **2013,** *34* (33), 8122-8130.
245. He, X. H.; Wang, W.; Liu, Y. M.; Jiang, M. Y.; Wu, F.; Deng, K.; Liu, Z.; Ju, X. J.; Xie, R.; Chu, L. Y., Microfluidic fabrication of bio-inspired microfibers with controllable magnetic spindle-knots for 3D assembly and water collection. *ACS Applied Materials & Interfaces* **2015,** *7* (31), 17471-17481.
246. Cheng, Y.; Zheng, F.; Lu, J.; Shang, L.; Xie, Z.; Zhao, Y.; Chen, Y.; Gu, Z., Bioinspired multicompartmental microfibers from microfluidics. *Advanced Materials* **2014**, 5184-5190.
247. Ahn, S. Y.; Mun, C. H.; Lee, S. H., Microfluidic spinning of fibrous alginate carrier having highly enhanced drug loading capability and delayed release profile. *RSC Advances* **2015,** *5* (20), 15172-15181.
248. Jeong, G. S.; Lee, S. H., Microfluidic spinning of grooved microfiber for guided neuronal cell culture using surface tension mediated grooved round channel. *Tissue Engineering and Regenerative Medicine* **2014,** *11* (4), 291-296.

249. Shin, S. J.; Park, J. Y.; Lee, J. Y.; Park, H.; Park, Y. D.; Lee, K. B.; Whang, C. M.; Lee, S. H., "On the fly" continuous generation of alginate fibers using a microfluidic device. *Langmuir: the ACS journal of surfaces and colloids* **2007,** *23* (17), 9104-9108.
250. Lee, K. H.; Shin, S. J.; Park, Y.; Lee, S. H., Synthesis of cell-laden alginate hollow fibers using microfluidic chips and microvascularized tissue-engineering applications. *Small* **2009,** *5* (11), 1264-1268.
251. Mun, C. H.; Hwang, J. Y.; Lee, S. H., Microfluidic spinning of the fibrous alginate scaffolds for modulation of the degradation profile. *Tissue Engineering and Regenerative Medicine* **2016,** *13* (2), 140-148.
252. Kang, E.; Jeong, G. S.; Choi, Y. Y.; Lee, K. H.; Khademhosseini, A.; Lee, S. H., Digitally tunable physicochemical coding of material composition and topography in continuous microfibres. *Nature Materials* **2011,** *10* (11), 877-883.
253. Onoe, H.; Okitsu, T.; Itou, A.; Kato-Negishi, M.; Gojo, R.; Kiriya, D.; Sato, K.; Miura, S.; Iwanaga, S.; Kuribayashi-Shigetomi, K.; Matsunaga, Y. T.; Shimoyama, Y.; Takeuchi, S., Metre-long cell-laden microfibres exhibit tissue morphologies and functions. *Nature Materials* **2013,** *12* (6), 584-590.
254. Park, D. Y.; Mun, C. H.; Kang, E.; No, D. Y.; Ju, J.; Lee, S. H., One-stop microfiber spinning and fabrication of a fibrous cell-encapsulated scaffold on a single microfluidic platform. *Biofabrication* **2014,** *6* (2), 024108.
255. Park, D.; Park, J.; Jang, H.; Cheng, J.; Hyun Kim, S.; Lee, S. H., Simultaneous microfluidic spinning of multiple strands of submicron fiber for the production of free-standing porous membranes for biological application. *Biofabrication* **2017,** *9* (2), 025026.
256. Chae, S. K.; Kang, E.; Khademhosseini, A.; Lee, S. H., Micro/nanometer-scale fiber with highly ordered structures by mimicking the spinning process of silkworm. *Advanced Materials* **2013,** *25* (22), 3071-3078.
257. Lee, B. R.; Lee, K. H.; Kang, E.; Kim, D. S.; Lee, S. H., Microfluidic wet spinning of chitosan-alginate microfibers and encapsulation of HepG2 cells in fibers. *Biomicrofluidics* **2011,** *5* (2), 022208.
258. Cheng, J.; Park, D.; Jun, Y.; Lee, J.; Hyun, J.; Lee, S. H., Biomimetic spinning of silk fibers and in situ cell encapsulation. *Lab on a Chip* **2016,** *16* (14), 2654-2661.
259. Lee, K. H.; Shin, S. J.; Kim, C. B.; Kim, J. K.; Cho, Y. W.; Chung, B. G.; Lee, S. H., Microfluidic synthesis of pure chitosan microfibers for bio-artificial liver chip. *Lab on a Chip* **2010,** *10* (10), 1328-1334.
260. He, X. H.; Wang, W.; Deng, K.; Xie, R.; Ju, X. J.; Liu, Z.; Chu, L. Y., Microfluidic fabrication of chitosan microfibers with controllable internals from tubular to peapod-like structures. *RSC Advances* **2015,** *5* (2), 928-936.
261. Yeh, C. H.; Lin, P. W.; Lin, Y. C., Chitosan microfiber fabrication using a microfluidic chip and its application to cell cultures. *Microfluidics and Nanofluidics* **2010,** *8* (1), 115-121.
262. Mittal, N.; Ansari, F.; Gowda, V. K.; Brouzet, C.; Chen, P.; Larsson, P. T.; Roth, S. V.; Lundell, F.; Wagberg, L.; Kotov, N. A.; Söderberg, L. D., Multiscale control of nanocellulose assembly: transferring remarkable nanoscale fibril mechanics to macroscale fibers. *ACS Nano* **2018,** *12* (7), 6378-6388.
263. Hakansson, K. M. O.; Fall, A. B.; Lundell, F.; Yu, S.; Krywka, C.; Roth, S. V.; Santoro, G.; Kvick, M.; Wittberg, L. P.; Wagberg, L.; Söderberg, L. D., Hydrodynamic alignment and assembly of nanofibrils resulting in strong cellulose filaments. *Nature Communications* **2014,** *5*, 4018.
264. Sharifi, F.; Patel, B. B.; Dzuilko, A. K.; Montazami, R.; Sakaguchi, D. S.; Hashemi, N., Polycaprolactone microfibrous scaffolds to navigate neural stem cells. *Biomacromolecules* **2016,** *17* (10), 3287-3297.

265. Hwang, C. M.; Khademhosseini, A.; Park, Y.; Sun, K.; Lee, S. H., Microfluidic chip-based fabrication of PLGA microfiber scaffolds for tissue engineering. *Langmuir : the ACS Journal of Surfaces and Colloids* **2008,** *24* (13), 6845-6851.
266. Hwang, C. M.; Park, Y.; Park, J. Y.; Lee, K.; Sun, K.; Khademhosseini, A.; Lee, S. H., Controlled cellular orientation on PLGA microfibers with defined diameters. *Biomedical Microdevices* **2009,** *11* (4), 739-746.
267. Sharifi, F.; Bai, Z. H.; Montazami, R.; Hashemi, N., Mechanical and physical properties of poly(vinyl alcohol) microfibers fabricated by a microfluidic approach. *RSC Advances* **2016,** *6* (60), 55343-55353.
268. Kamada, A.; Mittal, N.; Söderberg, L. D.; Ingverud, T.; Ohm, W.; Roth, S. V.; Lundell, F.; Lendel, C., Flow-assisted assembly of nanostructured protein microfibers. *Proceedings of the National Academy of Sciences of the United States of America* **2017**, 201617260.
269. Kinahan, M. E.; Filippidi, E.; Koster, S.; Hu, X.; Evans, H. M.; Pfohl, T.; Kaplan, D. L.; Wong, J., Tunable silk: using microfluidics to fabricate silk fibers with controllable properties. *Biomacromolecules* **2011,** *12* (5), 1504-1511.
270. Rammensee, S.; Slotta, U.; Scheibel, T.; Bausch, A. R., Assembly mechanism of recombinant spider silk proteins. *Proceedings of the National Academy of Sciences of the United States of America* **2008,** *105* (18), 6590-6595.
271. Renberg, B.; Andersson-Svahn, H.; Hedhammar, M., Mimicking silk spinning in a microchip. *Sensors and Actuators B-Chemical* **2014,** *195*, 404-408.
272. Koster, S.; Evans, H. M.; Wong, J. Y.; Pfohl, T., An in situ study of collagen self-assembly processes. *Biomacromolecules* **2008,** *9* (1), 199-207.
273. Luo, J.; Zhang, L. L.; Peng, Q. F.; Sun, M. J.; Zhang, Y. P.; Shao, H. L.; Hu, X. C., Tough silk fibers prepared in air using a biomimetic microfluidic chip. *International Journal of Biological Macromolecules* **2014,** *66*, 319-324.
274. Peng, Q. F.; Shao, H. L.; Hu, X. C.; Zhang, Y. P., Microfluidic dry-spinning and characterization of regenerated silk fibroin fibers. *Jove-Journal of Visualized Experiments* **2017,** (127), e56271.
275. Srivastava, Y.; Marquez, M.; Thorsen, T., Multijet electrospinning of conducting nanofibers from microfluidic manifolds. *Journal of Applied Polymer Science* **2007,** *106* (5), 3171-3178.
276. Srivastava, Y.; Loscertales, I.; Marquez, M.; Thorsen, T., Electrospinning of hollow and core/sheath nanofibers using a microfluidic manifold. *Microfluidics and Nanofluidics* **2008,** *4* (3), 245-250.
277. Srivastava, Y.; Marquez, M.; Thorsen, T., Microfluidic electrospinning of biphasic nanofibers with Janus morphology. *Biomicrofluidics* **2009,** *3* (1), 12801.
278. Zhang, X.; Gao, X.; Jiang, L.; Qin, J., Flexible generation of gradient electrospinning nanofibers using a microfluidic assisted approach. *Langmuir: the ACS Journal of Surfaces and Colloids* **2012,** *28* (26), 10026-10032.
279. Jun, Y.; Kang, E.; Chae, S.; Lee, S. H., Microfluidic spinning of micro- and nano-scale fibers for tissue engineering. *Lab on a Chip* **2014,** *14* (13), 2145-2160.
280. Wang, Z.; Lee, W. J.; Koh, B. T. H.; Hong, M.; Wang, W.; Lim, P. N.; Feng, J.; Park, L. S.; Kim, M.; Thian, E. S., Functional regeneration of tendons using scaffolds with physical anisotropy engineered via microarchitectural manipulation. *Science Advances* **2018,** *4* (10), eaat4537.
281. Huanglee, L. L. H.; Cheung, D. T.; Nimni, M. E., Biochemical-changes and cytotoxicity associated with the degradation of polymeric glutaraldehyde derived cross-Links. *Journal of Biomedical Materials Research* **1990,** *24* (9), 1185-1201.
282. Madaghiele, M.; Calo, E.; Salvatore, L.; Bonfrate, V.; Pedone, D.; Frigione, M.; Sannino, A., Assessment of collagen crosslinking and denaturation for the design of

regenerative scaffolds. *Journal of biomedical materials research. Part A* **2016,** *104* (1), 186-194.
283. Huang, Y.; Wang, Y. X.; Chen, L. Y.; Zhang, L. N., Facile construction of mechanically tough collagen fibers reinforced by chitin nanofibers as cell alignment templates. *Journal of Materials Chemistry B* **2018,** *6* (6), 918-929.
284. Hofmann, E.; Krüger, K.; Haynl, C.; Scheibel, T.; Trebbin, M.; Förster, S., Microfluidic nozzle device for ultrafine fiber solution blow spinning with precise diameter control. *Lab on a Chip* **2018,** *18* (15), 2225-2234.
285. Haynl, C.; Hofmann, E.; Pawar, K.; Förster, S.; Scheibel, T., Microfluidics-produced collagen fibers show extraordinary mechanical properties. *Nano Letters* **2016,** *16* (9), 5917-5922.
286. Pawar, K.; Welzel, G.; Haynl, C.; Schuster, S.; Scheibel, T., Recombinant spider silk and collagen-based nerve guidance conduits support neuronal cell differentiation and functionality in vitro. *ACS Applied Bio Materials* **2019,** *2* (11), 4872-4880.
287. Trebbin, M.; Krüger, K.; DePonte, D.; Roth, S. V.; Chapman, H. N.; Förster, S., Microfluidic liquid jet system with compatibility for atmospheric and high-vacuum conditions. *Lab on a Chip* **2014,** *14* (10), 1733-1745.
288. Ganan-Calvo, A. M., Generation of steady liquid microthreads and micron-sized monodisperse sprays in gas streams. *Physical Review Letters* **1998,** *80* (2), 285-288.
289. DePonte, D. P.; Weierstall, U.; Schmidt, K.; Warner, J.; Starodub, D.; Spence, J. C. H.; Doak, R. B., Gas dynamic virtual nozzle for generation of microscopic droplet streams. *Journal of Physics D: Applied Physics* **2008,** *41* (19), 195505.
290. Ingham, K. C., Precipitation of proteins with polyethylene-glycol - characterization of albumin. *Archives of Biochemistry and Biophysics* **1978,** *186* (1), 106-113.
291. Honig, W.; Kula, M. R., Selectivity of protein precipitation with polyethylene-glycol fractions of various molecular-weights. *Analytical Biochemistry* **1976,** *72* (1-2), 502-512.
292. Wiens, R.; Findlay, C. R.; Baldwin, S. G.; Kreplak, L.; Lee, J. M.; Veres, S. P.; Gough, K. M., High spatial resolution (1.1 μm and 20 nm) FTIR polarization contrast imaging reveals pre-rupture disorder in damaged tendon. *Faraday Discussions* **2016,** *187*, 555-573.
293. Bi, X.; Li, G.; Doty, S. B.; Camacho, N. P., A novel method for determination of collagen orientation in cartilage by Fourier transform infrared imaging spectroscopy (FT-IRIS). *Osteoarthritis and Cartilage* **2005,** *13* (12), 1050-1058.
294. Chae, H. G.; Kumar, S., Materials science - Making strong fibers. *Science* **2008,** *319* (5865), 908-909.
295. Tischfield, M. A.; Baris, H. N.; Wu, C.; Rudolph, G.; Van Maldergem, L.; He, W.; Chan, W. M.; Andrews, C.; Demer, J. L.; Robertson, R. L.; Mackey, D. A.; Ruddle, J. B.; Bird, T. D.; Gottlob, I.; Pieh, C.; Traboulsi, E. I.; Pomeroy, S. L.; Hunter, D. G.; Soul, J. S.; Newlin, A.; Sabol, L. J.; Doherty, E. J.; de Uzcategui, C. E.; de Uzcategui, N.; Collins, M. L.; Sener, E. C.; Wabbels, B.; Hellebrand, H.; Meitinger, T.; de Berardinis, T.; Magli, A.; Schiavi, C.; Pastore-Trossello, M.; Koc, F.; Wong, A. M.; Levin, A. V.; Geraghty, M. T.; Descartes, M.; Flaherty, M.; Jamieson, R. V.; Moller, H. U.; Meuthen, I.; Callen, D. F.; Kerwin, J.; Lindsay, S.; Meindl, A.; Gupta, M. L., Jr.; Pellman, D.; Engle, E. C., Human TUBB3 mutations perturb microtubule dynamics, kinesin interactions, and axon guidance. *Cell* **2010,** *140* (1), 74-87.
296. Tafoya, L. C. R.; Mameli, M.; Miyashita, T.; Guzowski, J. F.; Valenzuela, C. F.; Wilson, M. C., Expression and function of SNAP-25 as a universal SNARE component in GABAergic neurons. *Journal of Neuroscience* **2006,** *26* (30), 7826-7838.
297. Hodel, A., Snap-25. *The International Journal of Biochemistry & Cell Biology* **1998,** *30* (10), 1069-1073.

298. Bunaciu, A. A.; Aboul-Enein, H. Y.; Fleschin, S., Vibrational spectroscopy in clinical analysis. *Applied Spectroscopy Reviews* **2015,** *50* (2), 176-191.
299. Kacurakova, M.; Wilson, R. H., Developments in mid-infrared FT-IR spectroscopy of selected carbohydrates. *Carbohydrate Polymers* **2001,** *44* (4), 291-303.
300. Wiercigroch, E.; Szafraniec, E.; Czamara, K.; Pacia, M. Z.; Majzner, K.; Kochan, K.; Kaczor, A.; Baranska, M.; Malek, K., Raman and infrared spectroscopy of carbohydrates: A review. *Spectrochimica Acta Part a-Molecular and Biomolecular Spectroscopy* **2017,** *185*, 317-335.
301. Agnarsson, I.; Kuntner, M.; Blackledge, T. A., Bioprospecting finds the toughest biological material: extraordinary silk from a giant riverine orb spider. *Plos One* **2010,** *5* (9), e11234.
302. Guinea, G. V.; Elices, M.; Plaza, G. R.; Perea, G. B.; Daza, R.; Riekel, C.; Agullo-Rueda, F.; Hayashi, C.; Zhao, Y.; Perez-Rigueiro, J., Minor ampullate silks from *Nephila* and *Argiope* spiders: tensile properties and microstructural characterization. *Biomacromolecules* **2012,** *13* (7), 2087-2098.
303. Gosline, J. M.; Guerette, P. A.; Ortlepp, C. S.; Savage, K. N., The mechanical design of spider silks: from fibroin sequence to mechanical function. *The Journal of Experimental Biology* **1999,** *202* (Pt 23), 3295-3303.
304. Zhao, A. C.; Zhao, T. F.; Nakagaki, K.; Zhang, Y. S.; Sima, Y. H.; Miao, Y. G.; Shiomi, K.; Kajiura, Z.; Nagata, Y.; Takadera, M.; Nakagaki, M., Novel molecular and mechanical properties of egg case silk from wasp spider, *Argiope bruennichi*. *Biochemistry* **2006,** *45* (10), 3348-3356.
305. Hu, X. Y.; Kohler, K.; Falick, A. M.; Moore, A. M. F.; Jones, P. R.; Sparkman, O. D.; Vierra, C., Egg case protein-1 - A new class of silk proteins with fibroin-like properties from the spider *Latrodectus hesperus*. *Journal of Biological Chemistry* **2005,** *280* (22), 21220-21230.
306. Stubbs, D. G.; Tillinghast, E. K.; Townley, M. A.; Cherim, N. A., Fibrous Composite Structure in a Spider Silk. *Naturwissenschaften* **1992,** *79* (5), 231-234.
307. Haynl, C.; Vongsvivut, J.; Mayer, K. R. H.; Bargel, H.; Neubauer, V. J.; Tobin, M. J.; Elgar, M. A.; Scheibel, T., Free-standing spider silk webs of the thomisid *Saccodomus formivorus* are made of composites comprising micro- and submicron fibers. *Scientific Reports* **2020,** 10, 17624.

5 PUBLIKATIONSLISTE

1. Hofmann, E.; Krüger, K.; **Haynl, C.**; Scheibel, T.; Trebbin, M.; Förster, S.* Microfluidic nozzle device for ultrafine fiber solution blow spinning with precise diameter control. *Lab on a Chip* **2018**, 18*,* 2225-2234.

2. **Haynl, C.**; Hofmann, E.; Pawar, K.; Förster, S.; Scheibel, T.* Microfluidics-produced collagen fibers show extraordinary mechanical properties. *Nano Letters* **2016**, 16*,* 5917-5922.

3. Pawar, K.; Welzel, G.; **Haynl, C.**; Schuster, S.; Scheibel, T.* Recombinant spider silk and collagen-based nerve guidance conduits support neuronal cell differentiation and functionality *in vitro*. *ACS Applied Bio Materials* **2019**, 2, 4872-4880.

4. Aigner, T. B.**&**; **Haynl, C.&**; Salehi, S.; O'Connor, A.; Scheibel, T.* Nerve guidance conduit design based on self-rolling tubes. *Materials Today Bio* **2020**, 5, 100042.

5. **Haynl, C.**; Vongsvivut, J.; Mayer, K. R. H; Bargel, H.; Neubauer, V. J.; Tobin, M. J.; Elgar, M. A.*; Scheibel, T.* Free-standing spider silk webs of the thomisid *Saccodomus formivorus* are made of composites comprising micro- and submicron fibers. *Scientific Reports* **2020**, 10, 17624.

(6.) Haug, M.&; Reischl, B.&; Prölß, G.; Pollmann, C.; Buckert, T.; Keidel, C.; Schürmann, S.; Hock, M.; Rupitsch, S.; Heckel, M.; Pöschel, T.; Scheibel, T.; **Haynl, C.**; Kiriaev, L.; Head, S. I.; Friedrich, O.* The MyoRobot: A novel automated biomechatronics system to assess voltage/Ca2+ biosensors and active/passive biomechanics in muscle and biomaterials. *Biosensors and Bioelectronics* **2018**, 102, 589-599.

&: gleichwertige Autorenschaft

6 DARSTELLUNG DES EIGENANTEILS

Diese Dissertation umfasst 5 Publikationen, welche am Lehrstuhl Biomaterialien der Universität Bayreuth in Zusammenarbeit mit dem Lehrstuhl Physikalische Chemie I und dem Lehrstuhl Tierphysiologie der Universität Bayreuth, dem Department of Biomedical Engineering und der School of BioSciences der University of Melbourne sowie der Infrared Microspectroscopy Beamline des ANSTO Australian Synchrotron entstanden sind. Die jeweiligen Beiträge der daran beteiligten Personen soll im Folgenden erläutert werden.

Teilarbeit 1

Hofmann, E.; Krüger, K.; **Haynl, C.**; Scheibel, T.; Trebbin, M.; Förster, S.* Microfluidic nozzle device for ultrafine fiber solution blow spinning with precise diameter control. *Lab on a Chip* **2018,** 18, 2225-2234.

Dieses Projekt wurde von Martin Trebbin gestartet und von Stephan Förster betreut. Die Faserspinnversuche mit dem Polymer THV 221 und die Auswertung der Messdaten wurden von Eddie Hofmann durchgeführt. Kilian Krüger führte unterstützende Versuche durch und war an wissenschaftlichen Diskussionen beteiligt. Die Anwendung des hier vorgestellten mikrofluidischen Faserspinn-Verfahrens auf das im Allgemeinen körperverträgliche Biopolymer Polycaprolacton wurde von mir unter Betreuung von Thomas Scheibel etabliert und von Eddie Hofmann hinsichtlich der Prozess-Struktur-Beziehung untersucht. Das Manuskript wurde von Eddie Hofmann angefertigt und durch wissenschaftliche Beiträge seitens Kilian Krüger, Thomas Scheibel, Martin Trebbin, Stephan Förster und mir fertiggestellt.

Teilarbeit 2

Haynl, C.; Hofmann, E.; Pawar, K.; Förster, S.; Scheibel, T.* Microfluidics-produced collagen fibers show extraordinary mechanical properties. *Nano Letters* **2016,** 16, 5917-5922.

Das Design des Mikrofluidik-Chips wurde von Eddie Hofmann übernommen. Die Chips wurden von Eddie Hofmann und mir unter Betreuung von Stephan Förster gefertigt. Die Entwicklung des Kollagenfaserspinn-Verfahrens sowie die Charakterisierung der entstandenen Fasern mittels Lichtmikroskopie, Fourier-Transform Infrarot-Spektroskopie, Zugprüfung und thermischer Analyse wurden von mir unter Betreuung von Thomas Scheibel durchgeführt. Die Rasterelektronenmikroskopie-Abbildungen entstanden unter meiner Verantwortung. Die NG108-15 Zellkultivierung und die Durchführung der Zellfärbungen inklusive der fluoreszenzmikroskopischen Analysen wurden von Kiran Pawar in Absprache mit mir und unter Betreuung von Thomas Scheibel realisiert. Das Konzept dieser Veröffentlichung wurde

von Thomas Scheibel und mir entworfen. Das Manuskript inklusive der Abbildungen wurde von mir erstellt und von Thomas Scheibel überarbeitet. Nach finaler wissenschaftlicher Diskussion mit Eddie Hofmann, Kiran Pawar und Stephan Förster wurde das Manuskript von Thomas Scheibel und mir fertiggestellt.

Teilarbeit 3

Pawar, K.; Welzel, G.; **Haynl, C.**; Schuster, S.; Scheibel, T.* Recombinant spider silk and collagen-based nerve guidance conduits support neuronal cell differentiation and functionality *in vitro*. *ACS Applied Bio Materials* **2019**, 2, 4872-4880.

Kiran Pawar produzierte die elektrogesponnenen Vliesstoffe und führte alle Zellkulturversuche und -auswertungen unter Betreuung von Thomas Scheibel durch. Die Kollagenfasern wurden von mir produziert und für die Zellkulturversuche präpariert. Die Elektrophysiologie-Untersuchungen wurden von Georg Welzel unter Betreuung von Stefan Schuster etabliert, durchgeführt und ausgewertet. Fotographische Darstellungen wurden von Kiran Pawar und mir angefertigt. Rasterelektronenmikroskopische Abbildungen entstanden unter der Verantwortung von Kiran Pawar und mir. Das Manuskript wurde von Kiran Pawar erstellt und von Thomas Scheibel, Georg Welzel und mir überarbeitet sowie von Stefan Schuster wissenschaftlich begutachtet.

Teilarbeit 4

Aigner, T. B.&; **Haynl, C.&**; Salehi, S.; O'Connor, A.; Scheibel, T.* Nerve guidance conduit design based on self-rolling tubes. *Materials Today Bio* **2020**, 5, 100042.

Selbstrollende Filme mit und ohne Modifikation der resultierenden Röhreninnenwand wurden von Tamara Bernadette Aigner hergestellt. Das Herstellungsverfahren von Kollagen-Kryogelen wurde von mir mit Unterstützung von Andrea O'Connor entwickelt. Fotographische und stereomikroskopische Darstellungen wurden von mir generiert. Rasterelektronenmikroskopie-Aufnahmen wurden unter der Verantwortung von Tamara Bernadette Aigner und mir erstellt. Die quantitative Kryogel-Charakterisierung und die Messung mechanischer Eigenschaften wurde von mir durchgeführt. Die Zellkulturexperimente und -auswertungen wurden von Tamara Bernadette Aigner mit Unterstützung von Sahar Salehi durchgeführt. Das Manuskript wurde von Tamara Bernadette Aigner und mir zu gleichen Anteilen erstellt (gleichwertige Autorenschaft) und von Thomas Scheibel wissenschaftlich und konzeptuell überarbeitet sowie von allen Co-Autoren wissenschaftlich kommentiert.

&: gleichwertige Autorenschaft

Teilarbeit 5

Haynl, C.; Vongsvivut, J.; Mayer, K. R. H; Bargel, H.; Neubauer, V. J.; Tobin, M. J.; Elgar, M. A.*; Scheibel, T.* Free-standing spider silk webs of the thomisid *Saccodomus formivorus* are made of composites comprising micro- and submicron fibers. *Scientific Reports* **2020**, 10, 17624.

Das Projekt wurde von Mark Adrian Elgar und Thomas Scheibel initiiert. Die Spinnenseidennetze wurden von Mark Adrian Elgar identifiziert und gesammelt. Fotographische und stereomikroskopische Darstellungen wurden von mir generiert (mit Ausnahme des Fotos zu Abbildung 1a, welches durch Yeldem Koc im Rahmen ihres Forschungspraktikums aufgenommen wurde). Rasterelektronenmikroskopische Abbildungen gingen aus der Zusammenarbeit von Hendrik Bargel und mir hervor. Die Stabilitätsanalyse der Spinnenseide gegenüber chemischen Lösungsmitteln und die Wasserkontaktwinkelmessungen wurden von mir durchgeführt. Die Elementanalyse entstand unter meiner Verantwortung. Die mechanischen und infrarotspektroskopischen Eigenschaften wurden von mir ermittelt. Die Anträge auf Messzeit an der *IRM Beamline* des *Australian Synchrotron* wurden von mir mit Unterstützung von Jitraporn Vongsvivut, Mark Tobin und Thomas Scheibel erstellt. An den Synchrotron-Messungen waren Jitraporn Vongsvivut, Kai Ralph Hermann Mayer, Vanessa Jutta Neubauer, und ich beteiligt. Die Synchrotron-Daten wurden von mir mit Unterstützung von Jitraporn Vongsvivut ausgewertet. Die Ergebnisse der Laborexperimente wurden mit Thomas Scheibel und Mark Adrian Elgar diskutiert. Das Konzept der Veröffentlichung wurde von Thomas Scheibel, Mark Adrian Elgar und mir erstellt. Das Manuskript inklusive aller Abbildungen wurde von mir angefertigt und in Zusammenarbeit mit Thomas Scheibel, Mark Adrian Elgar und Jitraporn Vongsvivut überarbeitet sowie final von allen Co-Autoren kommentiert.

7 TEILARBEITEN

7.1 Teilarbeit 1

Reproduced from

Hofmann, E.; Krüger, K.; **Haynl, C.**; Scheibel, T.; Trebbin, M.; Förster, S.*

Microfluidic nozzle device for ultrafine fiber solution blow spinning with precise diameter control.

Lab on a Chip **2018,** 18, 2225-2234.

DOI: 10.1039/C8LC00304A

with permission from The Royal Society of Chemistry

Lab on a Chip

PAPER

View Article Online
View Journal | View Issue

Cite this: *Lab Chip*, 2018, **18**, 2225

Microfluidic nozzle device for ultrafine fiber solution blow spinning with precise diameter control†

Eddie Hofmann, [ab] Kilian Krüger,[ab] Christian Haynl,[c] Thomas Scheibel,[c] Martin Trebbin [d] and Stephan Förster *[ab]

Received 24th March 2018,
Accepted 31st May 2018

DOI: 10.1039/c8lc00304a

rsc.li/loc

We present a microfluidic nozzle device for the controlled continuous solution blow spinning of ultrafine fibers. The device is fabricated by soft lithography techniques and is based on the principle of a gas dynamic virtual nozzle for precise three-dimensional gas focusing of the spinning solution. Uniform fibers with virtually endless length can be produced in a continuous process while having accurate control over the fiber diameter. The nozzle device is used to produce ultrafine fibers of perfluorinated copolymers and of polycaprolactone, which are collected and drawn on a rotating cylinder. Hydrodynamics and mass balance quantitatively predict the fiber diameter, which is only a function of flow rate and air pressure, with a small correction accounting for viscous dissipation during jet formation, which slightly reduces the jet velocity. Because of the simplicity of the setup, the precise control of the fiber diameter, the positional stability of the exiting ultrafine fiber and the potential to implement arrays of parallel channels for high throughput, this methodology offers significant benefits compared to existing solution-based fiber production methods.

Introduction

Solution blow spinning is a technique that is used to produce micro- and nanofibers.[1,2] Especially ultrafine fibers and nanofibers have widely gained interest because of their unique mechanical properties and high surface to volume ratio, with applications in protective clothing,[3] air filtration,[4] the controlled release of drugs,[5] as wound dressings for skin regeneration,[6] and for tissue engineering.[7–9] Solution blow spinning combines concepts from melt blowing, solution spinning and electrospinning. It makes use of a concentric nozzle with two coaxial channels to inject a polymer solution through the inner channel into a high velocity gas flow from the surrounding outer channel.[1] Pressurized air confines the polymer solution to generate a fine liquid jet. During jetting, the solvent evaporates and a solid polymer fiber forms which can be collected on a target.[1]

As the main parameters, which influence the spinning process, are very similar for solution blow spinning and electrospinning, the micro- and nanofibers produced by these two techniques are equivalent in size and morphology.[1] Electrospinning uses electrostatic forces, while solution blow spinning uses pressurized gas to generate a liquid jet.[10] Surface tension is the main driving force for jet instability and breakup. It reduces the surface area per unit mass by transforming the jet into spherical droplets with a smaller overall surface area.[11] Conversely, viscosity resists rapid changes in shape, so that an increasing viscosity slows down the deformation and breakup of the polymer jet and thus favors formation of continuous fibers.[11] The viscosity of polymer solutions is strongly influenced by both concentration and molecular weight which affect the number of chain entanglements.[12] The entanglement number eventually determines whether a spray, a spindle-knotted fiber or a uniform fiber is obtained.[12] Further, a solvent with high vapor pressure is necessary as during fast solvent evaporation there is less time for flow instabilities to develop that deform the jet while spinning. For electrospinning specific additional parameters are the electric voltage and the net charge density, whereas for solution blow spinning flow rate and air pressure define fiber diameter and morphology.[1,13,14]

[a] *Department of Physical Chemistry I, University of Bayreuth, 95440 Bayreuth, Germany*
[b] *Jülich Centre for Neutron Science (JCNS-1/ICS-1), Forschungszentrum Jülich GmbH, 52425 Jülich, Germany. E-mail: s.foerster@fz-juelich.de; Fax: +49 2461 61 2610; Tel: +49 2461 61 85161*
[c] *Department for Biomaterials, University of Bayreuth, 95440 Bayreuth, Germany*
[d] *Centre for Ultrafast Imaging (CUI), University of Hamburg, 22761 Hamburg, Germany*

† Electronic supplementary information (ESI) available: Video of fiber spinning, slow-motion video of jet exiting the nozzle, calculation details, practical guide. See DOI: 10.1039/c8lc00304a

Solution blow spinning is an inexpensive technique that can be realized in a simple and compact setup. Compared to electrospinning, a higher rate of fiber production is possible, and there are fewer restrictions on the electrical properties of the polymer solution such as conductivity and dielectric constant.[1,15,16] Scaling-up by the use of multiple nozzles is possible, and the method has already demonstrated unique possibilities as for the fabrication of non-woven meshes that can be directly formed on tissue cultures or living tissue,[15] or for the coating of the internal side of tubular vascular prosthesis.[17]

Electrospinning has gained wide attention due to its versatility in spinning a large variety of polymeric fibers,[18] such that the influence of solution properties, electric potential and spinning parameters have already been well investigated.[13,14,19–24] Since solution blow spinning is a much younger technique, there are much fewer studies dealing with the prediction and control of fiber diameter and morphology.[1,25–27] Oliveira *et al.* showed a strong influence of flow rate, air pressure, concentration and viscosity,[1] whereas Wojasiński *et al.* did not observe any influence of processing parameters other than solution concentration in their study.[26] Sinha-Ray *et al.* developed a complex theoretical model of the solution blowing process showing that reasonable agreement with the experimental data could be observed for the predicted fiber-size distribution.[28] Thus, there still is a considerable lack of knowledge to predict and control the fiber diameter in solution blow spinning, and experimental results are partially contradicting.[1,15,26–30]

Microfluidic technology has not yet been used for solution blow spinning. The key element of the spinning process is the nozzle, for which microfluidic technology offers the possibility to use design principles based on the gas dynamic virtual nozzle-principle (GDVN) which would for the first time allow a precise control of the jet and thus the fiber diameter. The physics of the GDVN-principle to generate capillary jets was developed by Gañán-Calvo *et al.* This study used a simple plate-orifice geometry to create liquid jets and formulated a predictive model for the jet diameter.[31,32] In the model, the pressure difference imposed in axial direction, transmitted to the liquid stream by normal surface stress, is converted into kinetic energy to accelerate the fluid. With the assumption that viscous and capillary forces are sufficiently small compared to the liquid inertia, the jet diameter can be calculated in very good approximation.[33] The nozzle shape determines the boundaries of the stability and can be used to decrease jet diameters.[10] While Gañán-Calvo *et al.* started their investigations with the plate-orifice geometry,[31,33,34] later on, the converging–diverging nozzle made of glass capillaries was examined,[10,35] and Trebbin *et al.* developed a microfluidic nozzle device for generating liquid jets.[36]

Here we demonstrate that microfluidic nozzle devices based on the GDVN-principle can be used for continuous solution blow spinning with excellent prediction and control of the fiber diameter. The microfluidic device was made of poly(dimethylsiloxane) (PDMS), which enabled a fast and easy reproduction by replica molding. In an alteration of Trebbin *et al.*'s nozzle design,[36] the air flow focuses the polymer solution from an orthogonal direction. We demonstrate continuous stable spinning conditions at rates of 5–10 m s^{-1} for perfluorocopolymer and polycaprolactone solutions to produce ultrafine fibers with endless length and narrow size distribution. Thus, for the first time the fiber diameter can be precisely controlled by air pressure and solution flow rate in very good agreement with theoretical predictions, which now enables a rational, controlled and reproducible fabrication of endless fibers of the desired diameter by solution blow spinning.

Results and discussion

Fabrication and design of the nozzle device

The microfluidic nozzle devices for fiber spinning were fabricated by using established photolithography and soft lithography techniques.[37–40] In the first step of this sequence, a microstructured master was created which acted as a molding template for poly(dimethylsiloxane) (PDMS) subsequently. Multiple microfluidic chips could be produced from one single PDMS cast, which was divided into individual parts. After cutting, punching inlet ports and thorough cleaning with propan-2-ol, two matching parts were treated with air plasma, aligned accurately and permanently bonded. A schematic overview of the fabrication process is shown in Fig. 1. The final microfluidic chip contained a nozzle array with four separate nozzles side by side. Each nozzle had two inlet ports. One was connected to pressurized air, whereas the other was connected to a syringe pump containing the polymer solution.

As shown previously,[36] the GDVN-principle can be well used to focus a polymer solution into a liquid jet and encase it with a high-velocity air flow. In contrast to solution blow spinning with a concentric nozzle,[15] the inner nozzle, delivering the polymer solution, is not protruding with respect to the outlet of the compressed air. Within the microfluidic nozzle, the air stream is approaching perpendicularly from the sides. To ensure a complete three-dimensional focusing from every direction, also from above and below, the nozzle design is composed of multiple stacked layers to mimic a concentric nozzle. Therefore, two individually structured PDMS halves need to be combined into one microfluidic nozzle device. A precise alignment of these two parts is crucial for accurate nozzle geometry, but can easily be accomplished by integrated orientation structures, which hold both halves in place. The multi-layer architecture of the microfluidic nozzle device is shown in Fig. 2, where all relevant design parameters, listed in Table 1, are also depicted.

The nozzle design can easily be adapted, since master fabrication is a rapid prototyping process. In combination with PDMS, replica molding has a high reproducibility because the same master can be used repeatedly. As all nozzles are almost identical and also fast and simple to produce using soft lithography, the microfluidic chips are disposable consumables. The use of PDMS as chip material has benefits like transparency in UV-visible regions, compatibility with aqueous and polar solvents and chemical inertness.[41] However, if polar solvents are used, the PDMS needs a surface modification or coating.[42]

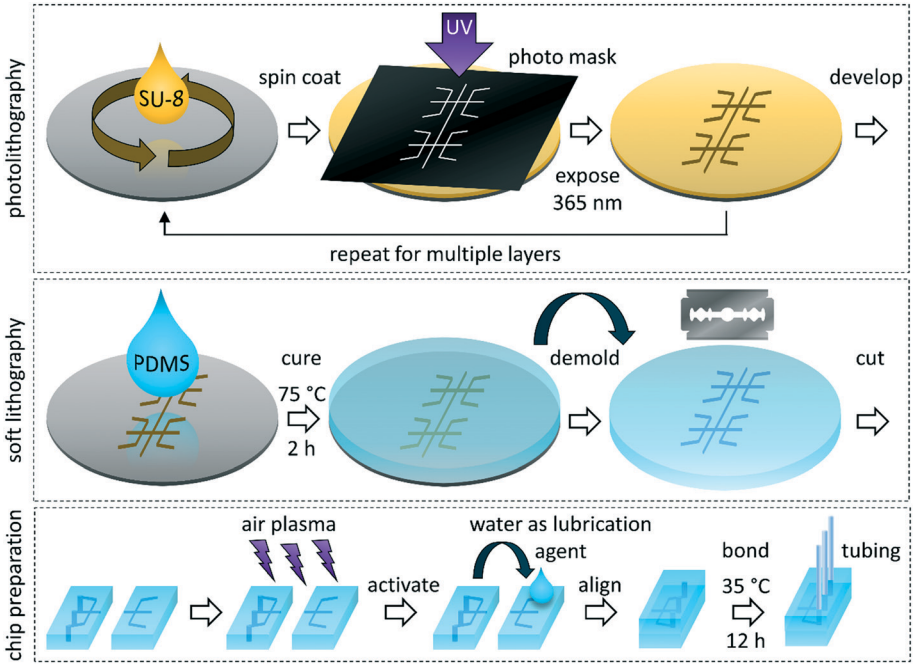

Fig. 1 Microfluidic nozzle devices for solution blow spinning are fabricated by using standard photolithography and soft lithography techniques. At first, a structured master is produced, which acts as a casting template for polydimethylsiloxane (PDMS). After curing, a microfluidic device is prepared by bonding two precisely tailored PDMS halves. Water is used as a lubrication agent to facilitate the precise alignment.

Spinning process and sample collection

In order to quantitatively investigate the conditions for continuous solution blow spinning, a reliable and steady jetting of the polymer solution was necessary. For this study, a special grade perfluorocopolymer (THV 221 from 3M Dyneon, abbreviated as THV) was used, which is soluble in acetone because of the relatively high amount of vinylidene fluoride.[43,44] Due to its fluorinated components, THV has great non-sticking properties to PDMS, which leads to a very stable spinning process. Acetone is well-suited as a solvent because of the high vapor pressure (240 hPa at 20 °C).[45] This results in a high evaporation rate of the solvent from the jetted polymer solution preventing jet instabilities to develop, which would lead to non-uniform fibers or alternatively to spraying or to discontinuous fibers. For comparison, a poly(caprolactone) (PCL) solution was spun using the microfluidic device in a similar manner but with hexafluoroisopropanol (HFIP) as a solvent.

High-precision syringe pumps were used to ensure a constant flow rate Q of the spinning solution. The pressure difference Δp between the compressed air and atmospheric pressure was adjusted by a pressure controller with a manometer. Employing suitable values for these parameters, uniform fibers could be produced by jetting the polymer solution out of the nozzle device in a steady process. While jetting through the air for a certain distance, the solvent evaporates, the fiber solidifies and could be collected on a cork spool. Both the working distance d_s between the nozzle and the spool and the rotational speed of the spool were adjustable. By changing the rotational speed, different drawing speeds v_s could be applied during the spinning process. Fig. 3 shows the spinning process (3A) and the setup for sample collection (3B). The jetted fiber exits in a very narrow cone of only a few degrees and can be collected on a spool, where it forms a strand of parallel fibers forming a torus (Fig. 3C). All fiber samples were investigated by scanning electron microscopy (SEM) to determine the quadratic mean (root mean square, RMS) and the standard deviation (SD) of the fiber diameter by evaluating multiple images statistically (see ESI†).

Under stable spinning conditions, continuous fibers of ~2.3 km length (5 min) and of narrow size distribution could be produced. The histogram in Fig. 4D confirms the narrow size distribution. The evaluation of 368 single fibers resulted in a mean diameter of 2.1 ± 0.3 μm for the following processing parameters: Q = 1.0 mL h^{-1}, Δp = 2.0 bar, v_s = 7.7 m s^{-1}, d_s = 8 cm, 20% (w/w) THV in acetone.

This successful application of a microfluidic nozzle design for the continuous production of fibers could, in principle, be extended to bio-based nanofibrils which have recently been demonstrated to be a promising material in fiber spinning technology.[46] This would only require a flow-focusing section prior to the gas virtual nozzle section, which has been recently demonstrated.[36]

Surface structure of fibers

The SEM images also reveal the morphology and surface structure of the THV fibers for all different sets of parameters. In Fig. 4A, the fiber sample is collected as a non-woven

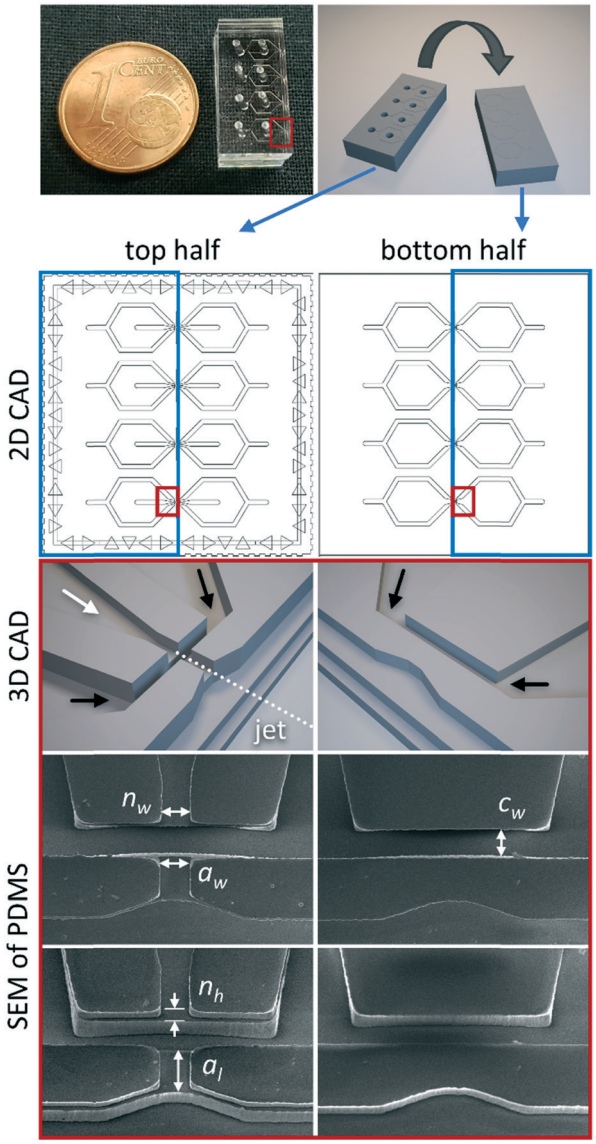

Fig. 2 The microfluidic device contains an array of four identical nozzles. Each nozzle is constructed with multiple layers on two individually structured halves, which need to be aligned precisely. Only this multi-layer architecture enables a complete three-dimensional focusing of the spinning solution by a surrounding air flow. Black arrows indicate the inlets of the pressurized air and a white arrow denotes the inlet of the polymer solution. Relevant design parameters are indicated in the SEM images of the nozzle (also see Table 1).

mesh on a plate, and in Fig. 4C as a strand of fibers on a spool. As shown in Fig. 4B, the fiber surface texture exhibits

Table 1 List of relevant design parameters for the nozzle layout along with the target size in CAD software and the actually measured size in SEM

Parameter	Target size	Measured size (SEM)
Nozzle width n_w	30 μm	32 μm
Nozzle height n_h	30 μm	28 μm
Air channel width c_w	30 μm	34 μm
Aperture width a_w	30 μm	31 μm
Aperture length a_l	50 μm	45 μm

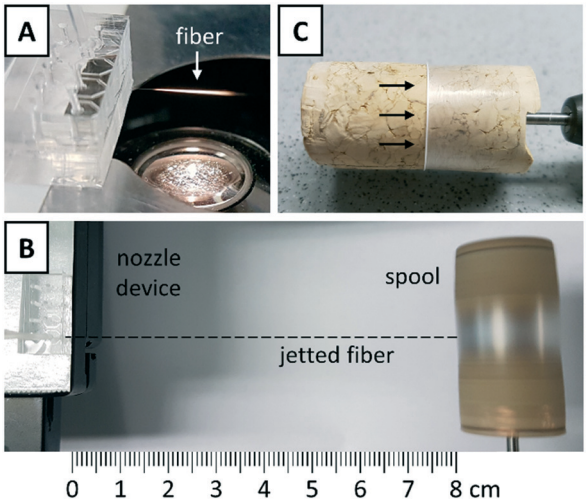

Fig. 3 Photos illustrating the process of spinning and collection of the fiber samples. The polymer solution is jetted out of the microfluidic device (A). While the jet travels through the air, the solvent is evaporating, and a solid fiber is forming, which is collected on a rotating cork spool (B). Afterwards, the fibers are bundled into a strand by carefully pushing them together (C).

small cavities with almost circular shape which emerge during solvent evaporation through the outer shell of the fiber, similarly as for electrospun fibers. Fibers with smooth surfaces are obtained when using solvents with lower vapor pressure. Fig. 5A shows an example of a fiber with smooth surface structure, which was spun from a 20% (w/v) solution of poly(caprolactone) (PCL) in hexafluoroisopropanol (HFIP).

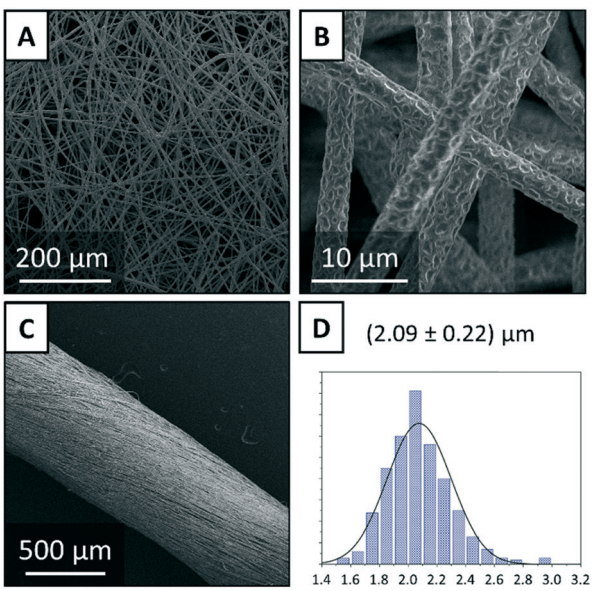

Fig. 4 SEM images of a non-woven mesh collected on a plate (A) and close-up image of the surface structure of the fiber (B) for 2.0 mL h^{-1}, 2.0 bar, 8 cm, 20% (w/w) THV in acetone, 3.7 ± 0.7 μm; strand of fibers after collection on a spool (C) and histogram showing the distribution of fiber diameters (D) for 1.0 mL h^{-1}, 2.0 bar, 7.7 m s^{-1}, 8 cm, 20% (w/w) THV in acetone, 2.1 ± 0.2 μm.

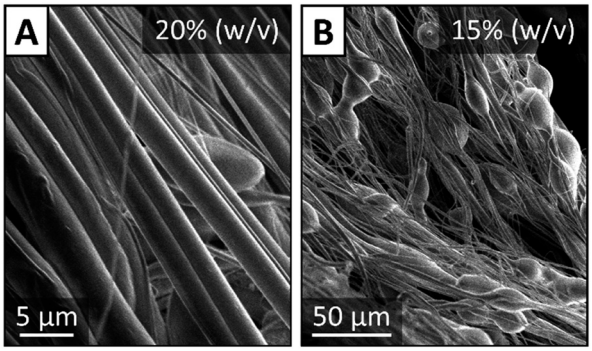

Fig. 5 Different morphologies of polycaprolactone fibers that can be achieved: SEM image of (A) smooth fiber (0.5 mL h^{-1}, 2.5 bar, 5.5 m s^{-1}, 10 cm, 20% (w/v) PCL in HFIP, 2.3 ± 1.1 µm) and (B) spindle-knotted fiber (1.0 mL h^{-1}, 2.0 bar, 10.3 m s^{-1}, 10 cm, 15% (w/v) PCL in HFIP).

Using a 15% (w/v) solution of PCL in addition to the slower evaporation rate caused by the lower vapor pressure of HFIP of 160 hPa (20 °C)[47] leads to a varying fiber diameter showing spindle-knotted fiber morphology (Fig. 5B) since there is more time for jet instabilities to develop. In general, as for electrospun fibers, spindle-knotted fibers could be useful for water collection in technical processes.[48–50] As a remedial measure, the overall evaporation time can be reduced by generating smaller jets which reduces the diffusion distance or by increasing the temperature. When the drawing speed was increased, the cavities on the THV fibers became more elongated, confirming that the fiber is stretched during jetting while forming between nozzle and spool.

Control of fiber diameter

A major aim of our investigation was to quantify the influence of the main spinning parameters on the fiber diameter to develop a fundamental understanding of the spinning process, and to establish a precise prediction of the fiber diameter. Therefore, an equation for calculating the fiber diameter d_f was derived, based on the conservation of volume of the THV polymer in the spinning solution and the final fiber.

The fiber diameter is only depending on the flow rate Q, the fiber velocity v_f and the volume fraction of THV ϕ_T in the polymer solution. A detailed derivation of eqn (1) can be found in the ESI.†

$$d_f = \sqrt{\frac{4 \cdot \phi_T \cdot Q}{\pi \cdot v_f}} \tag{1}$$

For a given polymer solution with a certain concentration, the fiber diameter is only proportional to $Q^{1/2}$ and $v_f^{-1/2}$. The velocity of the fiber v_f is supposed to be equal to the velocity of the jet v_j, which is determined by the pressure drop Δp of the compressed air. Alternatively, if the drawing speed v_s applied to the fiber by the rotating spool is even faster, the final diameter is determined by the drawing speed while collecting the fiber.

$$v_f = \begin{cases} v_j, & \text{if } v_j \geq v_s \\ v_s, & \text{if } v_j < v_s \end{cases} \tag{2}$$

A connection between the jet velocity v_j and the pressure difference Δp can be established by Bernoulli's equation for incompressible flows by comparing the two states inside the nozzle and inside the liquid jet.

$$v_j = \sqrt{\frac{2 \cdot \Delta p}{\rho_0}} \tag{3}$$

Eqn (3) shows, that the velocity increases in proportion to $\Delta p^{1/2}$. If we assume that the acceleration of the jet and the evaporation of the solvent happen successively, the mass density ρ_0 of the polymer solution stays constant while the jet is accelerated. We note that in this consideration, the loss of kinetic energy due to viscous dissipation and shear stress is neglected.[31] As a result, eqn (4) connects the fiber diameter to the pressure difference, showing a proportionality of $\Delta p^{-1/4}$.

$$d_f = \left(\frac{8 \cdot \rho_0 \cdot \phi_T^{\,2} \cdot Q^2}{\pi^2 \cdot \Delta p} \right)^{1/4} \tag{4}$$

Gañán-Calvo postulated an equation for the diameter of a jet d_j in the plate-orifice geometry using the GDVN-principle.[31] Trebbin *et al.* showed that this model can also be applied to microfluidic nozzle devices.[36]

$$d_j = \left(\frac{8 \cdot \rho_0}{\pi^2 \cdot \Delta p} \right)^{1/4} \cdot Q^{1/2} \tag{5}$$

The comparison between eqn (4) and (5) illustrates that the fiber diameter differs just by the term $\sqrt{\phi_T}$ from the Gañán-Calvo[31] equation for the jet diameter. The factor $\sqrt{\phi_T}$ takes account of the evaporation of the solvent causing the shrinkage in diameter.

$$d_f = \sqrt{\phi_T} \cdot d_j \tag{6}$$

The main spinning parameters were varied systematically to verify the proportionalities of flow rate, pressure difference and drawing speed. Therefore, different combinations for a 20% (w/w) solution of THV 221 in acetone were tested with flow rates between 1.0 mL h^{-1} and 4.0 mL h^{-1} and the drawing speed ranging from 5.5 m s^{-1} to 15.5 m s^{-1} at a constant pressure difference of 2.0 bar and a working distance of 8 cm. Additionally, the flow rate and the air pressure were varied between 1.0 mL h^{-1} and 3.0 mL h^{-1}, respectively between 1 bar and 2.5 bar at a constant drawing speed of 7.7 m s^{-1} and a working distance of 8 cm. The fiber diameter was ranging from 1.6 µm to 4.2 µm, as shown in Fig. 6.

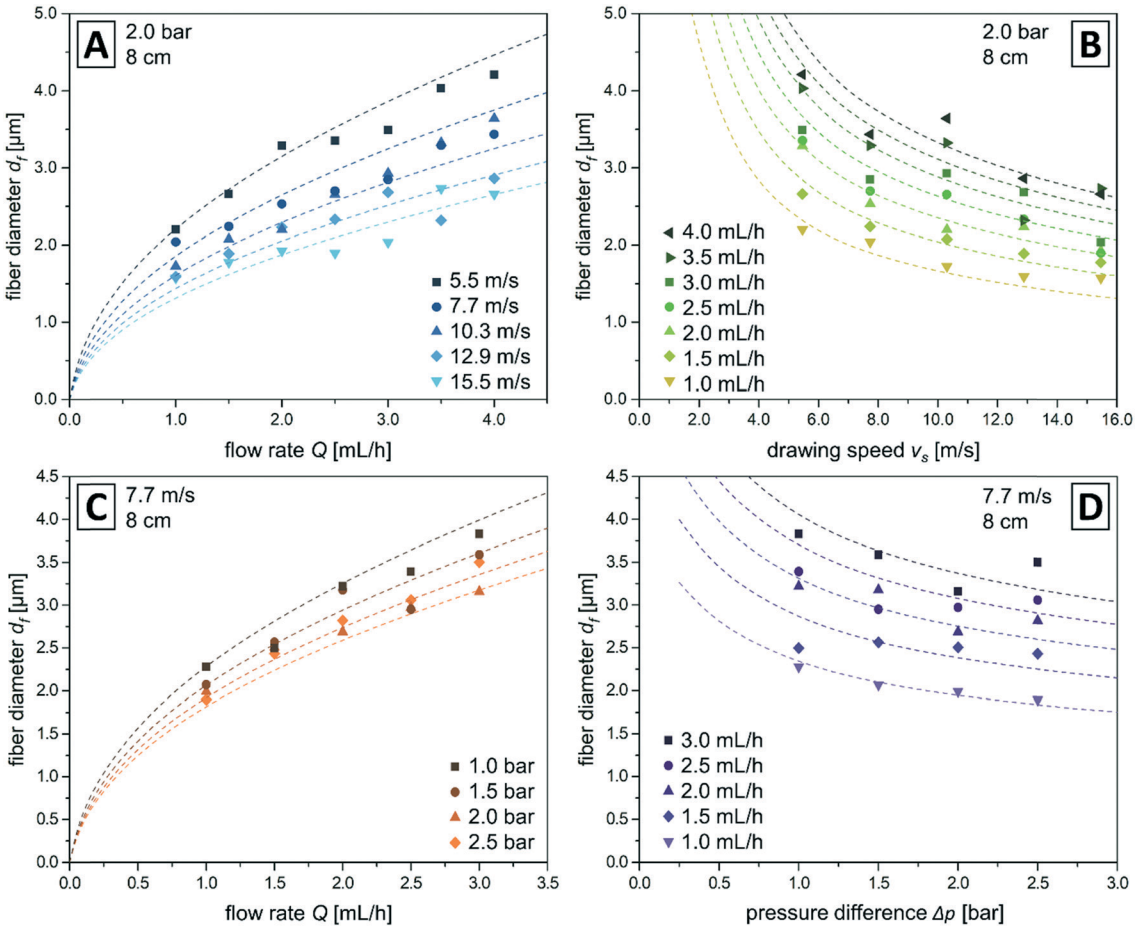

Fig. 6 Graphs showing the mean diameter of the THV fiber samples as a function of the investigated process parameters (flow rate (A and C), drawing speed (B) and pressure difference (D)). Dashed lines indicate the predicted fiber diameters according to eqn (7) and (8).

When performing a linear regression with the logarithmic values of the fiber diameter and the varied process parameter, the slope should be equivalent to the exponent of the corresponding parameter. The values for the linear regression are summarized in Table 2. The experimentally determined exponents coincided very well with the postulated power laws in eqn (1) and (4). This confirms that the assumed correlations are correct.

We noted above that the loss of kinetic energy due to viscous dissipation and surface tension were neglected in the derivation of eqn (1) and (4). In this light we introduced a factor f_{BC} for the fiber diameter derived in eqn (1), and a factor f_{AD} in eqn (4) to account for systematic deviations between calculated and measured fiber diameters.

$$d_f = f_{BC} \cdot \sqrt{\frac{4 \cdot \phi_T \cdot Q}{\pi \cdot v_f}} \quad (7)$$

$$d_f = f_{AD} \cdot \left(\frac{8 \cdot \rho_0 \cdot \phi_T^2 \cdot Q^2}{\pi^2 \cdot \Delta p} \right)^{1/4} \quad (8)$$

The values of the parameters were determined by linear regression with the slopes fixed to the theoretical values. As shown in Table 2 we thus obtained values of $f_{BC} = 0.91 \pm 0.04$ and $f_{AD} = 1.55 \pm 0.08$. The correction factor f_{BC} for $d_f(Q, v_f)$ is close to 1, confirming the excellent applicability of eqn (1), which is based on the conservation of volume.

The graphs in Fig. 6 show a very good agreement between the measured fiber diameters and the calculated values from eqn (7) and (8). The determined exponent of Δp deviates moderately from the theoretical one of −0.25. We note that the drawing speed v_s can only be used for the fiber velocity v_f, if it is faster than the velocity of the jet exiting v_j the nozzle. In this experiment, this is valid for all tested drawing speeds except the slowest one with 5.5 m s^{-1}. The jet velocity at the pressure difference of 2.0 bar is 6.1 m s^{-1} as shown with a high-speed camera (see Fig. 8).

In contrast, when calculating the fiber diameter $d_f(Q, \Delta p)$ with eqn (4), based on pressure difference and flow rate, the fiber diameter is around 1.55-times larger than the expected one. A larger fiber diameter is an indication for a slower jet and fiber velocity. As a consequence, the specific internal energy is not completely converted into specific kinetic energy and the jet is less accelerated. The finite energy loss due to viscous dissipation of the polymer solution is determined in the subsequent section.

Table 2 Results for the linear regressions of the fiber diameter support the power laws for the correlation with the tested processing parameters

	First linear regression		Second linear regression	
Equation	Expected slope	Calculated slope	Correction term	Correction factor
$\log d_f = \log C + \log Q$	$c = +0.5$	0.43 ± 0.07	$\log f_{BC} = -0.041 \pm 0.019$	$f_{BC} = 0.91 \pm 0.04$
$\log d_f = \log B - \log v$	$b = -0.5$	0.42 ± 0.05		
$\log d_f = \log D + d \times \log Q$	$d = +0.5$	0.48 ± 0.05	$\log f_{AD} = 0.192 \pm 0.022$	$f_{AD} = 1.55 \pm 0.08$
$\log d_f = \log A - a \times \log \Delta p$	$a = -0.25$	−0.13 ± 0.07		

Measurement of jet diameter

If there is an incomplete conversion of specific internal energy to specific kinetic energy, the measured jet diameters should be systematically larger than the calculated ones. Therefore, the jet diameter was investigated by optical microscopy and the results are reported in Fig. 7. The same trend as for the fiber diameter could be observed, which is shown by the graph in Fig. 7.

$$d_j = f_j \cdot \left(\frac{8 \cdot \rho_0 \cdot Q^2}{\pi^2 \cdot \Delta p} \right)^{1/4} \quad (9)$$

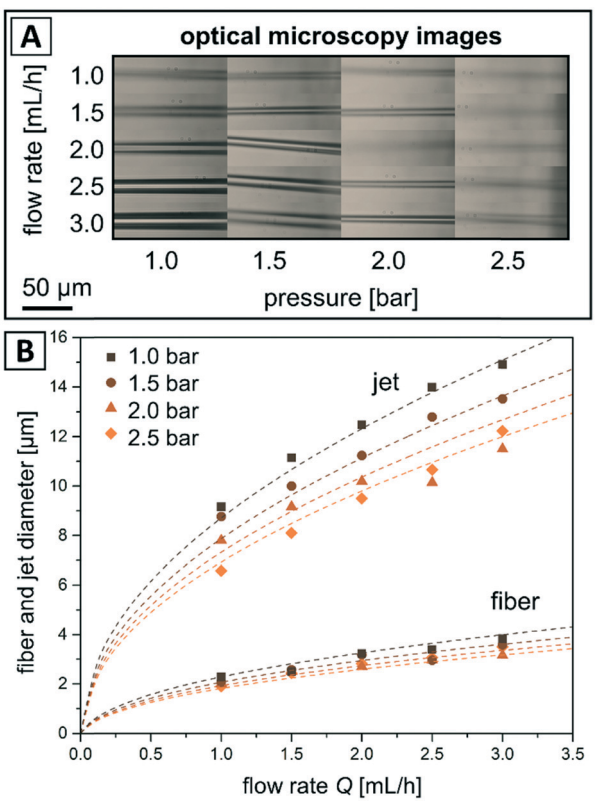

Fig. 7 Jet diameter of a 20% (w/w) THV solution measured directly after passing the nozzle at varied flow rates and pressure differences. The diameters of the jet and the fiber exhibit the same correlation, since both differ just in the factor $\sqrt{\phi_T}$ due to evaporation of the solvent. Images of the jet from optical microscopy (A); graph showing measured values (B) and predictions according to eqn (8) and (9) as dashed lines.

As expected, a correction factor f_j in eqn (9) was necessary to scale the jet diameter in eqn (5) appropriately. The correction factor $f_j = 1.79 \pm 0.10$ is close to the corresponding one f_{AD} for the fiber diameter.

Measurement of fiber velocity

Using a high-speed camera, the velocity of the polymer solution inside the nozzle v_n and the velocity of the polymer jet v_j could be measured directly. Therefore, an aqueous dispersion of polystyrene particles was pumped through the microfluidic device to determine v_n by measuring the travel distance of multiple particles between two images at a frame rate of 37 004 fps. The determined velocity of 0.273 m s^{-1} is equal to the velocity of 0.268 m s^{-1}, which can be calculated by dividing the flow rate (1.0 mL h^{-1}) by the cross section of the nozzle (1037 µm^2). The measurement of the jet velocity v_j was performed with the THV solution, complying exactly with the spinning conditions for sample collection. Infrequently occurring beads in the jet were used to calculate the jet velocity of 6.13 m s^{-1} (see Fig. 8B). This measured velocity is also equal to the expected velocity for a jet with a diameter of 7.6 µm at 1 mL h^{-1}. In conclusion, it could be shown by using a high-speed camera that the jet velocity can be calculated by

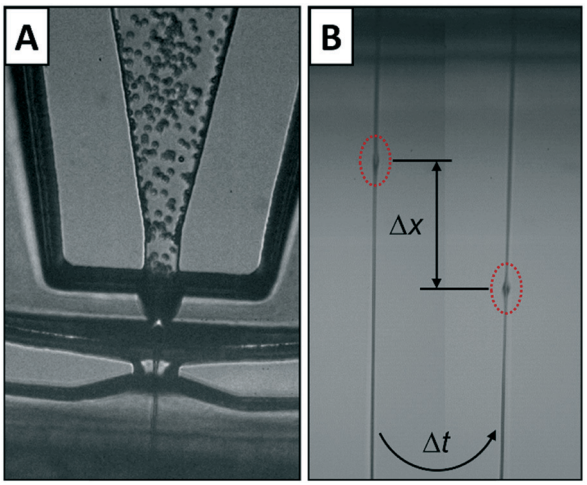

Fig. 8 The velocity of the stream (1 mL h^{-1}, 2 bar) was measured inside the nozzle by tracking of polymer particles (A) or inside the jet by following occasional beads (B) with a high-speed camera (frame rate: 37 004 fps (A); 31 019 fps (B)).

dividing the flow rate by the cross-sectional area. This confirms that the jet velocity is slower than expected in eqn (3).

Influence of other working parameters

As shown above the fiber diameter is completely determined by the flow rate Q and the pressure difference Δp, with a slight correction to account for viscous dissipation which reduces the velocity v_j of the jet exiting the nozzle. We additionally examined the influence of the distance d_s between the nozzle and the spool, which showed that the spool needs be positioned beyond a certain distance from the nozzle to allow for sufficient solvent evaporation to obtain fully developed fibers. Furthermore, we studied the influence of polymer concentration. In order to generate continuous fibers, the concentration needs to be in a range where it is sufficiently large to obtain continuous fibers, but still being low enough to have a viscosity where the solution can be pumped through the central channel. Finally, also conditions for narrow fiber diameter distributions were determined. Details of these additional studies are given in the ESI.†

Conclusion

In conclusion, we present a microfluidic nozzle device for solution blow spinning of ultrafine fibers offering significant benefits compared to existing approaches. Using the gas dynamic virtual nozzle-principle, uniform fibers with virtually endless length can be produced in a steady process while having precise control over fiber diameter and morphology. The fiber diameter can be quantitatively predicted and depends only the flow rate and air pressure, with a small correction accounting for viscous dissipation which reduces the jet velocity. Thus, for the first time the fiber diameter can be precisely controlled by air pressure and solution flow rate in very good agreement with theoretical predictions, which now enables a rational, controlled and reproducible fabrication of endless fibers of the desired diameter by solution blow spinning. Because of the simplicity of the setup, the positional stability of the exiting ultrafine fiber and the potential to implement arrays of parallel channels for high throughput this methodology is a versatile alternative to established solution-based fiber production methods.

Materials and methods

Photolithographic master fabrication

By using photolithography, a microstructured master was produced and afterwards cast with poly(dimethylsiloxane) (PDMS). The whole procedure of fabricating microfluidic devices with multi-layered channel structures is shown in Fig. 1. At first, the desired microfluidic nozzle structures were designed with AutoCAD (Autodesk Inc.) and printed on a high-resolution film photomask by JD Photo Data. The following steps were performed in a clean room. A 3″ silicon wafer was spin-coated (Cee 200X, Brewer Science Inc.) with a negative photoresist (SU-8 25 and SU-8 50, MicroChem Corp.). The structures on the photomask were transferred to the photoresist by exposing this thin layer of SU-8 through the photomask and hereby cross-linking the photoresist at the exposed areas. For this purpose, a contact mask aligner MJB4 (SÜSS MicroTec SE) with UV light of 365 nm was used. The previous steps of spin-coating and exposure were repeated to build up two additional layers. Precise alignment of photomask and substrate was necessary. In the subsequent development step, the uncured photoresist was removed with 1-methoxy-2-propanyl acetate (mr-Dev 600, micro resist technology GmbH). The resulting lithography master featured the channel design as inverted microstructure. The values of all geometric design parameters, which are shown in Fig. 2, are listed in Table 1.

PDMS device fabrication

The following steps of soft lithography and finalization of the microfluidic device were performed in a dust-free environment. For replication of the micro-structured master, a 10 : 1 mixture (monomer : curing agent) of PDMS (Sylgard 184 kit, Dow Corning Corp.) was poured onto the microstructured master, degassed and cured for 2 h at 75 °C. After demolding, the PDMS replica was cut with a razor blade along predefined grooves into individual parts. For later connection of the tubing, inlet ports were punched into the PDMS with an Integra® Miltex® biopsy punch with plunger (1 mm, Integra LifeSciences Corp.).

Two individual structured halves had to be combined, to create a 3D nozzle device. Therefore, the surfaces of two matching halves of PDMS were activated using air plasma (MiniFlecto®, plasma technology GmbH). In addition, a small drop of ultrapure water (Milli-Q, Merck KGaA) was added to generate a thin film of water, which enabled the alignment of the two individual parts prior to the final bonding. Bringing both parts in close contact allowed the integrated orientation structures to snap in and align the microstructures automatically. If necessary, fine adjustments were performed under a microscope. Removing the water in an oven at 35 °C for 12 h resulted in a permanent bonding of the microfluidic device.

Spinning solution

Microfluidic solution blow spinning requires a polymer solution with a volatile solvent. For most experiments, a 20% (w/w) polymer solution of 3M™ Dyneon™ THV 221GZ (3M Deutschland GmbH) in acetone was used. THV is a flexible and transparent fluoroplastic composed of tetrafluoroethylene, hexafluoropropylene and vinylidene fluoride. Acetone has a high vapor pressure of 240 hPa (20 °C),[44,45] which results in a fast evaporation rate of the solvent from the jetted solution. In addition, a solution of poly(caprolactone) (M_w = 45 000 g mol^{-1}, Sigma Aldrich Chemie GmbH) in hexafluoro-2-propanol, which has a vapor pressure of 160 hPa (20 °C),[47] was tested.

Microfluidic solution blow spinning and sample collection

The microfluidic nozzle device was connected *via* LDPE tubing (0.38 mm I.D., 1.09 mm O.D., Science Commodities Inc.) to a syringe pump (neMESYS 290N, Cetoni GmbH) and pressurized air. The spinning solution was filled into glass syringes (1.0 mL, Gastight 1000 Series, Hamilton Company) for precise pumping at flow rates between 0.5 mL h^{-1} and 4.0 mL h^{-1} and at constant air pressures between 0.5 bar and 2.5 bar. For the start-up procedure, the pressurized air was connected first and set to the desired value. Subsequently, the flow of the spinning solution was started, and the tubing plugged into the nozzle device to start the spinning process. The fiber spinning was conducted at ambient conditions of 23 °C room temperature and a relative humidity in the range of 45–55%. The spinning process was examined with an inverted optical microscope (IX71 and IX73, Olympus Corp.) and in combination with a DSLR camera (D7000, Nikon) high resolution images of the jetted spinning solution were taken.

Fiber samples were collected by means of a cork cylinder on a rotary tool (Proxxon GmbH), which was mounted in an adjustable distance to the nozzle device. The rotational speed was monitored with an optical revolution counter (UT372, UNI-T) and could be changed steplessly. Thus, it was possible to apply different drawing speeds to the fiber while collecting the sample. The drawing speed could be calculated from the rotational speed by using the perimeter of the cork cylinder (61.8 mm). The benefit of using a cork spool was that the fibers didn't adhere to it. After a predefined collection time, the spooled fiber was carefully pushed together to form a strand of fibers.

From each fiber sample, several representative images were taken with a scanning electron microscope (JSM-6510LV, JEOL GmbH) and statistically analyzed with ImageJ software (National Institutes of Health) to determine the quadratic mean of the fiber diameter (root mean square) and the standard deviation.

Velocity measurement with high-speed cinematography

The liquid jet of spinning dope exited the nozzle at a very high velocity in relation to its small scale. This fast process could only be observed by a high-speed camera (Phantom v1610, Vision Research Inc.). A highly intense, focused light source (halolux LED-30, STREPPEL Glasfaser-Optik GmbH & Co. KG) was used to get sufficient light for short exposure times down to 2 μs. In combination with a long-distance microscope (Model K1 CentriMax™, Infinity Photo-Optical Company) and a UPlanFL N 10×/0.30 objective (Olympus Corporation) the setup allows to measure the velocity of the solution inside the nozzle and the velocity of the jet directly after the nozzle outlet. The flow inside the nozzle was tracked using monodisperse polystyrene particles in aqueous dispersion (4.89 μm, SD = 0.08 μm, microParticles GmbH).

Conflicts of interest

There are no conflicts to declare.

Acknowledgements

We thank the European Research Council for financial support within the ERC Advanced Grant project STREAM (#291211). We also thank 3M for providing the fluoropolymers.

References

1 J. E. Oliveira, E. A. Moraes, R. G. F. Costa, A. S. Afonso, L. H. C. Mattoso, W. J. Orts and E. S. Medeiros, *J. Appl. Polym. Sci.*, 2011, **122**, 3396–3405.
2 R. M. D. C. Farias, R. R. Menezes, J. E. Oliveira and E. S. de Medeiros, *Mater. Lett.*, 2015, **149**, 47–49.
3 Z.-M. Huang, Y.-Z. Zhang, M. Kotaki and S. Ramakrishna, *Compos. Sci. Technol.*, 2003, **63**, 2223–2253.
4 E. Scholten, L. Bromberg, G. C. Rutledge and T. A. Hatton, *ACS Appl. Mater. Interfaces*, 2011, **3**, 3902–3909.
5 F. Sharifi, A. C. Sooriyarachchi, H. Altural, R. Montazami, M. N. Rylander and N. Hashemi, *ACS Biomater. Sci. Eng.*, 2016, **2**, 1411–1431.
6 M. Mirjalili and S. Zohoori, *J. Nanostruct. Chem.*, 2016, **6**, 207–213.
7 C. A. Martínez-Pérez, I. Olivas-Armendariz, J. S. Castro-Carmona and P. E. García-Casillas, in *Advances in regenerative medicine*, ed. S. Wislet-Gendebien, Intech, Rijeka, 2011.
8 R. Vasita and D. S. Katti, *Int. J. Nanomed.*, 2006, **1**, 15–30.
9 Q. P. Pham, U. Sharma and A. G. Mikos, *Biomacromolecules*, 2006, **7**, 2796–2805.
10 A. J. Acero, C. Ferrera, J. M. Montanero and A. M. Gañán-Calvo, *J. Micromech. Microeng.*, 2012, **22**, 65011.
11 H. Fong, I. Chun and D. H. Reneker, *Polymer*, 1999, **40**, 4585–4592.
12 S. L. Shenoy, W. D. Bates, H. L. Frisch and G. E. Wnek, *Polymer*, 2005, **46**, 3372–3384.
13 A. Haider, S. Haider and I.-K. Kang, *Arabian J. Chem.*, 2015, DOI: 10.1016/j.arabjc.2015.11.015.
14 J. M. Deitzel, J. Kleinmeyer, D. Harris and N. C. Beck Tan, *Polymer*, 2001, **42**, 261–272.
15 E. S. Medeiros, G. M. Glenn, A. P. Klamczynski, W. J. Orts and L. H. C. Mattoso, *J. Appl. Polym. Sci.*, 2009, **113**, 2322–2330.
16 W. K. Son, J. H. Youk, T. S. Lee and W. H. Park, *Polymer*, 2004, **45**, 2959–2966.
17 S. François, C. Sarra-Bournet, A. Jaffre, N. Chakfé, B. Durand and G. Laroche, *J. Biomed. Mater. Res., Part B*, 2010, **93**, 531–543.
18 T. Subbiah, G. S. Bhat, R. W. Tock, S. Parameswaran and S. S. Ramkumar, *J. Appl. Polym. Sci.*, 2005, **96**, 557–569.
19 C. J. Luo, M. Nangrejo and M. Edirisinghe, *Polymer*, 2010, **51**, 1654–1662.
20 A. Baji, Y.-W. Mai, S.-C. Wong, M. Abtahi and P. Chen, *Compos. Sci. Technol.*, 2010, **70**, 703–718.
21 C. Wang, H.-S. Chien, K.-W. Yan, C.-L. Hung, K.-L. Hung, S.-J. Tsai and H.-J. Jhang, *Polymer*, 2009, **50**, 6100–6110.

22 V. Beachley and X. Wen, *Mater. Sci. Eng., C*, 2009, **29**, 663–668.
23 S. Agarwal, A. Greiner and J. H. Wendorff, *Prog. Polym. Sci.*, 2013, **38**, 963–991.
24 G. Lang, S. Jokisch and T. Scheibel, *J. Visualized Exp.*, 2013, e50492.
25 L. Zhang, P. Kopperstad, M. West, N. Hedin and H. Fong, *J. Appl. Polym. Sci.*, 2009, **114**, 3479–3486.
26 M. Wojasiński, M. Pilarek and T. Ciach, *Pol. J. Chem. Technol.*, 2014, **16**(2), 43–50.
27 D. D. da Silva Parize, J. E. de Oliveira, M. M. Foschini, J. M. Marconcini and L. H. C. Mattoso, *J. Appl. Polym. Sci.*, 2016, **133**, 43379.
28 S. Sinha-Ray, S. Sinha-Ray, A. L. Yarin and B. Pourdeyhimi, *Polymer*, 2015, **56**, 452–463.
29 D. D. da Silva Parize, M. M. Foschini, J. E. de Oliveira, A. P. Klamczynski, G. M. Glenn, J. M. Marconcini and L. H. C. Mattoso, *J. Mater. Sci.*, 2016, **51**, 4627–4638.
30 J. Oliveira, G. S. Brichi, J. M. Marconcini, L. H. Capparelli Mattoso, G. M. Glenn and E. Souto Medeiros, *J. Eng. Fiber Fabr.*, 2014, **9**, 117–125.
31 A. M. Gañán-Calvo, *Phys. Rev. Lett.*, 1998, **80**, 285–288.
32 A. M. Gañán-Calvo, C. Ferrera and J. M. Montanero, *J. Fluid Mech.*, 2011, **670**, 427–438.
33 M. A. Herrada, A. M. Gañán-Calvo, A. Ojeda-Monge, B. Bluth and P. Riesco-Chueca, *Phys. Rev. E: Stat., Nonlinear, Soft Matter Phys.*, 2008, **78**, 36323.
34 T. Si, F. Li, X.-Y. Yin and X.-Z. Yin, *J. Fluid Mech.*, 2009, **629**, 1.
35 D. P. DePonte, U. Weierstall, K. Schmidt, J. Warner, D. Starodub, J. C. H. Spence and R. B. Doak, *J. Phys. D: Appl. Phys.*, 2008, **41**, 195505.
36 M. Trebbin, K. Krüger, D. DePonte, S. V. Roth, H. N. Chapman and S. Förster, *Lab Chip*, 2014, **14**, 1733.
37 Y. Xia and G. M. Whitesides, *Angew. Chem., Int. Ed.*, 1998, **37**, 550–575.
38 J. C. McDonald and G. M. Whitesides, *Acc. Chem. Res.*, 2002, **35**, 491–499.
39 J. C. McDonald, D. C. Duffy, J. R. Anderson, D. T. Chiu, H. Wu, O. J. A. Schueller and G. M. Whitesides, *Electrophoresis*, 2000, 27–40.
40 J. R. Anderson, D. T. Chiu, R. J. Jackman, O. Cherniavskaya, J. C. McDonald, H. Wu, S. H. Whitesides and G. M. Whitesides, *Anal. Chem.*, 2000, **72**, 3158–3164.
41 J. N. Lee, C. Park and G. M. Whitesides, *Anal. Chem.*, 2003, **75**, 6544–6554.
42 B.-Y. Kim, L.-Y. Hong, Y.-M. Chung, D.-P. Kim and C.-S. Lee, *Adv. Funct. Mater.*, 2009, **19**, 3796–3803.
43 3M Advanced Materials Division, *Product Data Sheet. 3M™ Dyneon™ Fluoroplasic Granules THV 221GZ*, available at: https://multimedia.3m.com/mws/media/571351O/fluoroplastic-granules-thv-221gz-data-sheet.pdf, accessed 27 October 2017.
44 J. G. Drobny, *Technology of Fluoropolymers*, CRC Press, 2nd edn, 2008.
45 Carl Roth GmbH + Co. KG, *Safety data sheet of acetone*, available at: https://www.carlroth.com/downloads/sdb/de/9/SDB_9372_DE_DE.pdf, accessed 17 November 2017.
46 A. Kamada, N. Mittal, L. D. Söderberg, T. Ingverud, W. Ohm, S. V. Roth, F. Lundell and C. Lendel, *Proc. Natl. Acad. Sci. U. S. A.*, 2017, **114**, 1232–1237.
47 Carl Roth GmbH + Co. KG, *Safety data sheet of 1,1,1,3,3,3-hexafluoro-2-propanol*, available at: https://www.carlroth.com/downloads/sdb/de/2/SDB_2473_DE_DE.pdf, accessed 17 November 2017.
48 H. Bai, R. Sun, J. Ju, X. Yao, Y. Zheng and L. Jiang, *Small*, 2011, **7**, 3429–3433.
49 Y. Chen, L. Wang, Y. Xue, L. Jiang and Y. Zheng, *Sci. Rep.*, 2013, **3**, 2927.
50 X. Tian, Y. Chen, Y. Zheng, H. Bai and L. Jiang, *Adv. Mater.*, 2011, **23**, 5486–5491.

Electronic Supplementary Material (ESI) for Lab on a Chip.

Electronic Supplementary Information

Microfluidic nozzle device for ultrafine fiber solution blow spinning with precise diameter control†

Eddie Hofmann,[a,b] Kilian Krüger,[a,b] Christian Haynl,[c] Thomas Scheibel,[c] Martin Trebbin,[d] Stephan Förster[a,b]

[a] Department of Physical Chemistry I, University of Bayreuth, 95440 Bayreuth, Germany.
[b] Jülich Centre for Neutron Science (JCNS-1/ICS-1), Forschungszentrum Jülich GmbH, 52425 Jülich, Germany.
[c] Department for Biomaterials, University of Bayreuth, 95440 Bayreuth, Germany.
[d] Centre for Ultrafast Imaging (CUI), University of Hamburg, 22761 Hamburg, Germany.

Analyzing the fiber diameter

When analyzing the fiber samples via scanning electron microscopy, the quadratic mean (RMS) and the standard deviation (SD) were determined. For each parameter set, an adequate number n of single fibers was measured. Since later calculations assume volume constancy, the arithmetic mean of the fiber volume (Eq. S2) is needed, and the RMS of the fiber radius (Eq. S5) was used instead of the arithmetic mean. The fiber volume is approximated by the volume of a cylinder:

$$V = r^2\pi \cdot l \tag{S1}$$

$$\bar{V} = \frac{1}{n} \cdot \sum_{i=1}^{n} V_i \tag{S2}$$

$$\bar{r}^2\pi \cdot l = \frac{1}{n} \cdot \sum_{i=1}^{n} {r_i}^2\pi \cdot l \tag{S3}$$

$$\bar{r}^2 = \frac{1}{n} \cdot \sum_{i=1}^{n} {r_i}^2 \tag{S4}$$

$$\bar{r} = \sqrt{\frac{1}{n} \cdot \sum_{i=1}^{n} {r_i}^2} \tag{S5}$$

Deviation of an equation to predict the fiber diameter

The flow rate Q states which volume of polymer solution V_0 is jetted by the nozzle in a predefined time t.

$$Q = \frac{V_0}{t} \tag{S6}$$

The created fiber volume V_f equals the volume V_T of THV in the jet, given by the volume fraction ϕ_T.

$$\frac{V_f}{t} = Q \cdot \frac{V_T}{V_0} = Q \cdot \phi_T \tag{S7}$$

As the cross section of the fiber is almost circular, the fiber volume is approximated by the volume of a cylinder. Length l_f per time t determines the velocity v_f of the fiber respectively of the jet, since we assume that the speed is constant, when the solvent evaporates and only the diameter reduces.

$$\frac{V_f}{t} = \frac{\left(\frac{d_f}{2}\right)^2 \pi \cdot l_f}{t} = \left(\frac{d_f}{2}\right)^2 \pi \cdot v_f \tag{S8}$$

Combining Eq. S7 and Eq. S8, we achieve an expression to calculate the fiber diameter d_f.

$$\left(\frac{d_f}{2}\right)^2 \pi \cdot v_f = Q \cdot \frac{V_T}{V_0} \tag{S9}$$

$$d_f = \sqrt{\frac{4 \cdot \phi_T \cdot Q}{\pi \cdot v_f}} \tag{S10}$$

For a given concentration and hence, a predefined volume fraction ϕ_T of THV in the polymer solution, the fiber diameter d_f is only depending on the flow rate Q and the fiber velocity v_f.

$$d_f = \underbrace{\left(\frac{4 \cdot \phi_T}{\pi \cdot v_f}\right)^{1/2}}_{C} \cdot Q^{1/2} \tag{S11}$$

$$d_f = \underbrace{\left(\frac{4 \cdot \phi_T \cdot Q}{\pi}\right)^{1/2}}_{B} \cdot {v_f}^{-1/2} \tag{S12}$$

The velocity of the fiber is caused by the extensional gas flow of the compressed air accelerating the polymer solution inside the nozzle or by the drawing speed of the rotating spool stretching the fiber depending on which one is faster.

A connection between the jet velocity and the pressure difference can be made by Bernoulli's equation. For incompressible flows, the specific energy is constant at any arbitrary point along a stream line.

$$\underbrace{e}_{\substack{specific\\energy}} = \underbrace{\frac{v^2}{2}}_{\substack{specific\\kinetic\\energy}} + \underbrace{\frac{p}{\rho}}_{\substack{specific\\internal\\energy}} + \underbrace{gz}_{\substack{specific\\potential\\energy}} = \text{constant} \tag{S13}$$

p: pressure

ρ: density of solution

g: acceleration due to gravity

z: height (z-coordinate)

Two states are distinguished: one inside the nozzle and the other inside the liquid jet.

$$\underbrace{e_n}_{\substack{specific\ energy\\inside\ nozzle}} = \underbrace{e_j}_{\substack{specific\ energy\\inside\ jet}} \tag{S14}$$

$$\frac{{v_n}^2}{2} + \frac{p_n}{\rho_0} + gz_n = \frac{{v_j}^2}{2} + \frac{p_j}{\rho_0} + gz_j \tag{S15}$$

When jetting horizontally, the potential energy is not changing ($z_n = z_j$).

$$\frac{{v_n}^2}{2} + \frac{p_n}{\rho_0} = \frac{{v_j}^2}{2} + \frac{p_j}{\rho_0} \tag{S16}$$

$$\frac{p_n}{\rho_0} - \frac{p_j}{\rho_0} = \frac{{v_j}^2}{2} - \frac{{v_n}^2}{2} \tag{S17}$$

The velocity inside the nozzle is much smaller than the velocity of the jet.

$$v_n \ll v_j \implies {v_j}^2 - {v_n}^2 \cong {v_j}^2 \tag{S18}$$

$$\frac{\Delta p}{\rho_0} = \frac{1}{2}{v_j}^2 \tag{S19}$$

$$\Delta p = \frac{1}{2}\rho_0 \cdot {v_j}^2 \tag{S20}$$

Δp: pressure difference between nozzle and jet ($\Delta p = p_n - p_j$)

The pressure difference determines the velocity of the jet.

$$v_j = \sqrt{\frac{2 \cdot \Delta p}{\rho_0}} \tag{S21}$$

We assume that the polymer solution is accelerated by the pressure difference first, while the density remains constant, and just afterwards, the evaporation of the solvent starts. Also, the loss of kinetic energy owing to viscous dissipation and surface tension is neglected.[1]

Combining Eq. S21 and Eq. S10 gives Eq. S22, which describes the fiber diameter in dependence of the flow rate and the pressure difference applied to the nozzle device.

$$d_f = \left(\frac{8 \cdot \rho_0 \cdot {\phi_T}^2 \cdot Q^2}{\pi^2 \cdot \Delta p}\right)^{1/4} \tag{S22}$$

$$d_f = \underbrace{\left(\frac{8 \cdot \rho_0 \cdot {\phi_T}^2}{\pi^2 \cdot \Delta p}\right)^{1/4}}_{D} \cdot Q^{1/2} \tag{S23}$$

$$d_f = \underbrace{\left(\frac{8 \cdot \rho_0 \cdot {\phi_T}^2 \cdot Q^2}{\pi^2}\right)^{1/4}}_{A} \cdot \Delta p^{-1/4} \tag{S24}$$

Eq. S22 differs just in the term $\sqrt{\phi_T}$ from the Gañán-Calvo equation[1] (Eq. S26) for the jet diameter d_j when using the gas dynamic virtual nozzle-principle.

$$d_f = \sqrt{\phi_T} \cdot \underbrace{\left(\frac{8 \cdot \rho_0}{\pi^2 \cdot \Delta p}\right)^{1/4} \cdot Q^{1/2}}_{\substack{Gañán-Calvo\ equation \\ for\ jet\ diameter\ d_j}} \tag{S25}$$

$$d_j = \left(\frac{8 \cdot \rho_0}{\pi^2 \cdot \Delta p}\right)^{1/4} \cdot Q^{1/2} \tag{S26}$$

The connection between the diameter of the jet and the fiber can also be shown by another simple consideration. The volume of the jet V_j diminishes due to evaporation of acetone.

$$V_f = V_j \cdot \phi_T \tag{S27}$$

$$\left(\frac{d_f}{2}\right)^2 \pi \cdot l_f = \left(\frac{d_j}{2}\right)^2 \pi \cdot l_j \cdot \phi_T \tag{S28}$$

The length of the jet stays constant when the solvent evaporates; just the diameter decreases ($l_f = l_j$).

$$\Longrightarrow \quad d_f = \sqrt{\phi_T} \cdot d_j \tag{S29}$$

Nozzle deformation during operation

For the calculation of the velocity inside the nozzle, it was necessary to determine the cross-sectional area of the nozzle. The microfluidic channel was cut orthogonally to the flow direction; subsequently, the width n_w and the height n_h of the nozzle were measured by SEM (see Table 1). However, as seen in Fig. S1, the PDMS channels are expanding when a pressure difference or flow rate is applied. The width of the nozzle could be measured during operation by means of an optical microscope. By applying the same expansion coefficient of the nozzle width to the nozzle height, the cross-sectional area during operation could be approximated (1037 µm²).

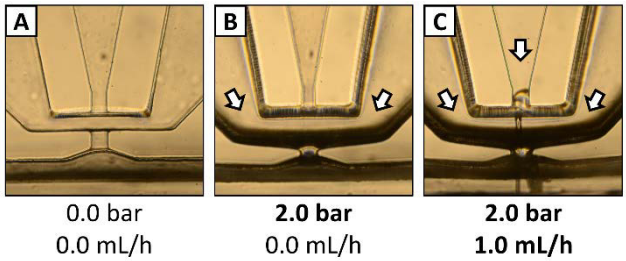

Figure S1: The microchannels of the nozzle are deforming during operation, since the device is made of PDMS elastomer. (A) Idle state, (B) with 2 bar pressure applied, (C) during operation with 1 mL/h and 2 bar.

Influence of working distances between nozzle and spool

The working distance d_s influences the fiber morphology rather than the fiber diameter. The distance d_s between the microfluidic chip and the spool for reeling off was reduced from 8 cm in steps of 1 cm. For a flow rate of 1 mL/h the minimal distance, where a steady fiber with a round cross-sectional shape could be spooled, was 2 cm. At a distance of 1 cm, the fibers fuse and build a network rather than individual fibers (see Fig. S2). Employing the velocity of the jet measured with high-speed cinematography, 3.3 ms are sufficient for the acetone to evaporate from the jetted solution. At flow rates of 2 mL/h and 3 mL/h a distance of 4 cm was needed, which equals a minimal jetting time of 6.5 ms.

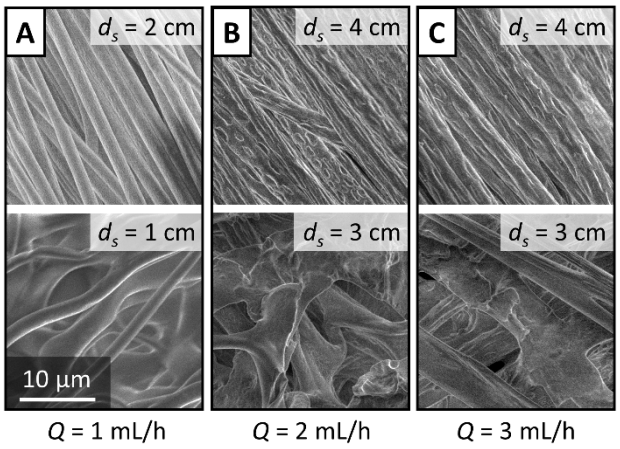

Figure S2: SEM images of bunches of individual fibers (top) and networks of fused fibers (bottom) at different flow rates. The working distance was reduced stepwise until the collected fibers fused into one network. The minimal travel time to form individual fibers could be estimated.

Influence of polymer concentration

The findings of other groups about the influence of polymer concentration on fiber morphology could be confirmed.[2–5] For a solution of a given polymer of a certain molecular weight, a continuous fibrous structure is only obtained above a critical concentration.[2,5] At low polymer concentrations, the formation of beaded fibers is favored.[2] The driving force is the surface tension, which causes oscillations within the jet due to Rayleigh instability.[3,6] Since the viscosity is too low and the chain entanglement density is poor, these oscillations cannot be attenuated.[4] Low surface tension and high evaporation rate would reduce the formation of beads. Higher concentrations also promote the formation of smooth fibers with uniform diameter, as viscoelastic forces retard the deformation of the jet.[3] When the concentration was increased even more, the viscosity got too high to produce fibers by solution blow spinning. Since uniform fibers were desirable for studying the fiber diameter, a reasonable high concentration was used.

Exemplary images for both morphologies can be found in Fig. 5 where the conditions are compared for making beaded and smooth polycaprolactone fibers. The THV fibers showed the same behavior when a solution of less than 20% (w/w) was used. For example, beaded fibers with thin segments of just a few hundred nanometers were obtained at 7–10% (w/w) THV in acetone.

Size distribution of fiber diameter

The uniformity of the fibers is also influenced by varied process parameters. An indicator for the degree of the fluctuation is the standard deviation (SD). Moreover, the relative SD is normalized to the fiber diameter, better illustrating a potential trend since the SD is naturally bigger for thicker fibers.

A close look at Fig. S3 reveals that the size distribution becomes wider when flow rate or drawing speed increases. The histograms confirm this trend which is in accordance to literature.[2] As mentioned before, the solvent needs more time to evaporate from bigger jets, allowing the instabilities to deform the developing fiber in the meantime. An unusually high relative standard deviation was noticed when the pressure difference was quite small being just 1 bar.

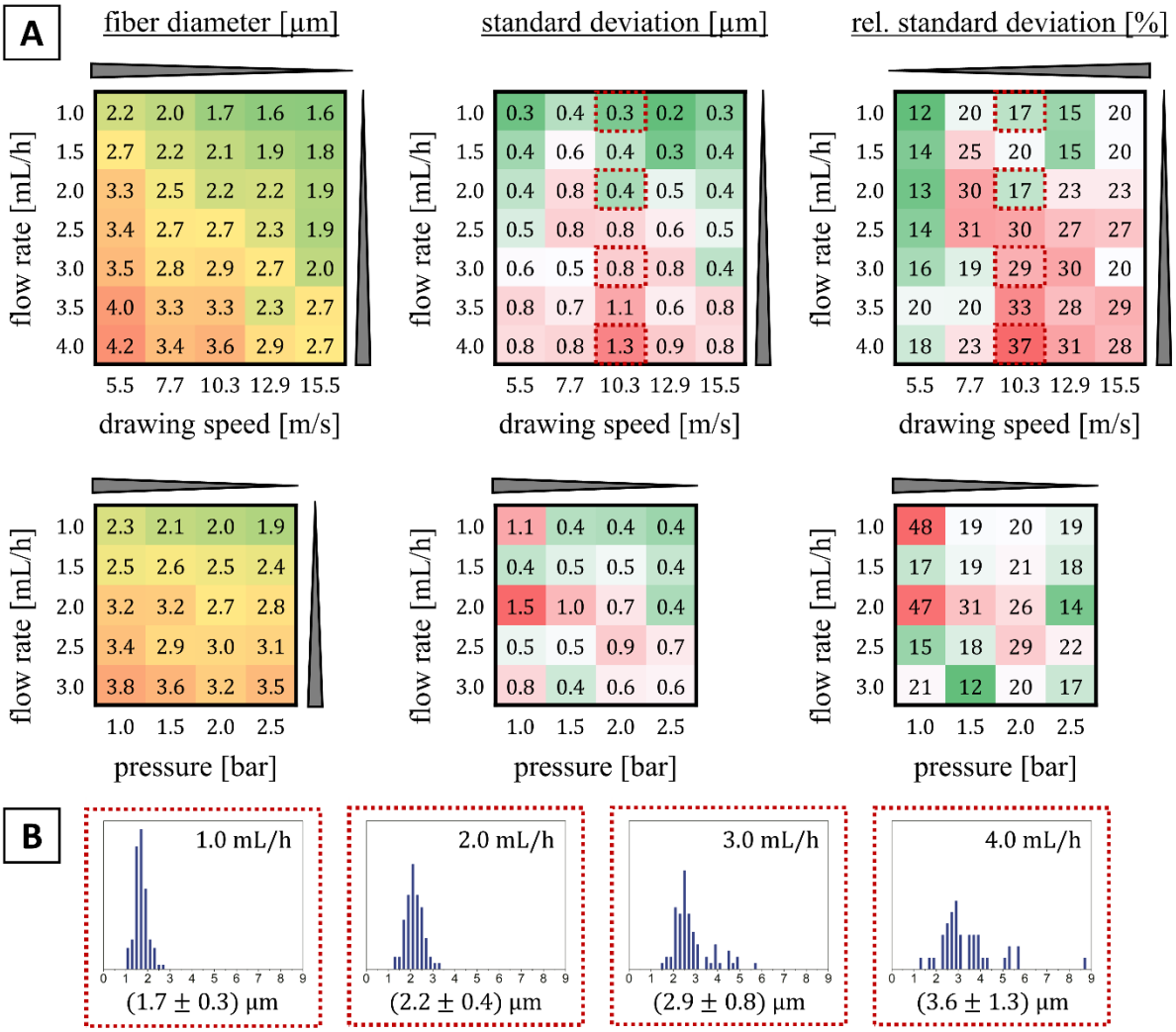

Figure S3: (A) Fiber diameter, standard deviation (SD) and relative SD of the THV fiber samples are presented in color-coded tables. Grey wedges indicate assumed trends in the data. (B) Histograms show exemplarily that the size distribution becomes wider when the flow rate increases. The color code only serves as a guide to the eye to visualize the general trends.

Practical guide for solution blow spinning

Microfluidic solution blow spinning may show similar difficulties as electrospinning since both techniques use a thin liquid jet of polymer solution. The following table lists some hints how to solve typical problems.[7]

Table S1: Some typical problems of solution blow spinning and possible adjustments are summarized in this table.

Problem	**Possible solution**
Spraying / no fiber at all	Increase weight concentration or molecular weight of the polymer
Formation of a beaded chain	Increase weight concentration
Fluctuating fiber diameter	Increase air pressure and decrease flow rate; decrease drawing speed; increase weight concentration; use another solvent with higher vapor pressure
Fusing of fibers / formation of network or film	Increase working distance between nozzle and collection spool; use another solvent with higher vapor pressure
Polymer solution extrudes from the nozzle	Decrease weight concentration of the polymer
Wetting and clogging of nozzle	Incompatible materials; try to switch polymer, solvent or chip to at least one fluorinated component

Literature

1 A. M. Gañán-Calvo, *Phys. Rev. Lett.*, 1998, **80**, 285–288.

2 J. E. Oliveira, E. A. Moraes, R. G. F. Costa, A. S. Afonso, L. H. C. Mattoso, W. J. Orts and E. S. Medeiros, *J. Appl. Polym. Sci.*, 2011, **122**, 3396–3405.

3 H. Fong, I. Chun and D.H. Reneker, *Polymer*, 1999, **40**, 4585–4592.

4 A. Baji, Y.-W. Mai, S.-C. Wong, M. Abtahi and P. Chen, *Composites Science and Technology*, 2010, **70**, 703–718.

5 S. L. Shenoy, W. D. Bates, H. L. Frisch and G. E. Wnek, *Polymer*, 2005, **46**, 3372–3384.

6 Rayleigh, *Proceedings of the London Mathematical Society*, 1878, **s1-10**, 4–13.

7 S. Agarwal, M. Burgard, A. Greiner and J. H. Wendorff, *Electrospinning. A practical guide to nanofibers*, De Gruyter, Berlin, Boston, 2016.

7.2 Teilarbeit 2

Reproduced with permission from

Haynl, C.; Hofmann, E.; Pawar, K.; Förster, S.; Scheibel, T.*

Microfluidics-produced collagen fibers show extraordinary mechanical properties.

Nano Letters **2016,** 16, 5917-5922.

DOI: 10.1021/acs.nanolett.6b02828

NANO LETTERS

Letter

pubs.acs.org/NanoLett

Microfluidics-Produced Collagen Fibers Show Extraordinary Mechanical Properties

Christian Haynl,[†] Eddie Hofmann,[‡] Kiran Pawar,[†] Stephan Förster,[‡,§,∥] and Thomas Scheibel*[,†,§,∥,⊥,#,▽]

[†]Lehrstuhl Biomaterialien, Fakultät für Ingenieurwissenschaften, [‡]Lehrstuhl Physikalische Chemie I, and [§]Bayreuther Zentrum für Kolloide und Grenzflächen (BZKG), Universität Bayreuth, Universitätsstraße 30, 95440 Bayreuth, Germany

[∥]Bayerisches Polymerinstitut (BPI), Universitätsstraße 30, 95440 Bayreuth, Germany

[⊥]Bayreuther Zentrum für Molekulare Biowissenschaften (BZMB), [#]Institut für Bio-Makromoleküle (bio-mac), and [▽]Bayreuther Materialzentrum (BayMAT), Universität Bayreuth, Universitätsstraße 30, 95440 Bayreuth, Germany

Supporting Information

ABSTRACT: Collagens are widely used as biomaterials in drug-delivery and tissue engineering applications due to their biodegradability, biocompatibility and hypoallergenicity. Besides gelatin-based materials, collagen microfibers are in the focus of biomedical research. Commonly, man-made fibers are produced by wet-spinning yielding fiber diameters higher than 8 μm. Here, assembly and continuous production of single collagen type I microfibers were established using a microfluidic chip. Microfluidics-produced microfibers exhibited tensile strength and Young's modulus exceeding that of fibers produced in classical wet-spinning devices and even that of natural tendon and they showed lower diameters. Their structural orientation was examined by polarized Fourier transform infrared spectroscopy (FTIR) showing fibril alignment within the microfiber. Cell culture tests using the neuronal cell line NG108-15 showed cell alignment and axon growth along the microfiber axes inaugurating potential applications in, for example, peripheral nerve repair.

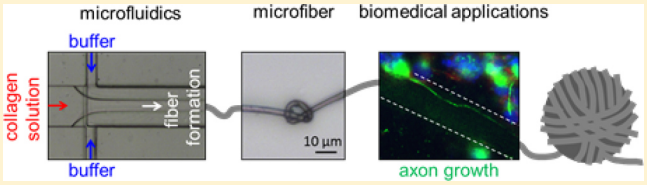

KEYWORDS: *Collagen, microfluidics, microfiber, mechanical properties, biomaterial, axon growth*

Protein fibers in nature are used for a great diversity of tasks including motility, scaffolding, stabilization, and protection.[1] One of the most abundant structural proteins is collagen mainly contributing to the extracellular matrix of vertebrates.[2,3] So far, more than 20 distinct types of collagen have been described. Thereof, collagen type I is the major collagen of tendon, ligament, skin, and bone and therefore the most studied one.[4] On the molecular level, collagen type I forms a characteristic triple helix consisting of three polypeptides termed α-chains (two α1[I] and one α2[I]). Previous examinations showed that a high amino acid homology exists between both types of α-chains, however the α1(I) chain comprises a lower hydrophobicity compared to the α2(I) chain.[5] Each α-chain exhibits a helical core domain mainly consisting of the repeating amino acid motif Gly-Xaa-Yaa (Xaa and Yaa could be any amino acid, but mostly proline and hydroxyproline residues are found) and flanking nonrepetitive sequences.[4,6−8] These triple-helical molecules self-assemble into fibrils and fibers in an entropy-driven process including the reduction of the contact area to the surrounding water.[6,9] Because of collagen's good mechanical stability, biocompatibility, biodegradability, low immunogenicity, and ability to promote cellular attachment and growth, collagenous materials, especially fibers, are used in medical and biomedical applications such as drug-delivery, wound healing, and tissue engineering.[10−14]

Up to now, numerous publications reported the processing of soluble collagen into fibers using wet-spinning devices.[13,15−19] Here, collagen microfibers were fabricated using a microfluidic system. In general, microfluidics deals with the processing of small amounts of fluids in channels with dimensions of tens to hundreds of micrometer,[20] which are mostly embedded in small chips regularly consisting of polydimethylsiloxane (PDMS). Besides analytical applications, microfluidic systems were shown to be suitable to fabricate fibers of synthetic polymers, polysaccharides such as chitosan or alginate and silk.[21,22] With regard to collagen type I, previous studies dealt with microfluidic channels acting either as a mold for the discontinuous collagen fibril formation[23] or as an environment for in situ analysis of collagen gelation.[24] Nevertheless, up to now microfluidic spinning did not allow to continuously fabricate collagen fibers due to its significant longer gelation/assembly time (minutes to hours),[25] which is in contrast to the very fast ionic cross-linking of polysaccharides such as chitosan and alginate. However, microfluidic fiber spinning methods were already used to incorporate collagen within polysaccharide fibers. Usually, chitosan or alginate have been used as a scaffold in which collagen was embedded, for

Received: July 8, 2016
Revised: August 9, 2016
Published: August 11, 2016

DOI: 10.1021/acs.nanolett.6b02828
Nano Lett. 2016, 16, 5917−5922

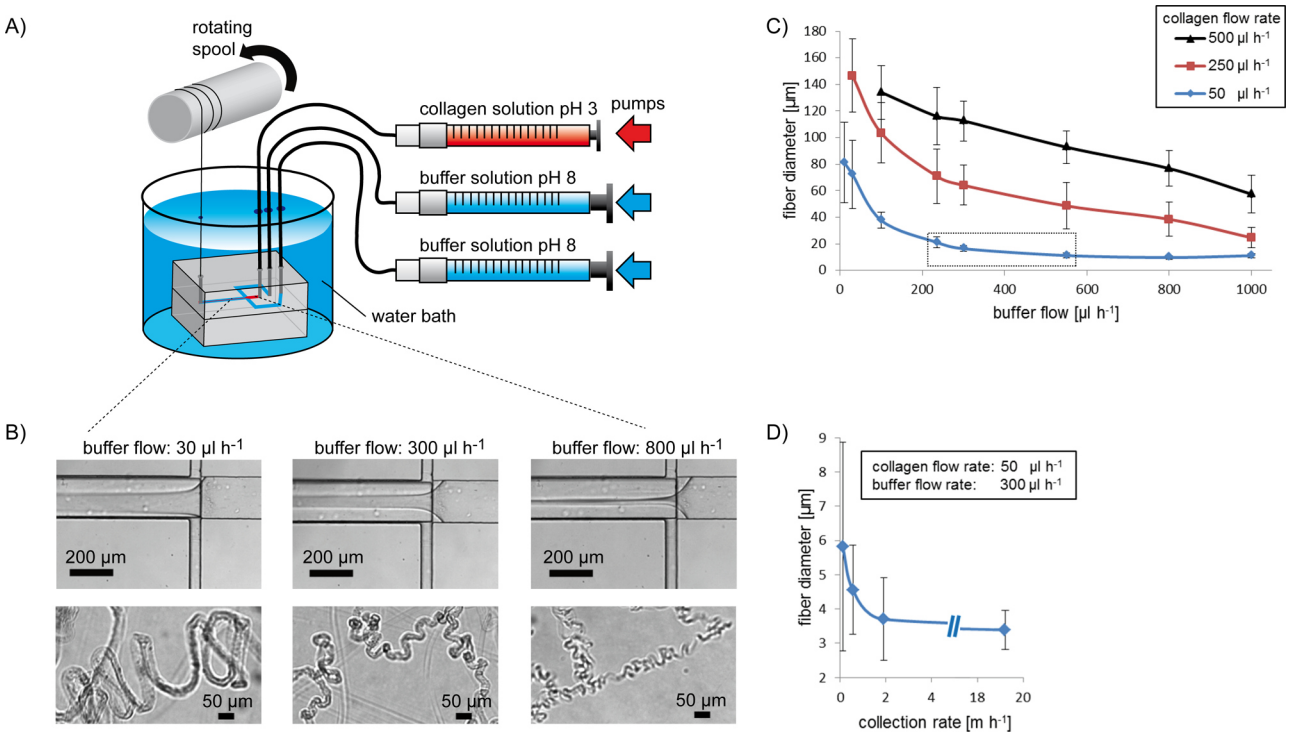

Figure 1. (A) A microfluidic chip is connected to three independent syringe pumps that allow simultaneous pumping of a collagen solution at pH 3 (red) and two PEG-containing buffer solutions at pH 8 (blue). Microfiber formation takes place at the cross junction within the microfluidic chip upon an increase of the pH and in the presence of PEG, and microfibers are extruded into a water bath and drawn by an automated spool. (B) Using a constant collagen flow (here, 50 μL h^{-1}) and varying buffer flow rates enables the extrusion of microfibers into water with adjustable diameters. (C) Diameters of extruded fibers depend on buffer and collagen flow rates. Collection of collagen fibers using a rotating spool is possible for a collagen flow of 50 μL h^{-1} and buffer flow rates in between 235 and 550 μL h^{-1} (shown by the box). (D) Dry microfiber diameters could be adjusted by changing the collection rate using a constant collagen flow of 50 μL h^{-1} and a buffer flow rate of 300 μL h^{-1} yielding final diameters from 6 to 3 μm.

example, as blended fibers[26] or as tubular fibers with a collagen hydrogel core[25] or simply coated onto the fiber surface.[27] Nevertheless, the production of endless, plain collagen fibers would be highly desirable due to a better performance in comparison to blended fibers including an expected higher mechanical stability, better biocompatibility, and less complexity in processing compared to polysaccharide-collagen blend fibers.

In this study, we introduce a microfluidic approach for the continuous production of adjustable collagen microfibers yielding minimum dry diameters of only 3 μm. Polarized Fourier transform infrared spectroscopy (FTIR) revealed fibril orientation along the microfiber axis supposed to be in part responsible for the excellent mechanical stability exceeding that of natural tendon fibers and previous wet-spun collagen fibers. Cell studies using the neuronal cell line NG108-15 showed directional cell growth and even axon elongation along the fiber axes. Therefore, we conclude that these fibers are of high interest for biomedical applications, especially for the use in peripheral nerve repair.

In order to produce endless collagen microfibers, we used a microfluidic device featuring one inlet channel for the collagen solution and two inlet channels for the sheath flows joining at a cross junction (90° angle) into one larger channel. A great challenge in producing continuous fibers with microfluidic devices is to reduce wall adhesion of the assembling polymer (here collagen) followed by irreversible clogging. Therefore, we designed a microfluidic chip, similar to Kinahan et al.,[22] which contained a tiered channel geometry, thus enabling the circulation of the sheath flow around the protein stream. The microfluidic chip, consisting of polydimethylsiloxane (PDMS), was fabricated by using the soft-lithography technology.

For microfiber assembly, collagen type I (with triple-helical conformation) was dissolved in diluted acetic acid at pH 3, and as sheath flows a buffer solution (112 mM phosphate, 30 mM TES, and 135 mM NaCl, pH 8) with 10% (w/v) polyethylene glycol (PEG) was used. The interaction between both types of solution at the cross intersection induced a neutralization of the collagen solution due to the high buffering capacity of the PEG solution. Shifting an acidic collagen type I solution to slightly basic conditions triggers the formation of fibrils.[28,29] As a result of the hydrodynamic focusing and the elongational flow in the microfluidic chip, fibrils were aligned and assembled into microfibers. Surprisingly, it was observed that the addition of polyethylene glycol to the surrounding buffer was essential for continuous microfiber formation, likely depending on the high hygroscopicity of PEG,[30] which contributes to protein precipitation by rapidly detracting water molecules therefrom.[31,32] Microfibers at the chip's exit were pulled through a water bath by a rotating spool to remove buffer components and PEG (Figure 1A). Washing-off of PEG from the microfibers was confirmed by Fourier transform infrared (FTIR) spectroscopy yielding spectra lacking the characteristic PEG signal at 1100 cm^{-1} (Figure 3B). Furthermore, water extrusion avoided the formation of spindle-knotted fiber morphologies, usually occurring when outer fiber layers are still liquid and breakup due to Rayleigh instabilities,[33−35] and microfibers exhibiting a homogeneous diameter along their longitudinal axes were generated (Figure 2). Because fiber morphology usually depends on the hydrodynamic focusing of

DOI: 10.1021/acs.nanolett.6b02828
Nano Lett. 2016, 16, 5917−5922

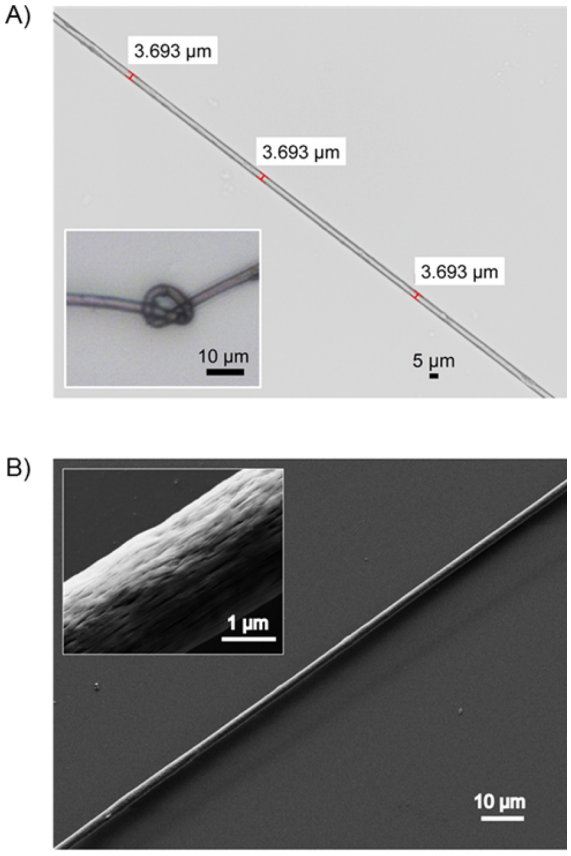

Figure 2. (A) Light-microscopy image of a microfluidics-produced collagen microfiber confirming a homogeneous fiber diameter. (Insert) Man-made knot within the microfiber. (B) SEM picture of a microfluidics-produced collagen microfiber and higher magnification (insert) showing longitudinal grooves.

the core solution within microchannels, we were able to extrude microfibers with varying diameters by changing the collagen and/or the buffer flow rates. As shown in Figure 1B,C, the diameter of extruded microfibers decreased upon increasing the buffer flow rates while applying a constant collagen flow. On the contrary, an increase of the collagen flow rate led to higher fiber diameters (Figure 1C). Using 250 or 500 μL h^{-1} collagen flows in combination with buffer flow rates lower than 30 respectively 100 μL h^{-1} prevented the extrusion of fibers exhibiting a well-defined fiber shape with a homogeneous diameter. Furthermore, it was noticed that the microfiber diameter after extrusion differed from the diameter of the hydrodynamically focused collagen stream at the cross-intersection. This could be attributed to the low fibrillogenesis rate of collagen,[25] supposedly inhibiting immediate hardening of the forming microfiber at the cross-intersection. For instance, by applying a constant collagen flow of 50 μL h^{-1} and 30, 300, and 800 μL h^{-1} buffer flows, the relative decline in microfiber diameter between the focusing zone and the outlet was 36, 74 and 74%, respectively. Collection of microfibers using a rotating spool was feasible for a collagen flow of 50 μL h^{-1} and buffer flow rates in between 235 and 550 μL h^{-1}. Applying lower buffer flow rates than 235 μL h^{-1} (and/or collagen flow rates higher than 50 μL h^{-1}) resulted in a loss of the hydrodynamic focusing of the collagen solution that hindered complete collagen assembly and reduced the shear forces necessary for fabrication of mechanically stable fibers. On the other side, rising the buffer flow rates to values higher than 550 μL h^{-1} (at a collagen flow rate of 50 μL h^{-1}) led to lower reaction times of collagen with the surrounding buffer solution, thereby inhibiting fiber collection, too. We observed that the collagen fiber collection by the rotating spool caused poststretching leading to even lower diameters. To investigate the effect of the collection rate on microfiber diameter, we used a 50 μL h^{-1} collagen flow and 300 μL h^{-1} buffer flows (which turned out to be the most robust processing condition for continuous fiber production) and varied the speed of the collecting spool (Figure 1D). We noticed that microfibers were stretched even with the lowest collection rate of 0.11 m h^{-1}, and their diameters decreased from original (i.e., no poststretching) 16 μm (see Figure 1C) to 6 μm during collection. The high standard deviation at slow collection rates could be explained by undirected agglomeration of extruded fibers hindering collection of untangled fibers (Figure S1 in Supporting Information). Microfibers drawn at a collection rate above 1.92 m h^{-1} resulted in fiber diameters of 3−4 μm, which obviously indicated that the maximum stretching capacity was reached. Continuous microfiber production was possible up to 19 m h^{-1}.

For microfiber characterization, we investigated microfibers produced at 50 μL h^{-1} collagen flow, 300 μL h^{-1} buffer flows and at a collection rate of 1.92 m h^{-1} (if not otherwise indicated). Light microscopy of collagen microfibers revealed that the fiber diameter was constant at 3.7 μm (Figure 2A). Scanning electron microscopy (SEM) allowed identifying small aligned grooves along the microfiber axis indicating an orientation of collagen fibrils within the microfiber (Figure 2B).

In order to test the molecule alignment as well as the structural integrity of the microfibers, polarized FTIR spectroscopy was used. Polarized FTIR is a technique to get information concerning orientation and/or ordering of molecules.[36] Former studies indicated that the ratio of the amide I and amide II peak area of collagenous tissues changes when examined using polarized infrared light from different angles due to the molecular dichroism.[36,37] Here, it was observed that microfibers exposed to polarized radiation exhibited a ratio of the amide I to amide II peak area of 2.7 when polarized perpendicular to the fiber axis, whereas the amide I/amide II area ratio was 1.1 upon polarization in parallel to the fiber axis, and it was 1.7 at nonpolarizing conditions, thereby indicating good collagen fibril orientation along the microfibers (Figure 3A). In comparison, natural fibers of tendon possess values for perpendicular, parallel and non-polarized conditions of 4, 1 and 1.8, respectively.[37]

Because the obtained microfibers could be easily hand knotted (Figure 2A, insertion), the mechanical stability of the fibers collected at a rate of 1.92 m h^{-1} was obviously quite good. Therefore, the mechanical properties of collagen microfibers were investigated by tensile testing at 30% humidity in more detail. Figure 4A shows a representative stress−strain curve of the obtained microfibers at the detected optimal processing conditions. Tensile strength of microfluidics-produced collagen microfibers was 383 ± 85 MPa and superior to that of tendon as well as of classically wet-spun collagen type I fibers. Moreover, the Young's modulus was also significantly higher (4138 ± 512 MPa) in comparison to that of tendon and artificial collagen fibers, while the extensibility of 25.0 ± 3.7% was similar between all fibers (Table 1). Fiber toughness was calculated to be 52.9 ± 14.7 MJ m^{-3}. Importantly, the average microfiber diameter was 3.7 ± 1.2 μm denoting the lowest fiber diameter ever published for wet-spun collagen fibers (≥8

DOI: 10.1021/acs.nanolett.6b02828
Nano Lett. 2016, 16, 5917−5922

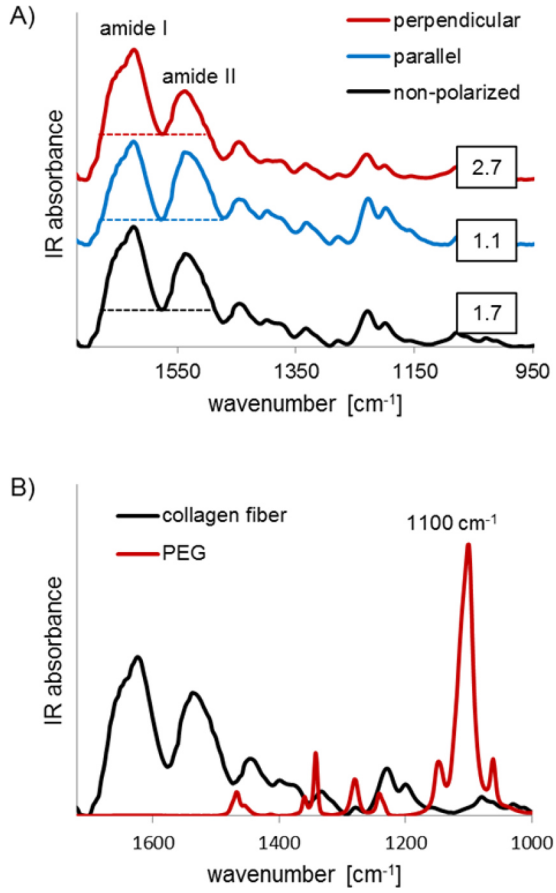

Figure 3. (A) Polarized FTIR spectroscopy of a microfluidics-produced collagen microfiber. The ratios of the amide I/amide II peak area change upon exposure to IR radiation polarized perpendicular or in parallel to the microfiber axis and under nonpolarizing conditions (shown in boxes). (B) IR spectrum of a microfluidics-produced collagen microfiber in comparison to that of polyethylene glycol (PEG) indicating that no PEG can be found within the microfiber.

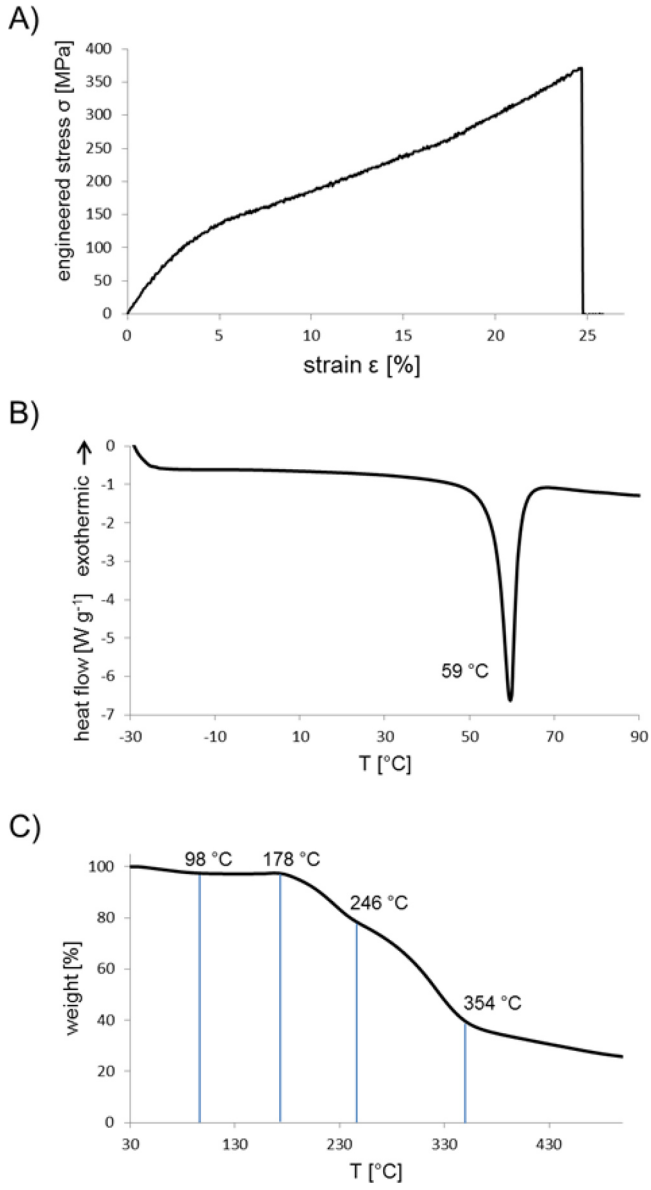

Figure 4. (A) Representative stress−strain plot, (B) DSC analysis, and (C) TGA of dry microfluidics-produced collagen microfibers.

μm).[13,15,17−19] Collagen microfibers collected at nonoptimal conditions, for example, at a rate of only 0.11 m h^{-1} led to lower tensile strength (361 ± 126 MPa) and Young's modulus (3201 ± 1026 MPa) (Figure S2 in Supporting Information). Although Yaari et al. recently produced wet-spun collagen fibers achieving a tensile strength of 378 MPa and a Young's modulus of 3.5 GPa, additional glutaraldehyde cross-linking of these fibers was required.[19] However, glutaraldehyde cross-linking is markedly cytotoxic,[15,38] and therefore, only EDC/NHS cross-linked fibers exhibiting 314 MPa tensile strength were used in Yaari et al. for cell culture applications.[19] In contrast, we did not need any chemical cross-linking to yield mechanically stable fibers. In addition, our microfluidic setup allowed the spinning of low concentrated collagen solutions with as little as 5 mg mL^{-1}. Such concentrations lead to a decrease in viscosity enabling enhanced fibril movement and more distinct alignment.[15]

It can be assumed that the smaller diameters of our microfibers led to increased mechanical stability due to better longitudinal orientation of collagen fibrils[18] and less defect structures like voids, entanglements, free chain ends, and foreign particles in contrast to the situation in bigger diameter fibers.[39] To confirm this, we had a closer look at the mechanical properties of collagen microfibers with varying diameters ranging from 5 to 10 μm with an average diameter of 6.8 μm (collected by 0.11 m h^{-1}). Actually, 6.8 μm diameter fibers showed a tensile strength of 284 ± 102 MPa and a Young's modulus of 2900 ± 1100 MPa, both being significantly lower than the mechanical properties of 3.7 μm fibers (for comparison of the mechanical properties see Figure S3 in Supporting Information). The high mechanical stability of our microfibers makes them accessible to the fabrication of textile scaffolds for tissue engineering and suture- or wound-dressing materials, whereas the adaption of the final mechanical properties to its environment could be controlled by the specific textile structure and the type of processing, for example, knitting, weaving, or braiding.

Next, the thermal stability of air-dried microfluidics-produced microfibers was characterized using differential scanning calorimetry (DSC) and thermogravimetric analysis (TGA). DSC measurements of the microfibers showed an endothermic peak at 59 °C referring to helix-to-coil transition (Figure 4B).[40−42] TGA revealed a residual internal water content of 3%,

DOI: 10.1021/acs.nanolett.6b02828
Nano Lett. 2016, 16, 5917−5922

Table 1. Mechanical Properties and Diameter of Microfluidics-Produced Collagen Microfibers (n = 36) in Comparison to That of Collagen Fibers after Wet-Spinning and That of Tendon

material	modulus E [MPa]	strength σ [MPa]	extensibility ε [%]	diameter d [μm]
microfluidics-produced microfiber	4138 ± 512	383 ± 85	25.0 ± 3.7	3.7 ± 1.2
wet-spun fibers				
Dunn et al., 1993[18]		200		20
Cavallaro et al., 1994[17]		224		≥25
Zeugolis et al., 2008[13]	1580	208	27.0	119
Siriwardane et al., 2014[15]	1265	262	18.4	46.5
fibers of tendon				
Hepworth et al., 2002[43]	2410	180	25.6	254
Gosline et al., 2002[44]	1200	120	13	

which was indicated by weight loss upon 98 °C, and the microfibers were thermally stable up to 178 °C before further weight loss occurred in a multistage decomposition manner (Figure 4C). As a result, the microfluidics-produced collagen microfibers were suitable concerning biomedical or tissue engineering applications usually only requiring human body temperature stability.

Because the microfluidics-produced collagen microfibers exhibited explicit mechanical stability and thermal characteristics and because collagen is known to be biocompatible[10,12] with biochemical cues allowing cell attachment,[45] we tested our microfibers in initial cell culture experiments. Exemplary, the neuronal cell line NG108-15 was analyzed in contact to our microfibers after 72 h of incubation. Low-magnification fluorescence images of cell nuclei marked with DAPI showed cell alignment along the collagen microfiber's longitudinal axes (Figure 5A). To get more detailed information about the cell morphology, higher-magnification phase contrast (Figure 5B), and fluorescence images (Figure 5B–F) were taken. DAPI-stained cell nuclei (Figure 5C) and phalloidin-labeled actin filaments (Figure 5D) revealed the general cell morphology in contact to microfibers. Cells were additionally labeled with an antibody against ßIII-tubulin, which is almost found exclusively in neuronal cell structures. Interestingly, we observed that cells exhibited axon growth. Axons were up to 100 μm in length and were aligned in microfiber direction (Figure 5E, white arrows). Figure 5F depicts merged fluorescence of all three channels.

Although recently progress was made concerning the production of polysaccharide fibers using microfluidics,[21,25−27] the microfluidic fabrication of collagen fibers has so far been less manageable because of the slow gelling rate of collagen. Here, the continuous assembly of acid-soluble collagen type I into microfibers was performed by microfluidics with asymmetric hydrodynamic focusing. The determination of appropriate assembly conditions and flow rates allowed the production of microfibers under nontoxic, all-aqueous conditions, and a maximum production rate of 19 m h^{-1}. These microfibers exhibited good mechanical properties exceeding the stability of previous wet-spun collagen fibers as well as even natural tendon without the need of chemical cross-linking, which could be harmful to cells. The high mechanical stability of our microfibers facilitates fiber processing, which allow textile fabrication and adjustment of the resulting mechanical textile properties to its respective application, for example, tendon repair. Neuronal NG108-15 cells migrated directionally along the longitudinal microfiber axes and showed axonal growth in direction of the microfiber axis. Therefore, these microfibers could be potentially useful in peripheral nerve repair to bridge long distance gaps allowing directional growth of neuronal cells for developing functional tissue. On the other side, according to little material consumption by our microfluidic approach (1 mg collagen ≙ 76 m microfiber using a collection rate of 19 m h^{-1}),

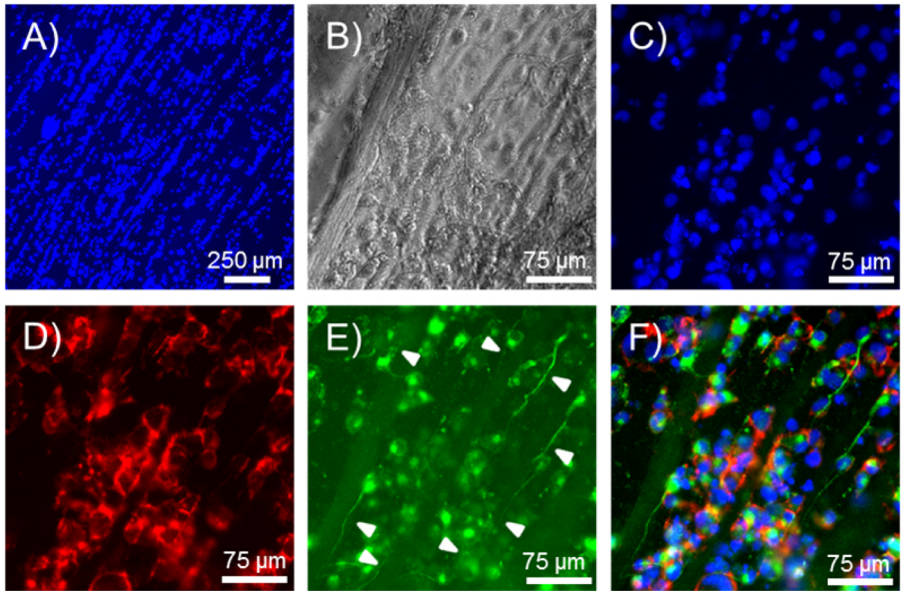

Figure 5. Cell culture analysis of neuronal NG108-15 cells on microfluidics-produced collagen microfibers after 72 h of incubation. (A) Fluorescence image of DAPI-stained cells. Cells align along the microfibers axes. (B) Phase-contrast image of cells on microfibers. Fluorescence images of (C) DAPI- and (D) phalloidin-stained cells in the presence of microfibers. (E) Immuno-staining of neuronal-specific ßIII-tubulin indicates axon growth in direction of the microfiber axes (white arrows). (F) Merged fluorescence image of (C), (D), and (E).

DOI: 10.1021/acs.nanolett.6b02828
Nano Lett. 2016, 16, 5917−5922

our setup is also of high importance for screening different fiber additives, for example, matrix proteins or polymers with regard to their functionality in collagen microfibers including their influence on mechanical properties or biocompatibility.

■ ASSOCIATED CONTENT

Supporting Information

The Supporting Information is available free of charge on the ACS Publications website at DOI: 10.1021/acs.nanolett.6b02828.

Materials and Methods. Light microscopic image showing fiber agglomeration by using slow collection rates (Figure S1). Comparison of the mechanical properties of collagen microfibers collected at 0.11 and 1.92 m h^{-1} (Figure S2) and of collagen microfibers with average diameters of 3.7 and 6.8 μm (Figure S3) (PDF)

■ AUTHOR INFORMATION

Corresponding Author

*E-mail: thomas.scheibel@bm.uni-bayreuth.de.

Notes

The authors declare no competing financial interest.

■ ACKNOWLEDGMENTS

This work was funded by Deutsche Forschungsgemeinschaft (SCHE 603/14-1) and ERC Advanced Grant (STREAM, No. 291211). We would like to thank Dr. H. Bargel for SEM pictures, A. Pellert for the support in cell culture experiments, and A. Schedl for the help with TGA measurements. Further, we want to thank A. Heidebrecht, Professor G. Lang and Professor M. Trebbin for experimental support.

■ REFERENCES

(1) Scheibel, T. *Curr. Opin. Biotechnol.* **2005**, *16*, 427−33.
(2) Kadler, K. E.; Baldock, C.; Bella, J.; Boot-Handford, R. P. *J. Cell Sci.* **2007**, *120*, 1955−1958.
(3) Zhu, B.; Li, W.; Lewis, R. V.; Segre, C. U.; Wang, R. *Biomacromolecules* **2015**, *16*, 202−213.
(4) Gelse, K.; Poschl, E.; Aigner, T. *Adv. Drug Delivery Rev.* **2003**, *55*, 1531−1546.
(5) Kuhn, K. *Connect. Tissue Res.* **1982**, *10*, 5−10.
(6) Kadler, K. E.; Holmes, D. F.; Trotter, J. A.; Chapman, J. A. *Biochem. J.* **1996**, *316*, 1−11.
(7) Shoulders, M. D.; Raines, R. T. *Annu. Rev. Biochem.* **2009**, *78*, 929−58.
(8) Lintz, E. S.; Scheibel, T. R. *Adv. Funct. Mater.* **2013**, *23*, 4467−4482.
(9) Parkinson, J.; Kadler, K. E.; Brass, A. *J. Mol. Biol.* **1995**, *247*, 823−831.
(10) Lee, C. H.; Singla, A.; Lee, Y. *Int. J. Pharm.* **2001**, *221*, 1−22.
(11) Maeda, M.; Tani, S.; Sano, A.; Fujioka, K. *J. Controlled Release* **1999**, *62*, 313−24.
(12) Parenteau-Bareil, R.; Gauvin, R.; Berthod, F. *Materials* **2010**, *3*, 1863−1887.
(13) Zeugolis, D. I.; Paul, R. G.; Attenburrow, G. *J. Appl. Polym. Sci.* **2008**, *108*, 2886−2894.
(14) Hagenau, A.; Suhre, M. H.; Scheibel, T. R. *Prog. Polym. Sci.* **2014**, *39*, 1564−1583.
(15) Siriwardane, M. L.; DeRosa, K.; Collins, G.; Pfister, B. J. *Biofabrication* **2014**, *6*, 015012.
(16) Caves, J. M.; Kumar, V. A.; Wen, J.; Cui, W.; Martinez, A.; Apkarian, R.; Coats, J. E.; Berland, K.; Chaikof, E. L. *J. Biomed Mater. Res. B Appl. Biomater* **2010**, *93*, 24−38.
(17) Cavallaro, J. F.; Kemp, P. D.; Kraus, K. H. *Biotechnol. Bioeng.* **1994**, *43*, 781−791.
(18) Dunn, M. G.; Avasarala, P. N.; Zawadsky, J. P. *J. Biomed. Mater. Res.* **1993**, *27*, 1545−1552.
(19) Yaari, A.; Schilt, Y.; Tamburu, C.; Raviv, U.; Shoseyov, O. *ACS Biomater. Sci. Eng.* **2016**, *2*, 349−360.
(20) Whitesides, G. M. *Nature* **2006**, *442*, 368−73.
(21) Jun, Y.; Kang, E.; Chae, S.; Lee, S. H. *Lab Chip* **2014**, *14*, 2145−60.
(22) Kinahan, M. E.; Filippidi, E.; Koster, S.; Hu, X.; Evans, H. M.; Pfohl, T.; Kaplan, D. L.; Wong, J. *Biomacromolecules* **2011**, *12*, 1504−11.
(23) Lee, P.; Lin, R.; Moon, J.; Lee, L. P. *Biomed. Microdevices* **2006**, *8*, 35−41.
(24) Koster, S.; Evans, H. M.; Wong, J. Y.; Pfohl, T. *Biomacromolecules* **2008**, *9*, 199−207.
(25) Onoe, H.; Okitsu, T.; Itou, A.; Kato-Negishi, M.; Gojo, R.; Kiriya, D.; Sato, K.; Miura, S.; Iwanaga, S.; Kuribayashi-Shigetomi, K.; Matsunaga, Y. T.; Shimoyama, Y.; Takeuchi, S. *Nat. Mater.* **2013**, *12*, 584−590.
(26) Jun, Y.; Kim, M. J.; Hwang, Y. H.; Jeon, E. A.; Kang, A. R.; Lee, S. H.; Lee, D. Y. *Biomaterials* **2013**, *34*, 8122−30.
(27) Yeh, C. H.; Lin, P. W.; Lin, Y. C. *Microfluid. Nanofluid.* **2010**, *8*, 115−121.
(28) Williams, B. R.; Gelman, R. A.; Poppke, D. C.; Piez, K. A. *J. Biol. Chem.* **1978**, *253*, 6578−85.
(29) Silver, F. H. *J. Biol. Chem.* **1981**, *256*, 4973−4977.
(30) Doblhofer, E.; Heidebrecht, A.; Scheibel, T. *Appl. Microbiol. Biotechnol.* **2015**, *99*, 9361−80.
(31) Ingham, K. C. *Arch. Biochem. Biophys.* **1978**, *186*, 106−113.
(32) Honig, W.; Kula, M. R. *Anal. Biochem.* **1976**, *72*, 502−512.
(33) Chen, Y.; Wang, L.; Xue, Y.; Jiang, L.; Zheng, Y. *Sci. Rep.* **2013**, *3*, 2927.
(34) Tian, X.; Chen, Y.; Zheng, Y.; Bai, H.; Jiang, L. *Adv. Mater.* **2011**, *23*, 5486−91.
(35) Bai, H.; Sun, R.; Ju, J.; Yao, X.; Zheng, Y.; Jiang, L. *Small* **2011**, *7*, 3429−33.
(36) Nguyen, T. T.; Eklouh-Molinier, C.; Sebiskveradze, D.; Feru, J.; Terryn, C.; Manfait, M.; Brassart-Pasco, S.; Piot, O. *Analyst* **2014**, *139*, 2482−8.
(37) Bi, X.; Li, G.; Doty, S. B.; Camacho, N. P. *Osteoarthritis Cartilage* **2005**, *13*, 1050−8.
(38) Huanglee, L. L. H.; Cheung, D. T.; Nimni, M. E. *J. Biomed. Mater. Res.* **1990**, *24*, 1185−1201.
(39) Chae, H. G.; Kumar, S. *Science* **2008**, *319*, 908−909.
(40) Miles, C. A.; Ghelashvili, M. *Biophys. J.* **1999**, *76*, 3243−3252.
(41) Walton, R. S.; Brand, D. D.; Czernuszka, J. T. *J. Mater. Sci.: Mater. Med.* **2010**, *21*, 451−461.
(42) Arafat, M. T.; Tronci, G.; Yin, J.; Wood, D. J.; Russell, S. J. *Polymer* **2015**, *77*, 102−112.
(43) Hepworth, D. G.; Smith, J. P. *Composites, Part A* **2002**, *33*, 797−803.
(44) Gosline, J.; Lillie, M.; Carrington, E.; Guerette, P.; Ortlepp, C.; Savage, K. *Philos. Trans. R. Soc., B* **2002**, *357*, 121−32.
(45) Kwak, E. A.; Ahn, S.; Jaworski, J. *Biomacromolecules* **2015**, *16*, 1761−70.

DOI: 10.1021/acs.nanolett.6b02828
Nano Lett. 2016, 16, 5917−5922

Supporting Information for

Microfluidics-produced collagen fibers show extraordinary mechanical properties

Christian Haynl,[†] *Eddie Hofmann,* [‡] *Kiran Pawar,* [†] *Stephan Förster,*[‡,ǁ,¶] *and Thomas Scheibel*[*,†,ǁ,¶,§,#,⊥]

[†]Lehrstuhl Biomaterialien, Fakultät für Ingenieurwissenschaften, Universität Bayreuth, Universitätsstraße 30, 95440 Bayreuth, Germany

[‡]Lehrstuhl Physikalische Chemie I, Universität Bayreuth, Universitätsstraße 30, 95440 Bayreuth, Germany

[ǁ]Bayreuther Zentrum für Kolloide und Grenzflächen (BZKG), Universität Bayreuth, Universitätsstraße 30, 95440 Bayreuth, Germany

[¶]Bayerisches Polymerinstitut (BPI), Universitätsstraße 30, 95440 Bayreuth, Germany

[§]Bayreuther Zentrum für Molekulare Biowissenschaften (BZMB), Universität Bayreuth, Universitätsstraße 30, 95440 Bayreuth, Germany

[#]Institut für Bio-Makromoleküle (bio-mac), Universität Bayreuth, Universitätsstraße 30, 95440 Bayreuth, Germany

[⊥]Bayreuther Materialzentrum (BayMAT), Universität Bayreuth, Universitätsstraße 30, 95440 Bayreuth, Germany

To whom correspondence should be adressed: thomas.scheibel@bm.uni-bayreuth.de

Materials and Methods

Microfluidic collagen microfiber production. Acid-soluble collagen type I extracted from calf skin was purchased from Sigma Aldrich Life Sciences. Collagen was dissolved in diluted acetic acid at pH 3 for 20 hours. The solution was centrifuged for 10 min at 17000 x g, and the supernatant was removed for further experimentation (4.8 mg ml^{-1}). For microfiber formation, a buffer solution was prepared with 10 % (w/v) PEG 20000, 4.14 mg ml^{-1} $NaH_2PO_4 \bullet 2\ H_2O$, 12.1 mg ml^{-1} Na_2HPO_4, 6.86 mg ml^{-1} TES (2-[(2-Hydroxy-1,1-bis(hydroxymethyl)ethyl)amino]-ethane-sulfonic acid) and 7.89 mg ml^{-1} NaCl and adjusted to pH 8 using NaOH.[1] The microfluidic chip device enabling asymmetric hydrodynamic focusing of the collagen solution was designed and produced similarly to Kinahan *et al*., 2011.[2] In brief, the chips consisted of a top and a bottom layer each contributing to the microchannel structure. PDMS (Sylgard® 184, Dow Corning) was mixed in a curing-agent-to-base ratio of 1:10, poured onto a silicon wafer acting as a microchannel stamp and degassed for 2 h. After incubation in an oven for 2 h at 75 °C, holes were punched into the upper chip half for creating inlets for the tubes. Subsequently, both halves were cleaned with isopropanol and dried in an air flow before applying them to a plasma oven (MiniFlecto® PC-MFC, Plasma Technology GmbH) for 30 s, 0.5 mbar, 64 W and an air supply of 10 sccm. Small water droplets were pipetted onto the two chip halves, and both were fitted to each other using a light microscope. Finally, the bonded chips were dried in an oven over night at 35 °C. The inlet channel for the collagen solution was 200 µm wide and 60 µm high. The inlet channel for the buffer was 50 µm wide and 150 µm high. The channel after the cross intersection possessed a size of 200 µm in width and 210 µm in height.

FTIR spectroscopy. Polarized FTIR spectra of collagen microfibers were taken on a Bruker Tensor 27 IR spectroscope connected to a hyperion unit. Microfibers were produced and air-

dried at room temperature for 3 days. Subsequently, microfibers were fixed to plastic frames and were exposed either to non-polarized or polarized (parallel or perpendicular to longitudinal microfiber axis) radiation. The resolution was 4 cm^{-1}. Peak areas of the amide I and amide II bands were integrated, and the ratio of the amide I to amide II peak area was calculated. The IR spectrum of polyethylene glycol (PEG) was measured on a Bruker Tensor 27 using an ATR module and a resolution of 4 cm^{-1}.

Tensile test. Mechanical measurements of air-dried (3 days) microfibers, fixed to plastic frames (gauge length of 2 mm) with a high-viscosity acrylate glue, were carried out at 30 % humidity on a tensile testing machine (Bose Electroforce 3220 equipped with a 0.49 N load cell) using an extension rate of 0.3 mm min^{-1}. Engineered stress σ was calculated as the force divided by the cross-sectional area assumed to be circular. The cross-sectional area was calculated upon measuring the microfiber diameter at ten different positions. Strain ε was defined as the change in microfiber length divided by its original length. Young's modulus E was determined as the slope of the stress-strain curve in the linear elastic deformation range (2 % strain). Microfiber toughness was assessed by integration of the stress-strain plot using Origin 8.1G.

Microscopy. Microfibers were air-dried for 3 days at room temperature and SEM pictures of platinum sputtered microfibers (2 nm platinum coating) were taken using a Zeiss 1540 EsB CrossBeam. Light microscopy was carried out using a Leica Microscope DMI 3000B.

Thermal characterization. Microfibers were air-dried for 3 days at room temperature. Differential scanning calorimetry (DSC) was conducted on a DSC1 (Mettler Toledo) by applying 1.3 mg of fibers under nitrogen-atmosphere conditions and a heating rate of 20 °C min^{-1}. Thermal weight loss was examined using thermogravimetric analysis (TGA) (TGA/SDTA 851e System). Curves were generated under oxygen-atmosphere conditions at a heating rate of 10 °C

min^{-1} using 3.9 mg of sample.

Cell culture. Microfibers for cell culture testing were continuously collected on metal frames as aligned fibers and sterilized with UV light treatment for 30 min. The neuronal cell line NG108-15 was obtained from the European Collection of Cell Culture (ECACC) and grown in complete Dulbecco's Modified Eagle Medium (DMEM) (Biochrom) containing 10 % v/v fetal bovine serum (Biochrom), 2 mM GlutaMAX (Gibco) and 1 % gentamicin in a humidified atmosphere with 5 % CO_2 at 37 °C. Cells were trypsinized for experiments after they became 80-90 % confluent and cells were seeded directly on microfibers at a density of 10^4 cells cm^{-2} in a small amount of complete medium without serum in order to induce axon growth.[3, 4] After 30 min of incubation, additional medium was added lacking serum. At day three (72 h) of incubation with 5 % CO_2 at 37 °C, the culture medium was removed, and cells were fixed with 4 % paraformaldehyde (PFA). Fixed cells were permeabilized using 0.1 % Triton X-100 (Sigma Aldrich) in phosphate buffered saline (PBS) (Sigma Aldrich) followed by blocking with 5 % bovine serum albumin (BSA) (Sigma Aldrich) in PBS. The primary rabbit antibody anti-ßIII-tubulin (polyclonal) (abcam) for detection of neuronal-specific cell structures was diluted 1:1000 in 0.1 % Triton X-100 in PBS, and cells were incubated for 2 h at room temperature. Subsequently, the secondary antibody Alexa fluor 488 goat anti-rabbit (1:1000 dilution in PBS with 0.1 % Triton X-100) (Invitrogen) was applied for further 2 h to detect the primary antibody. In order to detect actin filaments and cell nuclei, phalloidin (TRITC) (Sigma Aldrich) and Hoechst 33258 pentahydrate (Invitrogen) were used. Samples were imaged by using a fluorescence microscope (Leica DMi8). Experiments were carried out in non-treated culture plates (Thermo Scientific).

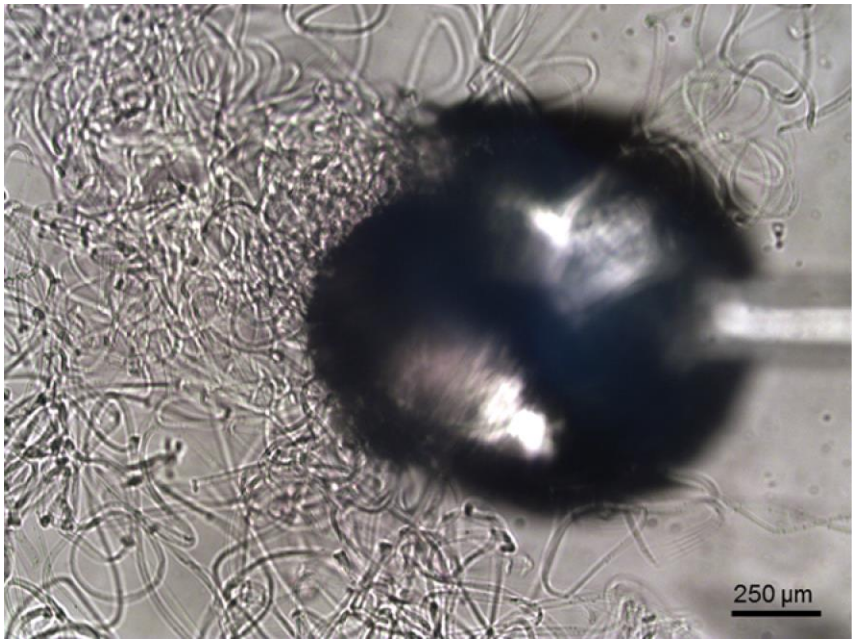

Figure S1. Light-microscopic image of the collagen fiber extrusion from the microfluidic chip outlet (black area) without collecting them on a rotating spool. Extruded fibers form agglomerations/entanglements due to absent (or slow) collection rates.

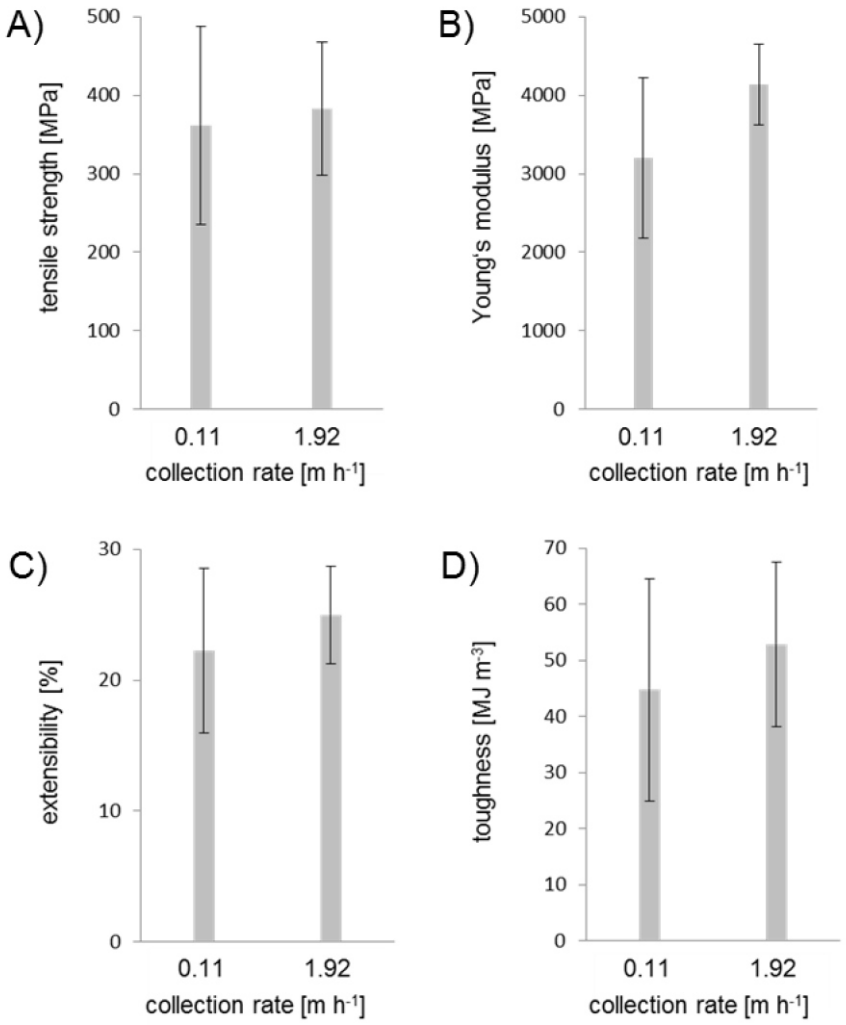

Figure S2. Comparison of the mechanical properties of collagen fibers drawn at a collection rate of 0.11 m h^{-1} versus 1.92 m h^{-1}. (A) Tensile strength, (B) Young's modulus, (C) extensibility and (D) toughness. Error bars indicate the standard deviation.

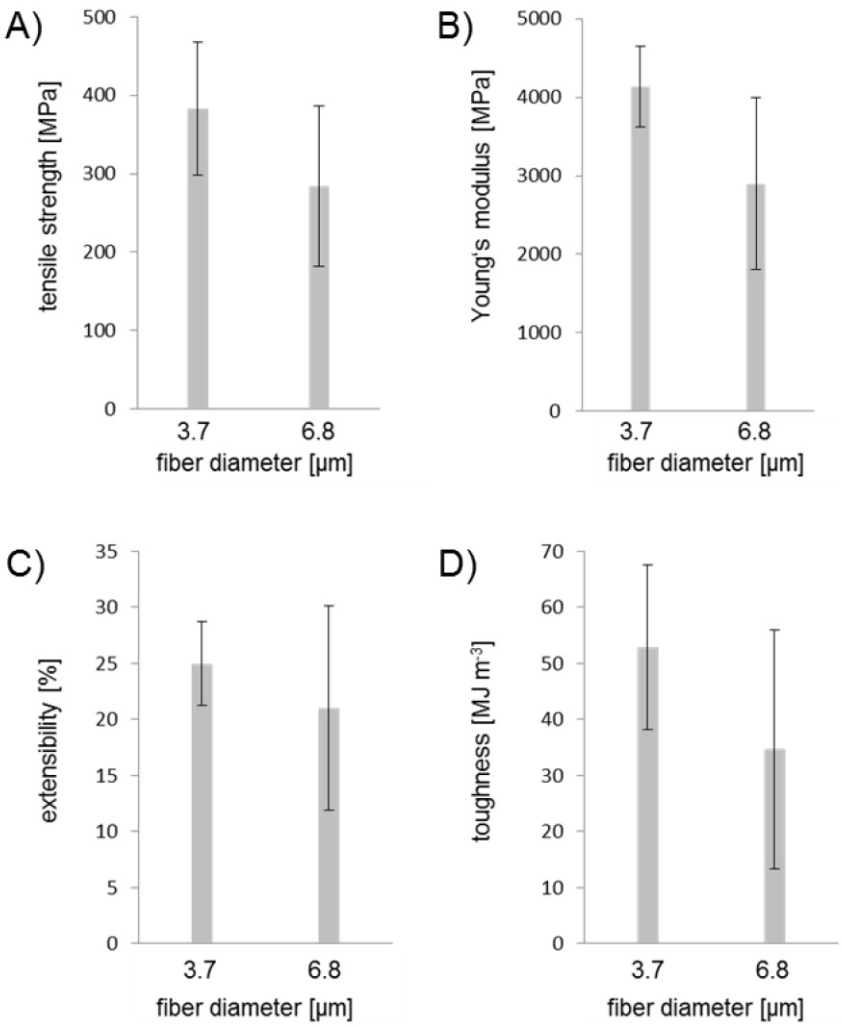

Figure S3. Comparison of the mechanical properties of collagen fibers having fiber diameters of 3.7 $^{+}$/- 1.2 and 6.8 $^{+}$/- 1.9 µm. (A) Tensile strength, (B) Young's modulus, (C) extensibility and (D) toughness. Error bars indicate the standard deviation.

REFERENCES

(1) Caves, J. M.; Kumar, V. A.; Wen, J.; Cui, W.; Martinez, A.; Apkarian, R.; Coats, J. E.; Berland, K.; Chaikof, E. L. *J Biomed Mater Res B Appl Biomater* **2010**, *93*, 24-38.

(2) Kinahan, M. E.; Filippidi, E.; Koster, S.; Hu, X.; Evans, H. M.; Pfohl, T.; Kaplan, D. L.; Wong, J. *Biomacromolecules* **2011**, *12*, 1504-11.

(3) Pun, S.; Yang, J. F.; Ng, Y. P.; Tsim, K. W. K. *Febs Lett* **1997**, *418*, 275-281.

(4) Dhir, V.; Natarajan, A.; Stancescu, M.; Chunder, A.; Bhargava, N.; Das, M.; Zhai, L.; Molnar, P. *Biotechnol Progr* **2009**, *25*, 594-603.

7.3 Teilarbeit 3

Pawar, K.; Welzel, G.; **Haynl, C.**; Schuster, S.; Scheibel, T.*

Recombinant spider silk and collagen-based nerve guidance conduits support neuronal cell differentiation and functionality *in vitro*.

ACS Applied Bio Materials **2019**, 2, 4872-4880

DOI: 10.1021/acsabm.9b00628

ACS APPLIED BIO MATERIALS
Cite This: ACS Appl. Bio Mater. 2019, 2, 4872−4880
Article
www.acsabm.org

Recombinant Spider Silk and Collagen-Based Nerve Guidance Conduits Support Neuronal Cell Differentiation and Functionality in Vitro

Kiran Pawar,[†,▽] Georg Welzel,[‡] Christian Haynl,[†] Stefan Schuster,[‡] and Thomas Scheibel*[,†,§,∥,⊥,#]

[†]Department for Biomaterials, University of Bayreuth, Prof.-Rüdiger-Bormann-Strasse 1, 95447 Bayreuth, Germany
[‡]Department of Animal Physiology, [§]Bayreuther Zentrum für Kolloide und Grenzflächen (BZKG), [∥]Bayreuther Zentrum für Molekulare Biowissenschaften (BZMB), [⊥]Bayreuther Materialzentrum (BayMAT), and [#]Bayerisches Polymerinstitut (BPI), University of Bayreuth, Universitätsstraße 30, 95447 Bayreuth, Germany

Supporting Information

ABSTRACT: Biomaterial scaffolds are under investigation as therapeutic tools to bridge nerve endings following traumatic peripheral nerve injury. The goal is to develop biocompatible nerve guidance conduits (NGCs) with internal guiding structures that promote longitudinally oriented cell migration and regeneration. In the present study, a nonwoven mesh (NWM) made of a recombinant spider silk protein was processed into a tubular structure, ensuring structural integrity of enclosed microfluidics-produced collagen fibers for cell and neurite guidance. The differentiated type of the neuroblastoma X glioma hybrid cell line NG108-15 was used as a model for studying neuronal differentiation on the individual components and on the complete NGC. Differentiated NG108-15 cells grown on recombinant spider silk NWM and collagen fibers formed neuronal networks and synapses. Additionally, whole-cell patch clamp recordings confirmed that all components supported the differentiation of NG108-15 cells into functional neurons. Our NGC demonstrated that tubes made of recombinant spider silk NWM filled with microfluidics-produced collagen fibers are well suited for peripheral nerve repair.

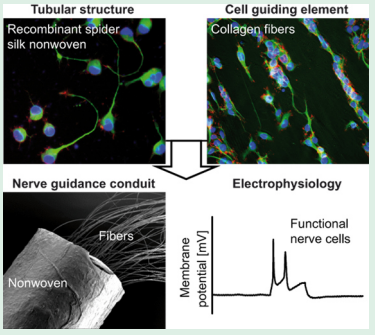

KEYWORDS: *recombinant spider silk, collagen, nerve guidance conduit, neuronal cell differentiation, electrophysiology*

INTRODUCTION

Traumatic peripheral nerve injury affects about 2.8% of all trauma patients, causing long-term disability and reduced function.[1] Twenty million Americans suffer from peripheral nerve injury caused by trauma and medical disorder, which results in approximately $150 billion spent in annual United States health care.[2] In Europe, approximately 300,000 cases of peripheral nerve injury occur every year.[3] To treat peripheral nerve injury, the gold standard in the current clinical approach is autologous nerve grafts that are used to compensate for loss and damage of nerve tissue. However, autologous grafts have severe disadvantages, such as their limited availability, the loss of sensation at the donor site, and the need for multiple surgeries.[4] Thus, biocompatible, non-degradable and degradable materials are under investigation for peripheral nerve repair. These materials include biocompatible, nondegradable, and degradable materials. The ideal biomaterial for nerve application is considered to be compatible with the host's immune system and should support cell adhesion, migration, proliferation, differentiation, cell−cell interaction, and should provide a favorable microenvironment for functional tissue regeneration. Furthermore, these materials should have appropriate degradation rates and suitable mechanical properties.[5,6] Vitally important in neural tissue engineering is the establishment of a physical guidance structure to allow controlled axon growth for bridging the lesion cavity.[7,8] In particular, regeneration of nerve tissue is enhanced when using aligned fibers, because those support the formation of the Büngner bands involved in peripheral nerve repair.[9] Fibers used for peripheral nerve repair are, besides naturally occurring ones such as silk, usually prepared using electro- and wet spinning.[9−11]

The biomaterials for peripheral nerve repair tested thus far include collagen,[12−14] polycaprolactone,[15,16] polyglycolic acid and polylactic acid,[17] chitosan,[18,19] alginate,[20] spider silk,[7,21] silkworm fibroin,[22−26] and other composites or derivatives made thereof.[8,27] Of particular interest is spider silk and collagen and combining them allows for the fabrication of materials with tailored biological activity and mechanical stability.[28] Spider silk is well-known for its good mechanical properties[29,30] and does not contain the sometimes problematic sericin as associated with silkworm silk.[31,32] Moreover, spider silk has been demonstrated to be suitable for peripheral nerve repair: natural spider silk placed in isogenic veins enabled the generation of nerve grafts bridging a 2 cm gap injury in the sciatic nerve of rats.[7] Nerve conduits, prepared by

Received: July 11, 2019
Accepted: October 3, 2019
Published: October 3, 2019

DOI: 10.1021/acsabm.9b00628
ACS Appl. Bio Mater. 2019, 2, 4872−4880

decellularized vein grafts filled with natural spider silk fibers, were implanted in 6 cm tibial nerve defects in adult sheep and exhibited axon regeneration and functional recovery through the nerve guidance conduits (NGCs).[21] Despite the beneficial properties of natural spider silk, its commercial use is very limited as sufficient amounts, especially with consistent quality, cannot be achieved due to difficulties (i.e., spider cannibalism) in spider farming.[32] Therefore, major efforts have been made toward the recombinant production of spider silk proteins, for example, using *Escherichia coli* as host.[33−36] Matrices based on recombinant spider silk have been evaluated regarding their suitability for in vitro cell culture and tissue engineering applications,[37−40] and neural stem cells cultured thereon differentiated efficiently into neurons and astrocytes.[41] The recombinant spider silk proteins used in the current study are based on ADF4 (*Araneus diadematus fibroin 4*), one of the major ampullate spidroins of the dragline silk of the European garden spider. The sequence of the spider silk gene was adapted (i.e., engineered) for recombinant production, and the encoded amino acid sequence consisted of 16 repeats of a consensus (C) sequence, which mimicked the repetitive core domain of native ADF4, therefore it was termed eADF4(C16) (abbreviated: C16).[42] Previous studies on electrospun C16 nonwoven matrices demonstrated their excellent biocompatibility, good cell interaction, and biodegradability,[43−45] and nanofibers thereof maintained good mechanical properties even at high humidity.[46] C16 was further modified with the cell-binding RGD amino acid motif yielding eADF4(C16)-RGD (abbreviated: C16-RGD). Films made thereof exhibited significantly improved attachment and proliferation of BALB/3T3 mouse fibroblasts in comparison to films of the unmodified C16 variant.[47]

Collagen as the major component of the extracellular matrix (ECM) is highly bioactive, supporting cell adhesion and migration as well as tissue scaffolding, morphogenesis, and repair,[48−50] but usually loses a certain degree of mechanical stability at wet conditions.[51,52] The internal structure of a peripheral nerve shows the epineurium, perineurium, and endoneurium, comprising single or bundled collagen fibrils and networks.[53] The endoneurium surrounds a collagen-rich basement membrane that provides myelinated axons with functional support.[6,54] Thus, collagen may be regarded as the material of choice for peripheral nerve repair. In a recent study, microfluidics-produced collagen fibers allowed neuronal cell adhesion, and neurites of differentiated cells were highly aligned along the fiber axes due to the low diameters.[12] The collagen fibers could be spun continuously and they exhibited mechanical properties, outcompeting that of previous collagen fibers without the need of cross-linking; thus, these fibers show high suitability in nerve repair among other possible applications.[12]

Currently, one of the limitations of commercially available NGCs is the length of the defect that can be treated and the lack of a suitable internal guidance.[55] This study was designed in order to investigate a novel NGC made of a recombinant spider silk nonwoven mesh (NWM) tube that ensures structural integrity of enclosed, microfluidics-produced collagen fibers, allowing guidance of neuronal cells and their neurites and at the same time allows for sufficient nutrient exchange. Each individual NGC component was investigated in terms of neuronal NG108-15 cell adhesion and differentiation. In order to test the functionality of the formed neural networks, differentiated cells on the NGC components were investigated electrophysiologically using whole-cell patch clamp tests. With this work, we demonstrate that the individual components, as well as our whole NGC, have the potential to be further investigated in in vivo injury models and clinical applications for nerve repair.

MATERIALS AND METHODS

Recombinant Spider Silk Protein Production. The engineered recombinant spider silk protein eADF4(C16) (abbreviated: C16) is based on the consensus sequence of one of the spidroins of the dragline silk of the European garden spider (*Araneus diadematus*). The consensus motif (C-module) of ADF4 (GSSAAAAAAAASGPGG-YGPENQGPSGPGGYGPGGP) is repeated 16 times in the recombinant protein. Production in *E. coli* and purification was performed as described by Huemmerich et al.[33] Production and purification of eADF4(C16)RGD (abbreviated: C16-RGD) was identical to that of C16 as described earlier by Wohlrab et al.[47]

Fabrication of Nerve Guidance Materials. In order to produce spider silk nonwoven meshes (NWMs), recombinant spider silk proteins were dissolved in 1,1,1,3,3,3-hexafluoro-2-propanol (10% w/v) (HFIP, Alfa Aesar, Germany) and electrospun as described in Leal-Egana et al.[44] A solution of 10% (w/v) spider silk protein in HFIP yielded fiber diameters of 120−150 nm after spinning. Resulting NWMs were exposed to ethanol or ethanol vapor in order to convert the α-helical protein structures into ß-sheet ones, thereby yielding water-insoluble spider silk nanofibers. NWMs collected on glass coverslips were immersed in ethanol, whereas NWMs wrapped on needle templates (1 mm outer diameter) to create tube structures were exposed to ethanol vapor in a closed beaker. The closed beaker was maintained in an oven for 4 h at 60 °C. Collagen fibers were produced using a microfluidic chip device according to Haynl et al.[12] Therefore, acid-soluble, purified collagen type I extracted from calf skin (Sigma-Aldrich Life Sciences, Germany) was dissolved in diluted acetic acid (0.5% v/v at pH 3) for 20 h to yield a collagen concentration of 0.48% (w/v). Fiber formation was induced within the microfluidic chip by interaction of the collagen solution with a buffer solution comprising PEG 20,000 (10% w/v) (Carl Roth, Germany), $NaH_2PO_4 \cdot 2H_2O$ (4.14 mg mL^{-1}) (Carl Roth, Germany), Na_2HPO_4 (12.1 mg mL^{-1}) (Carl Roth, Germany), TES (6.86 mg mL^{-1}) (2-[(2-hydroxy-1,1-bis(hydroxymethyl)ethyl)amino]-ethanesulfonic acid (Carl Roth, Germany), and NaCl (7.89 mg mL^{-1}) (Carl Roth, Germany) at pH 8. Collagen fibers were continuously collected on a rotating spool using a collagen flow rate of 50 μL h^{-1}, buffer flow of 300 μL h^{-1}, and a collection rate of 3.8 m h^{-1}. For producing the complete NGC, the endings of aligned collagen fibers were glued onto a wire and then inserted into the C16-RGD NWM tube. Finally, the wire was removed by cutting the collagen fibers next to it using a sharp razor blade.

Cell Culture Studies. Flat and tubular spider silk NWM and collagen fibers prepared on glass coverslips were used for cell culture studies. Furthermore, NWM tubes filled with aligned collagen fibers were analyzed in cell culture tests, too. The neuronal cell line NG108-15 was obtained from the European Collection of Cell Culture (ECACC) and grown in complete Dulbecco's Modified Eagle Medium (DMEM; Biochrom, Germany) containing fetal bovine serum (10% v/v) (Biochrom, Germany), GlutaMAX (2×10^{-3} M) (Gibco, U.S.A.), and gentamicin (1%) (Sigma-Aldrich, Germany) in a humidified atmosphere (5% CO_2) at 37 °C. Cells were trypsinized after they became 80−90% confluent and they were seeded directly on different substrates (density of 10^4 cells cm^{-2}) in a small amount of complete medium without fetal bovine serum in order to induce their differentiation.[56] For electrophysiology measurements, cells were cultured in complete medium without serum but with N_2 supplement (1% v/v) (Gibco, U.S.A.) and cyclic adenosine monophosphate (10×10^{-3} M) (cAMP; Sigma-Aldrich, Germany) for 3 weeks. Similar cell densities were used for cells cultured on individual morphologies (i.e., NWM and aligned collagen fibers) as well as on the complete NGC construct. For cell seeding in the NGC construct, a similar cell number was seeded in small aliquots. Cells were incubated with 5%

DOI: 10.1021/acsabm.9b00628
ACS Appl. Bio Mater. 2019, 2, 4872−4880

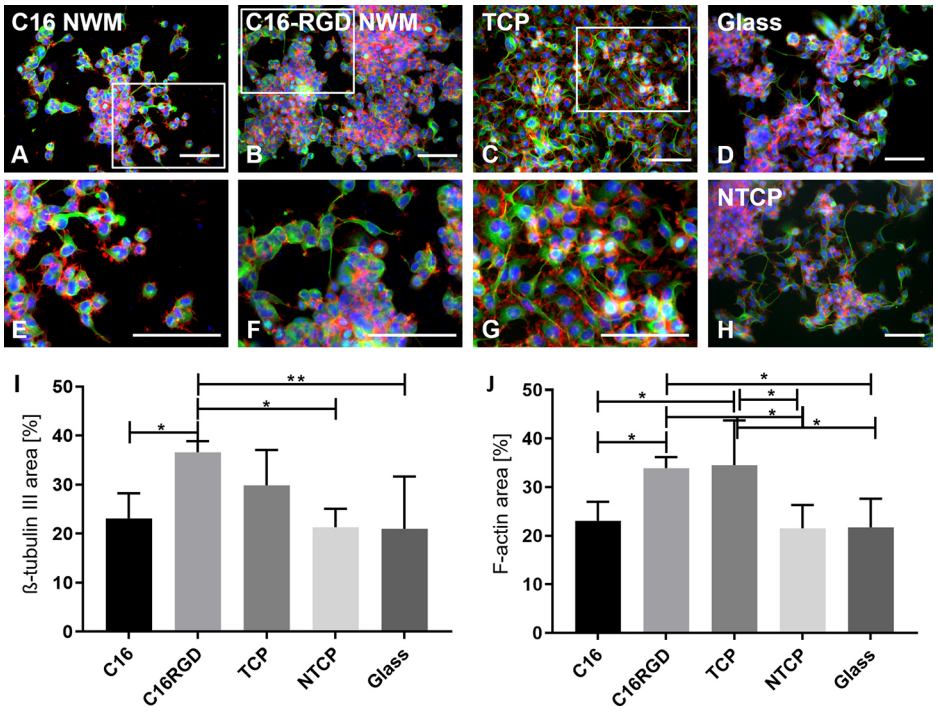

Figure 1. NG108-15 neuronal cell adhesion on recombinant spider silk NWM and controls at proliferation conditions after 3 days of culture. Fluorescence images of stained cells on (A) C16 NWM, (B) C16-RGD NWM, and (C) TCP used as a control for good cell adhesion. (E−G) Magnified images of selected areas (white squares) of panels A−C. (D) Glass and (H) NTCP were used as controls for poor cell adhesion. (I,J) Quantification of percentage area on different substrates due to positive staining of the axonal marker β-tubulin III (green) and F-actin visualized with phalloidin (red). Cell nuclei are indicated using Hoechst staining (blue). Scale bars: 100 μm. Significance levels: *($p < 0.05$), **($p < 0.005$).

CO_2 at 37 °C, the culture medium was removed and cells were fixed with paraformaldehyde (4% w/v) at day 3 and week 3. For immunocytochemistry, cells were permeabilized using Triton X-100 (0.1% v/v) (Sigma-Aldrich, Germany) in phosphate-buffered saline (PBS; Sigma-Aldrich, Germany) followed by blocking with bovine serum albumin (5% w/v in PBS) (Sigma-Aldrich, Germany). The primary rabbit antibody anti-ß-tubulin III (polyclonal) (Abcam, U.K.) for detection of neuronal specific cell structures and the mouse antibody anti-SNAP25 (monoclonal) (Abcam, U.K.) for detection of the cell membranes, cell junctions, and synapses were used. Antibodies were diluted (1:1000 in 0.1% v/v Triton X-100 in PBS) and cells were incubated for 2 h at room temperature. Subsequently, the secondary antibodies Alexa Fluor 488 goat anti-rabbit (Invitrogen, U.S.A.) or Alexa Fluor 594 goat anti-mouse (Abcam, U.K.) (respectively 1:1000 in 0.1% v/v Triton X-100 in PBS) were applied for additional 2 h to detect the primary antibody. In order to detect actin filaments, phalloidin-TRITC (Sigma-Aldrich, Germany) was used. Cell nuclei were stained using Hoechst 33258 pentahydrate (Invitrogen, U.S.A.). Samples were imaged using a fluorescence microscope (Leica DMi8, Germany), and images were processed using Leica Application Suite (LAS), Adobe Photoshop, and ImageJ. Experiments were carried out in nontreated culture plates (NTCP) (Thermo Scientific, Germany). The number of pixels occupied by β-tubulin III and F-actin was assessed using ImageJ software. For analysis of cell viability and morphology, cells cultured on C16-RGD NWM tubes and on collagen fibers were stained with Calcein acetoxymethyl ester (Calcein A/M; Invitrogen, U.S.A.) and ethidium homodimer-I (EthD-I; Invitrogen, U.S.A.). A solution containing Calcein and A/M (final concentration 2×10^{-6} M) and EthD-I (final concentration 4×10^{-6} M) was added to the samples and incubated for 30−40 min at 37 °C. After incubation, the staining solution was removed and fresh PBS was added. Live and dead cells were visualized using fluorescence microscopy (Leica DMi8, Germany).

Microscopy. Flat spider silk NWMs, tubular NWMs, and aligned collagen fibers were air-dried after production (and after post-treatment in case of the NWMs). Light microscopy images were obtained using a light microscope (Leica DMI, Germany). Scanning electron microscopy (SEM) images of sputter-coated samples (2 nm coating of platinum) were taken using a Zeiss Sigma VP 300.

Electrophysiology. NG108-15 cells were cultured on spider silk NWMs or collagen fibers, which were prepared on glass coverslips in advance. After 3 weeks in culture, the coverslips with the NWMs or collagen fibers and the NG108-15 cells were placed into a perfusion chamber (RC-25, Warner Instruments) located on the stage of an inverted microscope (Axio Vert.A1, Zeiss). The chamber was continuously perfused (0.5 mL min^{-1}) with an external solution (140×10^{-3} M NaCl, 3.5×10^{-3} M KCl, 2×10^{-3} M $MgCl_2$, 2×10^{-3} M $CaCl_2$, 10×10^{-3} M HEPES, and 10×10^{-3} M glucose at pH 7.3) using a peristaltic pump (Reglo Digital, Ismatec). Whole-cell patch clamp recordings of NG108-15 cells were performed using an EPC-10 patch-clamp amplifier controlled by Patchmaster software (HEKA Electronics). Recording electrodes (3−6 MΩ tip resistance) were pulled from borosilicate glass (BF150-86-10, Sutter Instruments) on a horizontal puller (P-97, Sutter Instruments) and filled with an internal solution (130×10^{-3} M K-gluconate, 2×10^{-3} M $MgCl_2$, 1×10^{-3} M EGTA, and 15×10^{-3} M Hepes at pH 7.2). External and internal solutions were sterile filtered prior to use. All recordings were performed at room temperature.

Statistical Analysis. Results are expressed as mean ± SD (standard deviation) unless otherwise indicated. One-way ANOVA with Tukey's multiple comparison tests was performed. Statistical evaluation was performed using GraphPad Prism 7 for Windows (GraphPad Software). Significance levels are indicated as follows: *($p < 0.05$), **($p < 0.005$), ***($p < 0.0005$), and ****($p < 0.0001$).

RESULTS AND DISCUSSION

Adhesion and Differentiation of Neuronal Cells on Recombinant Spider Silk Nonwoven Meshes. NWMs were produced by electrospinning of a spider silk solution onto glass coverslips (Figure S1), and neuronal NG108-15 cells were cultured thereon for 3 days either at proliferation or

DOI: 10.1021/acsabm.9b00628
ACS Appl. Bio Mater. 2019, 2, 4872−4880

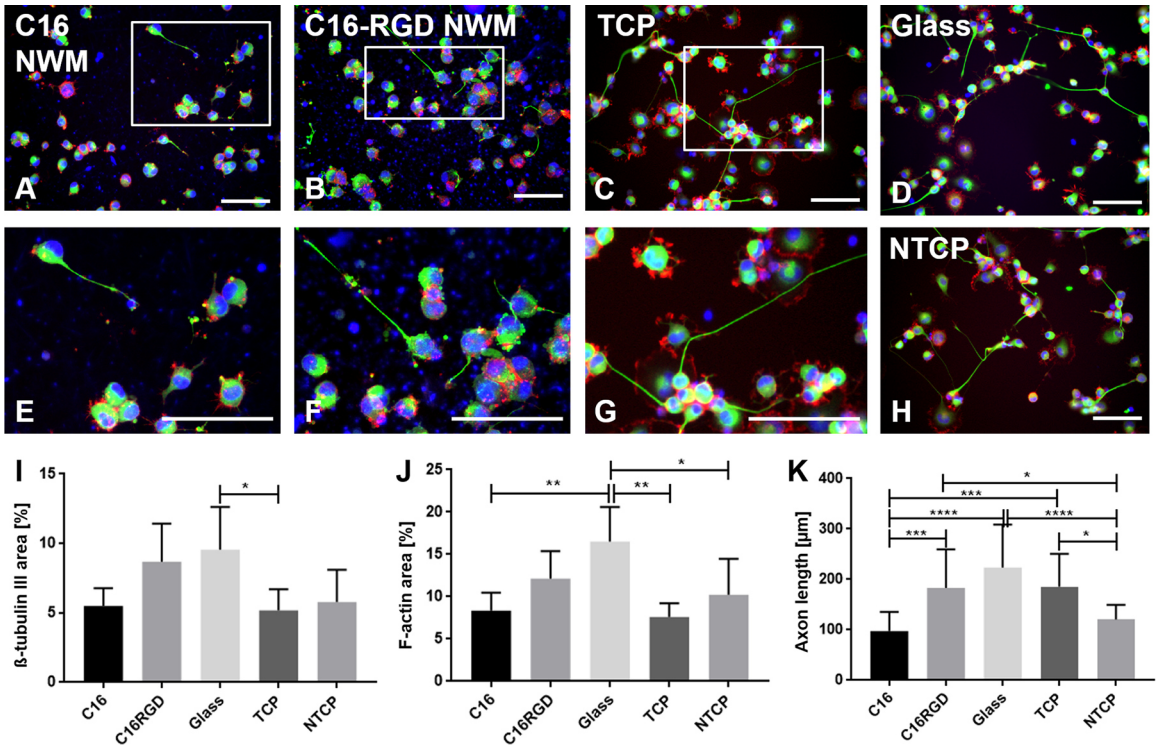

Figure 2. NG108-15 neuronal cells on recombinant spider silk NWM and controls upon differentiation after 3 days of culture. Fluorescence images of stained cells on (A) C16 NWM, (B) C16-RGD NWM, and (C) TCP used as a control for good cell adhesion. (E−G) Magnified images of selected areas (white squares) of panels A−C. (D) Glass and (H) NTCP were used as controls for poor cell adhesion. (I,J) Quantification of percentage area on different substrates due to positive staining of the axonal marker β-tubulin III (green) and F-actin visualized with phalloidin (red). (K) Axon length on different substrates. Cell nuclei are indicated using Hoechst staining (blue). Scale bars: 100 μm. Significance levels: *($p < 0.05$), **($p < 0.005$), ***($p < 0.0005$), ****($p < 0.0001$).

differentiation conditions. NG108-15 cells have been investigated in vitro in previous studies in terms of their neuronal differentiation as well as action potential generation.[57,58] Here, NG108-15 cells cultured at proliferation conditions (in complete medium with 10% fetal bovine serum) were investigated in terms of their adhesion only. At differentiation conditions (medium without fetal bovine serum), differentiated cells were examined in terms of their adhesion and their neurite lengths. We also investigated cell adhesion and differentiation on different substrates, that is, on a treated tissue culture plate (TCP) as a control for good cell adhesion, as well as on glass and on a nontreated tissue culture plates (NTCP) as a control for poor cell adhesion.

Cell adhesion and differentiation on NWMs and controls were investigated by immunostaining of ß-tubulin III, which is an axonal marker. Additionally, we used phalloidin-TRITC (hereafter phalloidin) for staining filamentous actin (F-actin), which visualized the cytoskeleton. Neuronal cells cultured on C16 NWM at proliferation conditions (Figure 1A,E) showed less cell adhesion compared to NWMs made of the variant with the cell binding RGD motif, C16-RGD (Figure 1B,F). Cells adhered better on C16-RGD NWM than on glass (Figure 1D) and NTCP (Figure 1H). In contrast, the TCP control (Figure 1C,G) showed a similar cell adhesion behavior compared to C16-RGD NWMs. Cells cultured on C16-RGD NWMs showed the highest percentage area calculated from the positive staining of ß-tubulin III (Figure 1I) followed by TCP, C16 NWM, NTCP, and glass. The percentage area derived from visualizing positive F-actin staining for C16-RGD NWMs was similar to that of TCP (Figure 1J). Quantifying the percentage area for positive ß-tubulin III and F-actin staining showed significant differences between C16 and C16-RGD NWMs ($p < 0.05$).

Cells cultured at differentiation conditions showed very few cells with neurite formation on C16 NWMs (Figure 2A,E) when compared to C16-RGD NWMs (Figure 2B,F). Consequently, we detected cells on C16-RGD NWMs with significantly longer neurite extensions ($p < 0.0005$) compared to C16 NWMs (Figure 2K) and with multiple neurites making contacts with adjacent cells forming small networks. Quantifying the percentage area showed no significant differences between C16 and C16-RGD NWMs, neither for ß-tubulin III nor F-actin expression (Figure 2I,J). At proliferation conditions, the glass negative control showed a lower cell density compared to the positive control TCP (as seen in Figure 1). This trend was not observed at differentiation conditions as the percentage area for ß-tubulin III and F-actin was greater in the glass control (Figure 2D,I,J) than on TCP (Figure 2C,G,I,J) and on NTCP (Figure 2H−J). The high percentage area in the negative controls may have resulted from the combined effect of cell aggregates and ECM deposition by cells. The ECM contributed to a higher number of positive pixels in the selected area for quantification compared to the monolayer control as obtained in TCP (Figure 2C,G). Cell aggregates showed also neurite extensions at differentiation.

Long-Term Neuronal Cell Culture. Next, we investigated NWMs made of C16 and C16-RGD as well as microfluidics-produced collagen fibers at differentiation conditions in long-term cell culture experiments, that is, in a 3 week culture, to

DOI: 10.1021/acsabm.9b00628
ACS Appl. Bio Mater. 2019, 2, 4872−4880

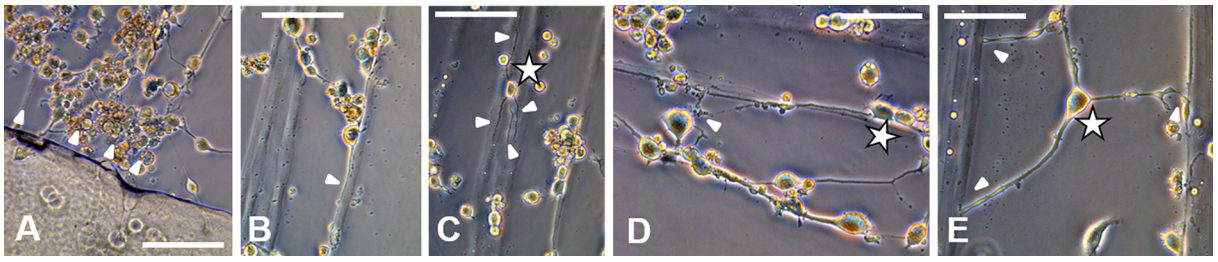

Figure 3. Light microscopy images showing NG108-15 neuronal cells on aligned collagen fibers at differentiation conditions after 3 weeks of culturing. (A) Aligned fibers glued onto a glass coverslip using silicon glue caused no cell toxicity during 3 weeks of incubation (arrowheads show fiber alignment). (B) Cells showing aligned neurite growth on/along fibers (indicated by the white arrowhead). (C) Cells on fibers with multiple neurites (asterisk indicates a single cell, arrowheads show neurites making connections with fibers). (D) Cells forming extended neural networks on fibers (asterisk shows connected cells). (E) Cells with neurite and growth cone formation making contact with fibers (asterisk shows a cell, arrowheads indicate neurites). Scale bars: 100 μm.

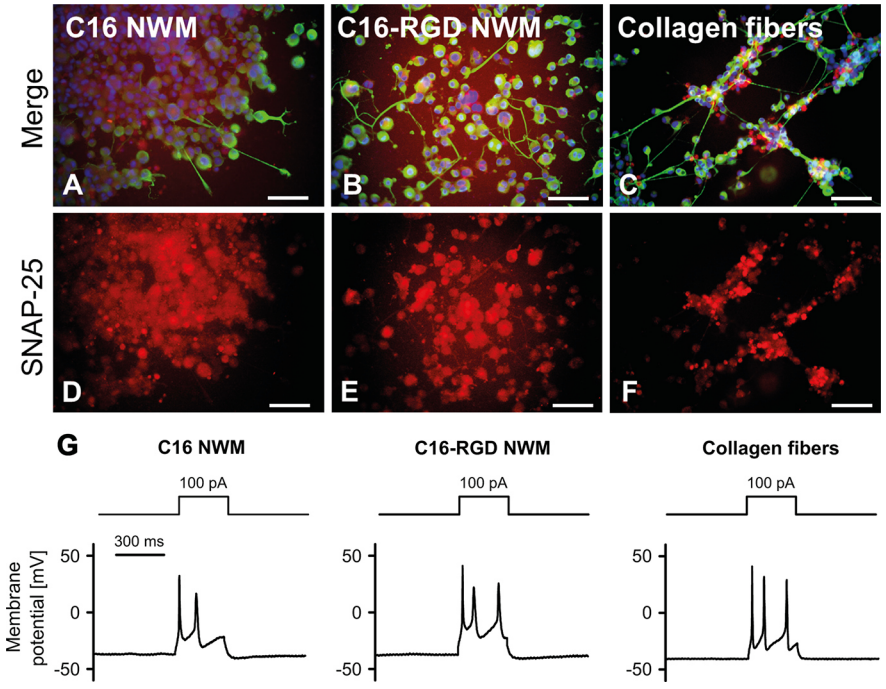

Figure 4. NG108-15 cells grown on recombinant spider silk NWM and collagen fibers differentiate into fully functional neurons after 3 weeks of culturing. Neural network formation on (A) C16 NWM, (B) C16-RGD NWM, and on (C) collagen fibers. SNAP-25 expression (red) shows synapse formation of cells grown on NWM made of (D) C16, (E) C16-RGD, and on (F) aligned collagen fibers. (G) Whole-cell patch clamp recordings from NG108-15 cells grown on NWM made of C16 and C16-RGD and on aligned collagen fibers, demonstrating the capability of generating action potentials in response to current injections (100 pA, 300 ms). Scale bars: 100 μm.

test neural network and synapse formation as well as functionality of NG108-15 cells. In accordance with a previously published study,[12] the used collagen fibers effectively supported cell adhesion and directed neurite outgrowth, which can be seen in Figures S2 and S3, respectively. The NWM for the long-term experiments were prepared on glass coverslips and showed no detachment from the glass during the 3 weeks of incubation. Conversely, it proved to be difficult to keep aligned collagen fibers in culture for 3 weeks without detachment. Therefore, we glued aligned collagen fibers onto glass coverslips using a biocompatible silicon glue (Figure 3A). Because of handling issues and floating fibers, ß-tubulin III and F-actin quantifications were not carried out and cell adhesion and axon outgrowth was shown qualitatively only. Cells attached to collagen fibers showed neurite outgrowth on and along the fiber axis (Figure 3B). Some cells on fibers showed multiple neurite formations (Figure 3C). We also observed cells with long neurite outgrowths forming connections with other cells along the fiber axis (Figure 3D). Some cells attached on the underlying glass surface showed multiple neurites with growth cones reaching out forming connections with the collagen fibers (Figure 3E). Interestingly, cells cultured on the glass control (without collagen fibers) did not show any cell adhesion, suggesting that cells in direct contact to collagen fibers secreted ECM components promoting cell adhesion.

To investigate neurite growth and synapse formation at differentiation conditions after 3 weeks of culturing, we visualized a similar ß-tubulin III expression as for the short-term (3 day) cell culture studies. In addition, we also visualized the synaptosomal-associated protein 25 (SNAP-25), a component of the soluble *N*-ethylmaleimide-sensitive-factor attachment receptor (SNARE) complex mediating the exocytotic release of neurotransmitters at chemical synapses.[59]

DOI: 10.1021/acsabm.9b00628
ACS Appl. Bio Mater. 2019, 2, 4872−4880

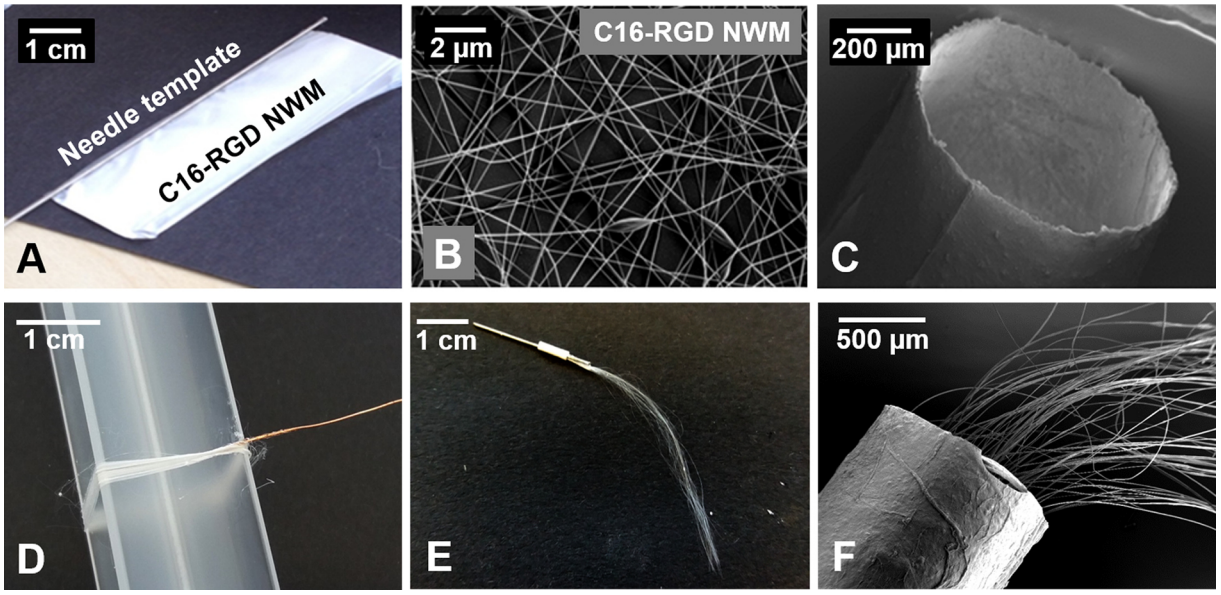

Figure 5. Snapshots of the processing of NGCs. (A) C16-RGD NWMs prepared using electrospinning were rolled around a needle template to form a tubular structure. (B) Scanning electron microscope (SEM) image of the underlying electrospun NWM. (C) The SEM image shows the achieved tube. (D) Collagen fibers were continuously spun using microfluidics and collected on a rotating spool. (E) Aligned collagen fibers, glued onto a wire, were inserted into the NWM tube. (F) SEM image showing collagen fibers within the NWM tube.

The NMWs made of both recombinant spider silk variants supported neurite extension as well as the formation of neural networks, but on C16-RGD NWMs they showed more networks in comparison to C16 NWMs (Figure 4A,B). All cells on the recombinant spider silk NWMs expressed the synaptic marker SNAP-25 (Figure 4D,E). Aligned collagen fibers provided the longest neurite extensions, and these extensions even crossed between different fibers forming layered networks (Figure 4C). On collagen fibers, cells also showed expression of SNAP-25 (Figure 4F). Some of the somata in our positive controls were stained with SNAP-25, but most of the SNAP-25 staining was observed in the contact area between cell bodies, where numerous neurites and small branches fasciculated (Figure S4).

To confirm the functionality of the apparently differentiated NG108-15 cells, we examined whole-cell current clamp recordings. These aimed at demonstrating neuronal excitability and the capability of generating action potentials as previously described.[60−62] It is crucial that the cells were capable of prodding action potentials as these are essential for neuronal excitation, propagation, and stimulus-evoked neurotransmitter release (which is important for neuron-to-neuron communication).[63] Because NG108-15 cells were shown previously to require up to 3 weeks of differentiation until they are capable of generating action potentials,[62] we cultured them for 3 weeks on both NWM variants and on collagen fibers. Strikingly, we demonstrated for all three substrates that NG108-15 cells were able to differentiate into functional neurons that fire action potentials in response to current injection (100 pA) (Figure 4G). In these cells, we identified differentiation-induced changes in membrane properties that were comparable to that of NG108-15 cells grown and differentiated on standard culture dishes.[62] In comparison to differentiated NG108-15 cells that were not able to generate action potentials after 3 weeks, the differentiated cells with action potentials had a more negative resting membrane potential, an increased maximum rate of depolarization, as well as an increased depolarization amplitude, and no significant differences were observed between the tested materials (Table S1 shows the mean values for all three materials). Because of handling problems with the TCP, laminin-coated samples were used as positive controls for the electrophysiological experiments, since they showed a comparable cell response to TCP in terms of neurite formation and SNAP-25 expression (Figure S4).

These findings confirmed that recombinant spider silk NWMs and microfluidics-produced collagen fibers are not only biocompatible but also support functionality of neuronal cells. Thus, both materials were combined to yield an NGC, allowing high neurite alignment on the collagen fibers, whereas a tube made of the recombinant spider silk NWM ensured the structural integrity of the enclosed collagen fibers as well as the supply of nutrients, and at the same time would prevent inflammatory cells from migrating into the nerve defect in vivo.

Nerve Guidance Conduits. Nerve guidance conduits (NGCs) were prepared using C16-RGD NWMs and aligned collagen fibers. NWMs were collected on black paper, removed, and wrapped around a needle template (Figure 5A). The surface morphology, as well as the final tubular structure, are depicted in Figure 5B,C, respectively. The NWM tube was post-treated in ethanol vapor to induce ß-sheet formation rendering the recombinant spider silk fibers water-insoluble.[64] Collagen fibers were produced continuously and were collected on a rotating spool (Figure 5D). For better handling, we glued aligned collagen fiber bundles at one site onto a wire and inserted them into the NWM tube (Figure 5E,F). For all in vitro experiments, the tubes were filled as much as possible with a thick fiber bundle.

We subsequently seeded the complete NGC with NG108-15 cells. Live−dead assays showed differentiated cells on the inner surface of the tube and on protruding collagen fibers, and very few dead cells after 3 days overall (Figure S5). Long-term cell culture studies (3 weeks) of neuronal cell differentiation in the NGC were carried out, and β-tubulin III and F-actin expression were visualized. In accordance with the previous

DOI: 10.1021/acsabm.9b00628
ACS Appl. Bio Mater. 2019, 2, 4872−4880

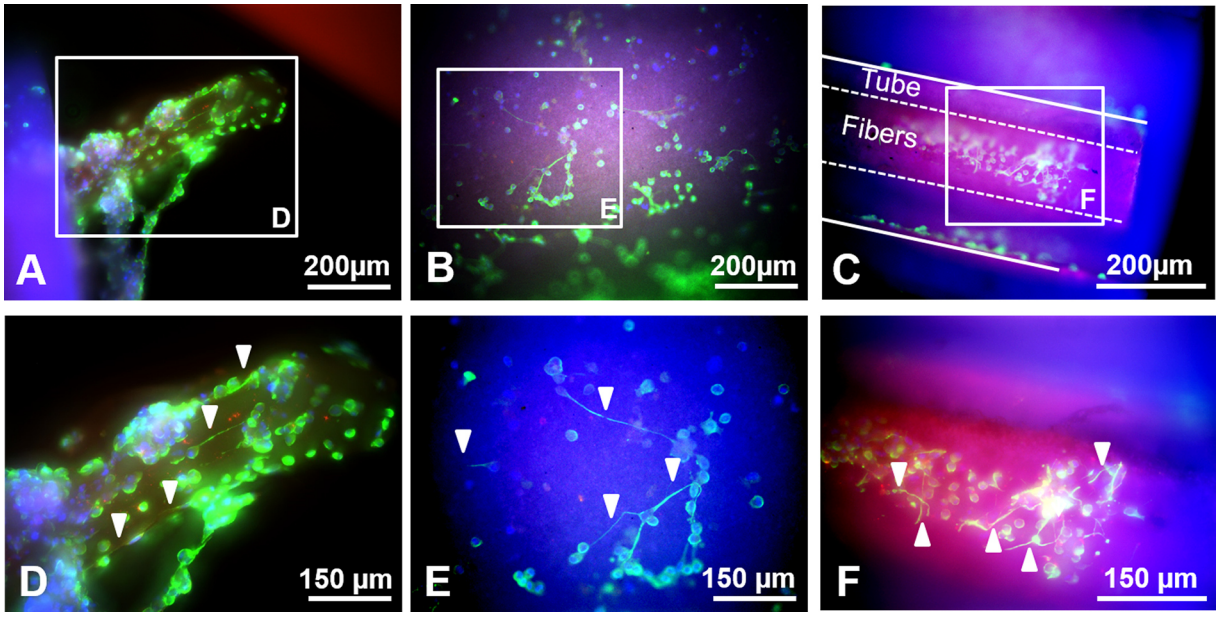

Figure 6. Expression of β-tubulin III (green) and F-actin (red) in NG108-15 cells upon differentiation in NGCs for 3 weeks.(A) Cells cultured in a C16-RGD NWM tube filled with aligned collagen fibers showed neurite formation on the protruding collagen fibers. (B) Neurite formation detected on the inner tube wall of the NGC. (C) Differentiated cells with neurites on collagen fibers within the NGC. Dotted lines enclose the inner section comprising fibers; solid lines show the tube walls. (D–F) Magnifications according to the white rectangles of images A–C. White arrowheads show neurites on the inner surface of the tube and on collagen fibers.

experiments using flat NWMs and collagen fibers separately, the whole NGC showed good cell adhesion and differentiation, indicated by neurite outgrowth along protruding collagen fibers (Figure 6A and D) and on the inner tube wall (Figure 6 B and E). Similarly, we showed that cells differentiated and formed networks on aligned collagen fibers within the tube (Figure 6C and F). It is worth mentioning that for microscopical analysis, the enclosed collagen fibers became disaligned during tube opening in contrast to the situation seen in Figure 6 A and D.

CONCLUSION

NGCs made of biocompatible and biodegradable materials are a promising material to support repair of completely transected nerves. Here, we prepared NWM tubes made of recombinant spider silk and filled them with aligned collagen fibers to yield a novel type of NGC. No chemical cross-linking was necessary to yield those materials. The NWM and the collagen fibers enabled neuronal cell differentiation with neurites forming networks. Most importantly, the neuronal cells that had formed in contact with the individual NGC components were fully capable of firing action potentials, and the expression of SNAP-25 indicated the formation of functional synapses. In summary, the combination of both materials is highly beneficial, because the collagen fibers allow high neurite alignment and a biomimetic environment, whereas the NWM tube ensures the structural integrity of the collagen fibers. The NWM tube will further prevent inflammatory cells from migrating into the nerve defect as well as maintain nutrient, gas, and waste metabolite removal due to its porous structure.

ASSOCIATED CONTENT

Supporting Information

The Supporting Information is available free of charge on the ACS Publications website at DOI: 10.1021/acsabm.9b00628.

Images of recombinant spider silk nonwovens on glass coverslips. Images showing adhesion and differentiation of NG108-15 cells on aligned collagen fibers. NG108-15 cell differentiation and synapse formation on a laminin-coated glass coverslip and on a treated tissue culture plate (TCP). Differentiation-induced changes in membrane properties of NG108-15 cells grown on recombinant spider silk NWM and on collagen fibers. Live dead staining of NG108-15 cells differentiated in the NGC (PDF)

AUTHOR INFORMATION

Corresponding Author

*E-mail: thomas.scheibel@bm.uni-bayreuth.de.

ORCID

Thomas Scheibel: 0000-0002-0457-2423

Present Address

$^{\nabla}$(K.P.) University of British Columbia, ICORD, 818 West 10th Avenue, Vancouver, Canada V5Z 1M9.

Author Contributions

The original manuscript draft was written by K.P., edited by C.H., G.W. and T.S. and proofread by S.S. All authors have given approval to the final version of the manuscript.

Funding

This work was funded by Elite Netzwerk Bayern, Technology Alliance Upper Franconia (TAO) and Bayerisches Polymerinstitut (BPI) (1524-BP-79–01).

Notes

The authors declare no competing financial interest.

ACKNOWLEDGMENTS

The authors would like to thank Dr. Hendrik Bargel for the help with taking SEM images, Alexandra Pellert for the support

during cell culture experiments, and Dr. Stephen Strassburg for language proofreading.

REFERENCES

(1) Chen, M. B.; Zhang, F.; Lineaweaver, W. C. Luminal fillers in nerve conduits for peripheral nerve repair. *Ann. Plast. Surg.* **2006**, *57*, 462−471.
(2) Grinsell, D.; Keating, C. P. Peripheral nerve reconstruction after Injury: a review of clinical and experimental therapies. *BioMed Res. Int.* **2014**, *2014*, 1.
(3) Cinteza, D.; Persinaru, I.; Maciuceanu Zarnescu, B. M.; Ionescu, D.; Lascar, I. Peripheral Nerve Regeneration - an Appraisal of the Current Treatment Options. *Maedica (Buchar)* **2015**, *10*, 65−68.
(4) Lee, S. K.; Wolfe, S. W. Peripheral Nerve Injury and Repair. *J. Am. Acad. Orthop. Surg.* **2000**, *8*, 243−252.
(5) Gu, X. Progress and perspectives of neural tissue engineering. *Front. Med.* **2015**, *9*, 401−411.
(6) Lackington, W. A.; Ryan, A. J.; O'Brien, F. J. Advances in nerve guidance conduit-based therapeutics for peripheral nerve repair. *ACS Biomater. Sci. Eng.* **2017**, *3*, 1221−1235.
(7) Allmeling, C.; Jokuszies, A.; Reimers, K.; Kall, S.; Choi, C. Y.; Brandes, G.; Kasper, C.; Scheper, T.; Guggenheim, M.; Vogt, P. M. Spider silk fibres in artificial nerve constructs promote peripheral nerve regeneration. *Cell Proliferation* **2008**, *41*, 408−420.
(8) Ciardelli, G.; Chiono, V. Materials for Peripheral Nerve Regeneration. *Macromol. Biosci.* **2006**, *6*, 13−26.
(9) Chew, S. Y.; Mi, R.; Hoke, A.; Leong, K. W. The effect of the alignment of electrospun fibrous scaffolds on Schwann cell maturation. *Biomaterials* **2008**, *29*, 653−661.
(10) Cai, J.; Peng, X.; Nelson, K. D.; Eberhart, R.; Smith, G. M. Permeable guidance channels containing microfilament scaffolds enhance axon growth and maturation. *J. Biomed. Mater. Res., Part A* **2005**, *75A*, 374−386.
(11) Siriwardane, M. L.; DeRosa, K.; Collins, G.; Pfister, B. J. Controlled formation of cross-linked collagen fibers for neural tissue engineering applications. *Biofabrication* **2014**, *6*, 015012.
(12) Haynl, C.; Hofmann, E.; Pawar, K.; Förster, S.; Scheibel, T. Microfluidics-produced collagen fibers show extraordinary mechanical properties. *Nano Lett.* **2016**, *16*, 5917−5922.
(13) Bozkurt, A.; Claeys, K. G.; Schrading, S.; Rodler, J. V.; Altinova, H.; Schulz, J. B.; Weis, J.; Pallua, N.; van Neerven, S. G. A. Clinical and biometrical 12-month follow-up in patients after reconstruction of the sural nerve biopsy defect by the collagen-based nerve guide Neuromaix. *Eur. J. Med.Res.* **2017**, *22*, 34.
(14) Yao, L.; DeBrot, A. Fabrication and Characterization of a Protein Composite Conduit for Neural Regeneration. *ACS Appl. Bio Mater.* **2019**.
(15) Daud, M. F. B.; Pawar, K. C.; Claeyssens, F.; Ryan, A. J.; Haycock, J. W. An aligned 3D neuronal-glial co-culture model for peripheral nerve studies. *Biomaterials* **2012**, *33*, 5901−5913.
(16) Panahi-Joo, Y.; Karkhaneh, A.; Nourinia, A.; Abd-Emami, B.; Negahdari, B.; Renaud, P.; Bonakdar, S. Design and fabrication of a nanofibrous polycaprolactone tubular nerve guide for peripheral nerve tissue engineering using a two-pole electrospinning system. *Biomed. Mater.* **2016**, *11*, 025017.
(17) Wang, Y.-L.; Gu, X.-M.; Kong, Y.; Feng, Q.-L.; Yang, Y.-M. Electrospun and woven silk fibroin/poly(lactic-co-glycolic acid) nerve guidance conduits for repairing peripheral nerve injury. *Neural Regener. Res.* **2015**, *10*, 1635−1642.
(18) Gu, Y.; Zhu, J.; Xue, C.; Li, Z.; Ding, F.; Yang, Y.; Gu, X. Chitosan/silk fibroin-based, Schwann cell-derived extracellular matrix-modified scaffolds for bridging rat sciatic nerve gaps. *Biomaterials* **2014**, *35*, 2253−2263.
(19) Biazar, E.; Keshel, S. H. Chitosan−Cross-Linked Nanofibrous PHBV Nerve Guide for Rat Sciatic Nerve Regeneration Across a Defect Bridge. *ASAIO J.* **2013**, *59*, 651−659.
(20) Pawar, K.; Mueller, R.; Caioni, M.; Prang, P.; Bogdahn, U.; Kunz, W.; Weidner, N. Increasing capillary diameter and the incorporation of gelatin enhance axon outgrowth in alginate-based anisotropic hydrogels. *Acta Biomater.* **2011**, *7*, 2826−2834.
(21) Radtke, C.; Allmeling, C.; Waldmann, K. H.; Reimers, K.; Thies, K.; Schenk, H. C.; Hillmer, A.; Guggenheim, M.; Brandes, G.; Vogt, P. M. Spider silk constructs enhance axonal regeneration and remyelination in long nerve defects in sheep. *PLoS One* **2011**, *6*, No. e16990.
(22) Hu, A.; Zuo, B.; Zhang, F.; Zhang, H.; Lan, Q. Evaluation of Electronspun Silk Fibroin-Based Transplants Used for Facial Nerve Repair. *Otol. Neurotol.* **2013**, *34*, 311−318.
(23) Xue, C. B.; Zhu, H.; Tan, D. H.; Ren, H. C.; Gu, X. K.; Zhao, Y. H.; Zhang, P.; Sun, Z. C.; Yang, Y. M.; Gu, J. H.; Gu, Y.; Gu, X. S. Electrospun silk fibroin-based neural scaffold for bridging a long sciatic nerve gap in dogs. *J. Tissue Eng. Regener. Med.* **2018**, *12*, E1143−E1153.
(24) White, J. D.; Wang, S.; Weiss, A. S.; Kaplan, D. L. Silk-tropoelastin protein films for nerve guidance. *Acta Biomater.* **2015**, *14*, 1−10.
(25) Uebersax, L.; Mattotti, M.; Papaloizos, M.; Merkle, H. P.; Gander, B.; Meinel, L. Silk fibroin matrices for the controlled release of nerve growth factor (NGF). *Biomaterials* **2007**, *28*, 4449−4460.
(26) Dinis, T. M.; Vidal, G.; Jose, R. R.; Vigneron, P.; Bresson, D.; Fitzpatrick, V.; Marin, F.; Kaplan, D. L.; Egles, C. Complementary effects of two growth factors in multifunctionalized silk nanofibers for nerve reconstruction. *PLoS One* **2014**, *9*, No. e109770.
(27) Dong, D.-m.; Wei, G.-j.; Meng; Wang, Y.-s.; Zhou, C.-w.; Wan, D.-y.; Lei, P.-z.; Jian; Lei, H.-w. Promotion of peripheral nerve regeneration of a peptide compound hydrogel scaffold. *Int. J. Nanomed.* **2013**, *8*, 3217−3225.
(28) Zhu, B.; Li, W.; Lewis, R. V.; Segre, C. U.; Wang, R. E-Spun Composite Fibers of Collagen and Dragline Silk Protein: Fiber Mechanics, Biocompatibility, and Application in Stem Cell Differentiation. *Biomacromolecules* **2015**, *16*, 202.
(29) Blackledge, T. A.; Hayashi, C. Y. Silken toolkits: biomechanics of silk fibers spun by the orb web spider Argiope argentata (Fabricius 1775). *J. Exp. Biol.* **2006**, *209*, 2452−2461.
(30) Madsen, B.; Shao, Z. Z.; Vollrath, F. Variability in the mechanical properties of spider silks on three levels: interspecific, intraspecific and intraindividual. *Int. J. Biol. Macromol.* **1999**, *24*, 301−306.
(31) DeLee, J. C.; Smith, M. T.; Green, D. P. The reaction of nerve tissue to various suture materials: A study in rabbits. *J. Hand. Surg. Am.* **1977**, *2*, 38−43.
(32) Schacht, K.; Scheibel, T. Processing of recombinant spider silk proteins into tailor-made materials for biomaterials applications. *Curr. Opin. Biotechnol.* **2014**, *29*, 62−69.
(33) Huemmerich, D.; Helsen, C. W.; Quedzuweit, S.; Oschmann, J.; Rudolph, R.; Scheibel, T. Primary Structure Elements of Spider Dragline Silks and Their Contribution to Protein Solubility. *Biochemistry* **2004**, *43*, 13604−13612.
(34) Heidebrecht, A.; Scheibel, T. Recombinant production of spider silk proteins. *Adv. Appl. Microbiol.* **2013**, *82*, 115−153.
(35) Doblhofer, E.; Heidebrecht, A.; Scheibel, T. To spin or not to spin: spider silk fibers and more. *Appl. Microbiol. Biotechnol.* **2015**, *99*, 9361−9380.
(36) Thamm, C.; Scheibel, T. Recombinant production, characterization, and fiber spinning of an engineered short major ampullate spidroin (MaSp1s). *Biomacromolecules* **2017**, *18*, 1365−1372.
(37) Schacht, K.; Vogt, J.; Scheibel, T. Foams made of engineered recombinant spider silk proteins as 3D scaffolds for cell growth. *ACS Biomater. Sci. Eng.* **2016**, *2*, 517−525.
(38) Aigner, T. B.; DeSimone, E.; Scheibel, T. Biomedical applications of recombinant silk-based materials. *Adv. Mater.* **2018**, *30*, No. 1704636.
(39) Schacht, K.; Jüngst, T.; Schweinlin, M.; Ewald, A.; Groll, J.; Scheibel, T. Biofabrication of cell-loaded 3D spider silk constructs. *Angew. Chem., Int. Ed.* **2015**, *54*, 2816−2820.

DOI: 10.1021/acsabm.9b00628
ACS Appl. Bio Mater. 2019, 2, 4872−4880

(40) DeSimone, E.; Schacht, K.; Pellert, A.; Scheibel, T. Recombinant spider silk-based bioinks. *Biofabrication* **2017**, *9*, 044104.
(41) Lewicka, M.; Hermanson, O.; Rising, A. U. Recombinant spider silk matrices for neural stem cell cultures. *Biomaterials* **2012**, *33*, 7712−7717.
(42) Scheibel, T. Spider silks: recombinant synthesis, assembly, spinning, and engineering of synthetic proteins. *Microb. Cell Fact.* **2004**, *3*, 14.
(43) Steiner, D.; Lang, G.; Fischer, L.; Winkler, S.; Fey, T.; Greil, P.; Scheibel, T.; Horch, R. E.; Arkudas, A. Intrinsic Vascularization of Recombinant eADF4(C16) Spider Silk Matrices in the Arteriovenous Loop Model. *Tissue Eng. Part A* **2019**.
(44) Leal-Egana, A.; Lang, G.; Mauerer, C.; Wickinghoff, J.; Weber, M.; Geimer, S.; Scheibel, T. Interactions of fibroblasts with different morphologies made of an engineered spider silk protein. *Adv. Eng. Mater.* **2012**, *14*, B67−B75.
(45) Müller-Herrmann, S.; Scheibel, T. Enzymatic Degradation of Films, Particles, and Nonwoven Meshes Made of a Recombinant Spider Silk Protein. *ACS Biomater. Sci. Eng.* **2015**, *1*, 247−259.
(46) Lang, G.; Neugirg, B. R.; Kluge, D.; Fery, A.; Scheibel, T. Mechanical Testing of Engineered Spider Silk Filaments Provides Insights into Molecular Features on a Mesoscale. *ACS Appl. Mater. Interfaces* **2017**, *9*, 892−900.
(47) Wohlrab, S.; Müller, S.; Schmidt, A.; Neubauer, S.; Kessler, H.; Leal-Egana, A.; Scheibel, T. Cell adhesion and proliferation on RGD-modified recombinant spider silk proteins. *Biomaterials* **2012**, *33*, 6650−6659.
(48) Kadler, K. E.; Baldock, C.; Bella, J.; Boot-Handford, R. P. Collagens at a glance. *J. Cell Sci.* **2007**, *120*, 1955−1958.
(49) Lin, K. L.; Zhang, D. W.; Macedo, M. H.; Cui, W. G.; Sarmento, B.; Shen, G. F. Advanced collagen-based biomaterials for regenerative biomedicine. *Adv. Funct. Mater.* **2019**, *29*, 1804943.
(50) Sorushanova, A.; Delgado, L. M.; Wu, Z. N.; Shologu, N.; Kshirsagar, A.; Raghunath, R.; Mullen, A. M.; Bayon, Y.; Pandit, A.; Raghunath, M.; Zeugolis, D. I. The collagen suprafamily: from biosynthesis to advanced biomaterial development. *Adv. Mater.* **2019**, *31*, 1801651.
(51) Cavallaro, J. F.; Kemp, P. D.; Kraus, K. H. Collagen fabrics as biomaterials. *Biotechnol. Bioeng.* **1994**, *43*, 781−791.
(52) Kato, Y. P.; Christiansen, D. L.; Hahn, R. A.; Shieh, S. J.; Goldstein, J. D.; Silver, F. H. Mechanical-properties of collagen-fibers - a comparison of reconstituted and rat tail tendon fibers. *Biomaterials* **1989**, *10*, 38−41.
(53) Ushiki, T.; Ide, C. Three-dimensional organization of the collagen fibrils in the rat sciatic nerve as revealed by transmission- and scanning electron microscopy. *Cell Tissue Res.* **1990**, *260*, 175−184.
(54) Koopmans, G.; Hasse, B.; Sinis, N. The role of collagen in peripheral nerve repair. *Int. Rev. Neurobiol.* **2009**, *87*, 363−379.
(55) Arslantunali, D.; Dursun, T.; Yucel, D.; Hasirci, N.; Hasirci, V. Peripheral nerve conduits: technology update. *Med. Devices: Evidence Res.* **2014**, *7*, 405−424.
(56) Seidman, K. J. N.; Barsuk, J. H.; Johnson, R. F.; Weyhenmeyer, J. A. Differentiation of NG108-15 Neuroblastoma Cells by Serum Starvation or Dimethyl Sulfoxide Results in Marked Differences in Angiotensin II Receptor Subtype Expression. *J. Neurochem.* **1996**, *66*, 1011−1018.
(57) Molnar, P.; Hickman, J. J. Modeling of action potential generation in NG108-15 cells. *Methods Mol. Biol.* **2014**, *1183*, 253−261.
(58) Molnar, P.; Hickman, J. J. Modeling of action potential generation in NG108-15 cells. *Methods Mol. Biol.* **2007**, *403*, 175−184.
(59) Tafoya, L. C. R.; Mameli, M.; Miyashita, T.; Guzowski, J. F.; Valenzuela, C. F.; Wilson, M. C. Expression and function of SNAP-25 as a universal SNARE component in GABAergic neurons. *J. Neurosci.* **2006**, *26*, 7826−7838.
(60) Daniels, M. P.; Hamprecht, B. The ultrastructure of neuroblastoma glioma somatic cell hybrids. Expression of neuronal characteristics stimulated by dibutyryl adenosine 3′,5′ cyclic monophosphate. *J. Cell Biol.* **1974**, *63*, 691−699.
(61) Dolezal, V.; Castell, X.; Tomasi, M.; Diebler, M. F. Stimuli that induce a cholinergic neuronal phenotype of NG108-15 cells upregulate ChAT and VAChT mRNAs but fail to increase VAChT protein. *Brain Res. Bull.* **2001**, *54*, 363−373.
(62) Liu, J. X.; Tu, H. Y.; Zhang, D. Z.; Zheng, H.; Li, Y. L. Voltage-gated sodium channel expression and action potential generation in differentiated NG108-15 cells. *BMC Neurosci.* **2012**, *13*, 129.
(63) Casale, A. E.; McCormick, D. A. Active action potential propagation but not initiation in thalamic interneuron dendrites. *J. Neurosci.* **2011**, *31*, 18289−18302.
(64) Lang, G.; Jokisch, S.; Scheibel, T. Air filter devices including nonwoven meshes of electrospun recombinant spider silk proteins. *J. Visualized Exp.* **2013**, No. 50492.

DOI: 10.1021/acsabm.9b00628
ACS Appl. Bio Mater. 2019, 2, 4872−4880

Supporting Information

Recombinant Spider Silk and Collagen-Based Nerve Guidance Conduits Support Neuronal Cell Differentiation and Functionality *in vitro*

Kiran Pawar,[1,†] Georg Welzel,[2] Christian Haynl,[1] Stefan Schuster[2] and Thomas Scheibel[1,3,4,5,6,*]

[1]University of Bayreuth, Department for Biomaterials, Prof.-Rüdiger-Bormann-Str.1, 95447 Bayreuth, Germany

[2]University of Bayreuth, Department of Animal Physiology, Universitätsstraße 30, 95447 Bayreuth, Germany

[3]University of Bayreuth, Bayreuther Zentrum für Kolloide und Grenzflächen (BZKG), Universitätsstraße 30, 95447 Bayreuth, Germany

[4]University of Bayreuth, Bayreuther Zentrum für Molekulare Biowissenschaften (BZMB), Universitätsstraße 30, 95447 Bayreuth, Germany

[5]University of Bayreuth, Bayreuther Materialzentrum (BayMAT), Universitätsstraße 30, 95447 Bayreuth, Germany

[6]University of Bayreuth, Bayerisches Polymerinstitut (BPI), Universitätsstraße 30, 95447 Bayreuth, Germany

[†]Present address: University of British Columbia, ICORD, 818 West 10th Avenue, Vancouver, BC Canada V5Z 1M9

*To whom correspondence should be addressed: thomas.scheibel@bm.uni-bayreuth.de

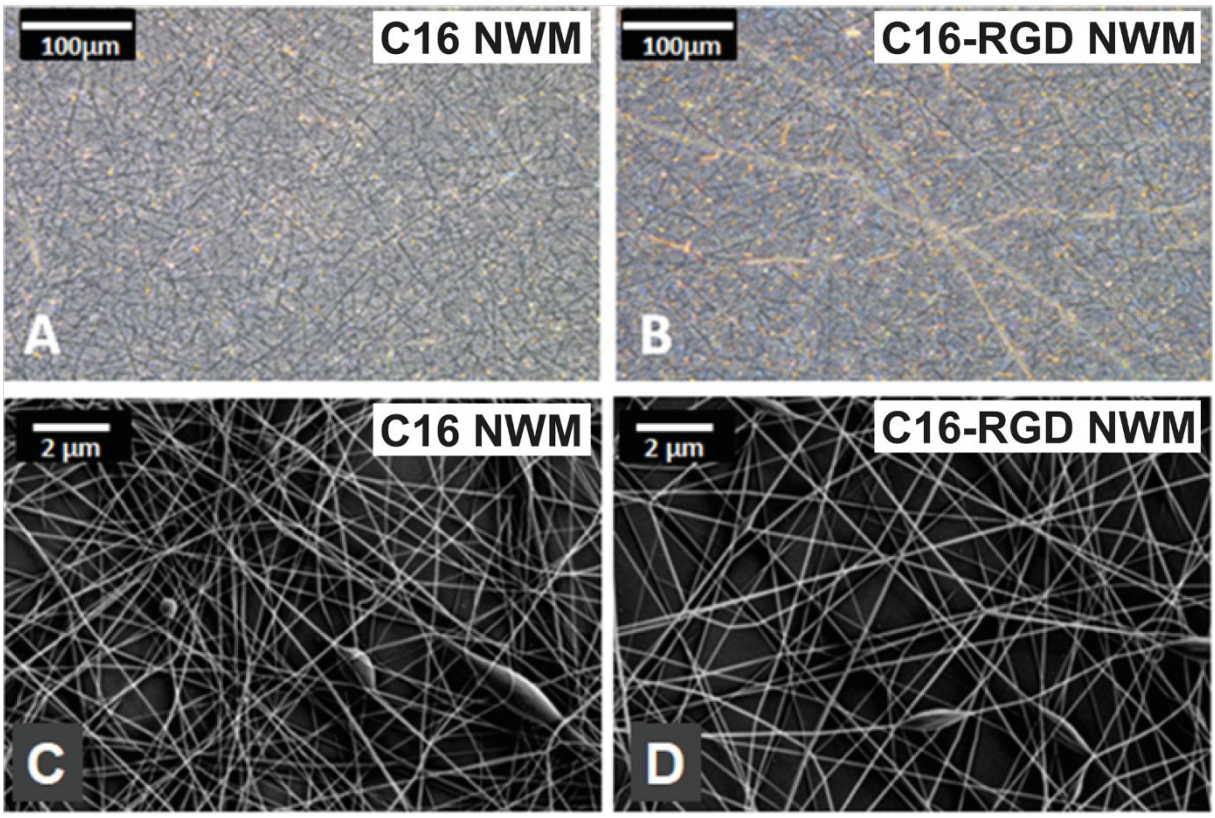

Figure S1. (A, B) Light microscopy images and (C, D) scanning electron microscopy (SEM) images of nonwoven meshes (NWM) collected on glass coverslips.

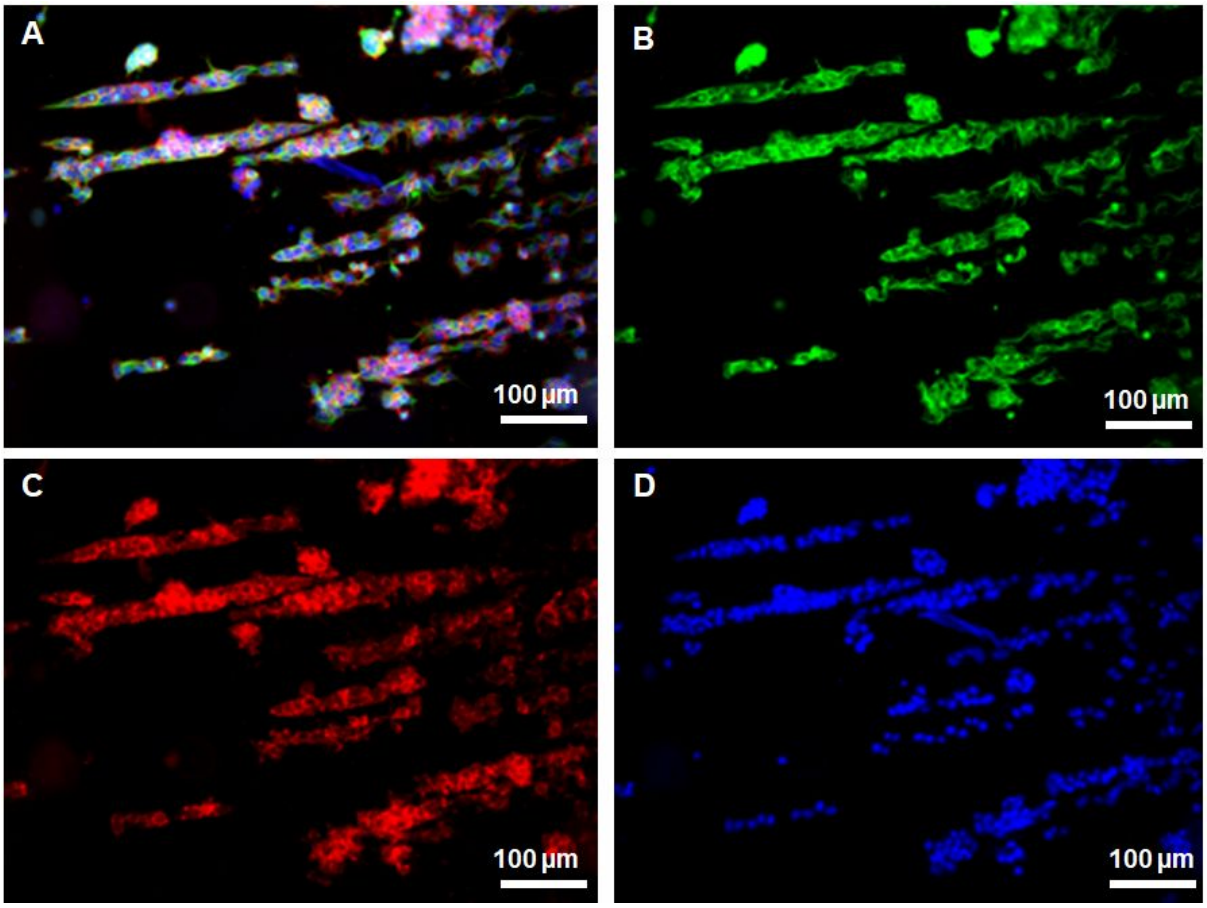

Figure S2: Fluorescence microscopy images of adhered NG108-15 cells on aligned collagen fibers on day 3 of culture. (A) Merge, (B) expression of ß-tubulin III, (C) expression of F-actin and (D) Hoechst staining showing cell nuclei.

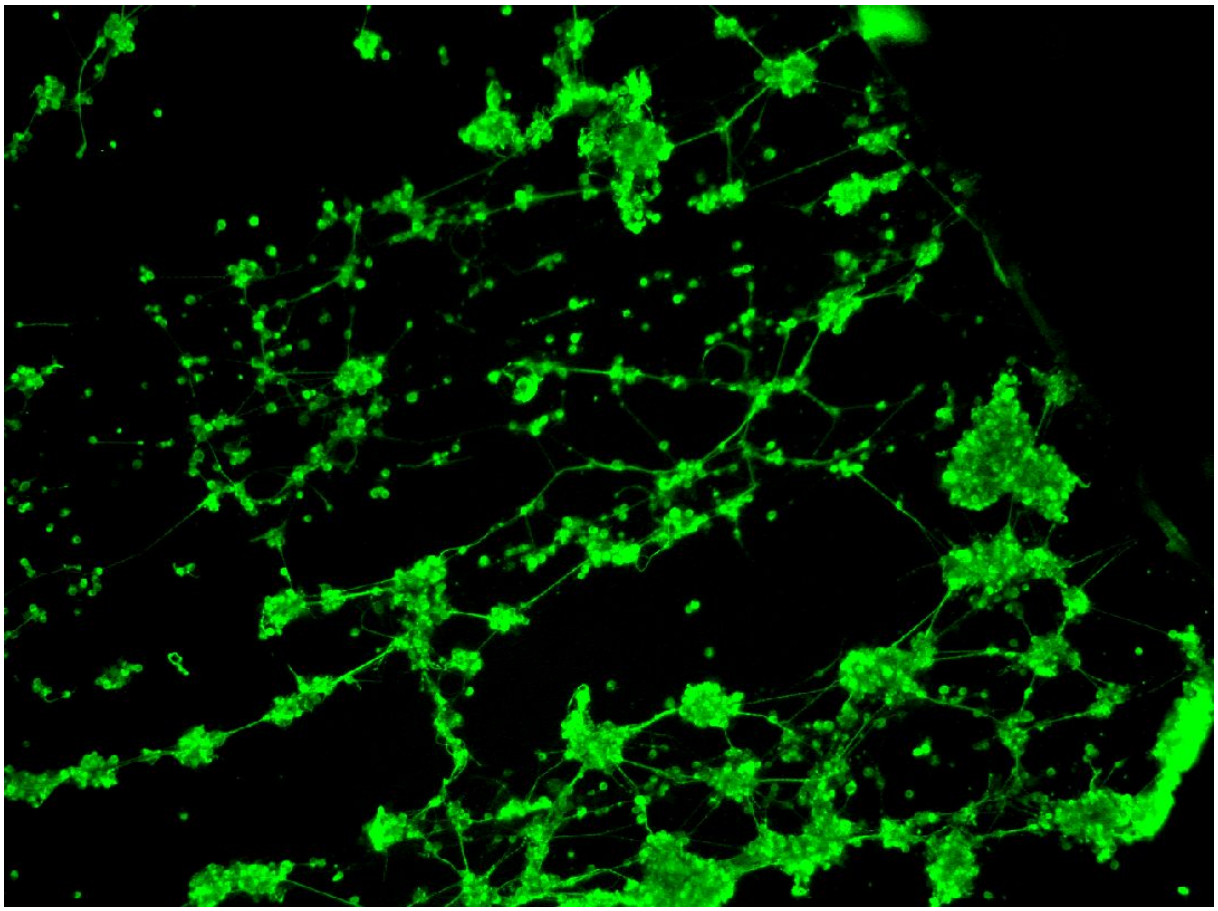

Figure S3: Fluorescence microscopy images of NG108-15 cells on aligned collagen fibers after differentiation on day 3 of culture. Green fluorescence indicates the expression of β-tubulin III.

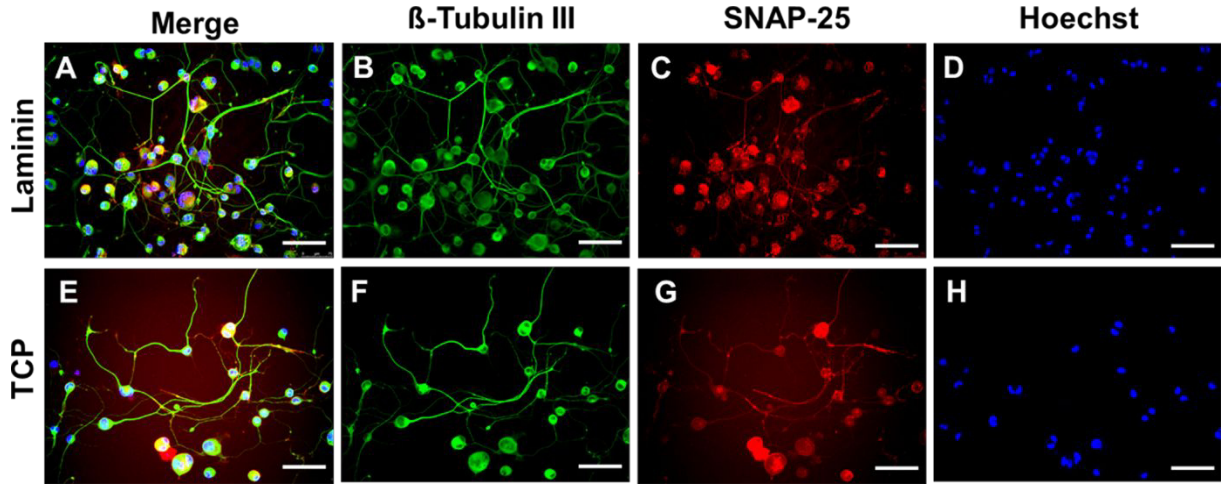

Figure S4. NG108-15 neuronal cell differentiation and synapse formation on a laminin-coated glass coverslip and on a treated tissue culture plate (TCP) after 3 weeks of culturing. Neuronal cells show long neurite growth and neuronal networks on (A) laminin-coated glass and on (E) TCP, both acting as positive controls. (B, F) Differentiated neurons are immunoreactive for β-tubulin III (green). (C, G) Neuronal networks form synapses and are immunoreactive for SNAP-25 (red). (D, H) Neuronal cell nuclei marked with Hoechst (blue). Scale bars: 100 µm.

Table S1. Differentiation-induced changes in membrane properties of NG108-15 cells grown on recombinant spider silk nonwoven meshes (NWM) and on collagen fibers. The resting membrane potential, the maximum rate of depolarization and the depolarization amplitude are shown in differentiated NG108-15 cells with (n = 9) and without (n = 13) the ability to generate action potentials. No significant differences were observed between the two NWM variants and the collagen fibers. All data are presented as mean ± SD.

NG108-15 cells	Resting membrane potential [mV]	Maximum rate of depolarization [mV ms^{-1}]	Depolarization amplitude [mV]
- action potentials	- 33.7 ± 2.1	22.5 ± 1.2	51.3 ± 3.5
+ action potentials	- 41.9 ± 3.0	49.2 ± 6.5	87.6 ± 4.7

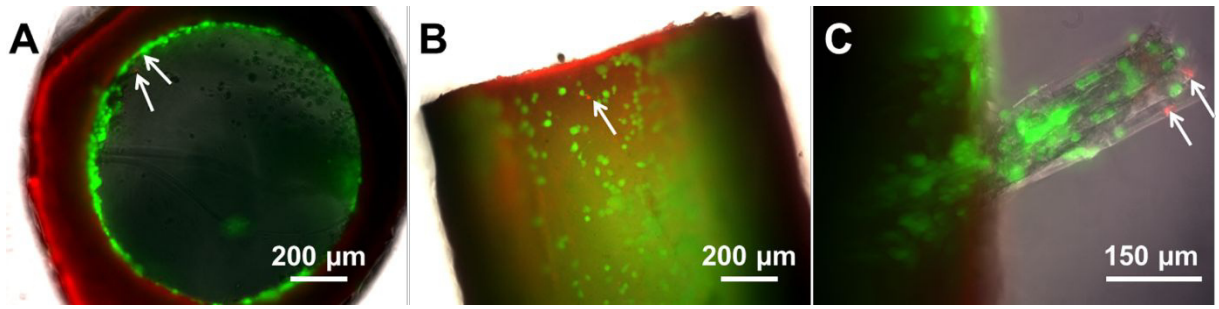

Figure S5. Live dead staining showing NG108-15 cells differentiated in the NGC after 3 days of culturing. (A) Neuronal cells showed an even distribution inside the C16-RGD NWM tube with very few dead cells in red (white arrows). (B) Differentiated live cells with neurites on the inner wall of the tube structure with negligible dead cells in red (white arrow). (C) Differentiated cells on collagen fibers in the tube structure with very few dead cells in red (white arrow).

7.4 Teilarbeit 4

Reproduced from

Aigner, T. B.[&]; **Haynl, C.[&]**; Salehi, S.; O'Connor, A.; Scheibel, T.[*]

&: gleichwertige Autorenschaft

Nerve guidance conduit design based on self-rolling tubes

Materials Today Bio **2020**, 5, 100042

DOI:10.1016/j.mtbio.2020.100042

Materials Today Bio 5 (2020) 100042

Contents lists available at ScienceDirect

Materials Today Bio

journal homepage: www.journals.elsevier.com/materials-today-bio

Nerve guidance conduit design based on self-rolling tubes

T.B. Aigner [a,g], C. Haynl [a,g], S. Salehi [a], A. O'Connor [b], T. Scheibel [a,c,d,e,f,*]

[a] University of Bayreuth, Department of Biomaterials, Prof.-Rüdiger-Bormann-Str.1, 95447, Bayreuth, Germany
[b] University of Melbourne, Department of Biomedical Engineering, Melbourne, Victoria, 3010, Australia
[c] University of Bayreuth, Bayreuther Zentrum für Kolloide und Grenzflächen (BZKG), Universitätsstraße 30, 95447, Bayreuth, Germany
[d] University of Bayreuth, Bayreuther Zentrum für Molekulare Biowissenschaften (BZMB), Universitätsstraße 30, 95447, Bayreuth, Germany
[e] University of Bayreuth, Bayreuther Materialzentrum (BayMAT), Universitätsstraße 30, 95447, Bayreuth, Germany
[f] University of Bayreuth, Bayerisches Polymerinstitut (BPI), Universitätsstraße 30, 95447, Bayreuth, Germany

ARTICLE INFO

Keywords:
Peripheral nerve repair
Electrospinning
Layer-by-layer film
Recombinant spider silk
Collagen
Cryogel

ABSTRACT

The current gold standard in peripheral nerve repair is nerve autografts for bridging gaps larger than a centimeter. However, autografts are associated with a low availability and the loss of function at the donor site. Nerve guidance conduits (NGCs) made of biocompatible and biodegradable materials reflect suitable alternatives. Clinically approved NGCs comprise either wraps that are rolled around the loose ends of the nerve or steady-state tubes; however, both lack internal guidance structures. Here, we established self-rolling NGCs to allow for gentle encapsulation of nerve cells together with supportive microenvironments, such as (1) an inner tube wall coating with a bioactive spider silk film, (2) an inner tube wall lining using an anisotropic spider silk non-woven mat, or (3) a luminal filler using an anisotropic collagen cryogel. Neuronal cells adhered and differentiated inside the modified tubes and formed neurites, which were oriented along the guidance structures provided by the spider silk non-woven mat or by the fibrillary structure of the collagen cryogel. Thus, our size-adaptable NGCs provide several features useful for peripheral nerve repair, and distinct combinations of the used elements might support and enhance the clinical outcome.

1. Introduction

Peripheral nerve injuries, such as crushes or sections, can be consequences of vehicle or industrial accidents, falls, or penetrating trauma [1]. The peripheral nervous system in vertebrates reacts to such injuries by active degeneration and regeneration [2,3]. Problematic are gaps, which are larger than 1 cm, thus, original nerve function cannot be restored using bioinert nerve guidance conduits (NGCs) [4,5]. In those cases, the current gold standard is nerve autografts, providing the extracellular matrix, viable Schwann cells, and growth factors needed for optimal regeneration [6–8]. Therewith, a physical guidance is given, allowing the nerve tissue cells to sprout their axons from the proximal end to the distal stump [9]. Unfortunately, the number of supplies in donor nerve tissue is limited and nerve removal causes a loss of function at the donor site. Further, a complete functional restoration cannot be guaranteed at the acceptor site [6,10]. An alternative to nerve autografts is using artificial NGCs [11–13].

Basically, there are several properties the NGC has to meet to increase the success of the clinical outcome. The NGC must be biocompatible and biodegradable to not provoke any immunological reaction or other side-effects and to avoid compression caused by non-degraded components [13]. The NGC must be flexible and soft because the gap to be bridged might cross a joint but at the same time should possess enough stability to be implanted by surgeons [13]. NGCs, which are mostly based on tubular structures, should be semipermeable allowing the diffusion of gases and nutrients but should avoid infiltration of inflammatory cells and scar tissue formation. Furthermore, the presence of bioactive molecules and adhesion of supporting cells, such as, for instance, Schwann cells, has been found to be crucial [11–14].

Filler materials within the tubular structure can create a cell friendly microenvironment promoting cell adhesion, proliferation, migration and differentiation, and directed growth of neuronal cells and their neurites. For instance, multilumen or microporous fillers, hydrogels or fiber containing conduits, and microgrooves or nanoimprints on the inner wall have been under investigation [11,12]. Another possibility is the use of

* Corresponding author.
E-mail address: thomas.scheibel@bm.uni-bayreuth.de (T. Scheibel).
[g] contributed equally.

https://doi.org/10.1016/j.mtbio.2020.100042
Received 21 October 2019; Received in revised form 17 January 2020; Accepted 18 January 2020
Available online 27 January 2020

cryogels, which provide a three-dimensional environment [15,16] favorable for this application.

Clinically approved NGCs are either wraps that are rolled around the loose ends of the nerve or steady-state tubes, in which both nerve ends are inserted [17]. Those NGC variants are not modified with internal guidance structures and they are made of either synthetic polymers, such as polyglycolic acid (Neurotube®), polylactide-caprolactone (Neurolac™) and polyvinyl alcohol (Salutunnel™), or collagen type I (NeuraGen®, NeuraWrap™, NeuroMend™, NeuroMatrix™, NeuroFlex™) [17], which is an extracellular matrix protein also found in peripheral nerves, providing myelinated axons with functional support [12,18,19] and generally exhibiting excellent biocompatibility, extremely low immunogenicity, chemotaxis, and biodegradability [20,21].

Besides collagen, other naturally derived materials such as chitosan and spider silk are promising candidates for NGC fabrication because of their excellent compatibility with the human body. Chitosan is a derivative of naturally occurring chitin, a by-product of the seafood industry. It shows antimicrobial properties [22] and is used in food, cosmetics, and pharmaceutical and biomedical applications [23,24], including peripheral nerve repair [25,26]. Natural spider silk fibers exhibit remarkable mechanical properties [27,28] and have performed well in *in vivo* peripheral nerve repair studies [29,30]. Owing to the difficulties (i.e., cannibalism) in spider farming, which prevent the production of large amounts and a constant material quality [31], recombinant spider silk proteins can nowadays be provided, and materials made thereof have exhibited suitable properties in neuronal *in vitro* tests [32–34]. Recombinant spider silks can be processed into several tailorable morphologies, for example, films, foams, non-woven mats, or hydrogels [35–42], and these materials were shown to not induce an immune response in the body and to degrade rather slowly [43–46]. In comparison with electro-spun collagen nanofibers, recombinant spider silk nanofibers are less prone to swelling [47], allowing a higher degree of nerve cell orientation along the fiber axes. Furthermore, different modifications are possible on the genetic level, for instance, the introduction of an arginine—glycine-aspartic acid (RGD)-bearing cell binding motif [48].

We have recently shown the application of self-rolling tubes as containers for enzymatic reactions [49]. In the present study, we designed a biocompatible and biodegradable self-rolling tubular NGC. Although the commercially available NeuroMend™ exhibits self-rolling properties, its lack of internal structures, which would be beneficial for cell vitality and differentiation, as well as directed nerve growth and neurite elongation, is regarded as one severe drawback limiting the success of the clinical outcome. Therefore, we studied the benefit of a self-rolling tube made of chitosan and different filler morphologies, which adapts to the dimensions of the injured peripheral nerve upon rolling around the loose ends and the filler material. It could be shown that the new NGCs ensured the viability of neuronal cells during encapsulation. In this study, all variants tested allowed differentiation of neuronal PC-12 cells within the NGCs, and anisotropic structures provided guidance of neurites. Our study combines the usefulness of the self-rolling property of a tube with the incorporation of suitable internal morphologies and is therefore of high importance to the development of new materials for peripheral nerve repair.

2. Materials and methods

2.1. Fabrication of self-rolling chitosan films

A filtered chitosan solution (1% w/v in 2% v/v formic acid, 190–310,000 g mol^{-1}, Sigma-Aldrich) was cast into a Petri dish (Sterilin™, diameter: 90 mm) yielding a density of 2.36 mg cm^{-2}, and the film was air dried overnight. This film was post-treated with 0.2 M NaOH for 5 min and subsequently washed with ultrapure water.

2.2. Fabrication of self-rolling chitosan films with an internal eADF4(C16)-RGD coating

The preparation of self-rolling chitosan tubes with an internal spider silk eADF4(C16)-RGD coating was conducted according to Aigner and Scheibel [49]. In brief, an eADF4(C16)-RGD [48] solution in 1,1,1,3,3,3-hexafluoro-2-propanol (HFIP, 8.33 mg ml^{-1}, 0.08 mg cm^{-2}, 48,583 g mol^{-1}) was cast into a Petri dish (Sterilin™, diameter: 90 mm) and, after drying, post-treated with 70% (v/v) ethanol to render the silk film to be insoluble in water by inducing β-sheet formation. Then, a chitosan film was cast on top of the eADF4(C16)-RGD film according to the procedure outlined in Section 2.1.

2.3. Fabrication of self-rolling chitosan films with an internal eADF4(C16) anisotropic non-woven mat

A chitosan film was prepared as depicted in 2.1 and removed from the Petri dish and fixed on a rotating drum with double-sided tape. The rotating drum allowed production of aligned fibers yielding an anisotropic non-woven mat. Electrospinning of eADF4(C16) was performed according to the study by Lang [50]. A 150 mg ml^{-1} solution of eADF4(C16) (47,698 g mol^{-1}, AMSilk GmbH) in HFIP was electrospun onto the chitosan film (voltage: 30 kV; distance to collector: 15 cm; flow rate: 300 µl min^{-1}; relative humidity: 50%). The spider silk non-woven mat was post-treated first in pure ethanol vapor for 3 h, followed by a treatment in 90% ethanol in the vapor phase (corresponds to 87% v/v ethanol) for 2 h to render the mat to be insoluble in water and to obtain a tight connection between the spider silk non-woven mat and the chitosan film.

2.4. Fabrication of anisotropic collagen cryogels

Collagen type I extracted from calf skin (Sigma-Aldrich) was dissolved in 0.5% (v/v) acetic acid at pH 3 for 20 h. After centrifugation at 17,700 g for 10 min, the supernatant was removed and showed a collagen concentration of 4.8 mg ml^{-1}. Then, an aqueous glutaraldehyde solution (25% v/v in water, Carl Roth GmbH + Co. KG) was mixed with the collagen solution yielding a final concentration of 1% glutaraldehyde (v/v). This solution was then immediately transferred into a vertically standing plastic tube, which was tightly fixed to a copper plate. After sealing the top opening of the filled plastic tube with parafilm and mounting a thermal insulation (tube filled with cotton wool) on top, the whole setup was transferred into a −20 °C temperature freezer for 48 h. Subsequently, the frozen collagen cryogel precursor was pushed out of the tube into phosphate buffered saline (PBS), pH 7.4 at room temperature to neutralize the acidic pH, thereby preventing reversible dissolution of the collagen cryogel. After 20 h gelation in PBS, the collagen cryogel was washed three times with PBS containing 0.1 M glycine. The washing was continued using two further washing steps during the next 24 h to ensure complete capture of any free glutaraldehyde groups. Finally, the collagen cryogel was washed using PBS and stored in PBS until further experiments were carried out.

2.5. Chitosan tube formation

The underlying self-rolling mechanism of the used chitosan film was based on the difference of the swelling behavior between its bottom and top layer (Section 2.1). A more detailed explanation of this process can be found in the study by Ionov [51]. Here, chitosan films were cut into rectangles with desired sizes. The self-rolling process was induced by immersing this film into an aqueous solution, that is, into phosphate buffered saline (pH 7.4). However, self-rolling was induced as well in contact with cell culture medium, which resulted in entrapping the cell suspension. To encapsulate cryogels, they were placed on the film, which self-rolled forming a tube filled with cryogel. The tube diameter could be tailored to a certain extend by varying the film thickness and the diameter of the filler, for example, the cryogel.

2.6. Morphological characterization of NGCs

NGC components were analyzed using stereo microscopy (Leica M205C) and scanning electron microscopy (SEM; Sigma VP 300, Zeiss). For SEM, the samples were mounted on aluminum studs with adhesive carbon tape and then sputter coated with platinum (2 nm). Collagen cryogels were prepared for imaging by washing and storing them for further use in 10 mM ammonium hydrogen carbonate buffer. After flash freezing in liquid nitrogen, the collagen cryogels were placed in a lyophilization device (Alpha 1–2 LDplus, Christ) for one week. The cryogel cross-section was prepared in advance to flash freezing and lyophilization by cutting the soaked cryogel using a sharp razor blade.

2.7. Determination of water content and swelling degree of collagen cryogels

Collagen cryogels were prepared having 2 cm in length (number of samples n = 6). The weight of the fully soaked cryogels in PBS (m_{soaked}) and of the cryogels after removing unbound PBS with a paper tissue ($m_{removed}$) was determined using a microbalance (Practum 224-1S, Sartorius Lab Instruments). The water content in soaked cryogels was calculated using Eq. (1).

$$\text{water content of collagen cryogels } [\%] = (m_{soaked} - m_{removed}) / m_{soaked} \times 100 \quad (1)$$

The swelling ratio of the collagen cryogels was calculated using Eq. (2). Therefore, the diameter of the fully soaked cryogels was measured in PBS (V_{soaked}) and that of the cryogels after removing unbound water with a paper tissue ($V_{removed}$) using a stereo microscope (Leica M205C) (number of samples n = 4). The cryogels were assumed to be tubular, and their volumes were calculated using their diameter values.

$$\text{swelling ratio } [\%] = (V_{soaked} - V_{removed}) / V_{removed} \times 100 \quad (2)$$

2.8. Mechanical characterization of chitosan films and collagen cryogels

The chitosan films used for conduit fabrication and the collagen cryogels were analyzed using a tensile testing device (Bose Electroforce 3220) equipped with a 2.45 N load cell. Dry chitosan films were glued onto plastic frames using a high viscosity glue (UHU® Supergel), and they were immediately transferred into a fume hood for drying. The films on the frames were incubated in PBS before analysis using a strain rate of 0.05 mm s^{-1} (number of samples n = 5). Engineered stress of the films was calculated as the force divided by their cross-sectional areas assumed to be rectangular (film width × film thickness).

The mechanical properties of the collagen cryogel were analyzed referring to its longitudinal axis. Free PBS in collagen cryogels was removed using a paper tissue, and the diameters after this procedure were measured at three different positions. The moist cryogel was clamped between two plastic frames, applied to the tensile testing device, and measured at a strain rate of 0.05 mm s^{-1} (number of samples n = 4). Engineering stress of the cryogels was calculated as the force divided by the respective cross-sectional area, which was assumed to be circular. In terms of the films and the cryogels, the gauge length was adjusted to 2 mm. Strain was defined as the change in sample length divided by its original length. The Young's modulus was determined as the slope of the stress-strain plot in the linear elastic deformation range.

2.9. Seeding of PC-12 cells on the individual components and in the NGC

The different NGC components were prepared in untreated cell culture plates (24 wells, Thermo Fisher). For collagen surface treatment, the collagen type I solution (diluted 1:5 with sterile PBS, Cellmatrix®, Nitta Gelatin Inc) was used to coat the wells for 30 s. Then the solution was removed and the film was air dried. The eADF4(C16)-RGD film was cast directly into the wells using HFIP (33.3 mg ml^{-1}, 0.25 mg cm^{-2}) as a solvent. After drying, films were post-treated with 70% ethanol (v/v). The eADF4(C16) non-woven mats were prepared by electrospinning of a 150 mg ml^{-1} eADF4(C16) solution in HFIP onto plastic coverslips (12 mm diameter, Thermo Fisher). The same spinning and post-treatment conditions were used as explained in section 2.3. A fixation of the plastic coverslips onto the rotating drum for fiber alignment was not possible, thus, an isotropic non-woven mat was spun onto the coverslips. The collagen cryogel was glued into well plates using a silicon glue.

The neuronal cell line PC-12 (ATCC® CRL1721™) [52] was cultured in the growth medium (Dulbecco's Modified Eagle's Medium (DMEM) with 10% (v/v) heat inactivated horse serum (Gibco), 5% (v/v) fetal bovine serum (FBS, Merck), 1% (v/v) GlutaMAX (Gibco), 1% (v/v) penicillin/streptomycin (10,000 U ml^{-1}, Thermo Fisher), 20 mM 4-(2-hydroxyethyl)-1-piperazineethanesulfonic acid buffer (HEPES, Carl Roth)). For the adhesion test, 25–30,000 cells were seeded per square centimeter on the aforementioned materials and allowed to adhere for 7 days with medium changes on day 3 and 5. Treated cell culture plates were used as control. After 1, 3, and 7 days, cell morphology was observed using bright field microscopy (Leica DMi8).

2.10. Differentiation of PC-12 cells on NGC components

A density of 10,000 cells cm^{-2} were cultured on the aforementioned materials and incubated in the growth medium. After 1 day of culture, the growth medium was exchanged with the differentiation medium (DMEM with 2% (v/v) horse serum, 1% (v/v) GlutaMAX, 1% (v/v) penicillin/streptomycin, 20 mM HEPES buffer, 100 ng ml^{-1} nerve growth factor (NGF, 2.5s Native Mouse Protein, Thermo Fisher)), which was changed on day 3 and 5 of differentiation. After 7 days of differentiation, the cells were immunostained for detecting endogenous levels of β-III tubulin, and neurite outgrowth was evaluated. The staining procedure was as follows: cells were fixed with formaldehyde (Carl Roth; 3.7% in water, 15 min, at room temperature) and made permeable with Triton x-100 (Carl Roth; 0.3% (v/v), 5 min, at room temperature). A glycine solution (Carl Roth, 300 mM, 10 min, at room temperature) was added to deactivate aldehydes. Bovine serum albumin (BSA) blocking buffer was applied (Carl Roth; 5% (w/v), 30 min, 37 C) before adding the image enhancer (30 min, 37 C) of the Alexa FluorTM 488 Goat Anti-Rabbit SFX Kit (Thermo Fisher). Then, the samples were incubated in primary polyclonal antibody anti-β-III tubulin (Abcam, rabbit; 1000 x diluted in 0.1% (w/v) BSA buffer, overnight, 4 °C). On the next day, cells were stained using the secondary antibody goat-anti-rabbit with an Alexa Fluor 488 label (Sigma-Aldrich; 1000 x diluted in 0.1% (w/v) BSA buffer, 1 h, 37 °C) and Hoechst (Invitrogen; 1000 × diluted in 0.1% (w/v) BSA buffer, 1 h, 37 °C). Imaging was performed using a fluorescence microscope (Leica DMi8). For cryogels, Z stacks were taken and overlaid using the maximal projection option provided by the software (LAS X 3.6.0).

2.11. Encapsulation of cells in tubes

Tube materials were cut to rectangular shapes (1.5 × 0.5 cm for pure chitosan, eADF4(C16)-RGD-chitosan and eADF4(C16) aligned fiber mat-chitosan tubes and 1.5 × 1 cm for chitosan tubes filled with the collagen cryogel), and the film thickness was determined to be 29.7 ± 3.0 μm [49]. These samples were allowed to roll in PC-12 cell suspension (10,000 cells ml^{-1}) to entrap the cells. In the case of the cryogel, the gel was first soaked in cell suspension and then applied on a chitosan film, which smoothly rolled around it. Collagen-coated cell culture plates were used as a positive control. After one day of culture, the medium was changed to differentiation medium. The differentiation medium was refreshed every two days. On day 7, cells were immunostained as described previously and analyzed using a wide field fluorescence microscope (Leica DMi8), and the images were processed using the software LAS X 3.6.0 by adjusting the brightness and the contrast. Z-stacks in combination with

the maximal projection mode were used to analyze all 3D samples. Importantly, cryogels were cut to slices giving a thickness of 1–3 cell layers (corresponding to 10–36 μm) and put on a glass slide covered with a coverslip to observe, whether adhered and differentiated cells could be found throughout all layers. Neurite length was determined by measuring neurites of nerve cells grown on each type of surface using ImageJ. The neurites were traced starting from their extrusion point from the cell body to the neurite's outer end, and this line was subsequently measured with the 'Measure' tool in ImageJ (collagen coating: 425 neurites, eADF4(C16)-RGD-coated tubes: 135 neurites, eADF4(C16) anisotropic non-woven mat tubes: 231 neurites, collagen cryogel in tube: 248 neurites). Then, the percentage of neurites was determined in each 10 μm length segment (0–10, 11–20, 21–30, and so on). Further, the number of cells in the images was counted using ImageJ 'Multi-point' modus to determine the neurite length per cell.

3. Results and discussion

3.1. Fabrication and characterization of NGCs

All NGC variants exhibited a tubular structure because of the used self-rolling chitosan film. The self-rolling mechanism has been recently described in Aigner and Scheibel [49] where the tubes were used as enzyme-reaction containers. The tubes could be prepared with various lengths (up to 10 cm), were stable between pH 3 and 11 and exhibited diffusion permeability with a molecular weight cutoff of 20,000 g mol^{-1}, which enables influx of nutrients, as well as gas exchange and metabolite removal. The self-rolling property of the chitosan film allowed an easy modification with other films or structured materials, the gentle and homogenous encapsulation of cells during rolling and, in principle, the adaption of the tube size to the nerve ends or filler material.

To test the applicability of the self-rolling chitosan-based tubes for nerve regeneration, three variants of inner tube materials were tested to yield NGCs. An overview of the three NGC variants is schematically depicted in Fig. 1. Setup 1 used a hollow tube with an inner film coating made of the spider silk variant eADF4(C16)-RGD to provide a surface, where cells can efficiently adhere to; setup 2 used a hollow tube with an inner surface made of an anisotropic eADF4(C16) non-woven mat to provide a structure, where cells can adhere to and align on; setup 3 used a tube filled with a collagen cryogel with an anisotropic lamellar structure allowing cell adhesion and alignment. The first two NGCs (setups 1 and 2) possessed quasi-irreversible physical connection between the tube and the modifying materials. On the contrary, the collagen cryogel structure (setup 3) was not strongly connected to the chitosan tube, due to the processing conditions.

Upon fabrication of setups 1 and 2, rolling was induced by incubating the modified chitosan sheets with a PC-12 nerve cell suspension. For the preparation of setup 3, the cryogel was soaked in the PC-12 suspension and subsequently transferred onto the chitosan sheet, whereby immediate rolling of the sheet occurred and the encapsulation of the cryogel with cells was accomplished. The PC-12 cells were entrapped without applying mechanical stress, and they differentiated to form neurites, which has been previously shown to be crucial for peripheral nerve repair [53].

Fig. 2a,A shows the cross-section of a plain chitosan tube, and in Fig. 2a,B, the inner surface topography is presented. The chitosan tube soaked in PBS exhibited high transparency (Fig. 2a,C). Modifying the chitosan inner tube wall with an eADF4(C16)-RGD film yielded bio-functionalization, which was not visible in the cross-section because of its low thickness (Fig. 2b,A). In the particular case, the poor solubility of the

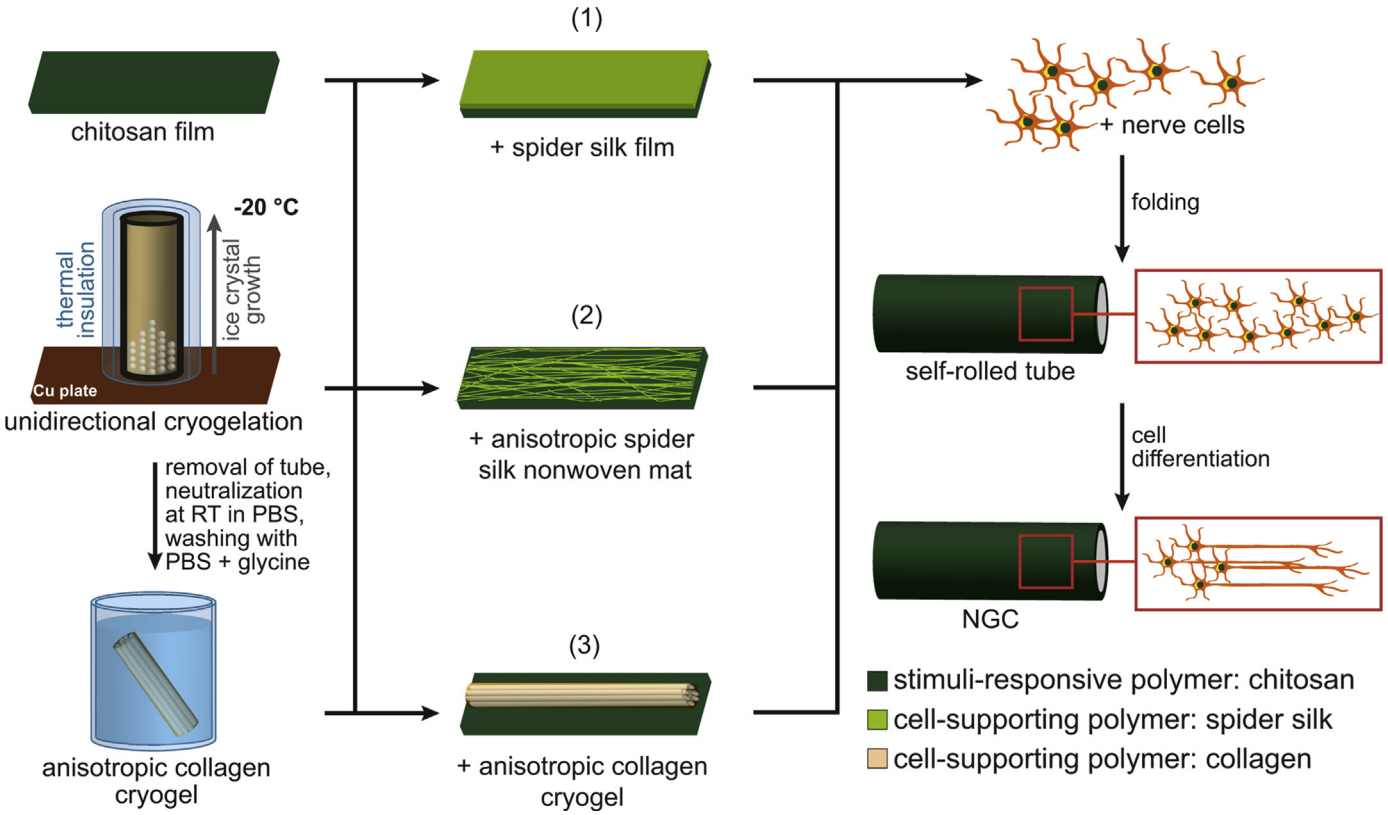

Fig. 1. Nerve guidance conduit (NGC) fabrication. Chitosan sheets were modified by either (1) a film on top of the inner wall made of the recombinant spider silk protein eADF4(C16)-RGD, (2) a layer of an anisotropic non-woven mat on top of the inner wall made of the recombinant spider silk protein eADF4(C16), or (3) an anisotropic collagen cryogel filling the inner volume of the tube. The collagen cryogel was produced using unidirectional cryogelation at −20 °C, followed by thawing, solvent neutralization, and several washing steps. The various NGC precursor constructs were placed in a PC-12 nerve cell suspension inducing self-rolling of the chitosan film used as the outer layer, and thereby encapsulated the cells, which had then the possibility to differentiate.

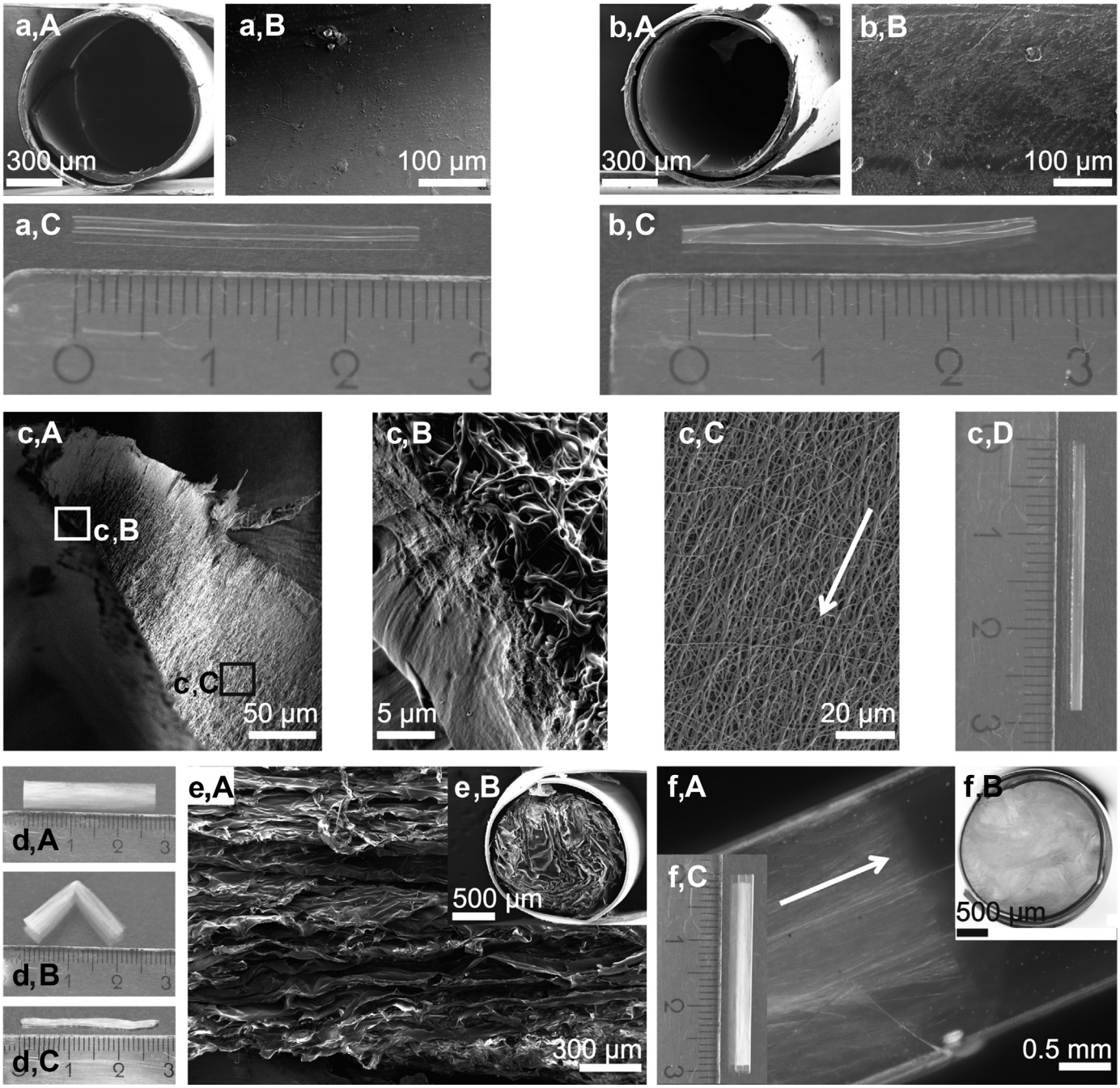

Fig. 2. Morphological characterization of NGCs. (a) (A) Scanning electron microscopy (SEM) image of the cross-section of the self-rolled chitosan tube; (B) its inner surface topography; and (C) photograph showing the whole tube after self-rolling in PBS. (b) (A) SEM image of the cross-section of the chitosan tube coated with eADF4(C16)-RGD on the inner surface (not visible here); (B) of the resulting inner surface topography; and (C) photograph showing the whole tube after self-rolling in PBS. (c) (A) SEM image of a chitosan tube comprising an inner lining with an anisotropic non-woven mat made of eADF4(C16); (B) magnified image of (c) (A) (white box): The chitosan tube and the non-woven mat are physically connected because of the processing conditions. (c) (C) Magnified image of (c) (A) (black box): The eADF4(C16) non-woven nanofibers were deposited on the chitosan inner surface in an anisotropic manner (the white arrow indicates the direction of nanofiber orientation). (c) (D) Photograph showing the whole tube after self-rolling in PBS. (d) (A) Photograph of a collagen cryogel stored in PBS; (B) Bending of the collagen cryogel in PBS resulted in a sharp bending edge indicating its anisotropic character; and (C) PBS removal from a collagen cryogel yielded a significant volume reduction. (e) (A) SEM image of a freeze-dried collagen cryogel and (B) its cross-section in the chitosan tube. (f) (A) Stereo microscopy image of the anisotropic collagen cryogel within a chitosan tube and (B) of its cross-section; (C) photograph of the chitosan tube filled with the anisotropic collagen cryogel. NGCs, nerve guidance conduits; PBS, phosphate buffered saline.

post-treated eADF4(C16)-RGD film at low pH values, compared with other biopolymers such as collagen, prevented its resolubilization when the acidic chitosan solution was cast thereon during fabrication. The eADF4(C16)-RGD layer exhibited a smooth surface topography (Fig. 2b,B). Owing to the preparation procedure of the bilayer, the eADF4(C16)-RGD layer was physically cross-linked with the chitosan layer [49]. This bilayer tube was slightly turbid (Fig. 2b,C) compared with the plain chitosan tube.

The second NGC variant had an anisotropic non-woven mat as a cell guiding element on the inner tube wall (Fig. 2c,A). Owing to the post-

treatment during tube fabrication, the chitosan surface was molten with the non-woven mat preventing delamination (Fig. 2c,B). The silk fibers with diameters ranging from 0.5 to 1.0 μm were longitudinally oriented (Fig. 2c,C) because of the processing condition (Section 2.3) and led to slight turbidity of the tube (Fig. 2c,D). Importantly, the low thickness of both, the spider silk film and the non-woven mat, was negligible in comparison with that of the chitosan layer. Therefore, no differences in the rolling behavior and only minuscule differences in bilayer thickness were observed (data not shown).

The third NGC was fabricated slightly differently: the tubular collagen cryogels were stored in PBS buffer, transferred to the PC-12 cell suspension, and enclosed with the self-rolling chitosan film. Upon bending the tubular cryogels, sharp edges appeared indicative of having anisotropic features within this material (Fig. 2d,A and B). The bending was observed to be fully reversible. Furthermore, removing all unbound water showed the high water absorption capacity of the collagen cryogels (Fig. 2d,C). The water content of the collagen cryogels, when fully soaked in PBS, was determined to be 90.7 ± 1.4% (w/w). Accordingly, the collagen cryogels showed an 11-fold volume increase during swelling. A closer look onto the surface of freeze-dried collagen cryogels using SEM revealed longitudinally oriented structures (Fig. 2e,A), and a lamellar structure could be observed in the cross-section (Fig. 2e,B). The anisotropic structure was well maintained after rolling (Fig. 2f,A), and the cryogel completely filled the chitosan tube lumen (Fig. 2f,B). Fig. 2f,C shows a photograph of the cryogel within the chitosan tube.

The chitosan films and the collagen cryogels were analyzed in wet/moist state using tensile testing. Because fully PBS-soaked collagen cryogels were observed to lose their unbound water during fixation, we removed the water in advance using a paper tissue, thereby ensuring a defined cross-sectional area for tensile property calculation. The tensile strength, maximum strain, and Young's modulus were determined to be 47 ± 17 MPa, 101 ± 24%, and 30 ± 13 MPa for wet chitosan films, and 0.15 ± 0.04 MPa, 70 ± 7%, and 0.22 ± 0.04 MPa for moist collagen cryogels, respectively, (values for rabbit tibial nerves are: 11.7 ± 0.7 MPa tensile strength and 38.5 ± 2% maximum strain [54]). Both the films and the cryogels showed large ramps of linear elastic deformation. In contrast to films, cryogels did not show a sharp material rupture but showed a gradual deformation after reaching the yield point (Supplementary Fig. S1). The deformation process of the cryogels continued up to 300% strain until no more force was detected. Importantly, the Young's modulus of the moist cryogels was in the range of that of peripheral nerve tissue (0.15–0.3 MPa) [55], presumably yielding a suitable environment for

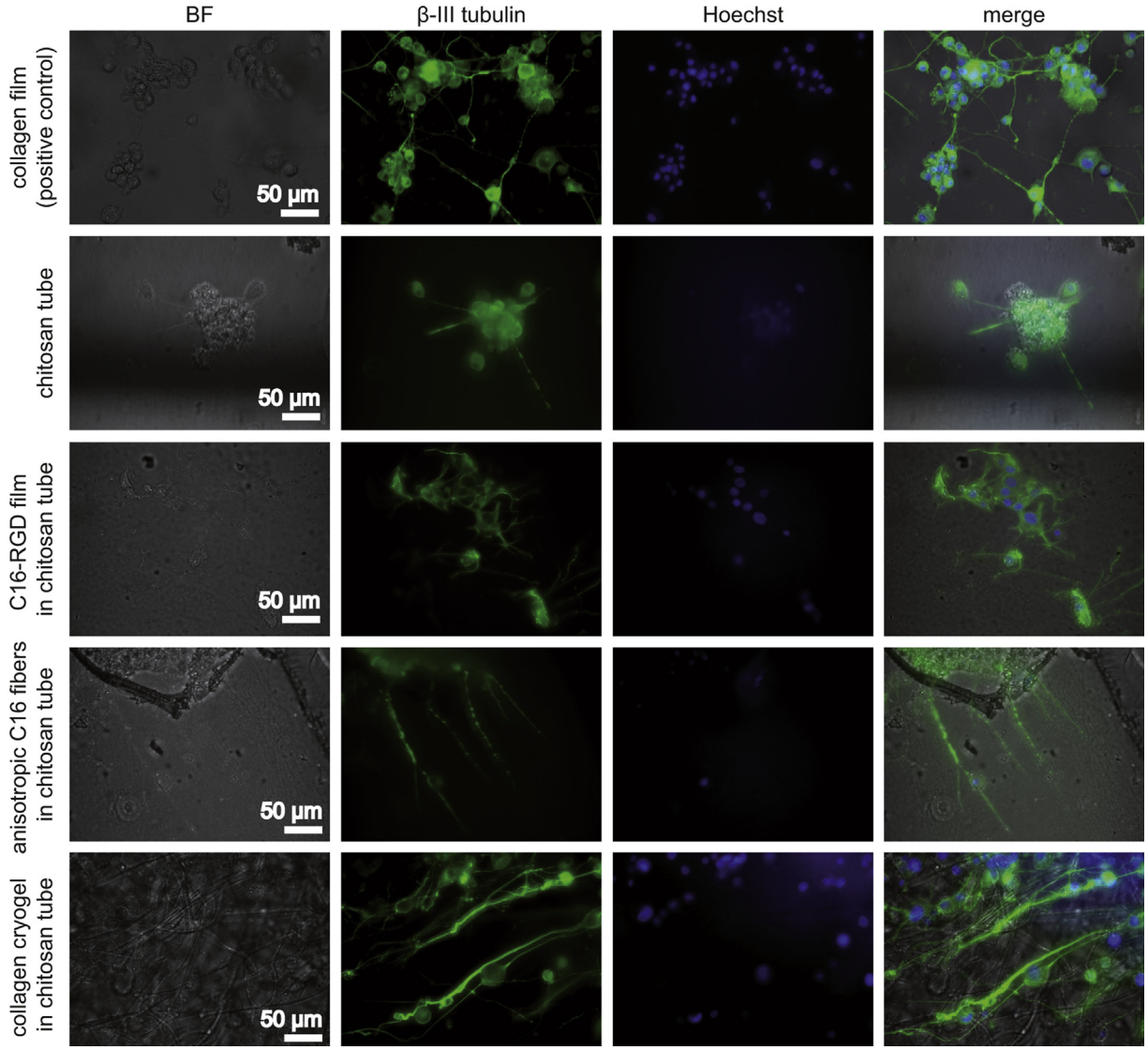

Fig. 3. Investigation of PC-12 nerve cell differentiation on all materials in tubes used in this study at day 7. A collagen film was used as a positive control for differentiation. Brightfield (BF) imaging showed the general material appearance; immunostaining against β-III tubulin (green) visualized the microtubule-forming protein present in differentiated neurons; Hoechst (blue) staining visualized cell nuclei. All images are at the same scale. C16, eADF4(C16)

nerve cells, while the chitosan film could provide stability during and after implantation, as well as structural integrity of the filler material and cells.

3.2. Differentiation of neuronal cells on individual materials

According to Orlowska et al. [56], attachment of PC-12 cells to polystyrene tissue culture flasks/plates is poor at laboratory conditions, and the cells form floating aggregates and grow in clusters [57]. Furthermore, this weak cell adhesion results in poor differentiation and insufficient levels of neurite outgrowth [57]. In agreement with Kleinman et al. [58], we therefore used collagen type I to coat the surface of our plates, yielding improved PC-12 cell attachment. Consequently, this coating was used as a positive control in our experiments. The suitability of the three different tube modifications in terms of PC-12 nerve cell adhesion was first investigated on plain materials individually. As it is shown in Supplementary Fig. S2, PC-12 cells equivalently adhered on a collagen film (positive control), an eADF4(C16)-RGD film, an eADF4(C16) spider silk non-woven mat, and on an anisotropic collagen cryogel. We did not observe any differences in terms of cell attachment or floating aggregates between these samples in comparison with the positive control within 7 days of culture.

PC-12 cells further possess the ability to differentiate upon lowering the serum content and adding NGFs [59]. This factor helps to protect neurons against camptothecin, serum deprivation, and etoposide-induced cell death. PC-12 cells offer advantages in comparison with cultured primary cortical neurons, including the ability to differentiate and show neurite formation. Studies have shown that a specific signaling pathway including the mitogen-activated protein kinase is the major mediator of PC-12 differentiation in response to NGFs. However, more signaling pathways are activated by the NGF, which is reviewed in detail [60]. Therefore, in a second experiment, the growth medium was exchanged with differentiation medium on day 2, and cells were then monitored for seven days. Since the specific doubling time of these nerve cells is 48 h [52], they were first given time to adhere to the surface without proliferation before initiating differentiation. Cells were immunostained for β-III tubulin expression, which is a microtubule-forming protein produced in the early differentiation phase of neuronal cells [61]. On all substrates, the majority of the cells differentiated as indicated by the formation of neurites (Supplementary Fig. S3). Although cells on eADF4(C16)-RGD films showed only few and short neurites, the positive β-III tubulin staining confirmed that the cells started to differentiate. Both, the collagen film and the eADF4(C16) non-woven mat showed clear neurite outgrowth. Remarkably, nerve cells cultured and differentiated on collagen cryogels showed a high number of neurites, which were aligned with the underlying structures and they were interacting with other neurites forming bundles (Supplementary Fig. S4).

3.3. Entrapment of neuronal cells in NGCs

PC-12 cells were entrapped in the self-rolling NGCs by allowing the rolling process to occur directly in cell suspension. Thereby, the cells were distributed homogeneously throughout the tube and they were subsequently induced to differentiate for seven days (Fig. 3). Pure chitosan tubes showed poor cell adhesion, and aggregated cell clusters indicated that chitosan tubes did not promote effective cell adhesion. In contrast, chitosan tubes modified with an eADF4(C16)-RGD film coating showed good cell adhesion and isotropic neurite outgrowth similar to that on collagen films (Figs. 3 and 4A, B) because no guidance cue was provided in both cases. Chitosan tubes lined with anisotropic eADF4(C16) non-woven mats yielded adhered and differentiated PC-

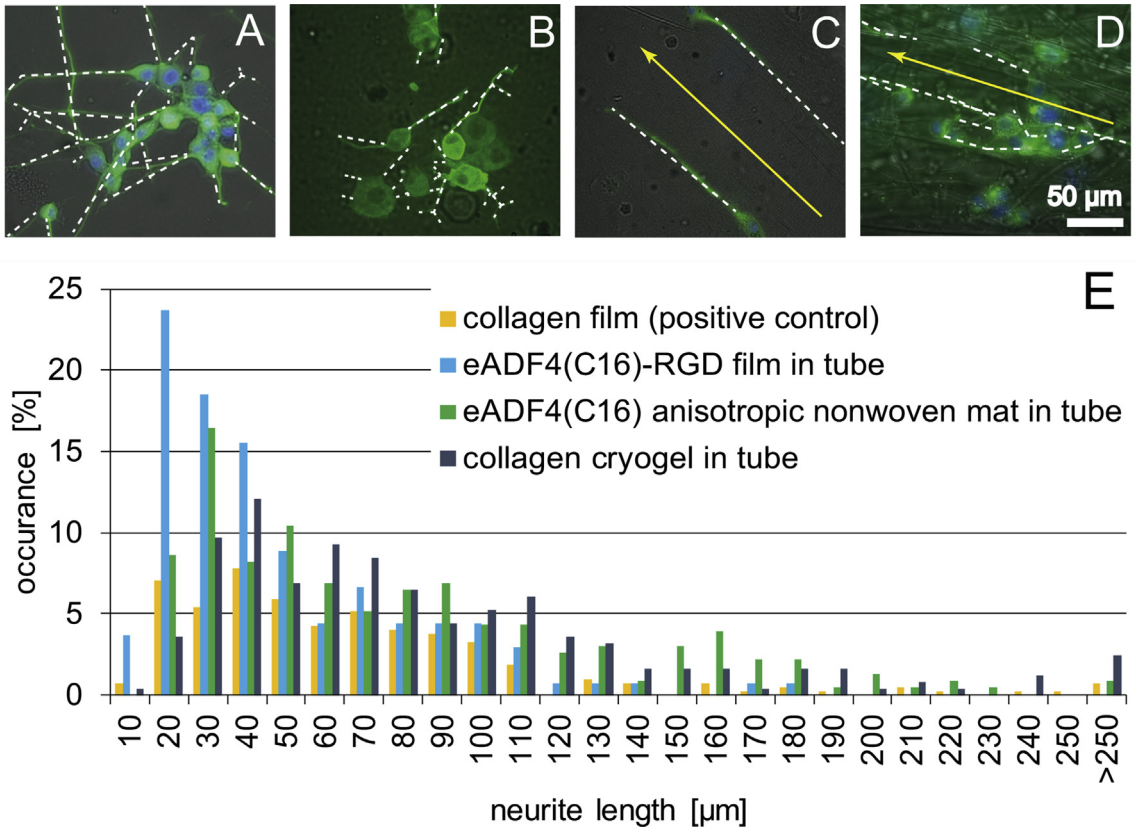

Fig. 4. Analysis of neurite lengths grown on the materials used in this study. Neurites are marked with white lines to highlight their direction of outgrowth. (A) On a collagen film (positive control) and (B) on an eADF4(C16)-RGD film, neurites grew isotropically, whereas (C) an anisotropic eADF4(C16) non-woven mat and (D) an anisotropic collagen cryogel allowed guidance of neurites into longitudinal direction. Yellow arrows indicate the orientation of anisotropic structures observed in the eADF4(C16) non-woven mat and in the collagen cryogel. (E) Neurite length distribution as detected on the materials used.

12 cells, which aligned with the nanofibers (Figs. 3 and 4C). The anisotropic collagen cryogels also allowed PC-12 cell adhesion and differentiation, and neurites followed their longitudinally oriented structure (Figs. 3 and 4D). To image the cells within the cryogels, they were cut into slices. The presence of cells within the interior of the cryogel confirmed that cells were able to migrate into the lamellar structures and that they spread their neurites longitudinally within the cryogels. Moreover, it can be assumed that sufficient perfusion of nutrients, oxygen, and waste metabolites throughout the cryogel supported the viability and differentiation of the cells. The spreading of long and parallel neurites within the lamellar structures of the cryogels is depicted in Fig. 3 and Fig. S4.

Next, neurite lengths were measured and the quantitative distribution of their lengths was determined. Therein, '10 μm' includes all neurites with a length ranging from 0 to 10 μm, '20 μm' includes all neurites with a length between 10 and 20 μm, and so on (Fig. 4E). NGCs comprising either an anisotropic eADF4(C16) non-woven mat or a collagen cryogel, as well as the collagen film (positive control) promoted outgrowth of neurites with lengths exceeding 250 μm. However, the longest neurites in the NGCs with an eADF4(C16)-RGD film were shown to have a length of 180 μm. Further, it could be observed that NGCs modified with an eADF4(C16)-RGD film showed the highest occurrence of neurite length in the range of 10–20 μm and, therefore, seemed to lead to the shortest neurites in this test. The chitosan tube with aligned eADF4(C16) non-woven mats peaked at 20–30 μm neurite length. The collagen film and constructs comprising the collagen cryogel exhibited most neurites at a length of 30–40 μm, hence, double the length as observed in eADF4(C16)-RGD–modified constructs. Most of the neurites longer than 250 μm were found in the collagen cryogel, which is remarkable, because the neurites in these samples could only be determined in a thin z-layer. Therefore, it can be assumed that the actual neurite length could be even longer.

To determine neurite length per cell, the number of cells in each image was counted. Cells on collagen films showed an average neurite length of 16 μm, 19 μm on eADF4(C16)-RGD films within a tube, 34 μm on eADF4(C16) anisotropic non-woven mats within a tube, and 47 μm on collagen cryogels within tube. This result further indicates the suitability of collagen cryogels encapsulated in self-rolled tubes as a promising candidate serving as an NGC.

4. Conclusions

Self-rolling tubes made of chitosan are beneficial for designing NGCs, because they enable gentle encapsulation of neuronal cells and the dedicated modification of the inner tube wall or its lumen with supporting materials, such as a bioactive recombinant spider silk film, an anisotropic recombinant spider silk non-woven mat, or an anisotropic collagen cryogel. All tube modifications were shown to be functional concerning enhancement of nerve cell attachment and differentiation. Anisotropic non-woven mats and collagen cryogels even supported guidance of neurites. This *in vitro* study opens the road toward *in vivo* studies to demonstrate the feasibility of the individual NGC or even combinations thereof and if the self-rolling properties of the NGCs will support the surgical procedure.

Author contributions

Tamara B. Aigner: Funding acquisition, Conceptualization, Methodology, Validation, Formal analysis, Investigation, Data curation, Writing - Original draft, Writing - Review and Editing, Visualization. Christian Haynl: Conceptualization, Methodology, Validation, Formal analysis, Investigation, Data curation, Writing - Original draft, Writing - Review and Editing, Visualization. Sahar Salehi: Funding acquisition, Conceptualization, Methodology, Validation, Writing - Review and Editing, Visualization. Andrea O'Connor: Funding acquisition, Writing – Review & Editing. Thomas Scheibel: Supervision, Funding acquisition, Writing – Review & Editing.

Funding

This work was supported by the Bavarian Research Foundation (DOK-175-15, to T.B.A.). The authors would like to thank the Deutsche Forschungsgemeinschaft (DFG) project-number 326998133 - TRR 225 (project B03 to S.S. and C01 to T.S.) and Grant N. SA 3575/1-1 (to S·S.). The authors further acknowledge financial support by the German Academic Exchange service (DAAD) through its Thematic Melbourne-Bayreuth Polymer/Colloid Network sponsored from funds of the Federal Ministry of Education and Research (BMBF).

Declaration of competing interest

The authors declare that they have no known competing financial interests or personal relationships that could have appeared to influence the work reported in this paper.

Acknowledgments

The authors would like to thank Dr. Hendrik Bargel for scanning electron microscopy imaging, Carolin Grill for help with electrospinning, and Johannes Diehl for fermentation and protein purification.

Appendix A. Supplementary data

Supplementary data to this article can be found online at https://doi.org/10.1016/j.mtbio.2020.100042.

References

[1] L.R. Robinson, Traumatic injury to peripheral nerves, Muscle Nerve 23 (6) (2000) 863–873.
[2] W. Daly, L. Yao, D. Zeugolis, A. Windebank, A. Pandit, A biomaterials approach to peripheral nerve regeneration: bridging the peripheral nerve gap and enhancing functional recovery, J. R. Soc. Interface 9 (67) (2012) 202–221.
[3] A. Magaz, A. Faroni, J.E. Gough, A.J. Reid, X. Li, J.J. Blaker, Bioactive silk-based nerve guidance conduits for augmenting peripheral nerve repair, Adv. Healthc. Mater. 7 (23) (2018) 1800308.
[4] E.G. Fine, I. Decosterd, M. Papaloïzos, A.D. Zurn, P. Aebischer, GDNF and NGF released by synthetic guidance channels support sciatic nerve regeneration across a long gap, Eur. J. Neurosci. 15 (4) (2002) 589–601.
[5] G. Lundborg, L.B. Dahlin, N. Danielsen, R.H. Gelberman, F.M. Longo, H.C. Powell, et al., Nerve regeneration in silicone chambers: influence of gap length and of distal stump components, Exp. Neurol. 76 (2) (1982) 361–375.
[6] N.P. Patel, K.A. Lyon, J.H. Huang, An update-tissue engineered nerve grafts for the repair of peripheral nerve injuries, Neural Regen. Res. 13 (5) (2018) 764–774.
[7] W.Z. Ray, S.E. Mackinnon, Management of nerve gaps: autografts, allografts, nerve transfers, and end-to-side neurorrhaphy, Exp. Neurol. 223 (1) (2010) 77–85.
[8] A. Berger, H. Millesi, Nerve grafting, Clin. Orthop. Relat. Res. 133 (1978) 49–55.
[9] A.M. Ghaznavi, L.E. Kokai, M.L. Lovett, D.L. Kaplan, K.G. Marra, Silk fibroin conduits: a cellular and functional assessment of peripheral nerve repair, Ann. Plast. Surg. 66 (3) (2011) 273–279.
[10] S.K. Lee, S.W. Wolfe, Peripheral nerve injury and repair, JAAOS - J. Am. Acad. Orthop.Surg. 8 (4) (2000) 243–252.
[11] P.A. Wieringa, A.R. Goncalves De Pinho, S. Micera, R.J.A. Van Wezel, L. Moroni, Biomimetic architectures for peripheral nerve repair: a review of biofabrication strategies, Adv. Healthc. Mater. 7 (8) (2018), e1701164.
[12] W.A. Lackington, A.J. Ryan, F.J. O'brien, Advances in nerve guidance conduit-based therapeutics for peripheral nerve repair, ACS Biomater. Sci. Eng. 3 (7) (2017) 1221–1235.
[13] G.C.W. De Ruiter, M.J.A. Malessy, M.J. Yaszemski, A.J. Windebank, R.J. Spinner, Designing ideal conduits for peripheral nerve repair, Neurosurg, Focus 26 (2) (2009). E5-E5.
[14] S. Kehoe, X.F. Zhang, D. Boyd, FDA approved guidance conduits and wraps for peripheral nerve injury: a review of materials and efficacy, Injury 43 (5) (2012) 553–572.
[15] T.M.A. Henderson, K. Ladewig, D.N. Haylock, K.M. Mclean, A.J. O'connor, Cryogels for biomedical applications, J. Mater. Chem. B 1 (21) (2013) 2682–2695.
[16] T.M. Henderson, K. Ladewig, D.N. Haylock, K.M. Mclean, A.J. O'connor, Formation and characterisation of a modifiable soft macro-porous hyaluronic acid cryogel platform, J. Biomater. Sci. Polym. Ed. 26 (13) (2015) 881–897.
[17] D. Arslantunali, T. Dursun, D. Yucel, N. Hasirci, V. Hasirci, Peripheral nerve conduits: technology update, Med. Devices (Auckl) 7 (2014) 405–424.
[18] G. Koopmans, B. Hasse, N. Sinis, The role of collagen in peripheral nerve repair, Int. Rev. Neurobiol. 87 (2009) 363–379.

[19] T. Ushiki, C. Ide, Three-dimensional organization of the collagen fibrils in the rat sciatic nerve as revealed by transmission- and scanning electron microscopy, Cell Tissue Res. 260 (1) (1990) 175–184.
[20] A. Sorushanova, L.M. Delgado, Z.N. Wu, N. Shologu, A. Kshirsagar, R. Raghunath, et al., The collagen suprafamily: from biosynthesis to advanced biomaterial development, Adv. Mater. 31 (1) (2019), 1801651.
[21] K.L. Lin, D.W. Zhang, M.H. Macedo, W.G. Cui, B. Sarmento, G.F. Shen, Advanced collagen-based biomaterials for regenerative biomedicine, Adv. Funct. Mater. 29 (3) (2019) 1804943.
[22] R.C. Goy, S.T.B. Morais, O.B.G. Assis, Evaluation of the antimicrobial activity of chitosan and its quaternized derivative on E. coli and S. aureus growth, Rev. Bras. de Farmacogn. 26 (1) (2016) 122–127.
[23] M. Rinaudo, Chitin and chitosan: properties and applications, Prog. Polym. Sci. 31 (7) (2006) 603–632.
[24] D.P. Biswas, P.A. Tran, C. Tallon, A.J. O'connor, Combining mechanical foaming and thermally induced phase separation to generate chitosan scaffolds for soft tissue engineering, J. Biomater. Sci. Polym. Ed. 28 (2) (2017) 207–226.
[25] M.J. Simoes, A. Gartner, Y. Shirosaki, R.M. Gil Da Costa, P.P. Cortez, F. Gartner, et al., In vitro and in vivo chitosan membranes testing for peripheral nerve reconstruction, Acta Med. Port. 24 (1) (2011) 43–52.
[26] Q. Guo, C. Liu, B. Hai, T. Ma, W. Zhang, J. Tan, et al., Chitosan conduits filled with simvastatin/Pluronic F-127 hydrogel promote peripheral nerve regeneration in rats, J. Biomed. Mater. Res. B Appl. Biomater. 106 (2) (2018) 787–799.
[27] T.A. Blackledge, C.Y. Hayashi, Silken toolkits: biomechanics of silk fibers spun by the orb web spider Argiope argentata (Fabricius 1775), J. Exp. Biol. 209 (13) (2006) 2452–2461.
[28] F. Vollrath, D. Porter, Spider silk as archetypal protein elastomer, Soft Matter 2 (5) (2006) 377–385.
[29] C. Radtke, C. Allmeling, K.H. Waldmann, K. Reimers, K. Thies, H.C. Schenk, et al., Spider silk constructs enhance axonal regeneration and remyelination in long nerve defects in sheep, PloS One 6 (2) (2011), e16990.
[30] C. Allmeling, A. Jokuszies, K. Reimers, S. Kall, C.Y. Choi, G. Brandes, et al., Spider silk fibres in artificial nerve constructs promote peripheral nerve regeneration, Cell Prolif 41 (3) (2008) 408–420.
[31] K. Schacht, T. Scheibel, Processing of recombinant spider silk proteins into tailor-made materials for biomaterials applications, Curr. Opin. Biotechnol. 29 (2014) 62–69.
[32] M. Lewicka, O. Hermanson, A.U. Rising, Recombinant spider silk matrices for neural stem cell cultures, Biomaterials 33 (31) (2012) 7712–7717.
[33] B. An, M.D. Tang-Schomer, W.W. Huang, J.Y. He, J.A. Jones, R.V. Lewis, et al., Physical and biological regulation of neuron regenerative growth and network formation on recombinant dragline silks, Biomaterials 48 (2015) 137–146.
[34] K. Pawar, G. Welzel, C. Haynl, S. Schuster, T. Scheibel, Recombinant spider silk and collagen-based nerve guidance conduits support neuronal cell differentiation and functionality in vitro, ACS Appl. Bio Mater. 2 (11) (2019) 4872–4880.
[35] T.B. Aigner, E. Desimone, T. Scheibel, Biomedical applications of recombinant silk-based materials, Adv. Mater. 30 (19) (2018), e1704636.
[36] K. Schacht, T. Jüngst, M. Schweinlin, A. Ewald, J. Groll, T. Scheibel, Biofabrication of cell-loaded 3D spider silk constructs, Angew. Chem. Int. Ed. 54 (9) (2015) 2816–2820.
[37] K. Schacht, J. Vogt, T. Scheibel, Foams made of engineered recombinant spider silk proteins as 3D scaffolds for cell growth, ACS Biomater. Sci. Eng. 2 (4) (2016) 517–525.
[38] A. Leal-Egana, G. Lang, C. Mauerer, J. Wickinghoff, M. Weber, S. Geimer, et al., Interactions of fibroblasts with different morphologies made of an engineered spider silk protein, Adv. Eng. Mater. 14 (3) (2012) B67–B75.
[39] C.B. Borkner, S. Wohlrab, E. Moller, G. Lang, T. Scheibel, Surface modification of polymeric biomaterials using recombinant spider silk proteins, ACS Biomater. Sci. Eng. 3 (5) (2017) 767–775.
[40] C.B. Borkner, M.B. Elsner, T. Scheibel, Coatings and films made of silk proteins, ACS Appl. Mater. Interfaces 6 (18) (2014) 15611–15625.
[41] E. Desimone, K. Schacht, A. Pellert, T. Scheibel, Recombinant spider silk-based bioinks, Biofabrication 9 (4) (2017), 044104.
[42] D. Steiner, G. Lang, L. Fischer, S. Winkler, T. Fey, P. Greil, et al., Intrinsic vascularization of recombinant eADF4(C16) spider silk matrices in the arteriovenous loop model, Tissue Eng. Part A (2019) 1504–1513.
[43] P.H. Zeplin, N.C. Maksimovikj, M.C. Jordan, J. Nickel, G. Lang, A.H. Leimer, et al., Spider silk coatings as a bioshield to reduce periprosthetic fibrous capsule formation, Adv. Funct. Mater. 24 (18) (2014) 2658–2666.
[44] P.H. Zeplin, A.K. Berninger, N.C. Maksimovikj, P. Van Gelder, T. Scheibel, H. Walles, Improving the biocompatibility of silicone implants using spider silk coatings: immunohistochemical analysis of capsule formation, Handchir. Mikrochir. Plast. Chir. 46 (6) (2014) 336–341.
[45] T.I. Harris, D.A. Gaztambide, B.A. Day, C.L. Brock, A.L. Ruben, J.A. Jones, et al., Sticky situation: an investigation of robust aqueous-based recombinant spider silk protein coatings and adhesives, Biomacromolecules 17 (11) (2016) 3761–3772.
[46] S. Müller-Herrmann, T. Scheibel, Enzymatic degradation of films, particles, and nonwoven meshes made of a recombinant spider silk protein, ACS Biomater. Sci. Eng. 1 (4) (2015) 247–259.
[47] B. Zhu, W. Li, R.V. Lewis, C.U. Segre, R. Wang, E-spun composite fibers of collagen and dragline silk protein: fiber mechanics, biocompatibility, and application in stem cell differentiation, Biomacromolecules (2014) 202–213.
[48] S. Wohlrab, S. Müller, A. Schmidt, S. Neubauer, H. Kessler, A. Leal-Egana, et al., Cell adhesion and proliferation on RGD-modified recombinant spider silk proteins, Biomaterials 33 (28) (2012) 6650–6659.
[49] T. Aigner, T. Scheibel, Self-rolling refillable tubular enzyme containers made of recombinant spider silk and chitosan, ACS Appl. Mater. Interfaces 11 (17) (2019) 15290–15297.
[50] G. Lang, Herstellung und Charakterisierung von Fasern aus rekombinanten Spinnenseidenproteinen und deren potentielle Applikationen, 2015. Dissertation, urn:nbn:de:bvb:703-epub-2038-3. (Accessed 15 July 2019).
[51] L. Ionov, Soft microorigami: self-folding polymer films, Soft Matter 7 (15) (2011) 6786–6791.
[52] ATCC, PC-12 (ATCC® CRL-1721™), 2016. https://www.lgcstandards-atcc.org/products/all/CRL-1721.aspx?geo_country=de#specifications. (Accessed 6 August 2019).
[53] M. Sarker, S. Naghieh, A.D. Mcinnes, D.J. Schreyer, X. Chen, Strategic design and fabrication of nerve guidance conduits for peripheral nerve regeneration, Biotechnol. J. 13 (7) (2018), 1700635.
[54] M.K. Kwan, E.J. Wall, J. Massie, S.R. Garfin, Strain, stress and stretch of peripheral nerve Rabbit experiments in vitro and in vivo, Acta Orthop. Scand. 63 (3) (1992) 267–272.
[55] J.B. Scott, M. Afshari, R. Kotek, J.M. Saul, The promotion of axon extension in vitro using polymer-templated fibrin scaffolds, Biomaterials 32 (21) (2011) 4830–4839.
[56] A. Orlowska, P.T. Perera, M. Al Kobaisi, A. Dias, H.K.D. Nguyen, S. Ghanaati, et al., The effect of coatings and nerve growth factor on attachment and differentiation of pheochromocytoma cells, Materials (Basel) 11 (1) (2017) 60.
[57] D.G. Attiah, R.A. Kopher, T.A. Desai, Characterization of PC12 cell proliferation and differentiation-stimulated by ECM adhesion proteins and neurotrophic factors, J. Mater. Sci. Mater. Med. 14 (11) (2003) 1005–1009.
[58] H.K. Kleinman, L. Luckenbill-Edds, F.W. Cannon, G.C. Sephel, Use of extracellular matrix components for cell culture, Anal. Biochem. 166 (1) (1987) 1–13.
[59] N. Kinarivala, K. Shah, T.J. Abbruscato, P.C. Trippier, Passage variation of PC12 cells results in inconsistent susceptibility to externally induced apoptosis, ACS Chem. Neurosci. 8 (1) (2017) 82–88.
[60] E.J. Huang, L.F. Reichardt, Trk receptors: roles in neuronal signal transduction, Annu. Rev. Biochem. 72 (1) (2003) 609–642.
[61] M.A. Tischfield, H.N. Baris, C. Wu, G. Rudolph, L. Van Maldergem, W. He, et al., Human TUBB3 mutations perturb microtubule dynamics, kinesin interactions, and axon guidance, Cell 140 (1) (2010) 74–87.

Supplementary data

Nerve guidance conduit design based on self-rolling tubes

T.B. Aigner,[a,&] C. Haynl,[a,&] S. Salehi,[a] A. O'Connor [b] and T. Scheibel[a,c,d,e,f,*]

[a]University of Bayreuth, Department of Biomaterials, Prof.-Rüdiger-Bormann-Str.1, 95447 Bayreuth, Germany

[b]University of Melbourne, Department of Biomedical Engineering, Melbourne, Victoria 3010, Australia

[c]University of Bayreuth, Bayreuther Zentrum für Kolloide und Grenzflächen (BZKG), Universitätsstraße 30, 95447 Bayreuth, Germany

[d]University of Bayreuth, Bayreuther Zentrum für Molekulare Biowissenschaften (BZMB), Universitätsstraße 30, 95447 Bayreuth, Germany

[e]University of Bayreuth, Bayreuther Materialzentrum (BayMAT), Universitätsstraße 30, 95447 Bayreuth, Germany

[f]University of Bayreuth, Bayerisches Polymerinstitut (BPI), Universitätsstraße 30, 95447 Bayreuth, Germany

To whom correspondence should be addressed: thomas.scheibel@bm.uni-bayreuth.de

[&]contributed equally

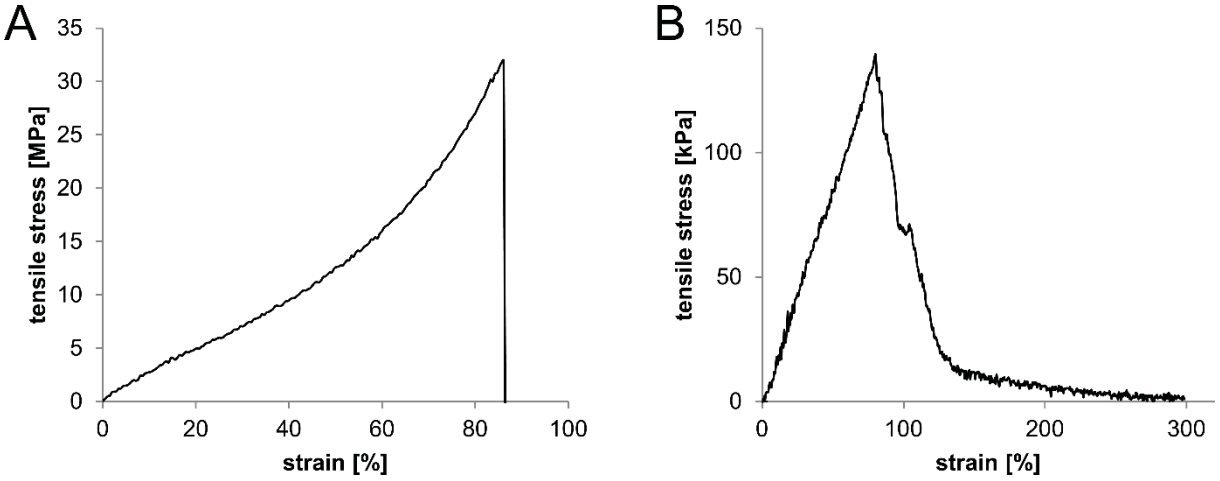

Fig. S1. Stress-strain plot of (A) a wet chitosan film used for fabricating self-rolling tubes and (B) a moist collagen cryogel.

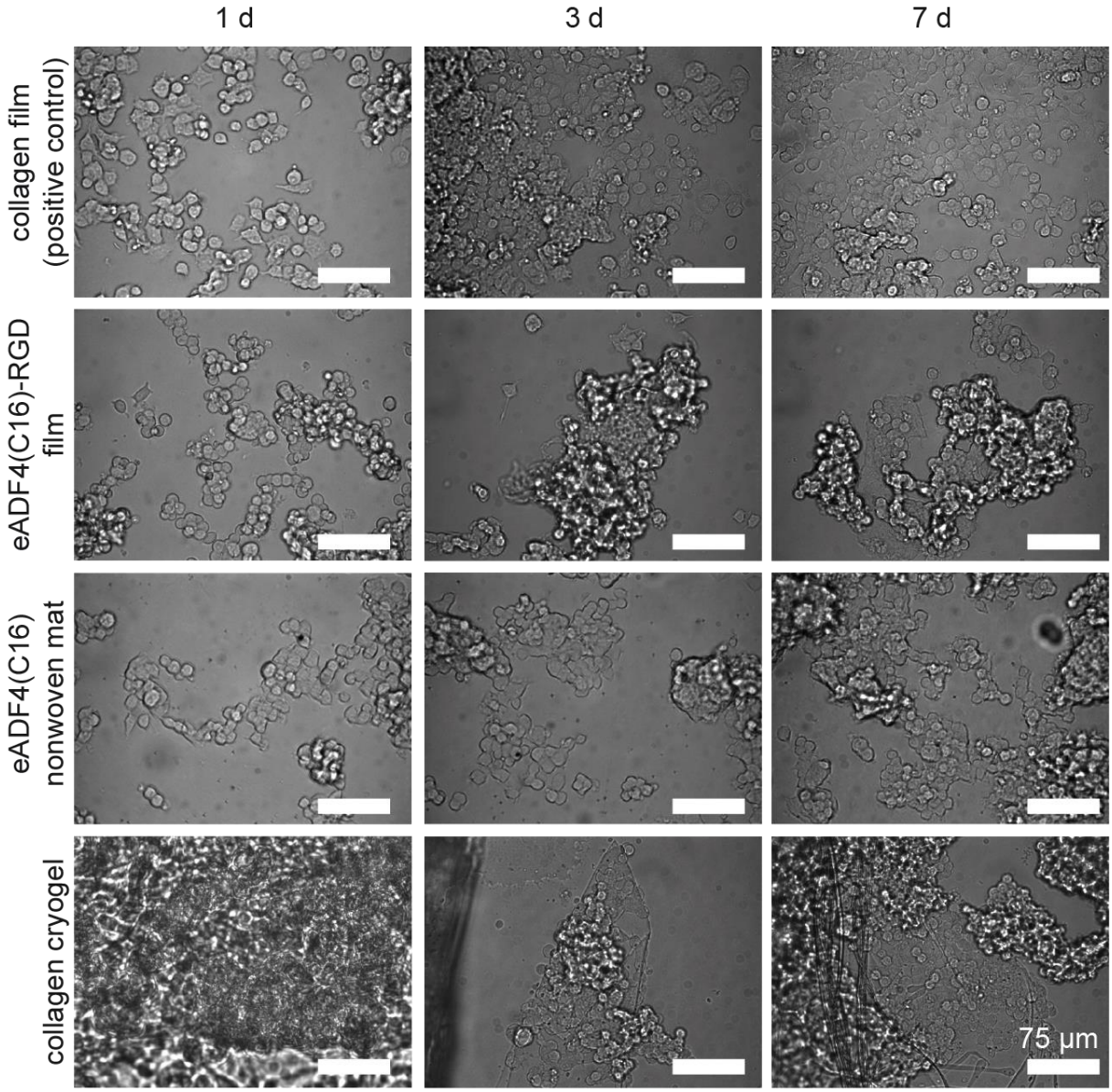

Fig. S2. Optical microscopy images showing adhesion of PC-12 cells on different substrates. Brightfield images of cells incubated in growth medium were taken after 1, 3 and 7 days to analyze cell adhesion on an eADF4(C16)-RGD film, an eADF4(C16) isotropic nonwoven mat and an anisotropic collagen cryogel in comparison to a collagen coating as the positive control. All scale bars correspond to 75 µm.

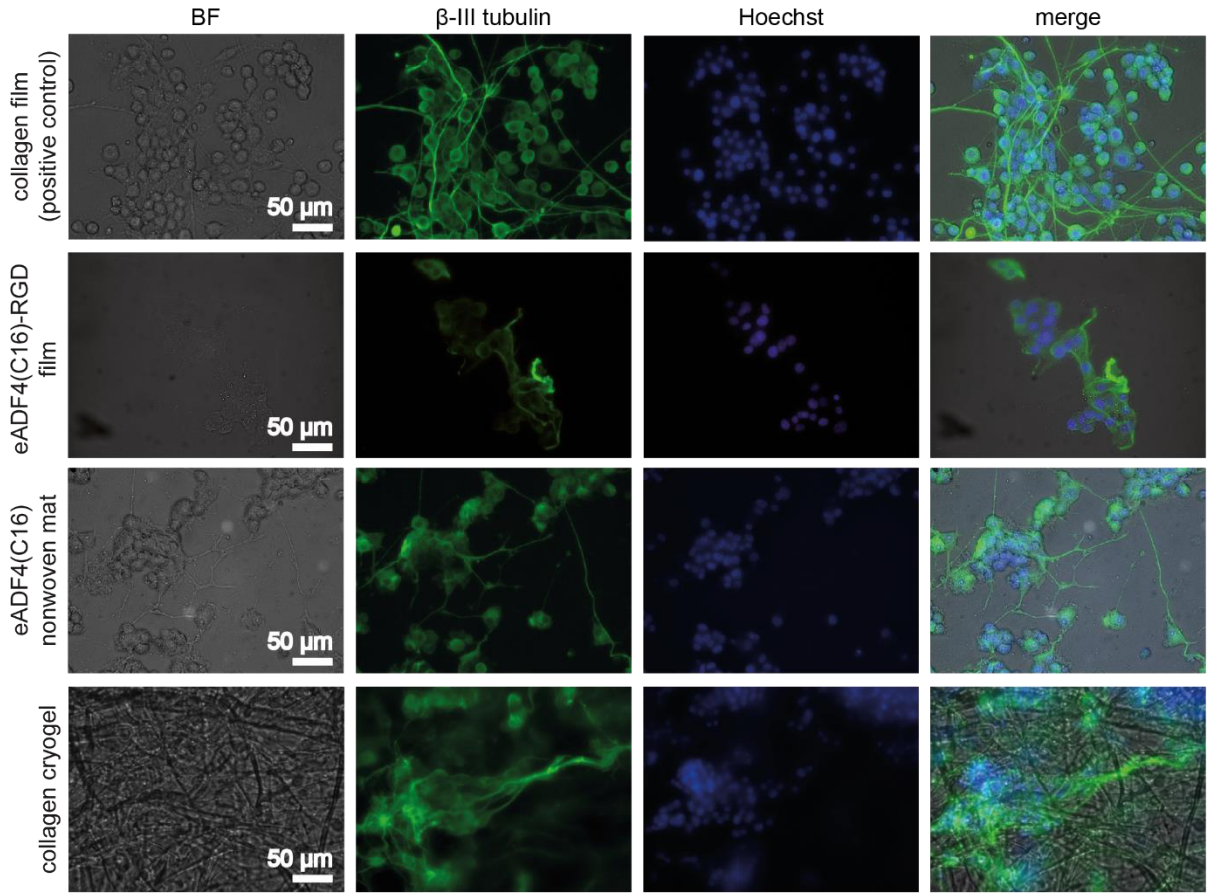

Fig. S3. PC-12 nerve cells on a collagen film (positive control), eADF4(C16)-RGD film, isotropic eADF4(C16) nonwoven mat and on an anisotropic collagen cryogel after 7 days of differentiation. Brightfield (BF) images show the surfaces of the films, nonwoven mat or the collagen cryogel. Immunostaining against β-III tubulin visualized the microtubule forming protein present in differentiated neurons, whereas Hoechst staining visualized cell nuclei.

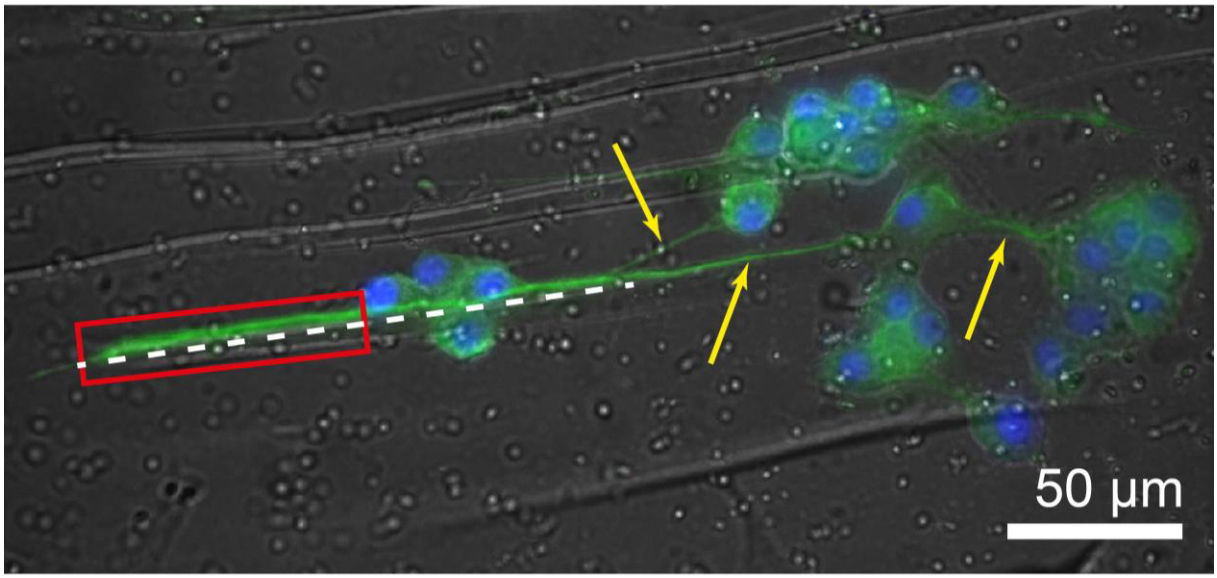

Fig. S4. PC-12 nerve cells on collagen cryogel forming bundle-like structures (red box) compared to single neurites (yellow arrows). The bundle-like structure is aligned with the collagen cryogel (dashed line).

7.5 Teilarbeit 5

Haynl, C.; Vongsvivut, J.; Mayer, K. R. H; Bargel, H.; Neubauer, V. J.; Tobin, M. J.; Elgar, M. A.; * Scheibel, T.*

Free-standing spider silk webs of the thomisid *Saccodomus formivorus* are made of composites comprising micro- and submicron fibers.

Scientific Reports **2020**, 10, 17624

DOI: 10.1038/s41598-020-74469-z

scientific reports

Check for updates

OPEN

Free-standing spider silk webs of the thomisid *Saccodomus formivorus* are made of composites comprising micro- and submicron fibers

Christian Haynl[1], Jitraporn Vongsvivut[2], Kai R. H. Mayer[1], Hendrik Bargel[1], Vanessa J. Neubauer[1], Mark J. Tobin[2], Mark A. Elgar[3]✉ & Thomas Scheibel[1,4,5,6,7]✉

Our understanding of the extraordinary mechanical and physico-chemical properties of spider silk is largely confined to the fibers produced by orb-weaving spiders, despite the diversity of foraging webs that occur across numerous spider families. Crab spiders (Thomisidae) are described as ambush predators that do not build webs, but nevertheless use silk for draglines, egg cases and assembling leaf-nests. A little-known exception is the Australian thomisid *Saccodomus formivorus*, which constructs a basket-like silk web of extraordinary dimensional stability and structural integrity that facilitates the capture of its ant prey. We examined the physical and chemical properties of this unusual web and revealed that the web threads comprise microfibers that are embedded within a biopolymeric matrix containing additionally longitudinally-oriented submicron fibers. We showed that the micro- and submicron fibers differ in their chemical composition and that the web threads show a remarkable lateral resilience compared with that of the major ampullate silk of a well-investigated orb weaver. Our novel analyses of these unusual web and silk characteristics highlight how investigations of non-model species can broaden our understanding of silks and the evolution of foraging webs.

The properties of orb web silks have been extensively characterized[1–6], and they typically comprise five silk types, with two additional types found in the egg cases[7,8]. The mechanical properties vary across the silk types[7,8] and depend, in part, on the content of crystalline and amorphous regions providing strength and extensibility[5,9–11]. All extant spiders produce silk, which may have originally been used to provide protection for the spiders and their eggs, and it is thought that foraging webs are derived from this ancestral state[12–14] with concomitant changes in silk properties[4]. Crab spiders (Thomisidae) are typically described as ambush predators, remaining concealed in the vegetation before seizing their prey, but do not build foraging webs[15–18]. These spiders nevertheless produce draglines and attachment discs[19], form egg cases and use silk to construct protective leaf nests[15]. The Australian thomisid *Saccodomus formivorus*[20] is a remarkable exception, constructing a basket-like web that facilitates the capture of its ant prey[20–23]. The spiders construct their webs on low-lying shrubs that are in close proximity to either the nests or foraging trails of ants (MAE, pers obs). Foraging worker ants of several different species may be attracted to the silk of these webs, and those that venture into the basket are subsequently captured by the resident spider[23]. Clearly, the silk of the basket web of *S. formivorus* has properties that differ from those of other, conventional foraging webs. In particular, the silk must support the remarkable feature of the basket-like design: high dimensional stability that allows a free-standing web structure. Here, we describe the micro-morphology

[1]Department for Biomaterials, University of Bayreuth, Prof.-Rüdiger-Bormann-Str.1, 95447 Bayreuth, Germany. [2]ANSTO Australian Synchrotron, Infrared Microspectroscopy Beamline, Clayton, VIC 3168, Australia. [3]School of BioSciences, The University of Melbourne, Melbourne, VIC 3010, Australia. [4]University of Bayreuth, Bayreuther Zentrum für Kolloide Und Grenzflächen (BZKG), Universitätsstraße 30, 95440 Bayreuth, Germany. [5]University of Bayreuth, Bayerisches Polymerinstitut (BPI), Universitätsstraße 30, 95440 Bayreuth, Germany. [6]University of Bayreuth, Bayreuther Zentrum für Molekulare Biowissenschaften (BZMB), Universitätsstraße 30, 95440 Bayreuth, Germany. [7]University of Bayreuth, Bayreuther Materialzentrum (BayMAT), Universitätsstraße 30, 95440 Bayreuth, Germany. ✉email: m.elgar@unimelb.edu.au; thomas.scheibel@bm.uni-bayreuth.de

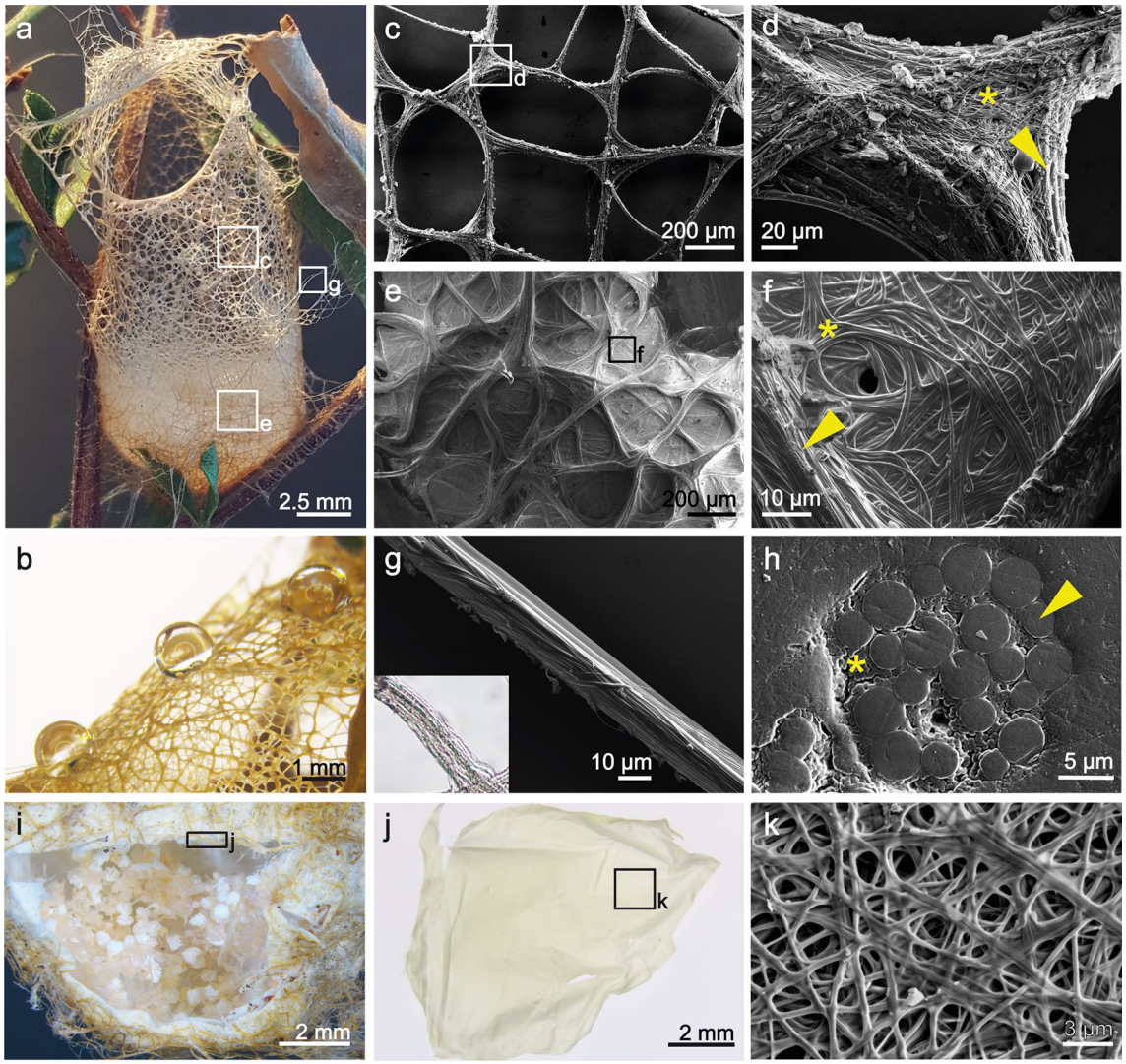

Figure 1. Morphological features of the silk of the web of *S. formivorus*. (**a**) Photograph of the entire basket web. (**b**) Water droplets on the web indicate high water contact angles. Scanning electron microscopy (SEM) images of (**c**) the upper and (**e**) the lower web sections originating from the zones marked in (**a**). (**d**, **f**) SEM images of marked sections in (**c**,**e**) (arrowheads indicate the presence of microfibers, asterisks show accumulated submicron fibers). (**g**) SEM image of a single protruding spider silk thread as marked in (**a**). The inset shows a light microscopic image of a protruding thread. (**h**) SEM micrograph of the thread cross-section comprising several microfibers embedded in a submicron fiber matrix (arrowhead indicates a microfiber cross-section, asterisk shows accumulated submicron fiber cross-sections). (**i**) Micrograph of the lower web section showing several hatched eggs. (**j**) Nonwoven-like sheet, which horizontally covered the eggs shown in (**i**). (**k**) SEM image of the nonwoven-like sheet as marked in (**j**).

of the basket web and its structural and mechanical properties. We reveal that micro- and submicron fibers, exhibiting a distinct chemical composition, yield threads that are extraordinarily resilient against lateral loads compared with the major ampullate silk of orb webs. We further reveal that the base of the basket web contains spider eggs: this is arguably the first documented example of an elaborate spider foraging web that has evolved as an extension of the protective egg case.

Results

Unique morphology of the basket webs of *S. formivorus*. The non-sticky webs of *S. formivorus* are cylindrical resembling a basket or "lobster pot" of 11 ± 3 mm diameter, 14 ± 4 mm depth (SD, $N = 4$) with an opening at the top that varies in size and shape. The web structure comprises crosslinked threads of varying diameters. The basket webs are firmly attached to branches and leaves by protruding threads originating throughout the web (Fig. 1a). The protruding threads resemble those that form the basket web, but are more uniform in diameter and show no crosslinks with other threads. The webs were highly water repellent (Fig. 1b), and the contact angle was estimated to be around 126° ± 11° (SD, $N = 3$).

The webs showed two distinct fiber types: microfibers of several micrometer diameter, and submicron fibers. The density of submicron fibers was lower in the upper section of the basket web (Fig. 1c), and they were distributed around the larger threads only (Fig. 1d), whereas the submicron fibers in the lower section (Fig. 1e) were also found in between the threads (Fig. 1f). As a result, the web resistance against compression increased from the upper to the lower part of the basket. At a closer look, the threads (Fig. 1g) comprised several microfibers with two to four micrometers in diameter, which were embedded in a matrix made of longitudinally oriented submicron fibers of around 400 nm in diameter (Fig. 1h).

The basket webs are not used exclusively as a retreat and foraging structure for the resident spider, as previously reported[20–23]. The base of some webs had a more pronounced submicron fiber architecture and contained hatched eggs (Fig. 1i) that were covered by a nonwoven-like sheet (Fig. 1j,k).

Two fiber types with distinct chemical features. We obtained spatially-resolved Fourier-transform infrared (FTIR) spectra of the thread cross-section (Fig. 2a) using synchrotron FTIR (S-FTIR) microspectroscopy, equipped with a macro attenuated total reflectance FTIR (ATR-FTIR) device, following Vongsvivut et al.[24].

A chemical map of the protein distribution across the thread cross-section was produced based on the integrated area under the amide I band (1720–1590 cm^{-1}) (Fig. 2b). Similarly, a chemical map of C–OH and/or C–O–C vibrational modes was acquired by integrating the area in the spectral range of 1200–990 cm^{-1} (Fig. 2c)[25–27]. The amide I chemical map in Fig. 2b corresponds well with the scanning electron microscopic (SEM) image of the thread cross-section (Fig. 2a), allowing the extraction of spectra on the specific areas that represented microfiber cross-sections (1–7), as well as submicron fiber cross-sections (A–G). In addition to the S-FTIR investigation, ATR-FTIR measurements of submicron fiber surfaces (i.e. of nonwoven-like sheets as illustrated in Fig. 1j,k) were conducted using a laboratory-based spectrometer equipped with a thermal IR (Globar) source. Average spectra of the micro- and submicron fiber cross-sections and of the submicron fiber surfaces are given in Fig. 2d.

Interestingly, the chemical maps showed high C–OH and/or C–O–C absorbance between the microfibers where the submicron fibers were present. In contrast, the C–OH and/or C–O–C absorbance observed on the submicron fiber surfaces was lower than that of the micro- and submicron fiber cross-sections (Fig. 2d). The second derivatives were calculated from each spectrum of the thread cross-section to identify putative crystallite regions, i.e. pleated β-sheets, which are one feature of spider silk fibers[9,10]. The integrated values of the respective band within the spectral range of 1638–1616 cm^{-1} were plotted to produce a chemical map allowing visualization of the spatial distribution of β-sheets across the thread cross-section (Fig. 2e), which clearly showed that both fiber types comprised β-sheets. The corresponding average second derivative spectra of the micro- and submicron fiber cross-sections are depicted in Fig. 2f, showing no significant structural differences based on their spectral features.

We used the seven extracted spectra of the microfiber cross-sections (1–7) and of the seven areas representing the submicron fiber cross-sections (A–G) for Fourier self-deconvolution (FSD) and curve fitting of the amide I bands. Therewith, we analyzed the approximate secondary protein structure proportions, which are determined by the ratio of the respective secondary protein structure sub-peak integrals to the total sub-peak integral (Fig. 2g,h). The results indicated that there are no significant differences between the cross-sections of the microfibers and submicron fibers. However, there are higher β-sheet and random coil contents, but less side chain, α-helix and turn elements in the cross-sections than on the submicron fiber surface (Fig. 2i).

Basket threads have distinct mechanical properties. The silk threads of *S. formivorus* have a remarkable mechanical property that has not been documented for any silk produced by spiders—namely, a resistance against lateral deformation that allows free-standing threads and webs. We determined the resiliencies of the basket threads upon lateral deformation (Fig. 3a,b). For comparison, we chose double-filament major ampullate silk of the Australian golden orb weaver *N. edulis* (Fig. 3c), which fairly reflect the mechanical properties of major ampullate silks of orb-webs[28,29]. The diameters of the examined threads of *S. formivorus* were much higher (14–80 µm) than those of the major ampullate silk of *N. edulis* (3–6 µm for single filaments). The distinct mechanical property of the basket web is revealed by comparing the resiliencies of the silk threads of *S. formivorus* that ranged from 19 to 625 mN, with that of the major ampullate double-filament silk of *N. edulis* that ranged from 25 to 107 mN (Fig. 3d).

We further analyzed the tensile properties of the threads of *S. formivorus* with a diameter range of 11–75 µm. A representative stress–strain plot and the real stress–strain data of the threads of two individual webs are given in Fig. 3e–i. In comparison to orb-webs, the tensile strength and Young's modulus of the basket threads was not as high as those of major ampullate[7,8,28,29] and minor ampullate silks[7,8,30], nor did the threads exhibit the remarkable extensibility of flagelliform silks[7,8,31]. Table 1 compares the mechanical properties of the basket threads with the complete set of silk types of a model orb-web spider (here: *A. argentata* has been chosen because it is the only species with a complete set of data obtained at consistent experimental conditions[8]).

Basket web threads exhibit spider silk typical chemical properties. The micro- and submicron fibers within the upper and lower sections of the basket web provided good chemical resistance, as commonly observed for spider silk fibers[32,33]. In particular, the basket threads were stable for at least 7 days against chaotropic agents such as 8 M urea and 6 M guanidinium thiocyanate, the organic solvent hexafluoroisopropanol (HFIP), the ionic liquid 1-ethyl-3-methylimidazolium acetate (EMIM acetate) and 98% formic acid. In contrast, both fiber types degraded within the first 72 h after incubation in 32% hydrochloric acid, and treatment with 10 M sodium hydroxide yielded isolated fiber fragments, which disappeared after 1 week of incubation (Supplementary Fig. S1).

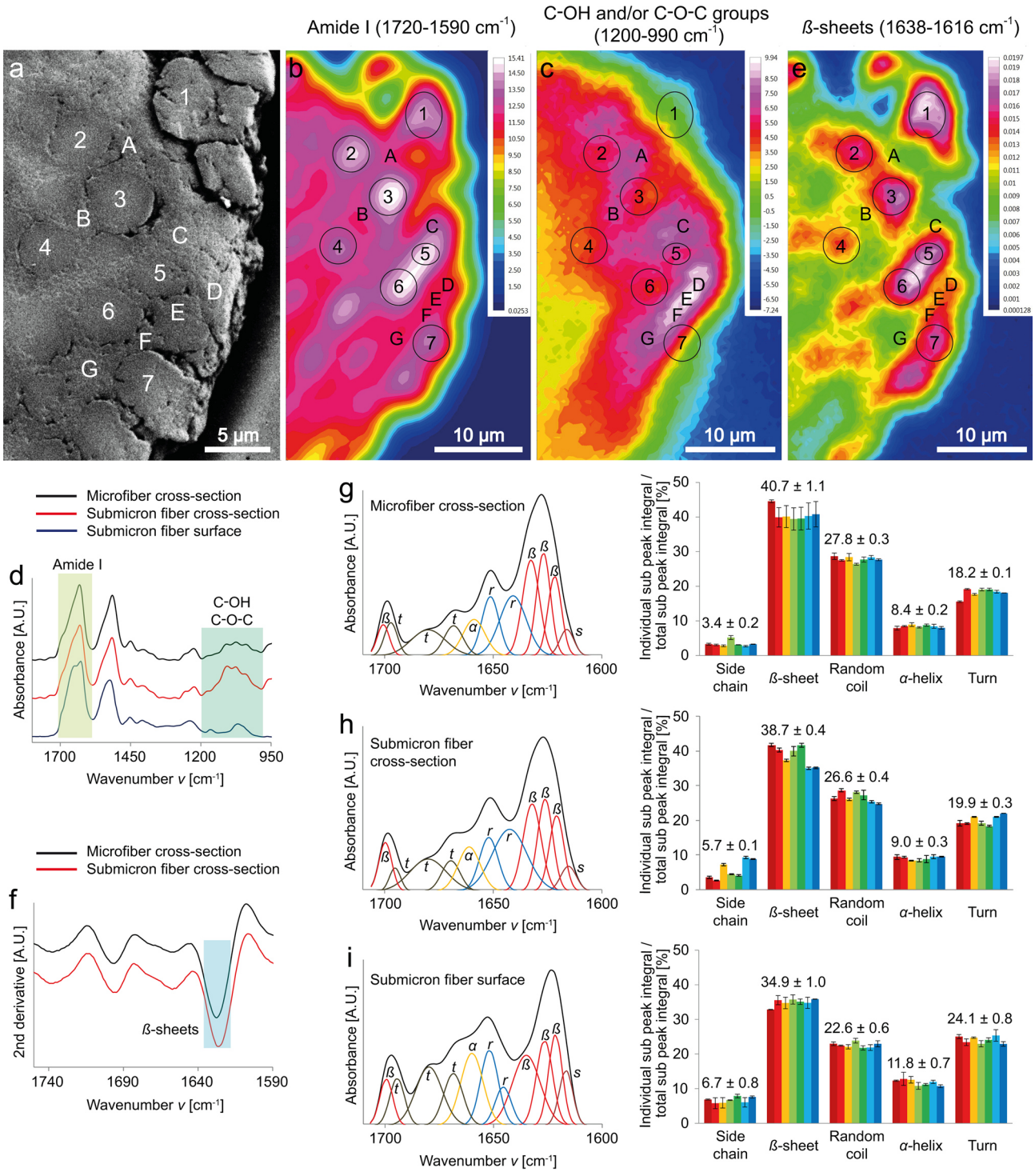

Figure 2. FTIR spectroscopic investigation of the silks in the basket web of *S. formivorus*. (**a**) SEM image of a thread cross-section comprising several microfibers (1–7) embedded in a submicron fiber matrix (A–G). The spatially-resolved chemical distribution (chemical map) of the thread cross-section was analyzed using synchrotron FTIR (S-FTIR) microspectroscopy, equipped with a macro ATR-FTIR device. (**b**,**c**) Chemical maps of the overall protein (i.e. amide I) distribution (1720–1590 cm^{-1}) and of C–OH and/or C–O–C groups (1200–990 cm^{-1}), respectively. The areas on the chemical images, indicated by number 1–7, match the location of microfibers depicted in (**a**), whereas those labelled A-G match the submicron fiber matrix. Absorption intensities correlate with the color scales and increase from blue to white. Blue-colored areas indicate no absorbance of chemicals of interest, and thereby suggesting the presence of the resin used for embedding. (**d**) Mean absorbance spectra of the microfiber cross-sections, submicron fiber cross-sections and submicron fiber surfaces. (**e**) Absorbance indicates *β*-sheet secondary protein conformation (1638–1616 cm^{-1}). (**f**) Mean second derivative spectra obtained from the micro- and submicron fiber cross-sections. (**g**–**i**) Left: Fourier self-deconvolved (FSD) amide I bands of the spectra obtained from the microfiber cross-section, submicron fiber cross-section and submicron fiber surface, which are presented along with their corresponding curve fitting sub peaks (*s* side chains, *β* *β*-sheets, *r* random coils, *α* *α*-helices, *t* turns). Right: secondary protein structure proportions determined by the ratio of the respective secondary protein structure sub-peak integral to the total sub-peak integral.

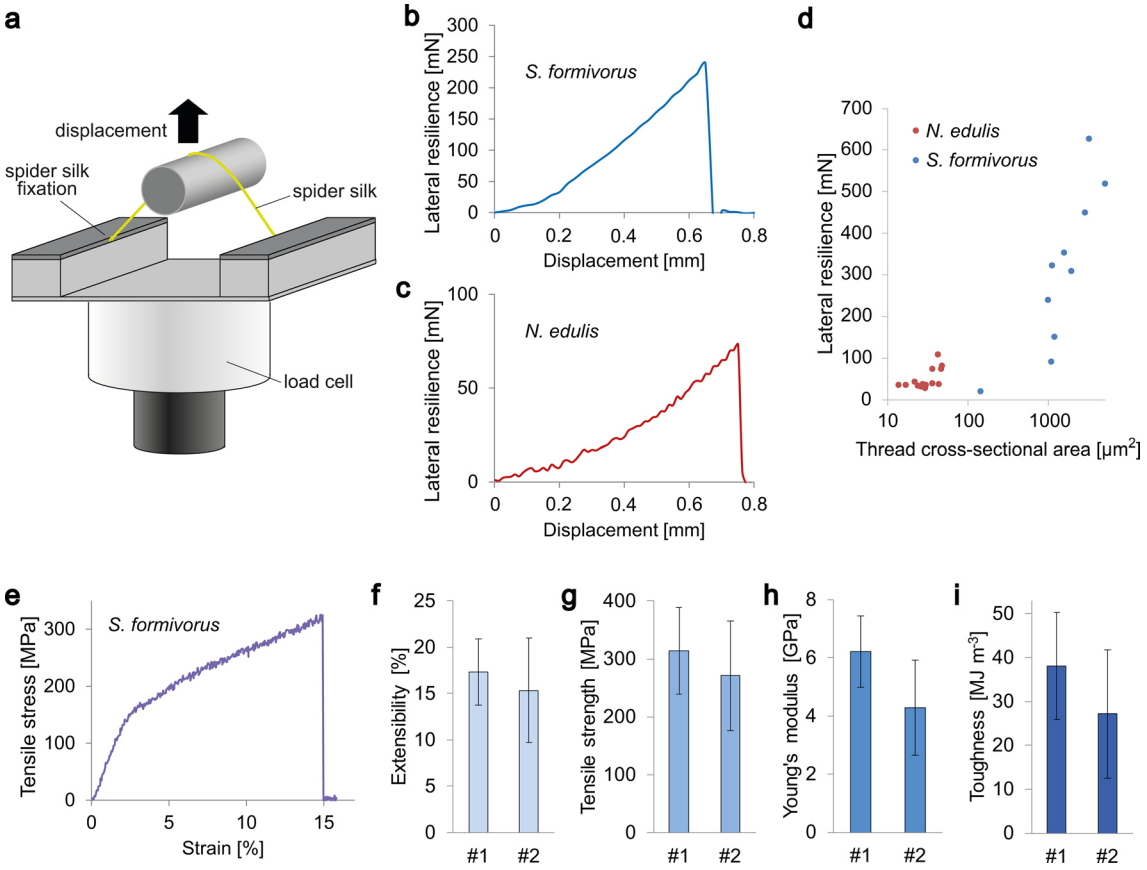

Figure 3. Mechanical properties of *S. formivorus* silk threads. (**a**) Schematic image of the lateral resilience test setup. (**b**) Exemplary lateral resilience–displacement plot of a thread of *S. formivorus*. (**c**) Exemplary lateral resilience–displacement plot of the double-filament major ampullate silk of the model orb weaver *N. edulis*. (**d**) Semi-logarithmic display comparing the lateral resiliencies of the silk of *N. edulis* with those of the threads of *S. formivorus*. (**e**) Representative stress–strain plot (real stress–strain) for a single thread of *S. formivorus* (according to inset g of Fig. 1a,g). (**f–i**) Real stress–strain data for threads originating from two webs of *S. formivorus* (#1 and #2). Error bars show standard deviation (SD).

Spider	Fiber type	Extensibility (%)	Tensile strength (MPa)	Young's modulus (GPa)	Toughness (MJ m^{-3})
S. formivorus					
#1	Composite threads	17 ± 4	314 ± 75	6.2 ± 1.2	38 ± 12
#2		15 ± 6	271 ± 95	4.3 ± 1.6	27 ± 15
A. argentata[8]	Major ampullate silk	20.5 ± 0.5	1495 ± 65	8 ± 0.8	136 ± 7
	Minor ampullate silk	33 ± 3.3	923 ± 154	10.6 ± 1.2	137 ± 22
	Flagelliform silk	172 ± 5.0	534 ± 40	0.001 ± 0.0001	75 ± 6
	Aciniform silk	40.4 ± 2.4	1052 ± 120	10.4 ± 1.4	230 ± 31
	Tubuliform silk	28.6 ± 1.5	476 ± 90	11.6 ± 2.1	95 ± 17

Table 1. Mechanical properties of threads of *S. formivorus* webs (real stress–strain data ± standard deviation (SD)) in comparison with representative orb-web spider silks of *A. argentata* (real stress–strain data ± standard error of the mean (SEM)).

We further investigated the molar percentage of carbon (*C*), hydrogen (*H*), nitrogen (*N*) and sulphur (*S*) in the threads of the upper and lower sections of the basket web. Although the lower section comprised more submicron fibers than the upper section, the *CHNS* composition in both fiber types was similar (Supplementary Table S1). The outstanding dry mass of around 35% may be attributed to oxygen atoms as a major element of proteins and to inorganic materials like dust particles, which were found in between the threads (Supplementary Fig. S1).

Discussion

The crab spider *S. formivorus* assembles micro- and submicron fibers into threads to build a basket web with an extraordinarily high dimensional stability, which provides a foraging platform to capture ants, as well as a protective refuge for the resident spider and its eggs. Although this basket web is unique across spider webs, some insects also build free-standing silken structures. For instance, the moths of the family Urodidae build cage-like, protective cocoons[34–36], which seem to possess a similar dimensional stability compared with the webs of *S. formivorus*. Free-standing, single silk threads were further observed with lacewings, forming egg stalks made of proteins with a cross-β structure[37].

Interestingly, the basket web of *S. formivorus* seems not to contain any ant deterrents such as 2-pyrrolidinone, which is found in the orb web of *Nephila antipodiana*[38] and provides protection from ant invasion. Rather, it is likely that the basket web contains an ant-attracting compound, similar to the allomone putrescine found in the silk of orb-webs, and which enhances the capture of flies[39].

The water repellent effect of the basket web may be partly due to the mesh-like surface of the web, which led to reduced physical interactions with water droplets, similar to the rough surface of non-wetting lotus plant leaves[40]. High hydrophobicity has also been observed in the silk used to form egg cases in other spider species[41,42]. The basket web further showed no overall stickiness, indicating the absence of aggregate-like silks, which provide the flagelliform silk of orb webs with adhesiveness for prey capturing[5,43].

Our examinations of the microfibers and submicron fibers confirmed considerable amounts of β-sheets, indicating that those fibers are most likely not related to the β-sheet-free flagelliform silks[11]. We further compared the secondary structure contents of the microfiber and submicron fibers in the thread cross-sections and found only negligible differences. This lack of significance could be the cause of the resolution of the macro-ATR technique that is 3.2 µm[24]. Nano-IR could be an ideal technique in future investigations to shed the light into a more accurate measure of the protein secondary structure contents of submicron fibers.

There are few accounts of the silk of spider egg cases, but large tubuliform silk fibers form the outer shell and small aciniform silk fibers line the interior of those examined[5,43]. Fiber diameters of these types of silks of orb-web (araneid) spiders (*Argiope bruennichi*: 7–8 µm and 600 nm[44], *Argiope aurantia*: 5–10 µm and 100–200 nm[45]) and tangleweb (theridiid) spiders (*Latrodectus hesperus*: 4–5 µm and 500 nm[46]) are similar to that of *S. formivorus* (2–4 µm, 400 nm). Thus, the unusual web of *S. formivorus* apparently comprises tubuliform and aciniform silks, and the foraging web has arguably evolved as an extension of the original protective egg case.

Using S-FTIR microspectroscopy, we showed that the submicron fibers within the thread cross-section had a higher content of C–OH and/or C–O–C groups compared with the microfibers, suggesting that submicron fibers in direct contact to the microfibers were modified by a C–OH and/or C–O–C-containing component (or that only the submicron fiber core comprises elevated amounts of C–OH and/or C–O–C groups, but not the submicron fiber surface). C–OH and/or C–O–C groups are basically found in saccharides[25–27], or in proteins that result from glycosylation[47], so these molecular compounds may be found in the threads of *S. formivorus*. Conjugated saccharides play a fundamental role in spider silk adhesiveness, facilitating attachment to substrates and cohesion of silk fibers[48]. Alternatively, C–OH absorbance might be additionally derived from conjugated amino acids such as serine, tyrosine and threonine. Longstanding research on orb web silks has deepened our understanding of their extraordinary material strength and elasticity[5,10,43]. Here, two distinct, longitudinally-oriented fiber types are assembled to form the composite threads of *S. formivorus*. In contrast to common fiber-reinforced plastics that receive their strength through incorporation of fibers into a polymer matrix[49,50], both fiber types of the threads of *S. formivorus* may contribute to the overall tensile properties. The tensile strength and Young's modulus of *S. formivorus* threads, assessed using tensile testing, were significantly lower than that of the major ampullate and minor ampullate silks of orb-web spiders[7,8,28–30]. In general, a fiber's tensile strength depends on the number of material imperfections, including voids, misaligned fibrils, and free and foreign particles[51]. We discovered a high degree of cavities in the submicron fiber matrix of *S. formivorus* threads (see Fig. 1h), potentially leading to a lower tensile strength.

The remarkable property of the silk threads of *S. formivorus* is their resilience against lateral loads, which has not been previously noted in spider silk. As illustrated in Fig. 3d, the lateral resilience correlates with the thread cross-sectional area. It may be that the lateral resilience is not a function of thread diameter only, but also that the biphasic structure plays a role in the thread's fractural mechanism. Crack propagation in the threads of *S. formivorus* may be stopped at the interface between micro- and submicron fibers similar to the situation in artificial and natural fiber-composites[52,53], which prevents early material failure.

In terms of biomimetics, the insights of the silk threads of *S. formivorus* could be inspiring twofold. First, the threads may be used as a natural blueprint for the design of man-made rigid threads, for example for tissue engineering or textile applications. Second, the unique structure of the threads comprising two different fiber types may inspire extrusion-based processes in order to fabricate rigid composite threads in a continuous manner.

Methods

Spider silk web collection. We collected webs of *S. formivorus* from locations in central NSW, Australia (NSW Scientific License SL101919). The basket webs were located on low bushes located adjacent to the nest entrances or foraging trails of the meat ant, *Iridomyrmex purpureus*. No animal ethics approval was required for this study.

Preparation of thread cross-sections. Thread cross-sections were prepared by embedding the threads of *S. formivorus* in epoxy resin (EpoFix, Struers) with a resin to hardener ratio of 15:2. After complete hardening for 3 days, the epoxy blocks were ground stepwise using silicon carbide abrasive paper discs ending up with an

abrasive particle size of 2.5 µm. Polishing was carried out using MD-Dac, MD-Nap and MD-Chem discs (Struers) applied with suspensions of diamonds with 3, 1 and 0.04 µm particle sizes, respectively.

Microscopy. Images of the webs were taken using a Leica M205C stereo microscope and a Leica Microscope DMI 3000B. For scanning electron microscopy (SEM), all samples were sputter-coated with platinum (2 nm coating) and imaged using a ZEISS Sigma VP 300.

Contact angle measurements. In order to estimate the water contact angles on three individual webs of *S. formivorus*, a contact angle goniometer (SURFTENS Universal, OEG) was used. Contact angles were determined 1 min after droplet deposition using 0.8 ± 0.1 µl of ultrapure water.

Chemical resistance tests. *Saccodomus formivorus* threads were incubated with either 8 M urea, 6 M guanidinium thiocyanate, hexafluoroisopropanol (HFIP), 1-ethyl-3-methylimidazolium acetate (EMIM acetate), 98% formic acid, 32% hydrochloric acid or 10 M sodium hydroxide at room temperature. After 3 and 7 days, images were taken using a Leica Microscope DMI 3000B.

Elemental (*CHNS*) analysis. The investigation of the carbon (*C*), hydrogen (*H*), nitrogen (*N*) and sulphur (*S*) content in the basket web threads of *S. formivorus* was performed using an elemental analyzer (EA 3000 HEKAtech). Respectively 2–3 mg of the upper and lower sections of three individual webs were extracted using a sharp razor blade and transferred to tin capsules. The samples were oxidatively degraded at 1050 °C in an oxygen atmosphere, whereby complete oxidation was ensured using a tungsten trioxide catalyst. The resulting compounds were separated and quantified using a gas chromatograph with helium as carrier gas and equipped with a thermal conductivity detector. The amount of substance (mol) of carbon (*C*), hydrogen (*H*), nitrogen (*N*) and sulphur (*S*) detected in the upper and lower web sections of the basket web of *S. formivorus* were related to the total *CHNS* amount of substance yielding molar fractions (mol%).

Infrared spectroscopy. The laboratory-based FTIR spectra of the submicron fiber surfaces originating from the webs of *S. formivorus*, i.e. of nonwoven-like sheets, were acquired using ATR-FTIR spectroscopy (Bruker TENSOR 27, Bruker Optik GmbH). The sheets were removed from the web interior using a sharp razor blade and were placed onto the sensing surface of the diamond ATR crystal before applying a pressure onto the top of the sample using an ergonomic clamp. Spectra were recorded using a spectrometer within a spectral range of 4000–600 cm^{-1} and a resolution of 4 cm^{-1} with 200 co-added scans. Background spectra of a clean ATR surface were acquired prior to each sample measurement using the same acquisition parameters. OPUS 8.0 software (Bruker Optik GmbH) was used for subsequent spectral processing and analysis.

Synchrotron macro attenuated total reflectance Fourier-transform infrared microspectroscopy. The spatial distribution of chemical groups and of secondary protein structures in the thread cross-section were analyzed using the synchrotron FTIR (S-FTIR) microspectroscopic technique at the Australian Synchrotron IR Microspectroscopy Beamline (Victoria, Australia). The S-FTIR measurement was performed using a Bruker VERTEX V80v spectrometer coupled with a HYPERION 2000 FTIR microscope and a liquid nitrogen-cooled narrow-band mercury cadmium telluride (MCT) detector. All synchrotron FTIR spectra were recorded within a spectral range of 3900–750 cm^{-1} using 4 cm^{-1} spectral resolution. Blackman-Harris 3-Term apodisation, Mertz phase correction, and zero-filling factor of 2 were set as default acquisition parameters using OPUS 8.0 software suite (Bruker Optik GmbH). In particular, the thread cross-sections were analyzed using an in-house developed macro ATR-FTIR device equipped with a germanium (Ge) ATR hemispherical crystal ($n_{Ge} = 4$) having a 250 µm diameter sensing facet and with a 20× IR objective (NA = 0.60; Bruker Optik GmbH) following Vongsvivut et al.[24]. The spectra were not processed using ATR correction, because the spectral comparison was all made based on the spectra data that was collected using the same setup, acquisition parameters and optical configuration. As described in Vongsvivut et al.[24], the observed spatial resolution of our synchrotron macro ATR-FTIR technique based on the parameters mentioned in the Experimental section was found to be ~ 3.20 µm. In practice, the thread cross-section, which was embedded in epoxy resin, was mounted on an aluminium disc using double-sided polyimide (Kapton) tape, and placed into the sample stage of the macro ATR-FTIR unit. First, the Ge ATR crystal was brought into the focus of the synchrotron IR beam below the 20× IR objective and, when the humidity in the nitrogen-purged enclosure surrounding the microscope stage had dropped to ~ 20%, a background spectrum was recorded in air in a non-contact mode using a projected beam size of 3.1 µm at 256 co-added scans. The thread cross-section sample was then brought into contact with the Ge ATR crystal. A rapid low-resolution overview synchrotron macro ATR-FTIR chemical map was initially acquired to determine the area and the quality of the sample contact at a 10 µm step interval using 8 co-added scans. A subsequent synchrotron macro ATR-FTIR mapping measurement was performed on specific locations within the overview map where the spectral fingerprint features of the thread cross-section were identified, using a smaller step interval of 0.5 µm and 8 co-added scans. Chemical maps were generated from the spectra by integration of the area under the specific peaks yielding spatial absorbance values as false-colored two-dimensional plots. In particular, the distribution of proteins was demonstrated by integrating the area under the amide I band (1720–1590 cm^{-1}), whereas integration of the absorbance bands in the range of 1200–990 cm^{-1} showed the presence of C–OH and/or C–O–C groups. Spatial distribution of the β-sheet secondary protein structure was generated by calculating the second derivative of the original spectra and integrating the peak areas in the range

of 1638–1616 cm^{-1}. The OPUS 8.0 software (Bruker Optik GmbH) was used for subsequent spectral processing and analysis.

Secondary protein structure content quantification. The secondary protein structure content was determined using Fourier self-deconvolution (FSD) and curve fitting of the amide I band (1720–1590 cm^{-1}). Curve fitting sub peaks were applied at wavelengths 1611, 1619, 1624, 1630, 1640, 1650, 1659, 1666, 1680, 1691 and 1698 cm^{-1} to the Fourier self-deconvolved amide I band and curve fitting was performed. Secondary structures were assigned based on a protocol from Hu et al.[54], with side chains (1605–1616 cm^{-1}), β-sheets (1616–1622, 1622–1628, 1628–1638 and 1697–1704 cm^{-1}), random coils (1638–1647 and 1647–1656 cm^{-1}), α-helices (1656–1663 cm^{-1}), and turns (1663–1671, 1671–1686 and 1686–1697 cm^{-1}), which was also successfully applied in other studies[55–58]. Quantification of the secondary structure proportions was determined by the ratio of the respective sub-peak integrals to the total sub-peak integral. For data analysis, respectively 7 microfiber cross-sections, areas of submicron fiber cross-sections and submicron fiber surfaces (i.e. nonwoven-like sheets) of one individual web were analyzed. Each amide I band (of respectively 7 spectra) was deconvolved and curve fitted for three times and the mean values were calculated. For FSD curve fitting, Opus 8.0 software (Bruker Optik GmbH) was used.

Investigation of the mechanical properties. The tensile properties of protruding (composite) threads of *S. fomivorus* webs were determined using a mechanical testing device (Bose ElectroForce 3220) equipped with a 0.49 N load cell. The dry threads were mounted onto plastic frames with a gauge length of 2 mm using a high viscosity glue (UHU Super glue) and placed into the fume hood for immediate drying. Subsequently, the threads were observed using a light microscope (Leica Microscope DMI 3000B) and their diameters were determined using Leica Application Suite X software. The threads were uniaxially loaded using an extension rate of 0.005 mm s^{-1} at a relative humidity of 30%. A total number of 27 protruding threads originating from two individual webs (#1 = 8 samples, #2 = 19 samples) were analyzed. For the calculation of real stress σ_r and real strain ε_r data, Eqs. (1) and (2) were used, whereas σ (engineered stress) was calculated as the force divided by the thread cross-sectional area (assumed to be circular) and ε (engineered strain) values were calculated as the change in thread length divided by its original length.

$$\sigma_r = \sigma(1 + \varepsilon) \tag{1}$$

$$\varepsilon_r = \ln(1 + \varepsilon) \tag{2}$$

The Young's modulus was determined as the slope of the stress–strain plot in the linear elastic deformation range, and only regression lines were considered for data evaluation possessing a coefficient of determination > 0.9. The material toughness was assessed by integrating the stress–strain plot using Origin 8.1G. All error bars show standard deviation (SD).

Mechanical tests were conducted to analyze the lateral resilience of threads originating from the web of *S. formivorus* and of double-filament major ampullate silk of the orb weaver *Nephila edulis* (*N. edulis*). The samples were mounted onto plastic frames with a gauge length of 2 mm using a high viscosity glue (UHU Super glue) and dried immediately in the fume hood. Subsequently, the frames were horizontally fixed into a mechanical testing device (Bose ElectroForce 3220 equipped with a 2.45 N load cell) and a lateral force was applied onto the threads/fibers at a rate of 0.05 mm s^{-1} until rupture. Lateral resiliencies were investigated using 10 threads of a single web of *S. formivorus* and 14 double-filament major ampullate silks extracted from a single *N. edulis* spider. The lateral resiliencies were plotted against the cross-sectional areas of the *S. formivorus* threads and of the double-filament *N. edulis* silks. Cross-sections of the *S. formivorus* threads as well as of the *N. edulis* single filament silks were assumed to be circular.

Data availability

The authors declare that the data supporting our findings are available within the article and Supplementary Information.

Received: 19 May 2020; Accepted: 30 September 2020
Published online: 19 October 2020

References

1. Humenik, M., Scheibel, T. & Smith, A. Spider silk: Understanding the structure–function relationship of a natural fiber. *Prog. Mol. Biol. Transl.* **103**, 131–185 (2011).
2. Babb, P. L. *et al.* The Nephila clavipes genome highlights the diversity of spider silk genes and their complex expression. *Nat. Genet.* **49**, 895–903 (2017).
3. Yarger, J. L., Cherry, B. R. & van der Vaart, A. Uncovering the structure–function relationship in spider silk. *Nat. Rev. Mater.* **3**, 18008 (2018).
4. Blamires, S. J., Blackledge, T. A. & Tso, I. M. Physicochemical property variation in spider silk: Ecology, evolution, and synthetic production. *Annu. Rev. Entomol.* **62**, 443–460 (2017).
5. Römer, L. & Scheibel, T. The elaborate structure of spider silk: Structure and function of a natural high performance fiber. *Prion* **2**, 154–161 (2008).
6. Garb, J. E. *et al.* The transcriptome of Darwin's bark spider silk glands predicts proteins contributing to dragline silk toughness. *Commun. Biol.* **2**, 275 (2019).
7. Vollrath, F. & Porter, D. Spider silk as archetypal protein elastomer. *Soft Matter* **2**, 377–385 (2006).

8. Blackledge, T. A. & Hayashi, C. Y. Silken toolkits: Biomechanics of silk fibers spun by the orb web spider Argiope argentata (Fabricius 1775). *J. Exp. Biol.* **209**, 2452–2461 (2006).
9. Huemmerich, D. *et al.* Novel assembly properties of recombinant spider dragline silk proteins. *Curr. Biol.* **14**, 2070–2074 (2004).
10. Anton, A. M. *et al.* Foundation of the outstanding toughness in biomimetic and natural spider silk. *Biomacromol* **18**, 3954–3962 (2017).
11. Hardy, J. G., Römer, L. M. & Scheibel, T. R. Polymeric materials based on silk proteins. *Polymer* **49**, 4309–4327 (2008).
12. Shear, W. A. The evolution of spider webs: A third generation of hypotheses. In *Spiders: Webs, Behavior and Evolution* (ed. Shear, W. A.) 364–400 (Stanford University Press, Stanford, 1986).
13. Coddington, J. A., Agnarsson, I., Hamilton, C. A. & Bond, J. E. Spiders did not repeatedly gain, but repeatedly lost, foraging webs. *Peerj* **7**, e6703 (2019).
14. Shultz, J. W. The origin of the spinning apparatus in spiders. *Biol. Rev.* **62**, 89–113 (1987).
15. Morse, D. H. *Predator Upon a Flower: Life History and Fitness in a Crab Spider* 377 (Harvard University Press, Cambridge, 2007).
16. Benjamin, S. P., Dimitrov, D., Gillespie, R. G. & Hormiga, G. Family ties: Molecular phylogeny of crab spiders (Araneae: Thomisidae). *Cladistics* **24**, 708–722 (2008).
17. Llandres, A. L. & Rodriguez-Girones, M. A. Spider movement, UV reflectance and size, but not spider crypsis, affect the response of honeybees to Australian crab spiders. *PLoS One* **6**, e17136 (2011).
18. Vieira, C., Ramires, E. N., Vasconcellos-Neto, J., Poppi, R. J. & Romero, G. Q. Crab spider lures prey in flowerless neighborhoods. *Sci. Rep.* **7**, 9188 (2017).
19. Grawe, I., Wolff, J. O. & Gorb, S. N. Composition and substrate-dependent strength of the silken attachment discs in spiders. *J. R. Soc. Interface.* **11**, 20140477–20140477 (2014).
20. Rainbow, W. J. Two new thomisids. *Rec. Aust. Museum* **3**, 169–175 (1900).
21. Rainbow, W. J. Descriptions of some new araneidae of new south wales. *Proc. Linnean Soc. NSW* **22**, 514–553 (1897).
22. Elgar, M. A. Inter-specific associations involving spiders: Kleptoparasitism, mimicry and mutualism. *Mem. QL. Museum* **33**, 411–430 (1993).
23. McKeown, K. C. *Australian Spiders: Their Lives and Habits* (Angus & Robertson, Sydney, 1952).
24. Vongsvivut, J. *et al.* Synchrotron macro ATR-FTIR microspectroscopy for high-resolution chemical mapping of single cells. *Analyst* **144**, 3226–3238 (2019).
25. Bunaciu, A. A., Aboul-Enein, H. Y. & Fleschin, S. Vibrational spectroscopy in clinical analysis. *Appl. Spectrosc. Rev.* **50**, 176–191 (2015).
26. Kacurakova, M. & Wilson, R. H. Developments in mid-infrared FT-IR spectroscopy of selected carbohydrates. *Carbohyd. Polym.* **44**, 291–303 (2001).
27. Wiercigroch, E. *et al.* Raman and infrared spectroscopy of carbohydrates: A review. *Spectrochim. Acta A* **185**, 317–335 (2017).
28. Madsen, B., Shao, Z. Z. & Vollrath, F. Variability in the mechanical properties of spider silks on three levels: Interspecific, intraspecific and intraindividual. *Int. J. Biol. Macromol.* **24**, 301–306 (1999).
29. Agnarsson, I., Kuntner, M. & Blackledge, T. A. Bioprospecting finds the toughest biological material: Extraordinary silk from a giant riverine orb spider. *PLoS One* **5**, e11234 (2010).
30. Guinea, G. V. *et al.* Minor ampullate silks from Nephila and Argiope spiders: Tensile properties and microstructural characterization. *Biomacromol* **13**, 2087–2098 (2012).
31. Gosline, J. M., Guerette, P. A., Ortlepp, C. S. & Savage, K. N. The mechanical design of spider silks: From fibroin sequence to mechanical function. *J. Exp. Biol.* **202**, 3295–3303 (1999).
32. Lombardi, S. J. & Kaplan, D. L. The amino-acid-composition of major ampullate gland silk (dragline) of Nephila clavipes (Araneae, Tetragnathidae). *J. Arachnol.* **18**, 297–306 (1990).
33. Winkler, S. & Kaplan, D. L. Molecular biology of spider silk. *J. Biotechnol.* **74**, 85–93 (2000).
34. Moreira, G. R. P., Brito, R., Isaias, R. M. S., Silveira, J. & Gonçalves, G. L. A redescription of Antispastis clarkei pastrana (Lepidoptera, Glyphipterigidae) immature stages, with notes on the life history and phylogenetic placement of the genus. *Rev. Bras. Entomol.* **63**, 183–194 (2019).
35. David, A., Karina, B., Jean-FranÇois, L. & Jae-Cheon, S. Two new species of Wockia heinemann (Lepidoptera: Urodidae) from coastal dry-forests in western México. *Proc. Entomol. Soc. Wash.* **111**, 166–182 (2009).
36. Kaila, L., Nupponen, K., Gorbunov, P. Y., Mutanen, M. & Heikkilä, M. Ustyurtiidae, a new family of Urodoidea with description of a new genus and two species from Kazakhstan, and discussion on possible affinity of Urodoidea to Schreckensteinioidea (Lepidoptera). *Insect Syst. Evol.* **51**, 444 (2020).
37. Bauer, F., Bertinetti, L., Masic, A. & Scheibel, T. Dependence of mechanical properties of lacewing egg stalks on relative humidity. *Biomacromol* **13**, 3730–3735 (2012).
38. Zhang, S. *et al.* A novel property of spider silk: Chemical defence against ants. *Proc. Biol. Sci.* **279**, 1824–1830 (2012).
39. Henneken, J., Goodger, J. Q. D., Jones, T. M. & Elgar, M. A. The potential role of web-based putrescine as a prey-attracting allomone. *Anim. Behav.* **129**, 205–210 (2017).
40. Neinhuis, C. & Barthlott, W. Characterization and distribution of water-repellent, self-cleaning plant surfaces. *Ann. Bot. Lond.* **79**, 667–677 (1997).
41. Vetter, R. S. *et al.* Efficacy of several pesticide products on brown widow spider (Araneae: Theridiidae) egg sacs and their penetration through the egg sac silk. *J. Econ. Entomol.* **109**, 267–272 (2016).
42. Correa-Garhwal, S. M. *et al.* Semi-aquatic spider silks: Transcripts, proteins, and silk fibres of the fishing spider, Dolomedes triton (Pisauridae). *Insect Mol. Biol.* **28**, 35–51 (2019).
43. Heim, M., Keerl, D. & Scheibel, T. Spider silk: From soluble protein to extraordinary fiber. *Angew. Chem. Int. Ed. Engl.* **48**, 3584–3596 (2009).
44. Zhao, A. C. *et al.* Novel molecular and mechanical properties of egg case silk from wasp spider, *Argiope bruennichi*. *Biochemistry* **45**, 3348–3356 (2006).
45. Stubbs, D. G., Tillinghast, E. K., Townley, M. A. & Cherim, N. A. Fibrous composite structure in a spider silk. *Naturwissenschaften* **79**, 231–234 (1992).
46. Hu, X. Y. *et al.* Egg case protein-1—a new class of silk proteins with fibroin-like properties from the spider latrodectus hesperus. *J. Biol. Chem.* **280**, 21220–21230 (2005).
47. Lee, H. S., Qi, Y. & Im, W. Effects of N-glycosylation on protein conformation and dynamics: Protein data bank analysis and molecular dynamics simulation study. *Sci. Rep.* **5**, 8926–8926 (2015).
48. Kovoor, J. & Zylberberg, L. Fine structural aspects of silk secretion in a spider (*Araneus diadematus*). I. Elaboration in the pyriform glands. *Tissue Cell* **12**, 547–556 (1980).
49. Saheb, D. N. & Jog, J. P. Natural fiber polymer composites: A review. *Adv. Polym. Technol.* **18**, 351–363 (1999).
50. Kalia, S., Kaith, B. S. & Kaur, I. Pretreatments of natural fibers and their application as reinforcing material in polymer composites—a review. *Polym. Eng. Sci.* **49**, 1253–1272 (2009).
51. Chae, H. G. & Kumar, S. Materials science—making strong fibers. *Science* **319**, 908–909 (2008).
52. Wolff, J. O., Grawe, I., Wirth, M., Karstedt, A. & Gorb, S. N. Spider's super-glue: Thread anchors are composite adhesives with synergistic hierarchical organization. *Soft Matter* **11**, 2394–2403 (2015).

53. Li, V. C. On engineered cementitious composites (ECC) a review of the material and its applications. *J. Adv. Concr. Technol.* **1**, 215–230 (2003).
54. Hu, X., Kaplan, D. & Cebe, P. Determining beta-sheet crystallinity in fibrous proteins by thermal analysis and infrared spectroscopy. *Macromolecules* **39**, 6161–6170 (2006).
55. Petzold, J. *et al.* Surface features of recombinant spider silk protein eADF4(kappa 16)-made materials are well-ssuited for cardiac tissue engineering. *Adv. Funct. Mater.* **27**, 1701427 (2017).
56. Borkner, C. B., Lentz, S., Müller, M., Fery, A. & Scheibel, T. Ultrathin spider silk films: Insights into spider silk assembly on surfaces. *ACS Appl. Polym. Mater.* **1**, 3366–3374 (2019).
57. Thamm, C. & Scheibel, T. Recombinant production, characterization, and fiber spinning of an engineered short major ampullate spidroin (MaSp1s). *Biomacromol* **18**, 1365–1372 (2017).
58. DeSimone, E., Aigner, T. B., Humenik, M., Lang, G. & Scheibel, T. Aqueous electrospinning of recombinant spider silk proteins. *Mater. Sci. Eng. C* **106**, 110145 (2020).

Acknowledgements

We would like to thank Yeldem Koc for her support in tensile testing and web photographs as well as Dr. Stefan Flauder, Margrit Fuchs and Tom Liensdorf for the help with the embedding and grinding of samples. Special thanks to Birgit Brunner for performing the elemental analysis and to Donna Menzies for technical support during the synchrotron beamtime. The synchrotron experiments were performed through the beamtime proposals ID M13022 and M13972. The authors acknowledge financial support by the German Academic Exchange service (DAAD) through its Thematic Network Melbourne-Bayreuth Polymer/Colloid Network sponsored from funds of the Federal Ministry of Education and Research (BMBF). This work was further financially supported by SFB 840 TP A8 to T.S., and the Australian Research Council (ARC A19331563) to M.A.E.

Author contributions

Conceptualization, C.H., M.A.E., T.S.; methodology, C.H., M.A.E., T.S.; investigation, C.H., J.V., K.R.H.M., H.B., V.J.N., M.A.E.; resources; C.H., J.V., M.J.T., M.A.E., T.S.; writing—original draft, C.H.; writing—review and editing, C.H., J.V., M.J.T., M.A.E., T.S.; visualization, C.H.; supervision, M.A.E., T.S.; project administration, C.H., J.V., M.J.T., M.A.E., T.S.; funding, M.A.E. and T.S.

Funding

Open Access funding enabled and organized by Projekt DEAL.

Competing interests

The authors declare no competing interests.

Additional information

Supplementary information is available for this paper at https://doi.org/10.1038/s41598-020-74469-z.

Correspondence and requests for materials should be addressed to M.A.E. or T.S.

Reprints and permissions information is available at www.nature.com/reprints.

Publisher's note Springer Nature remains neutral with regard to jurisdictional claims in published maps and institutional affiliations.

Supplementary Information for

Free-standing spider silk webs of the thomisid *Saccodomus formivorus* are made of composites comprising micro- and submicron fibers

Christian Haynl,[1] *Jitraporn Vongsvivut,*[2] *Kai R. H. Mayer,*[1] *Hendrik Bargel,*[1] *Vanessa J. Neubauer,*[1] *Mark J. Tobin,*[2] *Mark A. Elgar*[3,*] *and Thomas Scheibel*[1,4,5,6,7,*]

[1]University of Bayreuth, Department for Biomaterials, Prof.-Rüdiger-Bormann-Str.1, 95447 Bayreuth, Germany

[2]ANSTO Australian Synchrotron, Infrared Microspectroscopy Beamline, Clayton, Victoria 3168, Australia

[3]The University of Melbourne, School of BioSciences, Melbourne, Victoria 3010, Australia

[4]University of Bayreuth, Bayreuther Zentrum für Kolloide und Grenzflächen (BZKG), Universitätsstraße 30, 95440 Bayreuth, Germany

[5]University of Bayreuth, Bayerisches Polymerinstitut (BPI), Universitätsstraße 30, 95440 Bayreuth, Germany

[6]University of Bayreuth, Bayreuther Zentrum für Molekulare Biowissenschaften (BZMB), Universitätsstraße 30, 95440 Bayreuth, Germany

[7]University of Bayreuth, Bayreuther Materialzentrum (BayMAT), Universitätsstraße 30, 95440 Bayreuth, Germany

[*]To whom correspondence should be addressed: T.S. and M.A.E.

(thomas.scheibel@bm.uni-bayreuth.de, m.elgar@unimelb.edu.au)

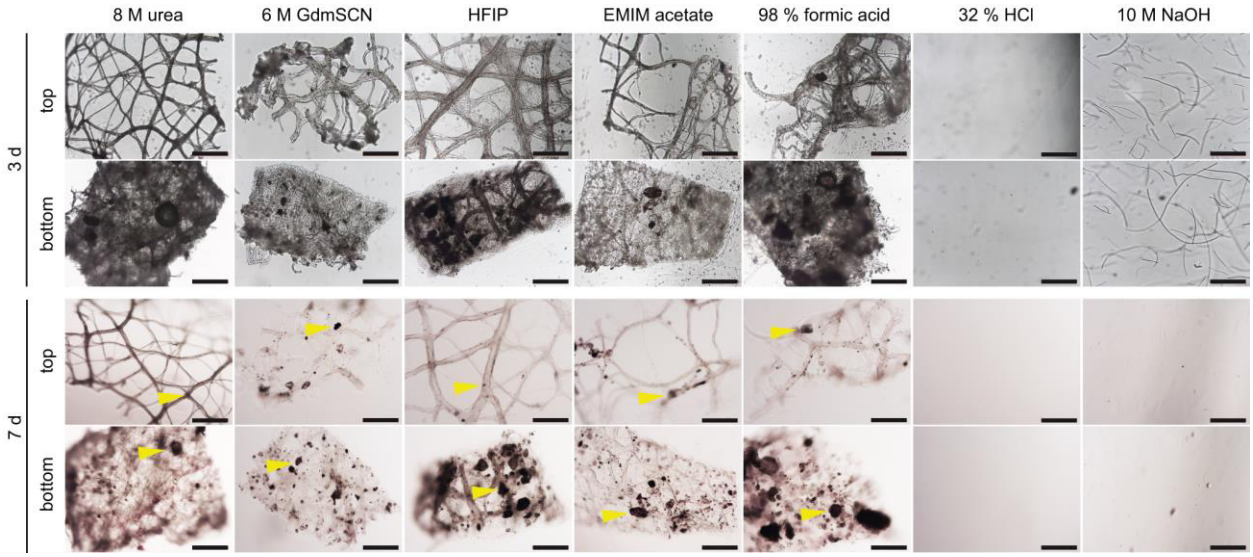

Figure S1. Chemical resistance of *S. formivorus* upper and lower web sections. Light microscopy images after 3 and 7 d incubation at room temperature in i) chaotropic agents including urea or guanidinium thiocyanate (GdmSCN), ii) hexafluoroisopropanol (HFIP), iii) 1-Ethyl-3-methylimidazolium acetate (EMIM acetate), iv) formic and hydrochloric acid and v) sodium hydroxide. Yellow arrowheads indicate dust particles. The scale bars are 500 µm.

Table S1. Molar fractions of carbon (*C*), hydrogen (*H*), nitrogen (*N*) and sulphur (*S*) found in the threads of the upper and lower sections of *S. formivorus* webs.

Material	**Carbon (*C*) [mol %]**	**Hydrogen (*H*) [mol %]**	**Nitrogen (*N*) [mol %]**	**Sulphur (*S*) [mol %]**
Upper section	33.97 ± 0.38	56.05 ± 0.29	9.97 ± 0.08	0.01 ± 0.01
Lower section	33.78 ± 0.52	56.56 ± 0.80	9.64 ± 0.49	0.02 ± 0.01

DANKSAGUNG

Ich danke meinem Doktorvater Prof. Dr. Thomas Scheibel
der mich in unglaublich spannende und herausfordernde Projekte einband
und der es auch während zäher Experimente mich zu motivieren verstand
Auch danke ich Ihm für das in mich gesetzte Vertrauen
und, dass er mir ermöglichte zu Forschungszwecken in Australien
auch über den deutschen Tellerrand hinweg zu schauen

Großer Dank geht an Prof. Dr. Stephan Förster und Eddie Hofmann für die tolle Kooperation
dadurch ergaben sich neue Mikrofluidik-Systeme mit interessanter Funktion

Ich danke Prof. Dr. Mark Elgar für die abenteuerliche Spinnennetzsuchaktivität
und Prof. Dr. Andrea O'Connor für die Tipps hinsichtlich der Gele mit erhöhter Porosität

Auch danke ich Prof. Dr. Stefan Schuster, Dr. Sahar Salehi, Dr. Kiran Pawar und Dr. Georg Welzel für die Zusammenarbeit im Bereich der neuronalen Differenzierung
und Birgit Brunner sowie Andreas Schedl für die chemische Quantifizierung

Besonders danke ich Dr. Hendrik Bargel für die gemeinsamen Stunden am REM
sowie Dr. Jitraporn Vongsvivut, Dr. Mark Tobin, Vanessa Neubauer und Kai Mayer für schlaflose Nächte an der Australian Synchrotron Beamline *IRM*

Dank gebührt Dr. Martin Humenik und Elise Liensdorf für das Gegenlesen meiner Dissertation
sowie meinen ehemaligen studentischen Hilfskräften Vanessa Trossmann und Yeldem Koc für ihre hohe Motivation

Großer Dank geht auch an Andrea Bodner, Sabrina Schwägerl und Christa Vogel für die großartige Hilfe bei organisatorischen Notwendigkeiten
und an Claudia Stemmann, Alexandra Pellert, Johannes Diehl und Andreas Schmidt für die Unterstützung bei zahlreichen labortechnischen Angelegenheiten

Danke auch an Kim Koeck, Angela Maria Arias Jaramillo und Dr. Martin Neuenfeldt für das gemeinsame sportliche Schwitzen
war wirklich jedes Mal eine erholsame Abwechslung nach dem stundenlangen Sitzen

Übergreifend möchte ich mich auch noch bei ALLEN aktuellen und früheren Biomat'lern für die wissenschaftlichen Diskussionen und die freundschaftliche Atmosphäre bedanken
und habe da im Speziellen meine ehemaligen Längerzeit-Bürokollegen Dr. Christopher Thamm, Dr. Joschka Bauer, Phillip Nowotny, Dr. Adrian Golser, David Sonnleitner sowie

meine Schreibbüro-Mitstreiter Elise Liensdorf, Tamara Aigner und Heike Herold
in Gedanken

Für den steten Rückenwind und für viele offene Ohren
danke ich zu guter Letzt meinen Eltern, meiner Freundin und meinen Freunden von dahoam

(Eidesstattliche) Versicherungen und Erklärungen

(§ 9 Satz 2 Nr. 3 PromO BayNAT)

Hiermit versichere ich eidesstattlich, dass ich die Arbeit selbstständig verfasst und keine anderen als die von mir angegebenen Quellen und Hilfsmittel benutzt habe (vgl. Art. 64 Abs. 1 Satz 6 BayHSchG).

(§ 9 Satz 2 Nr. 3 PromO BayNAT)

Hiermit erkläre ich, dass ich die Dissertation nicht bereits zur Erlangung eines akademischen Grades eingereicht habe und dass ich nicht bereits diese oder eine gleichartige Doktorprüfung endgültig nicht bestanden habe.

(§ 9 Satz 2 Nr. 4 PromO BayNAT)

Hiermit erkläre ich, dass ich Hilfe von gewerblichen Promotionsberatern bzw. -vermittlern oder ähnlichen Dienstleistern weder bisher in Anspruch genommen habe noch künftig in Anspruch nehmen werde.

(§ 9 Satz 2 Nr. 7 PromO BayNAT)

Hiermit erkläre ich mein Einverständnis, dass die elektronische Fassung meiner Dissertation unter Wahrung meiner Urheberrechte und des Datenschutzes einer gesonderten Überprüfung unterzogen werden kann.

(§ 9 Satz 2 Nr. 8 PromO BayNAT)

Hiermit erkläre ich mein Einverständnis, dass bei Verdacht wissenschaftlichen Fehlverhaltens Ermittlungen durch universitätsinterne Organe der wissenschaftlichen Selbstkontrolle stattfinden können.

…….
Ort, Datum, Unterschrift